New ways to tune the multi-functionality of oxide thin films for memory applications

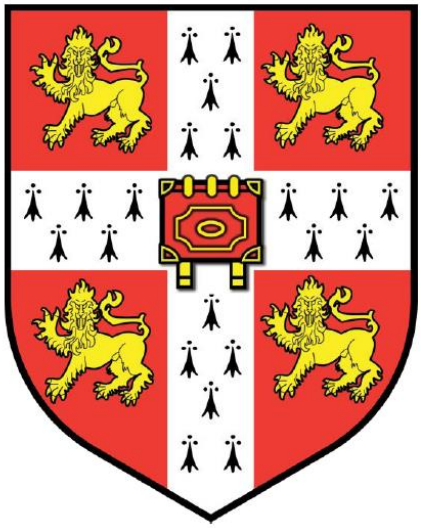

Chao Yun

King's College

Department of Materials Science & Metallurgy

University of Cambridge

A THESIS SUBMITTED FOR THE DEGREE OF

Doctor of Philosophy

January 2019

Declaration

This dissertation is the result of my own work and includes nothing which is the outcome of work done in collaboration except as declared in the Preface and specified in the text. It is not substantially the same as any that I have submitted, or, is being concurrently submitted for a degree or diploma or other qualification at the University of Cambridge or any other University or similar institution except as declared in the Preface and specified in the text. I further state that no substantial part of my thesis has already been submitted, or, is being concurrently submitted for any such degree, diploma or other qualification at the University of Cambridge or any other University or similar institution except as declared in the Preface and specified in the text. It does not exceed the prescribed word limit (60,000 words), exclusive of figure captions and bibliography.

This dissertation is submitted to the University of Cambridge for the degree of Doctor of Philosophy. The works described were carried out between January 2015 and December 2018 at the Department of Materials Science & Metallurgy, University of Cambridge under the supervision of Prof. Judith L. MacManus-Driscoll.

Chao Yun

January 2019

Cambridge

New ways to tune the multi-functionality of oxide thin films for memory applications

Chao Yun

Abstract

This thesis presents studies on engineering the electrical and magnetic properties in oxide thin films using vertically-aligned nanocomposites (VAN). The works aim to enhance their multi-functionality for various memory applications.

First, electroforming-free resistive switching (RS) with high ON/OFF ratio is realized in a novel model VAN system based on self-assembled Sm-doped CeO_2 and $SrTiO_3$ films that allow separate tailoring of nano-scale ionic and electronic channels at a high density (10^{12} $inch^{-2}$). These devices allow precise engineering of the resistance states, thus enabling large and tunable ON/OFF ratios and high stability for acting as resistive random access memory (RRAM) devices.

Second, the ferromagnetic insulating (FMI) and metallic (FMM) properties of $La_{0.9}Ba_{0.1}MnO_3$ (LBMO) are tuned using VAN. $La_{0.9}Ba_{0.1}MnO_3$ is FMI in bulk but usually shows metallicity in plain films. By using VAN consisting of CeO_2 nanocolumns embedded in a $La_{0.9}Ba_{0.1}MnO_3$ matrix, the FMI property is maintained in thin film form. The CeO_2 phase acts as strain-controlling nanocolumns and at the same time, produces light Ce doping of the LBMO and thus filling of intrinsic cation vacancies. Together these reduce the unwanted double exchange (DE) coupling. This is hard to realize in plain LBMO films which contain cation vacancies, and have

several strain-relaxing LBMO phases which result in an enhanced Mn^{4+}/Mn^{3+} ratio, and hence to DE coupling and metallicity. Besides, by varying the growth temperature of the LBMO–CeO_2 VAN, the system is engineered from a FMI to a FMM and the magnetoresistance is highly tunable, which are correlated to the tuning of the lateral size of both phases. These effects are attributed to a dimension change-induced change in the electronic band structure. The tunable properties of LBMO–CeO_2 VAN make it a good candidate as low-power-consumption, high-T_c FMI and FMM components in magnetic random access memory (MRAM) and spintronic devices.

Last, *in-situ* electric field tuning of magnetic properties is studied in $La_{0.9}Ba_{0.1}MnO_3$-ZnO VAN, a novel candidate for magnetoelectric random access memory (MERAM) devices. The *M-H* curves and the remanence are tuned by applying electric fields at a low temperature (10 K). The possible origins for the magnetic modifications are discussed rationally, which include Joule heating, piezoelectric strain, current-induced induction field and charge trapping/detrapping related to a resistive switching effect (which is found to be the most likely mechanism for a hysteretic tuning of the remanence). All these effects are correlated to the existence of the ZnO phase. This work helps to understand the charge doping effect in manganite-ZnO VAN systems.

To my beloved parents

致父母

Acknowledgments

Many people have provided valuable support for the completion of the work performed in this doctoral dissertation. First and foremost, I would like to thank my supervisor Prof. Judith MacManus-Driscoll for providing me the opportunity to work on my interested topics. I am forever indebted to her unconditional help throughout the entire period of my research. In the past four years, she was always enlightening and encouraging me and I cannot thank her enough for that. I would also like to thank her for patiently refining and proofreading my research papers as well as this thesis.

I would also like to thank Dr. Jason Robinson and Dr. Xavier Moya for providing me useful technical help. In addition, I would like to thank Dr. Seungho Cho, Dr. Eun-Mi Choi, Dr. Weiwei Li, and Dr. Rui Wu for discussions and helps on daily basis. Seungho provided me detailed instrumental training and we've established intimate collaborations in the early stage of my work. Eun-mi contributed countless theoretical guidance for data analysis and results interpretation. Weiwei patiently gave me innumerable experimental help and inspirations which cover the whole range of my research. Rui insightfully guided me on the research principles in every step of my work. Thanks also to Dr. Sen Zhang, Dr. José Kleibeuker, Dr. Ady Suwardi for technical help. Many thanks to Prof. Haiyan Wang (Purdue University, USA) and special thanks to Xing Sun and other members from her group (Jie Jian, Sichuang Xue), Dr. Ping Lu (Sandia National Laboratory, USA), and Dr. Quanxi Jia USA) for collaboration works on TEM.

I would like to give special thanks to Dr. Mary Vickers for her kind, detailed and patient guidance on XRD measurements. Without her, my knowledge in crystallography couldn't improve so fast. Besides, I would like to express my gratitude to Dr. Ahmed Kursumovic, who is always ready for help on technical problems with her unique insights. I would also like to thank Dr. Angelo_Di_Bernardo for technical support on physical property measurements and many thanks to his patience and endeavor to help maintain the Cryofree, wire bonder equipment in the group. I would also like to thank Dr. Nadia Stelmashenko, Dr. Cheng Liu for technical help. I am grateful to John Feighan, Samer Kurdi, Bhasi Nair, Samir Giri, Tuhin Maity to help me review my thesis.

I would like to thank the Cambridge Commonwealth, European & International Trust and King's College for supporting my study.

I would also like to give special thanks to Mr. Yisong Lin, Mr. Tiesheng Wang, Dr. Jingwei Hou, Mr. Zeyu Deng. You are really important to my PhD life, not only because of your valuable help on research but also because of our valuable friendship. I will never forget the moments when we enjoy life together. My PhD life would be much more boring without you. I would like to give my sincere wishes to all of you.

Last but not least, I am most grateful to my family, especially my grandfather, my parents and sister for their love, support and patience throughout my life. Thank you papa and mama for your encouragement all the time. Words cannot express my heartfelt gratitude to my family and I would like to dedicate this thesis to them.

Table of contents

List of figures

List of tables

List of Acronyms

AC	Alternating current
AFM	Atomic force microscopy
C-AFM	Conductive atomic force microscopy
DC	Direct current
DE	Double exchange
FMI	Ferromagnetic insulator (or ferromagnetic insulating)
FMM	Ferromagnetic metal (or ferromagnetic metallic)
FWHM	Full width half maximum
HRTEM	High-resolution transmission electron microscopy
ip	in-plane
LBMO	$La_{0.9}Ba_{0.1}MnO_3$
MERAM	Magnetoelectric random access memory
MRAM	Magnetic random access memory
NC	Nanocomposite
op	out-of-plane
PF	Plain film
PFM	Piezo force microscopy
PLD	Pulsed laser deposition
PPMS	Physical Properties Measurement System
RRAM	Resistive random access memory
RS	Resistive switching
RSM	Reciprocal space map
SAED	Selected area electron diffraction
SDC	Sm-doped CeO_2
SEM	Scanning electron microscopy
SQUID	Superconducting quantum interference device
STEM	Scanning tunneling electron microscopy
STO	$SrTiO_3$
T_c	Curie Temperature
T_M	Insulator-metal transition temperature
TEM	Tunneling electron microscopy
UV	Ultraviolet
VAN	Vertically-aligned nanocomposite
XPS	X-ray photoelectron spectroscopy
XRD	X-ray Diffraction

Chapter 1 Overview

1.1 Background

Metal oxides have a wide range of fascinating functionalities and hence have many applications ranging from microwave devices to sensors, actuators, and memories. The transition metals lie within a special range in the periodic table, from groups 3 to 12. The partially filled active *d* shells of the transition metals enable a strong coupling between spin-charge-orbital-lattice degrees of freedoms. This strong coupling, together with the versatile nature of oxygen, enable highly tunable multi-functionality of the transition metal oxides (TMO). Among their various physical features, electrical and magnetic properties are two of the most versatile and important functionalities. Recent breakthroughs in electronics, spintronics, and multiferroics are promising for bringing memory and logic applications to a new era.

Epitaxial oxide thin films are a special family of oxides grown on single-crystalline substrates. The epitaxy not only enables enhanced crystallinity compared with the polycrystalline bulk but also provides strain tuning and interfacial coupling, thus bringing about fascinating opportunities for the realization of improved properties and emergent electronic phenomena.

While the capabilities of single-phase oxide films have reached their limits, the pursuit of composite alternatives has triggered the development of tremendous materials-engineering methods. One striking example is self-assembled vertically-aligned nanocomposites (VAN), where one columnar phase is embedded inside another matrix phase. This vertical heteroepitaxy can integrate the advantages of both phases, or bring in new functionalities from vast strain tuning and interfacial coupling, greatly expanding the spectrum for engineering functional oxides.

1.2 Motivation

The works in this thesis are triggered by the need for tuning the electrical and magnetic properties of TMO thin films using new approaches (e.g. the VAN approach here), which aims to enhance their multi-functionality for potential applications in memory devices.

The development of the novel computing and digital industry has brought about various non-volatile memory techniques, including electrical-based, magnetic-based, and magnetoelectric approaches. Oxide-based memories are structurally compatible and have the potential to compete with $SrTiO_3$-buffered Si devices. Among all the novel memory candidates, several are widely studied in TMOs: resistive random access memory (RRAM) makes use of electrical signals (current or resistance) for storage, magnetic random access memory (MRAM) and spintronic devices rely on magnetic signals (the magnetic moment or spin), and magnetoelectric random access memory (MERAM) has the potential to integrate multiple electrical and magnetic signals in one device and thus enhance storage capabilities. Currently, there are several issues in the study of these memory techniques:

1. Firstly, RRAM devices suffer from several technical problems. First is the degradation of plain film-based devices in the artificial fabrication processes for dense, nano-scale memory cells. Second is the harmful/uncontrollable electroforming process, which shortens the device lifetime. Besides, the mixture of ion/electron conductance channels in single-phase oxides makes it difficult to study the physical mechanisms and limits the application of RRAM (e.g. in neuro computing). Thus, nano-scale self-assembled, electroforming-free RRAM devices with decoupled conductance channels are highly desired.

2. Secondly**,** in the MRAM (and spintronics) area, a major issue is the power consumption generated by electrical current flow used to “write” the memory signals. Thus, a new development direction is to replace electrical currents with an electric field or directly using pure spin flows as memory signals. Hence searching for

high-Curie-Temperature (T_c) ferromagnetic insulators (which are rare) to transport/filter spin currents or to endure electric fields is one possible solution. Apart from ferromagnetic insulators (FMI), ferromagnetic metals (FMM) are also important components in MRAM (and spintronic) devices. It is intriguing to tune and realize these two functionalities within one material and by using the same material for different device components, one can simplify the fabrication process and improve the integration compatibilities between components in one device. Plain oxide films only show limited tunability of these functionalities and thus it is worthwhile to develop new tuning approaches.

3. Lastly, in conventional plain film-based MERAM devices, the substrate strain clamping effect, the short charge screening length and the limited choice of coexisting ferromagnetic and ferroelectric constituents largely restrict the extent of magnetoelectric coupling and thus limits the device applications. It is intriguing to solve these problems through novel structural design and materials exploration.

The above bottlenecks or issues in memories can be addressed by nanoengineering through composites, and, as discussed above, the oxide VAN structure provides a new platform to realize this:

First, VAN enables self-assembly of nano-scale memory cells, which eliminates the need for artificial fabrication and avoids the related degradation problems for RRAM devices. The unique VAN structure can be divided into three independent components (as specified later in Fig. 4-5, Chapter 4), which helps to decouple the ionic and electronic channels. The vertical interface usually has enhanced electronic conductivity, which assists in eliminating the electroforming process. Electronic-active $SrTiO_3$ and ionic-conductive CeO_2, which are favorable for realizing these aims, are selected as candidate VAN components.

Second, the nano-scale vertical heteroepitaxy enables adequate interfacial coupling, strain control or charge transfer. This enables delicate nanoengineering to achieve the goal of obtaining high-T_c ferromagnetic insulators/metals or enhancing the tunability

of these properties, approaching the need for providing better-quality functional components for MRAM and spintronic devices. The versatile combination of constituent phases effectively enlarges the scope of coupling between magnetic and electrical degrees of freedom, aiming for novel and high performances for MERAMs. The lightly-doped manganite ($La_{0.9}Ba_{0.1}MnO_3$), which have highly tunable physical properties under physical and chemical stimuli, make all these issues addressable.

The ultimate goal of this work, as discussed above, is to use the VAN approach to design novel materials systems to stress the above issues raised in RAMs whilst demonstrating enhancement of the respective device performances.

1.3 Framing the thesis

- *Chapter 2* represents a general introduction, which includes the electrical/magnetic properties of TMOs, memory techniques using electrical/magnetic signals, an introduction to VAN, and the advances of VAN in tuning memory-related functionalities. A more detailed literature review regarding the research issues in different RAMs and materials selection for the study of these topics will also be provided at the beginning of each result chapter as a more specific introduction.
- *Chapter 3* describes the experimental methods used in the works.
- *Chapters 4* to *6* represent results and discussions:
  - *Chapter 4* is focused on enhancing the resistive switching (RS) performance in a RRAM candidate: a high-quality VAN of Sm-doped CeO_2 and $SrTiO_3$ (SDC-STO). First, electroforming-free RS with an enhanced ON/OFF ratio ($>10^4$) and suitable stability is realized by delicate optimization. Then, after studying the conduction mechanisms, the reason for elimination of the electroforming process is analyzed, and a model based on separate ionic/electronic channels is proposed as the mechanism for the RS effect. Further evidence is provided to prove this model, based on which separate

tailoring of the ionic and electronic channels is realized and a guideline is proposed and proved for synergetic improvement of the RRAM performance.

- *Chapter 5* is mainly focused on the tuning of ferromagnetic insulating/metallic properties of manganites for MRAM and spintronic applications. The materials system is a VAN of lightly-doped $La_{0.9}Ba_{0.1}MnO_3$ and CeO_2. This part consists of two sub-sections:
  - First, a new FMI candidate is studied: the $La_{0.9}Ba_{0.1}MnO_3$ (LBMO)-CeO_2 VAN. $La_{0.9}Ba_{0.1}MnO_3$ is a FMI in bulk but shows an insulator-metal transition in plain thin films. Using light strain+doping from CeO_2, the FMI properties of the LBMO phase are maintained in thin films. This result is shown in *Chapter 5.3*.
  - Then, a more comprehensive nanoengineering study on the LBMO-CeO_2 VAN is presented: the LBMO phase is tuned from a FMI to a FMM by changing the growth temperature. The tuning effect is correlated to the change in the self-assembly kinetics which results in a simultaneous change of the lateral size of the CeO_2 nanocolumns and the LBMO phase. This result is shown in *Chapter 5.4*.
- *Chapter 6* presents results on *in-situ* electric field tuning of ferromagnetism in a new ferromagnetic-nonferroelectric MERAM candidate: the $La_{0.9}Ba_{0.1}MnO_3$-ZnO VAN. The *M-H* curves and the remanence are tuned by applying electric fields at a low temperature (10 K). The possible origins for the magnetic modification are rationally discussed, which include Joule heating, piezoelectric strain, current-induced induction field and charge trapping/detrapping related to a resistive switching effect (which is found to be the most likely mechanism for a hysteretic tuning of the remanence). All of these effects are correlated to the existence of the ZnO phase.
- Lastly, *Chapter 7* provides a conclusion of the overall doctoral work, including a summary of the key findings and perspectives for future work.

1.4 Publications

1. Cho, S.[+]; **Yun, C.**[+]; Tappertzhofen, S.; Kursumovic, A.; Lee, S.; Lu, P.; Jia, Q.; Fan, M.; Jian, J.; Wang, H.; *et al*. Self-Assembled Oxide Films with Tailored Nanoscale Ionic and Electronic Channels. ***Nat. Commun.*** 2016, *7*, 12373. ([+]equal contribution)
2. **Yun, C.**; Choi, E.-M.; Li, W.; Sun, X.; Maity, T.; Wu, R.; Jian, J.; Xue, S.; Cho, S.; Wang, H.; MacManus-Driscoll, J. L. Achieving Ferromagnetic Insulating Properties of $La_{0.9}Ba_{0.1}MnO_3$ in Thin Films through Nanoengineering. *Under revision.*
3. **Yun, C.**; Li, W.; Sun, X.; Choi, E.-M.; Jian, J.; Wang, H.; MacManus-Driscoll, J. L. Nanoengineering $La_{0.9}Ba_{0.1}MnO_3$ from a ferromagnetic metal to a ferromagnetic insulator via self-assembled modulation of the lateral size. *In preparation*
3. Wu, R.[+]; **Yun, C.**[+]; Wang, X.; Lu, P.; Li, W.; Lin, Y.; Choi, E.-M.; Wang, H.; MacManus-Driscoll, J. L. All-Oxide Nanocomposites to Yield Large, Tunable Perpendicular Exchange Bias above Room Temperature. ***ACS Appl. Mater. Interfaces*** 2018, 10 (49), 42593–42602.
   My contribution: Film growth and characterization
4. Cho, S.[+]; **Yun, C.**[+]; Kim, Y. S.; Wang, H.; Jian, J.; Zhang, W.; Huang, J.; Wang, X.; Wang, H.; MacManus-Driscoll, J. L. Strongly Enhanced Dielectric and Energy Storage Properties in Lead-Free Perovskite Titanate Thin Films by Alloying. ***Nano Energy*** 2018, 45 (September 2017), 398–406.
   My contribution: Ferroelectric measurements
5. Wu, R.; Kursumovic, A.; Gao, X.; **Yun, C.**; Vickers, M. E.; Wang, H.; Cho, S.; MacManus-Driscoll, J. L. Design of a Vertical Composite Thin Film System with Ultralow Leakage To Yield Large Converse Magnetoelectric Effect. ***ACS Appl. Mater. Interfaces*** 2018, 10 (21), 18237–18245.
   My contribution: XRD measurements
6. Li, W.; Kleibeuker, J. E.; Wu, R.; Zhang, K. H. L.; **Yun, C.**; MacManus-Driscoll, J. L. Insulating-to-Conducting Behavior and Band Profile across the $La_{0.9}Ba_{0.1}MnO_3$/Nb-$SrTiO_3$ epitaxial interface. ***Phys. Rev. B*** 2017, 96 (16), 165103.
   My contribution: Electrical transport measurements

1.5 Conferences

1. **Yun, C.** *et al*. **"**Manipulating ionic and electronic channels for enhancing resistive switching in vertically-aligned nanocomposites**",** *UK Ceramics Talent 2018*, 10 Oct 2018, Queen Mary University of London, London, UK, Oral presentation.
2. **Yun, C.** *et al*. "Self-assembled oxide films with tailored nanoscale ionic and electronic channels for controlled resistive switching", *2nd Functional Oxide Thin Films for Advanced Energy and Information Technology*, 05~08 Mar 2016, Cancun, Mexico, poster presentation, **2nd prize in poster award.**
3. **Yun, C.** *et al*. "Resistive switching in self-assembled nanocomposites", *International School of Oxide Electronics*, 12~24 Oct 2015, Cargese, Corsica, France, poster presentation.

Chapter 2 Introduction

This chapter provides a general introduction to the background knowledge related to the works in this dissertation. A literature review in this chapter introduces the basics for electrical/magnetic properties in functional oxides, and then briefly discusses novel electrical/magnetic-based memory techniques, after which the VAN structure is introduced and the advantage of oxide VAN thin films for novel memory applications is discussed.

2.1 Functional oxides

Functional oxides represent a group of smart oxide systems in which their physical and chemical properties can be modified by adjusting the anionic deficiency, cationic valence, or lattice deformation. They have a variety of crystal structures and unique properties, covering all aspects of condensed matter physics. Many transition metal oxides (TMO) are classified into the strongly correlated oxide family, which exhibit a coupling among the orbital-lattice-spin-charge degrees of freedom. These strong correlations have generated a broad spectrum of electronic, magnetic properties and even a coupling between these properties. The study of these multi-functionalities has brought about a revolution in memory techniques.

2.1.1 Crystal structures of metal oxides

Metal oxides are built from ionic bonds. Different ionic radii and different geometries of ionic bonds result in different kinds of unit cell structures. In general, metal oxides are classified into binary and ternary (or multinary) based on the number of different metals in the crystal structure. A summary of metal oxide crystal structures is shown in Table 2-1. These structures cover most of the metal-oxide family. Among the functional oxides listed, perovskite oxides have gained increasing significance due to

their attractive properties (insulating dielectrics, ferroelectrics, ferromagnetics, multiferroics, etc) and are the main focus of this work. Detailed introduction to the crystal structures of the oxide phases used in this thesis will be presented at the beginning of each result chapter.

Table 2-1. Crystal structures of metal oxides[1]

	Structure	Materials
Binary metal oxide	Fluorite	CeO_2, ZrO_2, ThO_2
	Rocksalt	MgO, CoO, MnO, NiO
	Rutile	TiO_2, WO_2, MoO_2
	Corundum	Al_2O_3, V_2O_3, Cr_2O_3
	Wurtzite (Hexagonal)	ZnO, BeO
	Bixbyite	Sm_2O_3, Mn_2O_3, In_2O_3
Ternary (or multinary) metal oxide	Perovskite	$SrTiO_3$, $Re_{1-x}A_xMnO_3$, $BiFeO_3$
	Spinel	$CoFe_2O_4$, $NiFe_2O_4$, $MgAl_2O_4$
	Layered Perovskite	$ReBa_2Cu_3O_7$

**Re: Rare earth metal (La, Pr, Nd, Sm, etc.), A: Alkaline metal (Ca, Sr, Ba, etc.)*

2.1.2 Electrical property and electrical transport in metal oxides

◆ Band structures

Electronic materials can be classified into conductors (usually metals), semiconductors, and non-conductors (insulators) according to their conductivity. At a given temperature, the electrical conductivity of a semiconductor is lower than a metal, but much higher than an insulator. Metals have a positive temperature coefficient (their conductivity decreases with the increase in temperature) whereas semiconductors and insulators have a negative temperature coefficient (their conductivity tends to increase with the increase in temperature).

The difference of conductivity between metals, insulators and semiconductors can be understood based on the band theory for solid crystals[2]: the lattices of solids form

lattice potential fields. Instead of forming discrete energy levels as in the case of free atoms, the energy states of charge carriers form continuous energy bands in reciprocal space due to the crystal field. The energy bands in reciprocal space are separated by regions where no electron orbitals exist, and such forbidden regions are called forbidden bands. The band gap refers to the energy span of the last forbidden band, typically termed E_g. The bands above the band gap are called conduction band (C_B) while those below are called valence band (V_B). The highest occupied quantum state of the electrons is defined as the Fermi Energy (E_F) or the chemical potential. In the ground state, all energy bands below are occupied and all above are empty. The Fermi energy can be located in the band gap, C_B or V_B. Schematic band structures in the ground state are shown in Fig. 2-1. Crucial to the conductivity is how the charge carriers occupy the energy bands[3]:

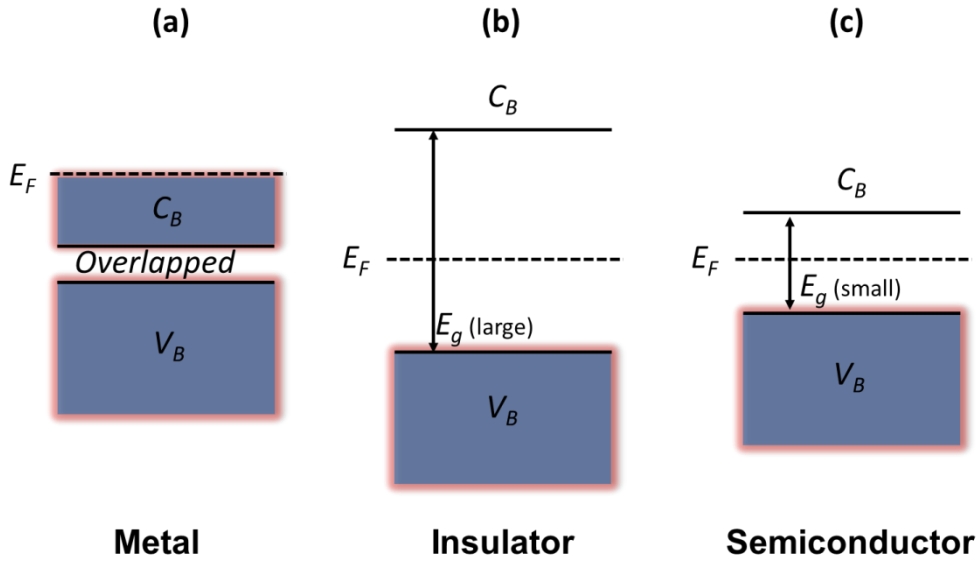

Figure 2-1. Schematic diagram of the band structure in ground state and the relative position of the Fermi Level (E_F) with respect to the Valence Band (V_B), the Conduction Band (C_B) and the Forbidden Band (E_g): (a) Metal, (b) Insulator and (c) Semiconductor.

1. If the bands are partly filled (typically between 10% and 90%), then the crystal behaves as a conductor (or metal). The C_B overlaps with the V_B and the E_F is located in the C_B, as shown in Fig. 2-1 (a).

2. If the energy bands are either filled or empty, the crystal behaves like an insulator. The electrons in the C_B are separated from the V_B by the E_g and the E_F is located in the E_g, as shown in Fig 2-1 (b).

3. If the bands are slightly filled (e.g. at a finite temperature) or empty, then the crystal is called a semiconductor. The E_g is small enough so that thermal or other excitations can bridge the gap. Similar to insulators, E_F is located in the forbidden band, but the E_g is much smaller, as shown in Fig. 2-1 (c). In semiconductors, the charge carriers are divided into electrons or holes based on the polarity of the charge: electrons (negative charge) are the majority carriers in *n*-type semiconductors while holes (positive charge) are dominant in *p*-type semiconductors.

◆ Metal-oxide interfaces

The measurement of transport properties in semiconductive or insulating oxides usually requires a metal-oxide-metal contact. When a metal makes contact with an oxide (semiconductor or insulator), potential barriers are formed at the metal/oxide interface due to their different work functions, as discussed below.

Fig. 2-2 (a) shows the band structure of a metal and an *n*-type semiconductor when there are no contacts in between. $e\varphi_m$ and $e\varphi_s$ are the respective work functions of the metal and semiconductor, defined as the energy needed to remove an electron from the Fermi level of a solid to the vacuum immediately outside the solid surface. The electron affinity (χ_s) of the semiconductor is defined as the energy that an electron requires to escape from the conduction band minimum into the vacuum. The E_C, E_F, and E_V are the conduction band minimum, the Fermi level and the valence band maximum, respectively. The $e\varphi_m$ and χ_s values of several metals and oxides are listed in Table 2-2.

Assuming that $e\varphi_s$ is smaller than $e\varphi_m$ ($E_{Fmetal}<E_{Fsemiconductor}$), when the metal and semiconductor are in contact with each other (assuming a perfect contact without additional interfacial insulating layer), the Fermi levels on both sides are forced to line up to establish thermal equilibrium with respect to the chemical potential in between[4].

Meanwhile, electrons will pass from the C_B of the semiconductor to the empty energy states above the E_F of the metal, leaving positive charges on the semiconductor side and negative charges on the metal side, as shown in Fig. 2-2 (b). This then results in the formation of a built-in contact potential V_d pointing from the semiconductor to the metal, which prevents the further motion of electrons. The built-in potential is given by the difference in work functions[5]:

$$eV_B = e\varphi_m - e\varphi_s \tag{2-1}$$

Here eV_B represents the height of barrier for an electron to move from the semiconductor to the metal. $e\varphi_m$ is constant while $e\varphi_s$ depends on the dopant concentration (i.e. the concentration of majority carriers) and therefore eV_B can be modified by doping.

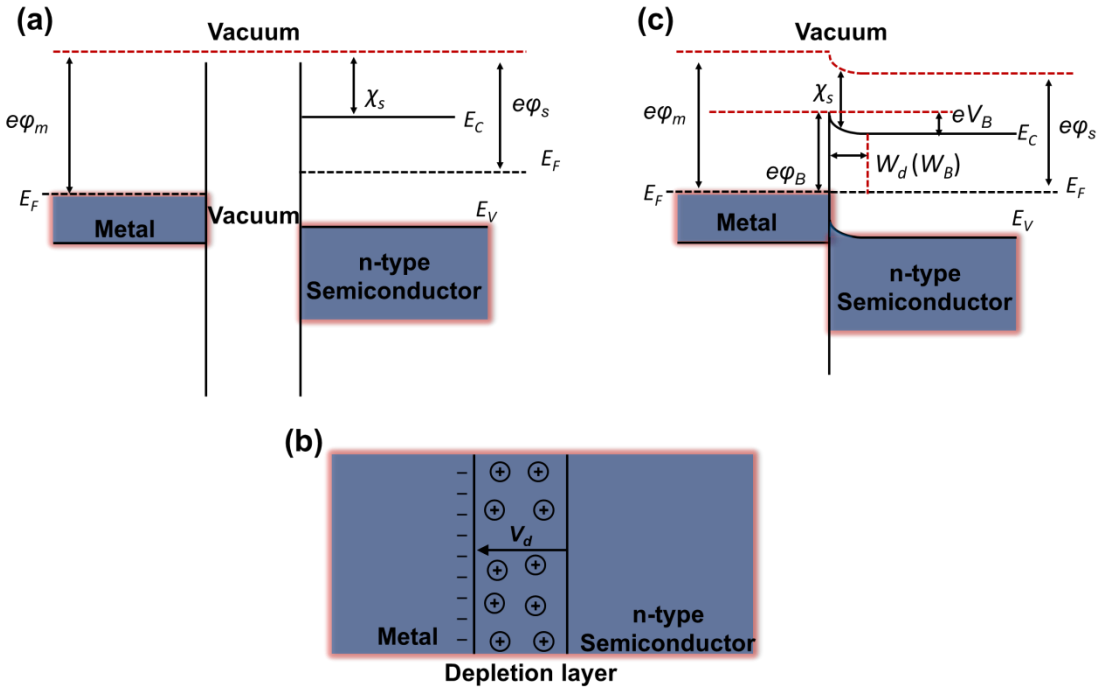

Figure 2-2. Formation of the metal-semiconductor Schottky barrier. (a) The band structure of a metal and an *n*-type semiconductor when there is no contact in between. (b) The depletion layer in a metal/*n*-type semiconductor interface. (c) The formation of the built-in potential (eV_B) and Schottky barrier ($e\varphi_B$) by alignment of the Fermi Level (E_F).

When a metal/semiconductor contact forms, electrons are removed from a certain depth within the semiconductor due to its relatively low charge density, and a

depletion region forms within the semiconductor, as shown in Fig. 2-2 (b). In the depletion region, the contact potential results in energy bands bending up from the semiconductor to the metal and the Fermi levels line up, as shown in Fig. 2-2 (c). The width of the depletion region is denoted by W_d.

Viewing from the side of the metal, there is also a barrier for electrons to move to the semiconductor (Fig. 2-2 (c)), where the barrier height ($e\varphi_B$) is equal to the difference between the metal work function ($e\varphi_m$) and the semiconductor electron affinity (χ_s)[5]:

$$e\varphi_B = e\varphi_m - \chi_s = eV_B - (E_C - E_F) \tag{2-2}$$

Here, E_C and E_F are the conduction band minimum and the Fermi level of the semiconductor. This potential barrier is called a Schottky-like barrier (shortened to Schottky barrier), which controls the leakage of current at the interface. The leakage occurs due to the emission (or tunneling) of electrons from the Fermi level of the metal to the conduction band of the semiconductor under an applied electric field. The potential barrier is not only characterized by its height ($e\varphi_B$) but also by its width (which is correlated to the depletion layer width W_d), as illustrated in Fig. 2-2 (c).

In zero bias, the movement of electrons from the semiconductor to the metal is balanced by the contact potential and therefore there is no current. Assuming no change in the dopant concentration in the *n*-type semiconductor[5]:

When applying a positive bias (from metal to semiconductor), electrons face a semiconductor-to-metal barrier eV_B (given by equation (2-1), shown in Fig. 2 (c)). The external potential is opposite to the built-in potential, and the E_Fs no longer line up, but shift with one another depending on the applied bias, which decreases eV_B, and therefore electrons have a lower barrier to overcome before reaching the metal. This results in a current flow which increases with the increase in the positive bias.

On the other hand, when a negative bias is applied, the semiconductor-to-metal barrier is higher. Electrons now flow in the opposite direction, facing a

metal-to-semiconductor barrier $e\varphi_B$ (given by equation (2-2), shown in Fig. 2 (c)). The application of a negative bias lowers the barrier height $e\varphi_B$, due to the "image force" effect[4] in which an electron near the surface of a metal is attracted to it by a positive image charge, and the attraction force produces an effect of reducing the barrier height by an amount which depends on the bias applied. The effective lowering of the barrier height can be expressed as[6]:

$$\Delta\varphi = \sqrt{\frac{eE}{4\pi\varepsilon_0\varepsilon_r}} \tag{2-3}$$

Table 2-2. Work functions and electron affinities of different metals and oxides[7–10]

Metal	$e\varphi_m$ (eV)	Oxide	χ_s (eV)
Pt	5.3-5.6	STO	3.9
Au	5.3-5.4	CeO_2	3.5
Ag	4.6-4.7	Nb-STO	4.0

◆ **Conduction mechanisms[4,6,11–13]:**

A mechanism for conduction was first proposed by Ohm in 1827, who stated a linear dependence of current on the potential difference across a conductor (metal). In metal-oxide-metal contacts, different metals and semiconductors have different work functions and electron affinities, which usually result in nonlinear *I-V* relationships as well as different electron transport mechanisms. The current conduction can be influenced by both temperature (*T*) and electric field (*E*). In general, conduction mechanisms are classified into interface-limited or bulk-limited types. In some cases, current conduction is dominated by the metal-oxide interface, e.g. the metal-oxide Schottky-barrier, and the bulk is believed to be more conductive than the interface. In other cases, the interface doesn't limit the injection of carriers into the bulk and the bulk properties of the oxide are more dominant, e.g. the trap level, dielectric relaxation time or the density of states[12]. Interface-limited conduction mechanisms mainly include: (1) Schottky or thermionic emission, (2) Fowler-Nordheim (F-N)

tunneling, (3) direct tunneling and (4) interface-limited trap-assisted tunneling (TAT), while bulk-limited conduction mechanisms include: (1) Poole-Frenkel (P-F) emission, (2) Ohmic conduction, (3) Space Charge Limited Conduction, (4) ionic conduction, (5) hopping conduction and (6) bulk-limited TAT.

It is worth mentioning that both interface-limited Schottky emission and bulk-limited P-F emission are based on the thermionic emission theory, where the conduction is caused by the escape of electrons from the materials by surmounting the potential barrier due to thermal excitation. On the other hand, interface-limited F-N tunneling and bulk-limited TAT mechanisms are based on the theory of quantum mechanical tunneling, where the conduction is determined by the ability of the electrons to penetrate through a potential barrier[6].

A comprehensive description of conduction mechanisms with their temperature and electric field dependences is given below:

Schottky emission

When the electrons in a metal gain enough energy to overcome the Schottky barrier $e\varphi_B$ by thermal activation, then conduction happens as a result of electron emission. The Schottky emission process (under a negative bias) is illustrated in Fig. 2-3. The metal-oxide interface energy barrier height can be lowered by the image force, a phenomenon known as the Schottky effect. Schottky emission is one of the most common conduction mechanisms in dielectric films at relatively high temperatures. The current density can be expressed as:

$$J = A^* T^2 \exp\left[\frac{-e\left(\varphi_B - \sqrt{\frac{eE}{4\pi\varepsilon_r\varepsilon_0}}\right)}{kT}\right] \tag{2-4}$$

$$A^* = \frac{4\pi q k^2 m^*}{h^3} = \frac{120 m^*}{m_0} \tag{2-5}$$

where J is the current density, A^* is the effective Richardson constant, m_0 is the free electron mass, m^* is the effective electron mass in dielectric, T is the absolute temperature, e is the electronic charge, eφ_B is the Schottky barrier height (i.e.

conduction band offset), E is the electric field, k is the Boltzmann's constant, h is the Planck's constant, ε_0 is the permittivity in a vacuum, and ε_r is the optical dielectric constant.

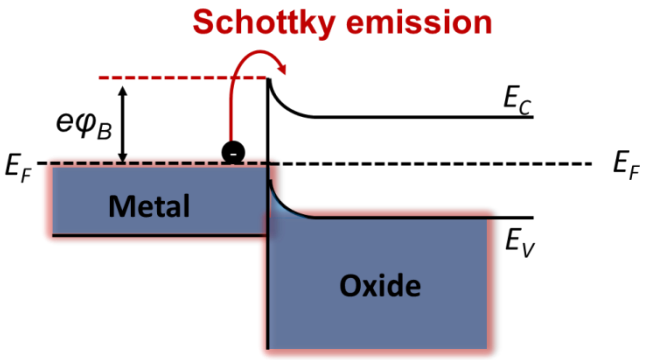

Figure 2-3. Schematic band diagram of the Schottky emission process in a metal-oxide (insulator or semiconductor) interface.

Fowler–Nordheim (F-N) Tunneling (and direct tunneling)

Based on classical physics, incident electrons cannot overcome the Schottky barrier when the energy is lower than the barrier height. However, when the potential barrier is thin enough (e.g. <10 nm) and a high electric field is applied, quantum mechanics predicts that the electron wave function will penetrate through the barrier into the conduction band of the oxide (Fig. 2-4). Hence, electron tunneling occurs, and the probability of electrons existing on the other side of the potential barrier is non-zero. Generally, direct tunneling occurs when the oxide layer is very thin (<3 nm), while F-N tunneling is more dominant when the barrier is thicker[13]. The expressions of the current density for F-N tunneling and direct tunneling are:

$$J = \frac{e^2E^2}{8\pi h\varphi_B}\exp\left[\frac{-8\pi\sqrt{2m^*}(e\varphi_B)^{\frac{3}{2}}}{3ehE}\right] \quad \text{(F-N tunneling)} \tag{2-6}$$

$$J = \exp\left\{\frac{-8\pi\sqrt{2e}(m^*e\varphi_B)^{\frac{1}{2}}}{3h}\kappa t_{ox,eq}\right\} \quad \text{(Direct tunneling)} \tag{2-7}$$

where κ is the relative dielectric constant, $t_{ox,eq}$ is the effective thickness of the oxide layer, and other notations are the same as defined before.

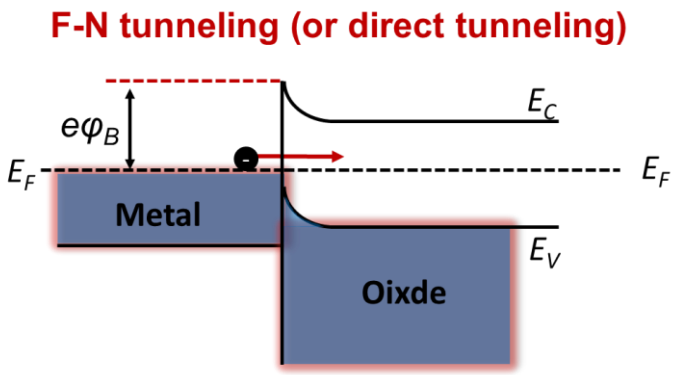

Figure 2-4. Schematic band diagram of the Fowler–Nordheim Tunneling (or direct tunneling) process in a metal-oxide interface.

Poole-Frenkel (P-F) emission

As mentioned above, the theoretical foundation of P-F emission is the same as for Schottky emission, but with the difference being that electrons are emitted into the conduction band of the oxide from trap sites formed by defects in the oxides. Therefore, the potential barrier $e\varphi_B$ in Fig. 2-3 is replaced with the depth of the potential well of the traps $e\varphi_T$, which is the location of the trap level below the conduction band minimum. The application of an electric field decreases the potential barrier height and increases the probability of trapping and detrapping of electrons from the bulk. The general expression for P-F emission is:

$$J = e\mu N_C E \exp\left[\frac{-e\left(\varphi_T - \sqrt{\frac{eE}{\pi\varepsilon_r\varepsilon_0}}\right)}{kT}\right] \tag{2-8}$$

where μ is the electronic drift mobility, N_C is the conduction band density of states and $e\varphi_T$ is the trap energy level.

Trap-assisted tunneling (TAT)

Similar to P-F emission, the occurrence of tunneling can also be assisted by defects in the oxide. In contrast to single-step tunneling such as F-N tunneling, TAT usually consists of a two-step process: the electrons firstly escape from the anode, get

captured into the trap sites and are then emitted into the cathode. A generalized expression of the current density in the TAT model is:

$$J = A\exp[\frac{-8\pi\sqrt{2m^*}(e\varphi_T)^{\frac{3}{2}}}{3ehE}] \quad (2\text{-}9)$$

where $e\varphi_T$ is the trap energy level.

The four conduction mechanisms discussed above are the most widely reported in metal-oxide systems. In real cases, it is challenging to differentiate between them. Luckily, there are several empirical guidelines[6]: (1) Most researchers believe that Schottky emission is more dominant than the P-F mechanism if the leakage current density curve is asymmetric with respect to the voltage polarity[13]. (2) If the height of the Schottky barrier controls the leakage current at a weak electric field, the abrupt increase in the leakage current in a strong electric field is due to the narrowing of the width of the Schottky barrier, which can be modeled by F-N tunneling. In contrast, if the P-F mechanisms control the leakage current through the bulk, TAT would be responsible for high leakage currents in strong electric fields.

There are other mechanisms which contribute to the current conductions:

Ohmic conduction

Ohmic conduction is caused by the movement of mobile electrons in the conduction band (and holes in the valence band) in the oxide itself. In this conduction mechanism, a linear relationship exists between the current and the electric field:

$$J = \sigma E = ne\mu E \quad (2\text{-}10)$$

$$n = N_C\exp[-\frac{E_C - E_F}{kT}] \quad (2\text{-}11)$$

where σ is the electrical conductivity, n is the number of electrons in the conduction band, E_C and E_F are the conduction band minimum and Fermi level of the oxide, respectively. Ohmic conduction can be dominant when there is no significant contribution from other conduction mechanisms.

Space Charge Limited Conduction (SCLC)

The SCLC mechanism is similar to the electron transport in a vacuum diode. It is believed that the probability of SCLC conduction is higher if the electrode contact is highly carrier injective. The conduction arises from thermionic injection of electrons from the cathode to the trap sites of the oxide in an Ohmic contact. This mechanism can be easily identified when there are three distinct regions in the *J*-*V* curve:

Ohmic conduction ($I \propto V$) is observed at low applied voltages where only partial trap sites are filled by the injected carriers, and the density of thermally-generated free carriers are larger than the injected carriers:

$$J_{Ohm} = en_0\mu\frac{V}{d} \quad \text{(Ohm's law region)} \tag{2-12}$$

At high applied voltages, the traps are filled and a space charge appears. A quadratic dependence ($I \propto V^2$) of the current density takes over above a transition voltage (V_{Tr}):

$$J_{TFL} = \frac{9}{8}\mu\varepsilon\theta\frac{V^2}{d^3} \quad \text{(Trap-filled-limited region)} \tag{2-13}$$

After all the trap sites are filled up, subsequently injected carriers will move freely in the oxide, and a rapid current jump occurs at a subthreshold traps-filled-limit voltage (V_{TFL}), after which the Child's law ($I \propto V^2$) takes over:

$$J_{Child} = \frac{9}{8}\mu\varepsilon\frac{V^2}{d^3} \quad \text{(Child's square law region)} \tag{2-14}$$

Here n_0 is the concentration of free charge carriers in thermal equilibrium, θ is the ratio of the free carrier density to total carrier (free and trapped) density, V is the applied voltage, d is the film thickness, ε is the dielectric constant.

When increasing the voltage further, a more rapid increase in the current occurs and even a larger exponent (than 2) can be expected in the *J*-*V* relation.

Grain boundary-limited conduction[12]

In polycrystalline materials, the resistivity of the grain boundary is likely to be much higher than that of the grains, and the conduction current can be limited by the electrical properties of the grain boundaries. An energy barrier is formed at grain boundaries, which is inversely proportional to the relative dielectric constant of the material.

Hopping conduction

Hopping conduction originates from the transport of electrons between localized states (trap sites, etc.), which often occurs in low-doped semiconductors or insulators where emission or tunneling are difficult. The conductivity usually shows a strong temperature dependence in hopping conductions.

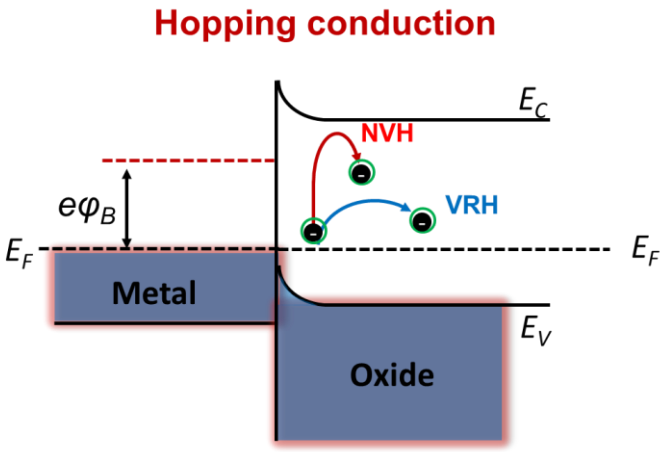

Figure 2-5. Schematic band diagram of the Nearest Neighbor Hopping (NNH) and Variable-range Hopping (VRH) model in an insulating oxide.

1. Nearest neighbor hopping (NNH)[13,14]**:** The simplest form of hopping conductivity occurs between nearest neighbors, i.e. the hop of electrons from one trap site to the nearest trap site through tunneling. A sufficient density of traps that are only partially occupied is required for nearest-neighbor hopping. The *J-E* relationship of hopping conduction is similar to that of Ohmic conduction, where a linear dependence is exhibited:

$$J_{NNH} = \sigma_0 E e^{-\frac{T_0}{T}} \tag{2-15}$$

where σ_0 is the electrical conductivity at the temperature of T_0. The temperature dependence of the resistivity is expressed as:

$$\rho(T) = \rho_0 e^{\frac{E_b}{kT}} \tag{2-16}$$

where E_b is the approximate ionization energy of the impurity**.**

2. Mott Variable range hopping (VRH)[13,14]**:** NNH is also called fixed range hopping (FRH). In contrast to FRH (where the electrons only hop into the nearest trap sites), the electrons in the VRH scheme can hop into the trap sites which are farther away but with lower trap energies. The difference between NNH and VRH conduction is schematically illustrated in Fig. 2-5.

The *J-E* relationship of VRH hopping has a similar linear dependence with that of the NNH mechanism, but the temperature dependence is different, which can be expressed generally as:

$$\rho(T) = \rho_0 e^{(\frac{T_0}{T})^{\frac{1}{d+1}}} \tag{2-17}$$

where *d* empirically stands for the dimensionality of the system, i.e., the distribution of trap sites. In a three dimensional insulator, *d*=3 and a $\frac{1}{4}$ law is exhibited, whereas in thin films with two-dimensional distributions, *d*=2.

3. Small polaron hopping (SPH)[15–18]**:** In highly insulating oxides (such as perovskite and spinel oxides), the energy bands are narrow, which slows down the electron motion substantially and thus the band theory fails to explain the conduction. When the electron-lattice (phonon) interaction energy is greater than the bandwidth, the slow-moving electrons distort and polarize the lattice and then polarons are formed which carry the lattice deformation along with them under the electric field. The potential wells produced by the deformation act as trap sites. There are two kinds of polarons: large and small, depending on the ratio of their radius to the lattice constant. Large polarons have similar hopping behavior as that of electrons or holes, while

small polarons follow an Arrhenius-like formula for hopping, with an exponent that depends on the activation energy and temperature. Therefore, the hopping of polaron quasiparticles is very different from that of electron hopping.

The temperature dependence of the resistivity in the Emin-Holstein model of small polaron hopping in the adiabatic regime[16] is expressed as:

$$\rho(T) = ATe^{\frac{E_A}{kT}} \tag{2-18}$$

where $A = \frac{2k}{3ne^2a^2v}$, n is the polaron concentration, a is the site-to-site hopping distance, v is the attempt frequency, k is the Boltzmann constant, and E_A is the activation energy, i.e., the height of the equivalent potential barrier.

Ionic conduction[19]

The conduction mechanisms discussed above are all based on electronic conductivity, where the carriers of charges are electrons or holes under electric fields. The charge carriers of ionic conductivity, on the other hand, are the ionic species that hop or diffuse within a material medium. In solids, ions typically occupy fixed positions in the crystal lattice and are not mobile. However, ionic conduction can occur when the structure is defective or when the temperature is raised up. Both cations and anions can be carriers of current in ionic solids. Cations usually have higher mobility due to their smaller ionic radius, but anion conductors also exist, with the relatively small O^{2-} (1.26 Å) and F^- (1.19 Å) being the most widely studied.

Ionic conductivity in the solid state is generally overshadowed by electronic conductivity, as many ionic conductors are also electronic conductors (known as mixed conductors).

There are several important factors that influence ionic conductivity in a solid, such as the charge carrier concentration, temperature, defect density of the crystal, and the activation energy (i.e. the free energy barrier an ion has to overcome for hopping between neighboring defect sites). Ionic conduction usually follows the Arrhenius expression given by:

$$\sigma(T)_{ionic} = \frac{A}{T} e^{\frac{E_a}{kT}} \quad (2\text{-}19)$$

where A is a proportionality constant and E_a is the activation energy. The electric field dependence of current density is expressed as:

$$J = J_0 e^{-(\frac{e\varphi_B}{kT} - \frac{ed}{2kT}E)} \quad (2\text{-}20)$$

where J_0 is a proportionality constant, $e\varphi_B$ is the potential barrier height for ion hopping, and d is the distance between two hopping sites.

The above nine conduction mechanisms constitute the primary contributions to current conduction observed in most reported works. By modeling the dependence of current on electric field or the dependence of resistivity on temperature, the conduction mechanism can be elucidated.

◆ **Electric charge polarization in metal oxides**

Polarization occurs when an electric field distorts the negative electron cloud around the positive atomic nuclei in a direction opposite to the field, which leaves one side of the object with an excess amount of positive charges, and the other side with negative charges. In oxides which lack central symmetry, the centers of the positive and negative charges do not overlap and these oxides show charge polarization when mechanical stress is applied (or vice versa), and these oxides are called piezoelectric oxides. When a piezoelectric oxide possesses a polar axis and spontaneous charge polarization (in the absence of an electric field) that can be reversed by the application of an external electric field, it is called a ferroelectric oxide.

2.1.3 Magnetism in metal oxides

◆ **The origin of magnetism**

Magnetization is the vector sum of all the magnetic moments in a material per unit volume. The magnetic moment arises from individual electrons in the atom, which can be divided into three sources: the orbital angular momentum with respect to the

nucleus (orbital moment), the intrinsic spin of the electrons (spin moment), and the change in orbital moment induced by a magnetic field[2]. The orbital moment is usually much smaller than the spin moment and therefore, magnetism is largely influenced by the behavior of electron spins.

In SI units the relationship between the applied magnetic field and magnetization is expressed as:

$$B = \mu_0(H + M) \tag{2-21}$$

where B is the magnetic flux density or magnetic induction (unit: Tesla (T)), $\mu_0 = 1.256637 \times 10^{-6}$ in T.m/A is the magnetic permeability of the free space, H is the magnetic field strength (unit: A/m) and M is the magnetization (unit: in A/m).

The degree of magnetization of a material in response to an applied magnetic field is defined as the magnetic susceptibility (χ):

$$\chi = \partial M/\partial H \tag{2-22}$$

The magnetic susceptibility and its dependence on the magnetic field and temperature determine different magnetic behaviors.

◆ **Classification of magnetism**

Depending on the distribution of magnetic moments without a magnetic field and the response with respect to an applied magnetic field, magnetism can be classified into 5 categories:

1. Paramagnetic (PM) materials do not possess spontaneous magnetization and have a weak linear response to an applied magnetic field (a small χ).

2. Ferromagnetic (FM) materials exhibit spontaneous parallel alignment of magnetic moments, which results in a net magnetization in the absence of a magnetic field. This FM order exists only below a critical temperature (the Curie Temperature (T_c)). Below T_c, the moments are correlated and align over macroscopically large areas (the magnetic domain). Above T_c, the moments are randomly oriented in a PM distribution,

resulting in a net magnetization of zero. The magnetic moments in a FM material tend to align in some favorable directions (called easy directions, or easy axes). The easy axes are determined by the crystal structure, atomic-scale texture, strain state, or shape of the sample, which give rise to anisotropic magnetic properties (called magnetic anisotropy).

3. Diamagnetic (DIM) materials only possess magnetization when an external magnetic field is applied, and the induced magnetic moments are antiparallel to the magnetic field.

4. Anti-ferromagnetic (AFM) materials have equal but antiparallel sublattice moments and show zero net magnetization in the absence of a magnetic field. The critical temperature for AFM ordering is called the Neel Temperature (T_N).

5. Ferrimagnetic (FIM) materials have similar sublattice arrangements as AFM materials, but the magnetic moments of the sublattices are not equal and thus a net magnetization is present.

The spin arrangements in FM, AFM, and FIM domains are illustrated in Fig. 2-6.

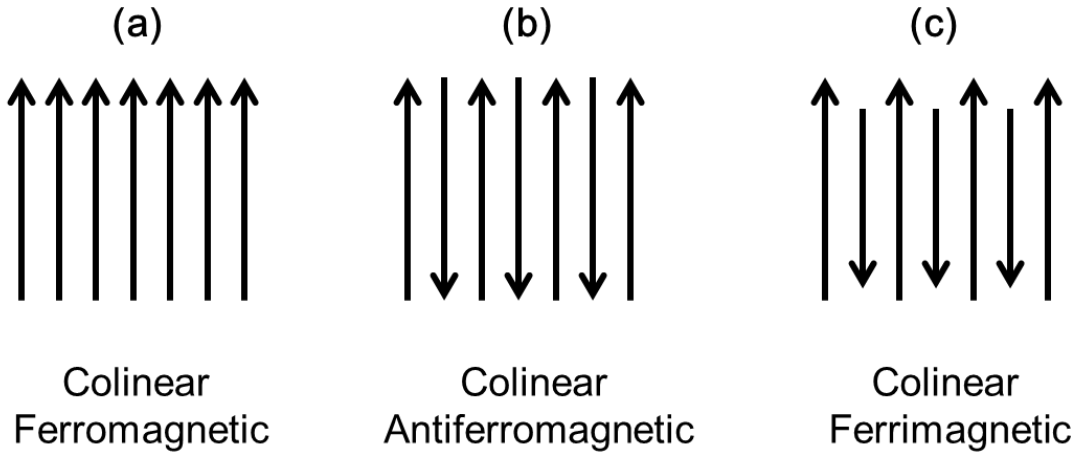

Figure 2-6. The electron spin arrangement in (a) a ferromagnetic, (b) an antiferromagnetic and (c) a ferrimagnetic domain.

◆ Magnetic hysteresis loop

The response of the magnetic induction *B* (or magnetization *M*) to an applied magnetic field *H* describes the magnetic behavior of a FM material and has a hysteretic shape, which is called the magnetic hysteresis loop, as shown in Fig. 2-7. By using equation 2-21, the *B-H* loop can be converted to the corresponding *M-H* loop.

The *M-H* loop in Fig. 2-7 reflects the magnetization process. Starting from the unmagnetized state ("0" state), the net magnetic moment is zero because the magnetic domains are randomly aligned. With the application of a magnetic field, the domains tend to align parallel to the easy axis through moving of domain walls ("1" state), which results in a sharp nonlinear increase in the magnetic moment until all the domains are aligned along the easy axis to form a single-domain state ("2" state). When the magnetic field increases further, the moment tends to align further to the direction of the magnetic field, which increases the measured magnetic moment until a saturated state is reached ("3" state). This measured moment is called saturation magnetization (*Ms*). No further increase in magnetization happens when the magnetic field is increased. When the magnetic field is reduced and returns to zero, the magnetization of a ferromagnetic material does not drop to zero, but rather a remnant magnetization (*Mr*) is retained ("4" state). In order to reduce the magnetization to zero, a negative magnetic field is needed ("5" state), which is called the coercive field (*Hc*).

Depending on the shape of the *M-H* curve, FM materials are classified into soft or hard magnets. In the case of hard magnets, the *Mr* and *Hc* and the dissipated magnetic energy (the area of the *M-H* curve) are generally larger than those of a soft one. These materials can keep a large magnetization after the applied magnetic field is removed so that they are usually used as permanent magnets. On the other hand, soft magnets can be easily magnetized and demagnetized, and have wide applications in magnetic storage devices. The magnetic anisotropy gives *M-H* curves with different shapes (with different values of *Mr* and *Hc*) in one material when the magnetic field is

applied along different directions.

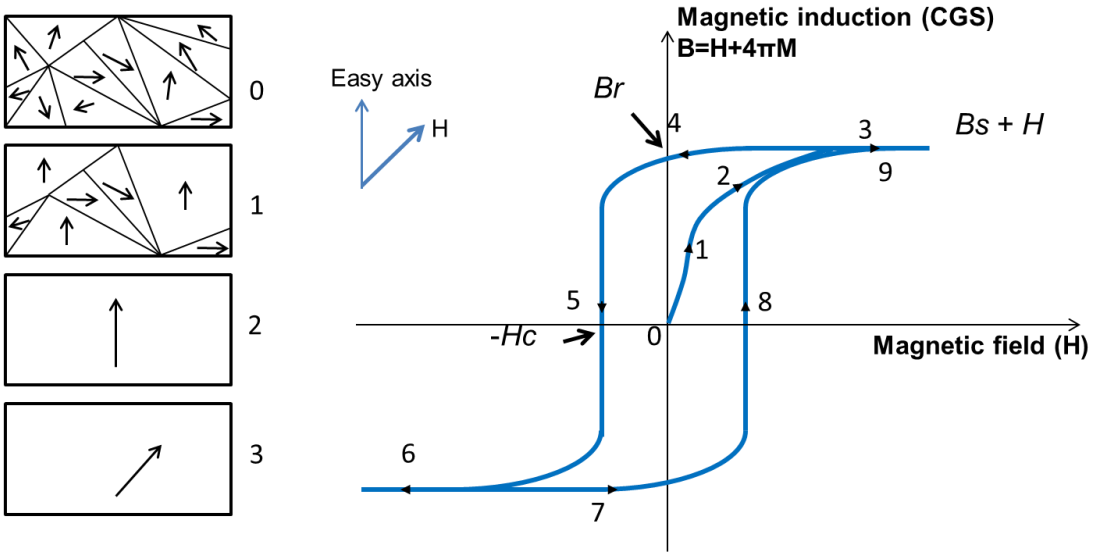

Figure 2-7. The technical magnetization curve (magnetic hysteresis loop, on the right) and the corresponding schematic illustration of the evolution of domain structures (on the left) in a ferromagnetic material.

◆ Magnetic interactions in metal oxides

In metal oxides, the existence of metal-oxygen ionic bonds precludes direct interactions between metal ions and therefore indirect couplings are responsible for the magnetic interactions. A number of exchange coupling models in magnetic oxides have been developed to address how indirect exchanges interact through the nonmagnetic bridge (oxygen ions in metal oxides). Classic models include super-exchange (SE), double exchange (DE), and RKKY coupling[20,21].

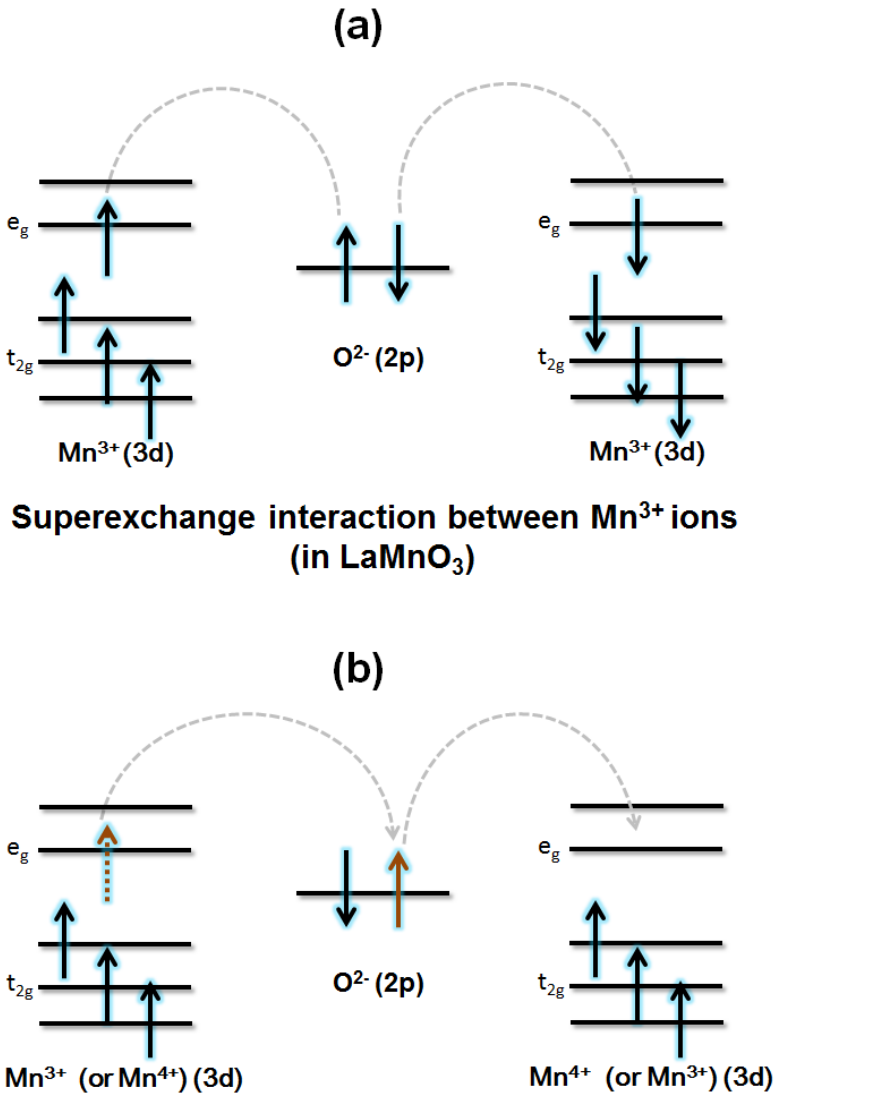

Figure 2-8. Schematic diagram of magnetic interactions in metal oxides: (a) superexchange (taking $LaMnO_3$ as an example) and (b) double exchange (taking alkaline-doped $LaMnO_3$ as an example).

Super-exchange (SE): The model was proposed by Kramer in 1934 and developed by Anderson in 1950[22]. It takes place between two cations with unpaired spins bound by an anion without unpaired spins, where the cations have the same valence. The coupling can be either FM or AFM depending on the differences in electron orbitals. Fig. 2-8 (a) shows an example of SE coupling: the oxygen bonding leads to an anti-parallel spin alignment of nearest neighboring Mn^{3+} in $LaMnO_3$: The orbital

hybridization process results in electron orbital overlap and electrons are donated from the O 2*p* to the Mn 3*d* orbitals. Mn^{3+} ions ($3d^4$) in $LaMnO_3$ have less than half-filled 3*d* orbitals. By Hund's rule, the donated spins from O^{2-} should be parallel to the spins in Mn^{3+}. Since the 2*p* spins of O^{2-} are antiparallel with each other, the result is a collective antiparallel spin alignment of nearest neighbor Mn^{3+} ions.

***Double exchange (DE)*:** The DE model was proposed by Zener in 1951[23], which describes FM coupling in mixed-valence compounds. In SE coupling, the valences of the metal ions are the same and do not change, while the DE interaction occurs only when one ion has an extra electron compared to the other, and a change in valence occurs. Fig. 2-8 (b) shows the DE process in an alkaline (Ca, Sr or Ba)-doped $LaMnO_3$, where Mn^{4+} is produced and coexists with Mn^{3+}. The electron conduction and FM coupling proceed through a double-step process in which electrons jump back and forth in neighboring Mn sites across the oxygen bridge. The electron is thus delocalized over the entire Mn^{3+}–O^{2-}–Mn^{4+} group. Since spin-flips are not allowed in electron hopping processes, a parallel alignment between the two Mn ions is more energetically favorable, thus leading to a FM alignment between the spins of the neighboring Mn^{3+} and Mn^{4+}.

***RKKY coupling*:** RKKY coupling exists when magnetic ions are too far apart to interact with each other, and a localized spin polarizes the spin of surrounding conduction electrons which creates an effective field to influence the polarization of nearby localized ion spins with the polarization decaying in an oscillatory manner[21]. RKKY coupling can be used to explain magnetic coupling in dilute magnetic semiconductor systems and Giant Magnetoresistance in magnetic heterostructures[20,21].

2.2 Non-volatile memories (NVM)

The industry has stepped into an era with rapidly growing information process systems, where advanced data storage techniques are emerging to compete with the development speed of computing logic technology and overcome the so-called

"memory wall"[24]. The essence of nonvolatile data storage is the switch between distinct logic states ("1" or "0") of a memory signal in a memory cell. The memory signal can be electrical (charge, current, resistance) or magnetic (spin, magnetic moment). The storage operation includes "write" and "read" processes, which can be either electrical (electrical current or field) or magnetic (magnetic field).

2.2.1 Bottlenecks in conventional memories

Traditional CMOS-based memories, including Dynamic Random Access Memory (DRAM), Static RAM (SRAM) and Flash memory, have slowed down the pace of memory development due to various performance-cost tradeoffs[24,25]: The DRAM has a large storage density, but is volatile, and thus must be powered continuously to retain its memory states. Although Flash memory is nonvolatile, this advantage comes at the price of a limited cycling endurance and slow write speed, and thus its application is restricted to solid-state hard disks and storage media for digital cameras and cellphones. SRAM exhibits high speed but is compromised by its low density, which limits the increase in on-chip memory capacity.

2.2.2 Novel electrical/magnetic NVMs

The rapid development of information technology calls for novel non-volatile random access memory (NV-RAM) devices, which not only retain the memory data when the power source is cut off but also have optimized performance and cost[26]. Advances in NV-RAMs have featured several materials systems ranging from metals, transition metal oxides, chalcogenides to carbon-based materials. Meanwhile, numerous novel physical mechanisms have also emerged, expanding from classical electronics to quantum mechanics, ionic transport, strong correlation among spin-charge-orbital degrees of freedom, etc. Most of the emerging NVMs are based on two-terminal switching elements, which are compatible with miniaturized high-density memory architectures such as cross-bar arrays[24].

The newly-developed NV-RAMs, including Phase-Change RAM (PCRAM), Resistive RAM (RRAM), Ferroelectric RAM (FeRAM) and Magnetic RAM (MRAM)[24,27], utilize either single or integrated electrical/magnetic properties of materials. These novel memories combine the speed of SRAM, the density of DRAM and the nonvolatility of Flash memory, providing enormous possibilities to greatly enhance the data storage capacity and reduce the cost. This makes NV-RAMs a viable replacement to the extant expensive-to-build silicon chips/CMOS which currently act as the memory cells in all kinds of electronic devices (such as microphones and cameras) and computing systems[28].

This section briefly introduces NV-RAM techniques related to this thesis, mainly focusing on the basic technical aspects (the memory signals, the memory cell structures and the "write" and "read" approaches). Specific issues in each technique will be raised and the proposal for materials-engineering solutions will be discussed in detail at the beginning of each result chapter.

◆ **Resistive RAM (RRAM)**[26]

Electronic charge, which is used as the storage signal in traditional memory techniques, has a shortage of limited miniaturization of memory cells, as the amount of electrons to be retained becomes increasingly difficult when the memory cell shrinks[26]. RRAMs overcome this obstacle as they use resistance for information storage, rather than charge. RRAM has attracted lots of attention due to its compatibility with conventional semiconductor processes[28]. A RRAM memory cell is a two-terminal metal-insulator-metal (MIM) unit (see Fig. 4-1), and the data storage relies on the ability of the insulating material to be switched between two or several resistance states with the application of an electric field. The switching of the resistance state relies either on the formation/rupture of a conductive filament inside the insulating matrix, or the modification of the metal-oxide interfacial Schottky barrier. Transition metal oxides provide a good platform for studying RRAM due to their versatile nature of oxygen and cations. In RRAM devices, the "read" signal is electrical resistance (or current) while the "write" method is electrical field (or

voltage). Improvement of RRAM performance using VAN will be discussed in detail in Chapter 4 of this thesis.

◆ **Magnetic RAM (MRAM) and spintronics**

MRAM stores information using magnetic moments (spin). The use of the electron spin in addition to its charge brings about the development of spin electronics (or spintronics). Several terms need to be clarified before discussing MRAM techniques:

Magnetic tunneling junction (MTJ) and Tunneling Magnetoresistance (TMR). A MTJ is comprised of two ferromagnetic layers separated by a thin insulating layer, as shown in Fig. 2-9. The magnetization of one ferromagnetic layer is fixed (fixed layer) while that of the other layer (free layer) can be flipped during the "write" operation. If the insulating layer is thin enough, quantum mechanical tunneling of electrons can occur from one ferromagnetic layer to another. The current flow is determined by the relative spin configuration of the two ferromagnetic layers: a parallel spin alignment results in higher tunneling rates leading to a low resistance state while an antiparallel spin alignment yields a high resistance state. The application of a magnetic field can alter the spin configurations of the two ferromagnetic layers and thus leads to spin-polarized tunneling (called tunneling magnetoresistance (TMR)), resulting in switching between different resistance states.

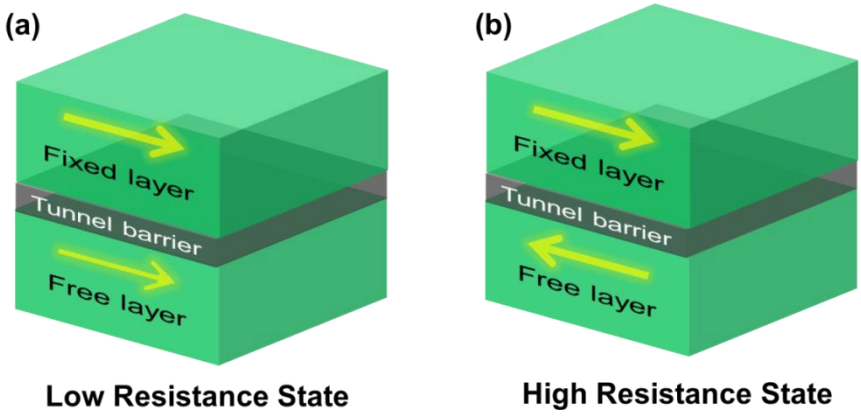

Figure 2-9. Schematic diagram of a Magnetic Tunneling Junction (MTJ). When the spins of the fixed layer and the free layer are parallel, the Tunneling Magnetoresistance (TMR) is lower (a), while the antiparallel alignment gives a high resistance state (b).

Spin-polarized current. Electrical current is transported by charge carriers such as electrons which have intrinsic spins. If the current contains more electrons with either spin direction (up or down), then it is termed as a spin-polarized current. The spin polarization is defined as the degree to which the spins are aligned in one direction, which is determined by the density of states near the Fermi level. Materials with high spin polarization, such as ferromagnetic metallic manganites[29], are termed as "half-metals".

MTJ is the basic memory cell in MRAMs. In a MRAM, the "write" process relies on the degree of spin alignment of the two magnetic layers, while the "read" process detects the resistance change caused by the alteration of spin alignments. Conventional MRAM, which uses electrical currents to induce magnetic fields to flip the spins in the "write" operation, is limited by its high power consumption and low scalability. These limitations triggered the development of a novel MRAM, Spin-Transfer-Torque RAM (STT-RAM), which directly uses spin-polarized currents (instead of magnetic fields) to switch the spin alignment of magnetic layers: a current flowing through the spin-polarized ferromagnetic "fixed layer" is being spin polarized, which then transfers the angular momentum of the polarized spin to the spins in the "free layer", resulting in parallel spin alignment between the free and fixed layer. An opposite current flow can result in antiparallel spin alignment, as the spins antiparallel to the fixed layer are scattered and then transfer their momentum to the spins in the free layer. By changing the direction and magnitude of the current flow, the relative spin alignment between the free and fixed layers is changed and thus relying on TMR of the MTJ, switching between different resistance states occurs[28]. It is worth pointing out that the spin switching in both MRAM and STT-RAM relies on electrical current, which brings with it the problem of power consumption. This problem can be overcome by replacing the electrical current with spin flow, and a pure spin flow can be carried by a ferromagnetic insulator (FMI)[30]. FMIs have gained increasing attention due to their capability to manipulate the spin interactions/dynamics of electrons without unrequired electron current flow[31].

Obtaining highly spin-polarized electron tunneling is important in STT-RAM. While the common method is by tunneling through a ferromagnetic metallic layer through a nonmagnetic insulator (such as MgO), tunneling through a ferromagnetic insulator is a high-efficiency alternative[32]. The barrier heights for spin-up and spin-down electrons of ferromagnetic insulators are very different due to the exchange splitting of the density of states. Since the tunneling current has an exponential dependence on the barrier height, highly efficient spin filtering can be generated[33]. This brings about the development of spin filter tunneling junctions. A spin filter device has a sandwiched structure similar to that in Fig. 2-9, but one metal layer should be non-magnetic acting as a spin injection layer. A thin ferromagnetic insulator (FMI) layer then acts as the spin filtering (tunneling) layer and a ferromagnetic metal (FMM) is used as the spin detection layer which collects spins depending on its relative spin alignment with respect to the filtering layer using a MTJ[34].

As discussed above, FMM and FMI are both important components for MRAM and spintronic devices. Chapter 5 of this thesis will discuss nanoengineering of new FMM and FMI candidates using VAN.

◆ **Magnetoelectric RAM (MERAM)**[35,36]

Although MRAMs have exhibited equal or better access time and endurance properties compared to other alternative NV-RAMs, the need for electric current in the "write" process usually inevitably causes high power consumption, in both conventional MRAMs and STT-RAMs. Apart from replacing electric current with a pure spin flow mentioned above, another alternative solution is to use an electric field (or voltage) in the "write" process. This can be realized in a system with magnetoelectric (ME) coupling, where the magnetic order can be tuned by an electric field (or the charge polarization can be altered by a magnetic field). Electric field tuning of magnetization is realized either in one-material systems with coexisting ferromagnetic (FM) and ferroelectric (FE) order (multiferroics), or via interfacial strain coupling/charge transfer in composites.

A MERAM device enables an electric field to control the magnetization in the FM phase through interfacial exchange coupling. This not only eliminates the need for using a magnetic field or electrical current in data storage but also makes it possible for the integration of multiple memory signals in one memory device. For example, in a multiferroic composite where FM and FE orders coexist, the application of an electric field can not only polarize the electrical charge in the FE component but also tune the magnetic property (moment, anisotropy, etc.) of the FM component. Thus, both the charge polarization and the magnetization can be used as memory signals.

Since magnetic switching is purely dependent on electric field instead of current, a FMI is preferably needed to endure an electric field. The effective coupling between the electrical and magnetic degrees of freedom is important for enhanced working efficiency of a MERAM. Trials on novel MERAM systems will be presented in Chapter 6.

2.3 Vertically-aligned nanocomposites (VAN)

The vertically-aligned nanocomposite (VAN) provides a novel platform to tune and integrate the multi-functionality for various memory devices. The VAN structure is self-assembled through epitaxy. This section starts from the introduction to epitaxy films and then to the unique features of VANs.

2.3.1 Epitaxial thin films

The growing need for miniaturized memory devices triggered the research interests of low-dimensional systems rather than bulk. Epitaxial thin films are a highly versatile candidate system.

Epitaxial oxide thin films are grown on and adapt to the atomic-scale crystal features of single-crystalline substrates. The epitaxy not only enables enhanced crystallinity compared to the bulk but also provides strain tuning and interfacial coupling, thus bringing about fascinating opportunities for the realization of improved properties and emergent electronic phenomena. The study of functional oxide thin

films benefits from newly-developed growth techniques and characterization methods. Advanced thin film growth techniques create non-equilibrium deposition conditions that result in large variations in microstructure, stoichiometry and thus tunable functionalities. Ultra-thin functional oxide films (⩽100 nm) are now of great interest in studying low-dimensional systems. Various applications of ultra-thin oxide films have been achieved in electronic and renewable energy technologies.

The films grown on a substrate with different lattice parameters may be liable to strain to accommodate the lattice mismatch. In a pseudomorphic (fully-strained) growth, when the substrate lattice is larger than that of the film ($a_{substrate}>a_{film}$), the film is under tensile strain in the in-plane direction, while a compressive strain is realized in the opposite case ($a_{substrate}>a_{film}$). The crystal lattice of the film is forced to be equal to that of the substrate and deforms accordingly under elastic constraints which results in different structural and physical properties as compared to the bulk. In some cases, misfit dislocations may be formed to relax the strain, and a fully relaxed film phase is formed, which resembles that of the bulk.

2.3.2 VAN films and their structural features

The tunability of oxide films is reaching its limit in single-phase form. Composites, as an alternative, exhibit more tunable and enhanced properties due to the coupling of functionalities between the different systems. In a nanocomposite, at least one phase has dimension in the nanometer scale, which enlarges the interface areas and improves aspect ratios[37]. Fig. 2-10 shows 3 types of nanocomposite structures: nanoparticles in a matrix (0-3 type), lamellar multilayer nanocomposite (2-2 type) and vertically aligned heteroepitaxial nanocomposite (1-3 type)[38].

The unique 1-3 type epitaxy in VAN structures is created by self-assembly, which is a “bottom-up” nanofabrication technique[39]. The self-assembly approaches surpass the “top-down” (i.e. lithography) methods for fabricating nano-scale features due to their simple and cost-effective fabrication process and the availability to reach smaller sizes (⩽10 nm). In contrast to self-assembly, the conventional lithography not only needs

multi-steps (such as etching) but also needs great effort to improve the resolution.

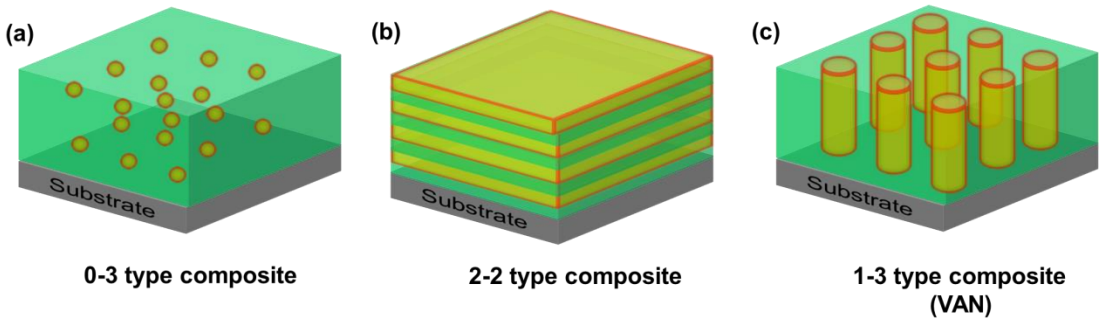

Figure 2-10. Schematic diagrams showing the three types of nanocomposite structures: (a) nanoparticles in a matrix (0-3 type), (b) lamellar multilayers (2-2 type) and (c) vertically aligned heteroepitaxial nanocomposite (1-3 type).

Fig. 2-10 (c) shows a typical VAN structure, where a nanocolumn phase is embedded vertically inside a continuous matrix phase and both phases form epitaxy onto a substrate. In some cases, a checkboard layout is formed, where both phases grow into separate columns. In VAN structures, epitaxy exists both in the out-of-plane (*op*) direction (between the two phases) and in the in-plane (*ip*) direction (between film and substrate), and thus two types of strain are generated, resulting in a 3-dimensional (3D) strain state for both phases.

Compared with a conventional plain film (PF), VAN exhibits a lot of advantages:

1. 3D strain engineering. A stiff nanocolumn embedded within a softer matrix can effectively tune both the *op* and *ip* strain states of the matrix phase. Overall, the resulting 3D strain is totally different to what can be achieved in a PF[40,41].

2. Thickness freedom and Strain uniformity. In PFs, the substrate clamps the strain when the film is thin, making it difficult to tune the physical properties using external forces. Also, the substrate strain is restricted up to a critical thickness, from a few to 10s of nm, after which the strain relaxes in complex ways. In contrast to PFs, vertical strain in VAN can be maintained without thickness limitation[42] whenever vertical epitaxy is achieved. While the matrix phase is initially clamped by the substrate *ip*, after a certain thickness the columns dominate the strain state of the matrix phase[43] in

both the *ip* and *op* directions[40,44]. The columns act as "anchors" to maintain a stable and uniform strain of the matrix, without inhomogeneity or relaxation. The lesser constraints from the substrate clamping or relaxation enhance the tunability of functionality in thin VANs and the structural homogeneity in thick VANs.

3. Improved crystal quality. Vertical interfaces in VAN films are different from the lateral substrate/film interfaces in PFs. When PFs are ultrathin, the resultant strong modification by substrates leads to the formation of various kinds of defects to compensate for the strain, which sometimes results in a "dead layer effect"[45]. In VAN films, the growth rate of the VAN vertical interface is much slower than that of the substrate/film interfaces. This likely enables misfit dislocations to form readily instead of other deleterious defects[45–47].

4. Easy interface probing. In a planar structure, the interface is buried in the lateral direction, while in VANs, the exposed vertical interfaces can be easily probed using microscopic imaging, providing opportunities for studying the properties of the bulk and interfacial parts separately (and simultaneously).

5. Tunable structure and property through nanoengineering. First, the combination of constituent phases can be artificially designed. Second, the molar ratio between the two certain phases can be altered. The growth rate and temperature of one VAN composition can also be varied with ease. These growth parameters strongly influence the growth kinetics of VANs, and the resulting nanocomposite structures can have different length scales and even morphologies (such as pyramidal crystallites, nanoparticles, nanoplates or nanocolumns[38]). The tunable structures enable highly tunable physical properties, which are hard to realize in PFs.

2.3.3 Growth of VAN

◆ **Selection guidelines for the constituent phases**

Numerous oxide structures exist in nature, but random combinations may not necessarily create desired VANs due to thermal-dynamic constraints. Before growth,

choosing the right materials is an imperative step to obtain phase-separated, highly epitaxial and ordered structures. The criteria for the selection of VAN precursors, according to MacManus-Driscoll *et al.*[43,48], are as follows:

1. The targeted constituent phases (at least one phase) should be able to have good epitaxy when independently grown on the substrate. Epitaxy is more favorable when the film and the substrate have similar crystal structures and lattice parameters.

2. Both constituent phases should have similar growth kinetics within an overlapping growth window (e.g. growth temperature and oxygen partial pressure).

3. The targeted phases are not necessarily the phases which are present in the precursor target (which are sometimes solid solutions) but should be the most thermodynamically favorable phases to form epitaxy on the substrate under the designed growth condition.

4. The solubility limit is the most important factor to consider in order to obtain clean constituent phases. A sufficient difference in cation radii is required to prevent intermixing between the two phases. A difference in crystal symmetry can also reduce the solubility level.

5. Two phases with different elastic moduli are preferred to enable effective strain control of the softer phase by the stiffer phase.

◆ Mechanisms for epitaxial thin film growth

Before discussing the phase separation mechanisms of VANs, it is necessary to make clear how a thin film grows. In a physical vapor deposition process, when the adatoms initially wet onto the substrate, the growth mode is determined by the surface energy between (1) adatoms/adatoms and (2) adatoms/substrate and is described by the droplet theory of nucleation[20]. The equilibrium among the horizontal component tensions between the film phase and the substrate, as shown in Fig. 2-11, is described by Young's equation[20]:

$$\gamma_{sv} = \gamma_{fs} + \gamma_{fv} \cos\theta \qquad (2\text{-}23)$$

where γ_{sv}, γ_{fs} and γ_{fv} represent the substrate surface energy, the substrate/film interfacial energy and the film surface energy, respectively, and θ is the wetting angle.

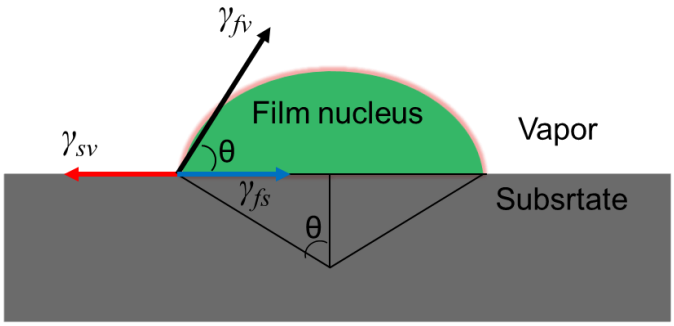

Figure 2-11. Schematic diagram of an atomistic nucleation process showing the relationships between surface energies during a vapor deposition process.

The difference between the substrate surface energy γ_{sv} and substrate/film interfacial energy γ_{fs} is termed as the wetting strength:

$$\Delta\gamma = \gamma_{fs} - \gamma_{sv} = -\gamma_{fv}\, cos\theta \qquad (2\text{-}24)$$

Using Young's equation as a theoretical guide, different wetting angles θ correlate to different wetting strengths, resulting in different thin film growth modes[49,50]:

Island growth **(**Volmer-Weber growth**)** (Fig. 2-12 (a)): when θ is large (>0), γ_{fs} is large. The substrate/film interfacial energy exceeds that of the substrate surface energy (resulting in a small wetting strength), and the deposited adatoms have stronger bonds with each other than with the substrate, and thus they tend to form clusters and grow into 3D islands. This growth mode usually occurs when the substrate and film materials are different.

Layer-by-layer growth (Frank-Van der Merwe growth) (Fig. 2-12 (b)): when $\theta = 0^{o}$, γ_{fs} is small. Adatoms have stronger bonds with the substrate and wet on the substrate completely, forming 2D layers. This is the ideal case for planar film growth and usually occurs when the growth rate is low and the growth temperature is high.

Mixed island-layer growth (Stranski–Krastanov growth) (Fig. 2-12 (c)): in some cases, layer-by-layer growth is initially favorable but then taken over by island

growth.

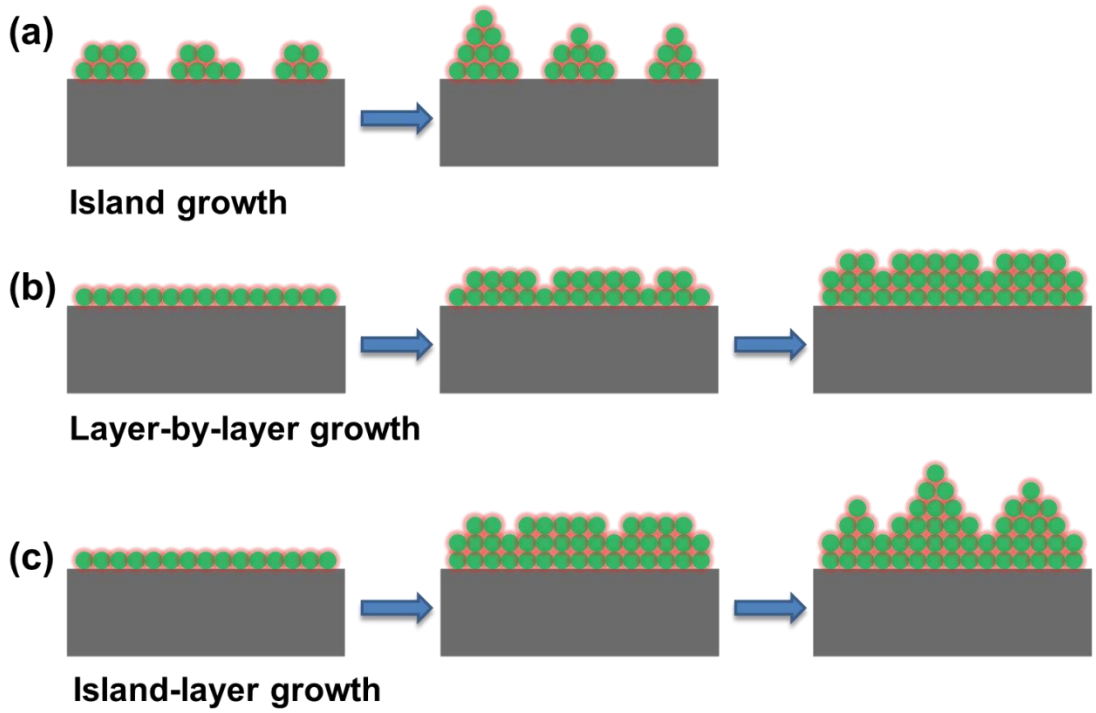

Figure 2-12. Schematic diagrams of three thin film growth mechanisms: (a) 3D island growth, (d) 2D layer-by-layer growth and (c) Mixed island-layer growth.

◆ **Mechanisms for self-assembly in VANs**

The growth of a VAN, in most cases, only partially obeys the classical thin film growth mode, and most likely show the 3D island growth mode[51]. Due to the different wetting strengths of different constituent phases, it is difficult for them to have even or uniform spread on the substrate.

A self-assembled VAN is formed by two simultaneous processes: the growth of the constituent phases and a spontaneous phase separation process (which is absent in plain films). Depending on the miscibility between the two phases (termed as AO_α and BO_α), MacManus-Driscoll *et al.*[48] pointed out three mechanisms for the phase separation of VANs:

Nucleation and Growth

When the two phases are immiscible over the whole temperature range, there is no

solid solution between AO_α and BO_α, and the two phases form on the substrate by "Nucleation and Growth". Depending on (1) the A: B ratio, (2) the surface energies and the crystallographic relations between the two phases and between each phase and the substrate, and (3) the growth kinetics, the resulting morphology is likely to be nanopillars, nanoparticles, nanoplates, etc. One example of this growth mode is the perovskite-spinel combination, such as $BiFeO_3$-$CoFe_2O_4$.

According to Chen *et al.*[38], the nucleation-and-growth of a VAN structure usually undergoes three stages, as illustrated in Fig. 2-13:

(a) Surface diffusion of adatoms. Different species first arrive and are trapped onto the substrate surface, and adatoms with the same phase tend to agglomerate due to similar surface energies. (b) Nucleation and island growth, which occurs after the diffusion process and reduces the free energy. (c) Final phase separation, which is realized through further column growth after nucleation.

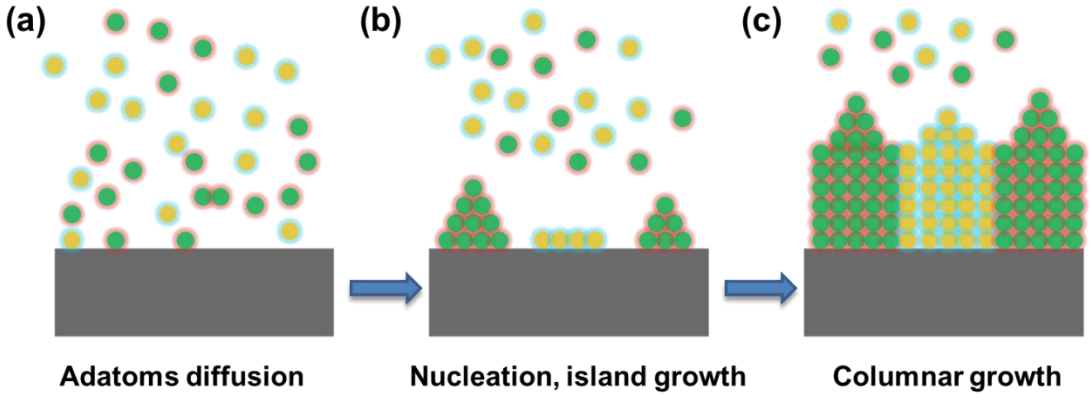

Figure 2-13. Schematic diagrams showing the nucleation and growth process of the VAN thin films: (a) adatoms diffusion, (b) nucleation and island growth and (c) columnar growth.

Spinodal decomposition

When the cations of the two phases are widely soluble at high temperatures but the crystal structures become incompatible and tend to cluster upon cooling down, composition fluctuations occur due to lowering of the free energy, which leads to phase separation.

The composition fluctuations start from sinusoidal compositional variations which are then "squared off" over time and with lowering temperature, eventually resulting in the formation of discrete phases with sharp phase boundaries. Depending on the range of miscibility regions, the system either undergoes strong phase separation into distinct structures or simply forms into a single mixed phase consisting of compositionally rich and poor regions. The clustering process is influenced strongly by time, temperature and composition. In most oxides, spinodal decomposition occurs below 500℃. Fig. 2-14 shows a schematic diagram of a spinodal decomposition process from a disordered state to an ordered checkerboard nanostructure.

One example of this growth mode is the phase separation between a multinary oxide (AO_α) and a binary oxide BO_α (a subset of AO_α). For example, when growing $NiFe_2O_4$-NiO, excessive amounts of NiO powders are added into the precursor target (a mixture of Fe_2O_3 and NiO), which results in precipitation of the NiO phase through spinodal decomposition[52].

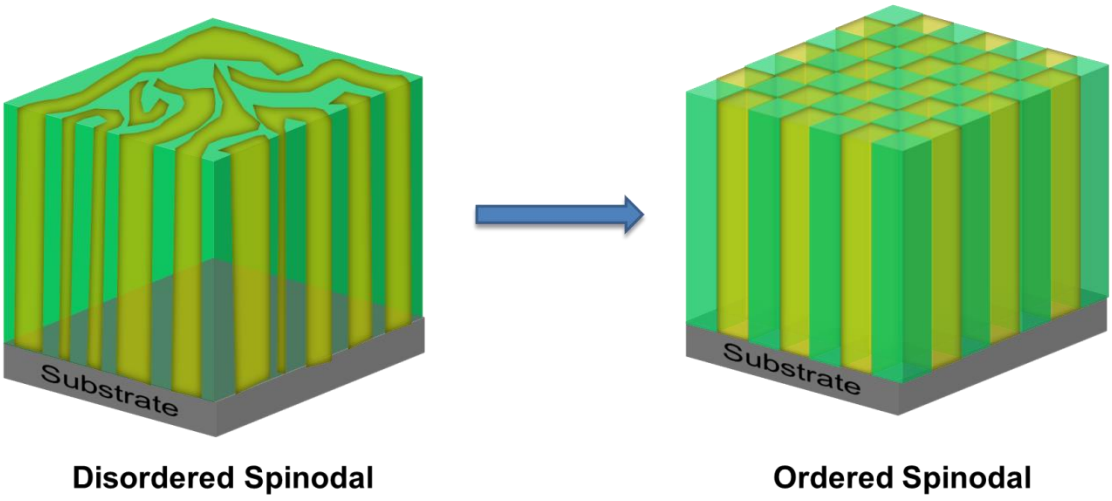

Figure 2-14. Schematic diagram of the decomposition from a disordered spinodal state to an ordered spinodal state.

"Pseudo-spinodal" Decomposition

This process includes both "nucleation and growth" and "spinodal decomposition", and usually occurs in oxide systems with partial miscibility and different symmetries.

In this growth process, an initially random mixture of cations decomposes into coherent precipitates, and the precipitates form by nucleation and growth. The resultant composite contains a low-symmetry phase embedded in a high-symmetry matrix phase (for example, the growth of tetragonal precipitates in a cubic matrix).

Apart from the above-mentioned phase separation modes, several other factors should be taken into consideration for the determination of the eventual nanostructures and compositions, including but not limited to lattice mismatch, surface energies, volume fractions, elastic moduli, and growth kinetics.

First, in the nucleation and growth mode, the phase which has the highest crystallographic matching with the substrate has a higher tendency to form the matrix phase. The epitaxy of the column phase, on the other hand, can be realized either through epitaxy with the substrate or with the matrix phase. In some cases, when the column phase does not show good epitaxy with the substrate, epitaxial growth of this phase can still be realized in the vertical direction with the help of the matrix "epitaxy stabilizer"[53].

Second, surface energies strongly influence the surface feature of the constituent phases in VAN films. For example, in the $CoFe_2O_4$-$BiFeO_3$ VAN grown on the $SrTiO_3$ (001) substrate, pyramidal crystallites of $CoFe_2O_4$ are formed. This feature is due to the lowest surface energy of the pyramidal $CoFe_2O_4$ (111) planes[54] which determines the surface termination of the crystals.

Moreover, in Pulsed Laser Deposition (PLD), the growth temperature and growth rate influence the growth kinetics drastically. It has been reported that the increase in growth temperature and the decrease in growth rate generate a larger diffusion length of adatoms and thus result in larger feature sizes of the constituent phases[54,55]. Chapter 4.5 and Chapter 5.4 will study this in detail.

2.3.4 Development and advances of VAN

The first studied self-assembled nanocomposite system was the $(La_{0.7}Ca_{0.3}MnO_3)_{1-x}$:

$(MgO)_x$ film reported by Lebedev *et al.*[56] and Moshnyaga *et al.*[41] almost at the same time (around 2003). The films were grown by metal-organic aerosol deposition (MAD). The magnetoresistance and phase transition of $La_{0.7}Ca_{0.3}MnO_3$ were tuned via a 3D tensile strain from MgO. However, the two phases grown using this solution-based method were not well oriented. From then on, extensive research on VANs has benefitted from the development of more advanced growth techniques such as Pulsed Laser Deposition (PLD) and Molecular Beam Epitaxy (MBE).

Highly oriented $BaTiO_3$-$CoFe_2O_4$ (BTO-CFO) VAN was first grown by Zheng *et al.*[57] in 2004 using PLD: a spinel magnetostrictive CFO was embedded inside a perovskite ferroelectric (piezoelectric) BTO matrix and strong coupling between the magnetic/ferroelectric order parameters was realized. This prompted subsequent studies on more multiferroic perovskite-spinel VAN systems, such as $BiFeO_3$-$CoFe_2O_4$[58], $BiFeO_3$-$NiFe_2O_4$[59], and $PbTiO_3$-$CoFe_2O_4$[60]. Meanwhile, other combinations, such as perovskite-perovskite[61], perovskite-binary oxide[62,63] have also been extensively studied.

A comprehensive summary of the reported VAN systems is listed in Table 2-3. The advances are mainly achieved through, but are not limited to the strain tuning of physical properties and the use of interfacial coupling effects. This simple but elegant self-assembly process makes it much easier to integrate functionalities without resorting to other complex device-fabrication techniques such as lithography. Apart from these classical VAN systems, more fascinating structural designs are being explored extensively, bringing in novel architectures/properties that can never be realized in conventional materials systems. For example, a double VAN stack enabled improved crystallinity and ionic conductivity in $Y:ZrO_2$ by seeding the growth of a $Y:ZrO_2$-$SrTiO_3$ VAN on a sub Sm: CeO_2-STO VAN layer[64]. Hierarchical Templating of a highly oriented $BiFeO_3$-$CoFe_2O_4$ was realized using a self-assembled triblock terpolymer[65]. 3D strain tuning through alternating growth of CeO_2 planar layers with LSMO-CeO_2 VANs gave rise to a highly tunable magnetoresistance[66]. An auxetic-like strain effect was realized when a stiff nanocolumn phase was embedded in a soft

matrix, where the thermal shrinkage of the column phase upon cooling down after deposition resulted in both *ip* and *op* tension in the matrix phase, which could never be realized through elastic coupling in planar structures[44].

Table 2-3. Summary of VAN systems

VAN Composition	Crystal Structure	Growth Method	Application
$BaTiO_3$-Sm_2O_3[62]	Perovskite-Bixbyite	PLD	Strain tuning of ferromagnetic, ferroelectric, dielectric properties
$BaTiO_3$-CeO_2[67]	Perovskite-Fluorite	PLD	
$BiFeO_3$-Sm_2O_3[43]	Perovskite-Bixbyite	PLD	
$Ba_{0.6}Sr_{0.4}TiO_3$-Sm_2O_3[68]	Perovskite-Bixbyite	PLD	
$SrTiO_3$-Sm_2O_3 [69]	Perovskite-Bixbyite	PLD	
$SrRuO_3$-$CoFe_2O_4$[70]	Perovskite-Spinel	PLD	Tuning of electronic or ionic transport
$La_{0.67}Ca_{0.33}MnO_3$-NiO[71]	Perovskite-Rocksalt	PAD	
$La_{0.7}Sr_{0.3}MnO_3$-CeO_2[72]	Perovskite-Fluorite	PLD	
$La_{0.7}Sr_{0.3}MnO_3$-ZnO[73]	Perovskite-Wurtzite	PLD	
$La_{0.7}Ca_{0.3}MnO_3$-MgO[41,56]	Perovskite-Rocksalt	MAD	
Sm:CeO_2-$SrTiO_3$[74]	Perovskite-Fluorite	PLD	
Y:ZrO_2-$SrTiO_3$[64]	Perovskite-Fluorite	PLD	
$BaTiO_3$-$CoFe_2O_4$[57]	Perovskite-Spinel	PLD	Magnetoelectrics and multiferroics
$BiFeO_3$-$CoFe_2O_4$[58]	Perovskite-Spinel	PLD	
$Pb(Zr_{0.52}Ti_{0.48})O_3$-$CoFe_2O_4$[75]	Perovskite-Spinel	PLD	
$Na_{0.5}Bi_{0.5}TiO_3$-$CoFe_2O_4$[76]	Perovskite-Spinel	PLD	
La_2CoMnO_6-ZnO[77]	Double perovskite-Wurtzite	PLD	
NiO-NiF_2O_4[52]	Rocksalt-Spinel	PLD	Interfacial coupling (Exchange bias, etc)
$La_{0.7}Sr_{0.3}MnO_3$-$BiFeO_3$[61]	Perovskite-Perovskite	PLD	
$La_{0.7}Sr_{0.3}MnO_3$-$LaFeO_3$[78]	Perovskite-Perovskite	PLD	

**PAD: Polymer-Assisted Deposition, MAD: Metal-organic Aerosol Deposition*

Recently, the assembly of VAN films on Si substrates and the growth of VAN using sputtering have pushed VAN closer to industrial applications[49,79]. More possibilities can be further explored by broadening the scope of VAN structures from all-oxide systems to metal-oxide composites[80] or even polymers. The VAN field is young but has lots of potentials.

2.3.5 The potential of VAN for tuning the multi-functionality for NV-RAMs

One ultimate goal for tuning the multi-functionality of oxide thin films is to address the issues in memory techniques raised in Chapter 1 and Chapter 2.2.2. As summarized in Table 2-3, the unique structure of VAN provides a good platform for the study and improvement of properties:

First, the VAN structure can be divided into three parts: the column, matrix and vertical interface. The strain uniformity and structural distinction in VANs not only favor the tailoring of electronic and ionic transport but also makes it possible to decouple the transport channels for different charge carriers.

Second, the 3D VAN strain provides more versatile ways for nanoengineering. The highly tunable self-assembly kinetics also makes it easier to tune the dimensionalities and engineer the physical properties through self-assembled (rather than artificial) dimension control. These make the ferromagnetic, ferroelectric, dielectric and other properties highly tunable.

The freedom from substrate clamping and the intimate interfacial strain coupling/charge transfer between the constituent phases in VAN are also intriguing for the coupling/integration of the above-mentioned multi-functionality via exchange interactions through the vertical interfaces.

In this thesis, nanoengineering of multiple properties (including electronic/ionic conduction, electrical transport and ferromagnetism) of oxide thin films using VAN approaches will be presented in each result Chapter (4 to 6). The ultimate goal of these works is to improve the performances for application in various memory devices.

Chapter 3 Experimental Methods

This chapter presents an introduction to the basic working principles of all experimental methods used in my works, including film growth, characterization, and measurements. More detailed experimental parameters of any particular technique will be provided in each result chapter (Chapter 4 to 6) when the technique is used.

3.1 Thin film growth

3.1.1 Making the precursors: target synthesis

Pulsed Laser Deposition (PLD) (details will be described later) is one of the most widely-used techniques to grow vertically-aligned nanocomposites (VAN). The self-assembly process occurs via spontaneous phase separation in a one-step process, by ablating one ceramic composite target or alternatively ablating several targets. The ceramic targets are sintered via solid-state reactions. In order to enhance the phase purity and stoichiometry, several factors should be taken into consideration in the target making process:

1. The materials selection should follow the three phase-separation principles discussed in Chapter 2.3.2: either with non-miscibility (for nucleation-and-growth) or with non-miscibility gaps (for spinodal decomposition). One way to minimize the intermix between the different phases is to firstly crystalize the powder of one phase at a high temperature, which is then followed by an additional sintering after mixing with the powder of the second phase. Fig. 3-1 shows the two-step solid-state reaction process of the target sintering for the $La_{0.9}Ba_{0.1}MnO_3$-CeO_2 VAN films studied in Chapter 5.

2. The sintering temperature of ceramic phases should be set at around 50-75% of the melting point[81]. For most oxides, the melting temperature is around 2000℃ and

therefore 1100℃–1300℃ is a commonly used sintering temperature for oxide ceramic targets.

3. For targets containing volatile elements (such as Bi and K), a slightly excessive amount of the volatile element should be added into the precursor powder when making the targets[76].

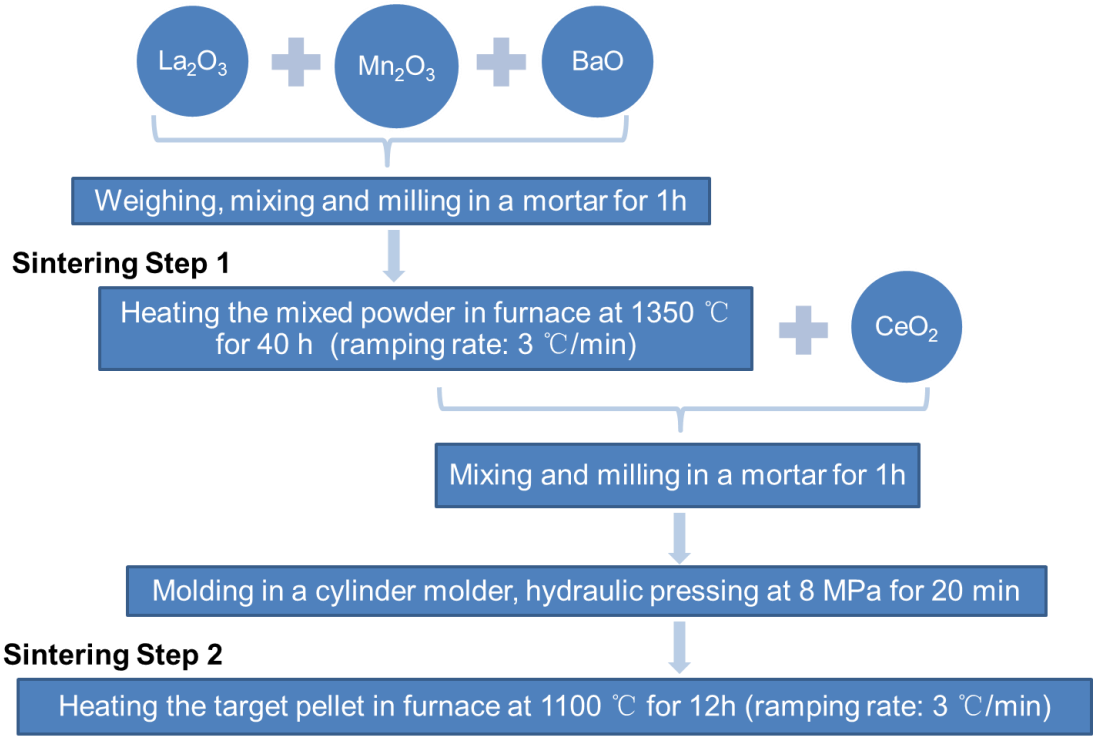

Figure 3-1. Flow diagram for the solid-state chemistry route used to elaborate the ceramic perovskite $La_{0.9}Ba_{0.1}MnO_3$-CeO_2 target for the Pulsed Laser Deposition (PLD) of the $La_{0.9}Ba_{0.1}MnO_3$ matrix with the vertically aligned CeO_2 nanocolumn phases.

Table 3-1 lists the synthesis processes for all the targets related to this thesis. Some targets were sintered using the two-step process described in Fig. 3-1, while others were obtained through just one step. All the oxide nanopowders listed in Table 3-1 were purchased from Sigma-Aldrich (with purity >99.9%).

Table 3-1. Summary of the synthesis process for all the oxide targets used

Target composition	One/two step?	Raw Oxide Nanopowders used	Ramping rate (℃/min)	Sintering temperature (℃)	Sintering duration (h)	Remarks
CeO_2-$SrTiO_3$ (1:1)	One	CeO_2 +$SrTiO_3$	2	1100	6	Made by Dr. Seungho Cho
10%Sm:CeO_2-$SrTiO_3$ (1:1)	Two	Sm_2O_3,CeO_2 (step 1) +$SrTiO_3$ (step 2)	2	1450 (step 1) +1100 (step 2)	24 (step1) +6 (step 2)	Made by Dr. Seungho Cho
20%Sm:CeO_2-$SrTiO_3$ (1:1)	Two	Sm_2O_3,CeO_2 (step 1) +$SrTiO_3$ (step 2)	2	1450 (step 1) +1100 (step 2)	24 (step1) +6 (step 2)	Made by Dr. Seungho Cho
30%Sm:CeO_2-$SrTiO_3$ (1:1)	Two	Sm_2O_3,CeO_2 (step 1) +$SrTiO_3$ (step 2)	2	1450 (step 1) +1100 (step 2)	24 (step1) +6 (step 2)	Made by Dr. Seungho Cho
$La_{0.9}Ba_{0.1}MnO_3$-CeO_2 (1:1)	Two	La_2O_3, Mn_2O_3, BaO (step 1)+ CeO_2 (step 2)	3	1350 (step 1) +1100 (step 2)	40 (step1) +12 (step 2)	
$La_{0.9}Ba_{0.1}MnO_3$-ZnO (1:1)	Two	La_2O_3, Mn_2O_3, BaO (step 1)+ ZnO (step 2)	3	1350 (step 1) +1100 (step 2)	40 (step1) +12 (step 2)	

3.1.2 Growth of VAN films using Pulsed Laser Deposition (PLD)

The developments in thin film fabrication have brought about many advanced synthesis techniques, which can be classified into Physical Vapor Deposition (PVD) and Chemical Vapor Deposition (CVD). Molecular Beam Epitaxy (MBE) is one of the most advanced PVD methods, but is limited by its extremely slow growth speed and high cost for system components and target materials[20]. Sputtering is a more economical PVD method to produce films on large scales, but the composition of the target cannot be stoichiometrically transferred to the film as the sputtering yield varies for different elements[82], which causes problems for growing oxide thin films. In terms of CVD, metal organic chemical vapor deposition (MOCVD) excels in its uniform deposition rate which is favorable for high-quality surface of the films, but identification and storage of the precursors are challenging[20,82].

In our work, we used Pulsed Laser Deposition (PLD) (one PVD route) to grow oxide thin films, for the following advantages over the methods listed above: It has the capability of stoichiometric transfer (compared to sputtering) and the target is easy to make (compared to MOCVD); also, it has a cost-effective setup, high growth efficiency (compared to MBE) and highly controllable growth kinetics[49,50,82,83]. Although being claimed to have problems of explosive ejection of particles and splashing, PLD is still the most widely-used method for the growth of oxide films as

well as oxide VAN films, since it offers the fastest route to the precise prototyping of complex phases[84].

The PLD technique was first introduced in the 1960s and then developed in the 1980–1990s[85,86]. Nowadays, many advanced PLD systems incorporate reflection high energy electron diffraction (RHEED) to allow *in-situ* monitoring of the growth process. The use of the laser heating technique enables more homogeneous heating of the substrate for higher quality films. The user-friendly system of PLD also allows the incorporation of x-ray photoelectron and scanning probe measurements and other synchrotron-based techniques[82].

Fig. 3-2 shows a schematic diagram for the PLD equipment setup used in our experiments. A 248 nm monochromatic laser beam with a wavelength of 248 nm is generated by a KrF excimer laser generator (Models COMPEX 201 and 205, Lambda Physik®, denoted as (1) in Fig. 3-2). After being focused by a series of optical lenses (2), the laser beam enters the vacuum chamber, and then the target material (6) is ablated by the laser, producing molecules, ions, and plasma with high energies. These clustered species form the "plumes" (3), which travel all the way to the opposite side of the target and are then deposited onto the substrate attached to the heater plate (8) at a high temperature. The temperature of the homemade heater block is controlled by a temperature controller (7). The substrate temperature can be measured by a K-type thermocouple embedded in the heater block or by an infra-red pyrometer from outside the chamber.

The PLD film growth starts with a substrate/target loading process. The substrates were cleaned ultrasonically (10 mins acetone followed by 10 mins isopropanol). Then the cleaned substrate was pasted onto the heater plate using silver paint. Meanwhile, the surface of the target was cleaned using sandpapers and wiped with acetone+isopropanol. Finally, the substrate and the target were loaded into the vacuum chamber.

After loading, the chamber was evacuated by a turbo-molecular pump coupled with

a rotary pump (4 in Fig. 3-2) to get a base pressure of $<10^{-7}$ Torr. Then, a proper oxygen pressure was adjusted through a mass flow controller (MFC) equipped in the vacuum system (4 in Fig. 3-2); meanwhile, the substrate was heated up to 600-800℃. Next, the deposition was done by ablating the target using high-energy laser pulses. The laser spot size focused on the target was around 8 mm^2, and the target-substrate distance was fixed at 5 cm. The laser power was adjusted and monitored using a laser energy controller and a laser energy meter, respectively. During the deposition, the target was rotated to ensure homogeneous ablation. More detailed growth conditions for different VAN systems will be mentioned in each result chapter.

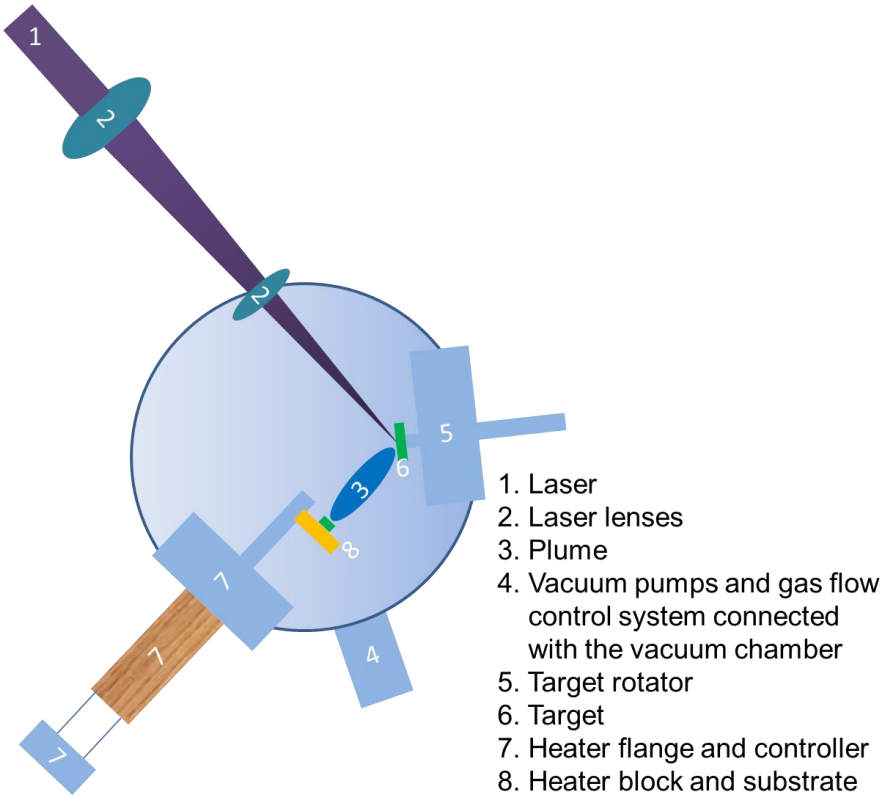

Figure 3-2. Schematic diagram showing the PLD system used in this work

The following growth parameters are key factors to be considered, not only for the growth of single-phase oxide thin films but also for VAN films[38]:

1. Laser fluence (Energy density): The laser fluence is defined as the laser energy divided by the laser spot size (J/cm^2). A low laser fluence is not enough for a proper crystallization or stoichiometry transfer due to the lack of sufficient kinetic energy for

the adatoms or the selective ejection of species from the target. On the other hand, a high laser fluence may result in a rough surface morphology due to the heavy bombardment of adatoms[49,50]. For the growth of VAN, an empirical range of the laser fluence is 1–4 J/cm^2. In this work, the optimized laser fluence is 1–2 J/cm^2 depending on the materials systems.

2. Growth temperature: A higher growth temperature generally leads to a more effective diffusion of adatoms, which ensures a better crystal quality for most kinds of oxide phases. However, a high growth temperature may also result in the formation of unexpected phases or the deficiency of volatile elements. Considering the phase separation of VAN, growth or treatment at high temperatures may also apply extra heat which results in inter-diffusion of the constituent phases. Therefore, a compromise should be balanced for the growth of a proper VAN[38].

The growth temperature also has a big influence on the morphology of the VAN phases. As the feature size of the matrix/nanocolumn phase is mainly determined by the diffusion length of the adatoms' on the substrate, a higher growth temperature usually results in a larger column size[38].

In our works, the growth temperature varies from 690-825℃.

3. Oxygen pressure: The growth of oxide thin films with multi-species requires the inclusion of oxygen as a component in the plasma. The proper amount of oxygen gas depends on the thermodynamic stability and oxidation state of the desired phases, which is controlled by the oxygen partial pressure in the PLD chamber. In addition to the oxygen stoichiometry control, the kinetic energies are also influenced largely by the oxygen gas pressure, with a higher pressure favoring lower growth kinetics and a lower growth rate[49]. The proper deposition atmosphere for oxide phases varies quite a lot, ranging from 10^{-5} to 10^{-1} mbar. In this work, an optimized oxygen pressure is 0.1–0.3 mbar depending on the materials systems.

4. Growth rate: The growth rate is defined as the thickness of the films gained per unit time (nm/s). It is generally accepted that a lower growth rate is correlated to an

improved crystal quality of the films due to an adequate diffusion time for the ad-atoms. Apart from this general influence, the growth rate has more impact on the VAN films than on single-phase plain films. The surface diffusion of ad-atoms is an important process for the 3D columnar growth of the VAN phases in the nucleation-and-growth mode during the laser pulses (recall Fig. 2-13). The diffusion length is expressed as $L \approx 2\sqrt{D\tau}$, where D is the diffusion coefficient (influenced by the growth temperature) and τ is the diffusion time (influenced by the laser repetition rate)[38,87]. Therefore, the laser repetition rate (which can be varied from 1 to 10 Hz) and the growth temperature are two important factors for the diffusion length in the columnar growth process, and thus the morphology of the VAN structure. Detailed studies on these two factors will be presented in Chapter 4 and 5, respectively. The oxygen gas pressure and laser energy (fluence) also play a role on influencing the growth rate, as mentioned above.

The above-mentioned four growth parameters are the most important factors in PLD growth. They can be controlled independently, but the resulting effects are influenced by one another. There are many other factors which also contribute to the final result of the crystallization, phase formation and morphology of the films, such as target-substrate distance, base pressure, laser wavelength, etc. PLD growth itself can be a massive work. In order to obtain an optimized phase, systematic trials should be done.

3.1.3 Deposition of electrodes for electrical measurements

For the electrical/transport property measurements, platinum (Pt) or gold (Au) electrodes were deposited onto the sample using an Emitech K550 or K575 series DC sputtering coater. The sputtering chamber was firstly pumped down to around 1×10^{-3} mbar using a rotary pump and then ironized Ar gas was generated by an electrical current of 40 mA. A Pt (or Au) target was bombarded by the ionized Ar, which results in the ejection of Pt (or Au) species that are finally coated onto the sample surfaces.

Different shadow masks were used to deposit electrodes with various sizes and features. For electrical measurements, patterned electrode dots with three diameters (100, 300 and 400 μm) were fabricated. For magnetic measurements with applied electric fields, a large portion of the film surface was covered with a continuous electrode pad deposited onside, with the edges left clean.

3.2 Structural characterization

3.2.1 X-ray Diffraction (XRD)

XRD is one of the most useful tools to determine the crystal structures, quantify the lattice constants, analyze the crystallographic orientations, coherent length, tilt, and other structural information. In XRD equipment, a beam of electrons is accelerated, which then bombards a metal target (such as Cu). The inner-shell electrons of the metal are excited and the x-ray is then radiated in the process of electron transition. After the x-ray is incident on a crystal, the diffraction condition is satisfied when the x-ray wavelength is close to the lattice constant. According to Bragg's Law:

$$2dsin\theta = n\lambda \tag{3-1}$$

where λ is the wavelength, θ is the incident angle, and d is the lattice interspacing. The diffraction peak shows up when these variables satisfy equation (3-1). The interference intensity is a complicated function of the atomic scattering factor and the structural factor of the crystal, while these factors are related to the diffraction angle, crystal symmetry, atomic structures and electron cloud distribution[88]. Miller indices (*h k l*) can be used to identify different crystal planes and orientations.

In our experiments, x-ray powder diffraction measurements were conducted for determining the crystal structure of the polycrystalline target, and a Bruker® D8 Gen 10 two-circle diffractometer with an x-ray generator and scintillation counter was used. For analyzing epitaxial thin films, a Panalytical Empyrean® vertical four-circle diffractometer was used, which is coupled with a hybrid two bounce monochromator,

programmable PASS (programmable anti-scatter slits) and a scintillation counter. The diffractometer has 4 drives, namely: omega (ω), 2theta (2θ), chi (χ) and phi (φ) (as illustrated in Fig. 3-3), which can adjust the geometry of the sample in the 3D space. Here ω is the incident angle (the angle between the incident beam and the sample surface) and θ is the diffraction angle (the angle between the incident and diffracted beam). A monochromator was used to ensure that only the Cu K-α_1 beam can pass through.

Before the XRD measurement, the sample position was calibrated so that the initial geometry was the same as the nominal instrumental settings, as an offset of ω may exist either due to dirt/imperfections on the back side of the substrate or the deviation of the sample stage to the optimum setups. To calibrate the sample position, the height of the sample stage was aligned first and then the four drives were adjusted with respect to the substrate orientation with the highest diffraction intensity (for example, for $SrTiO_3$ (001) substrates, $SrTiO_3$ (002) peaks were used for the calibration).

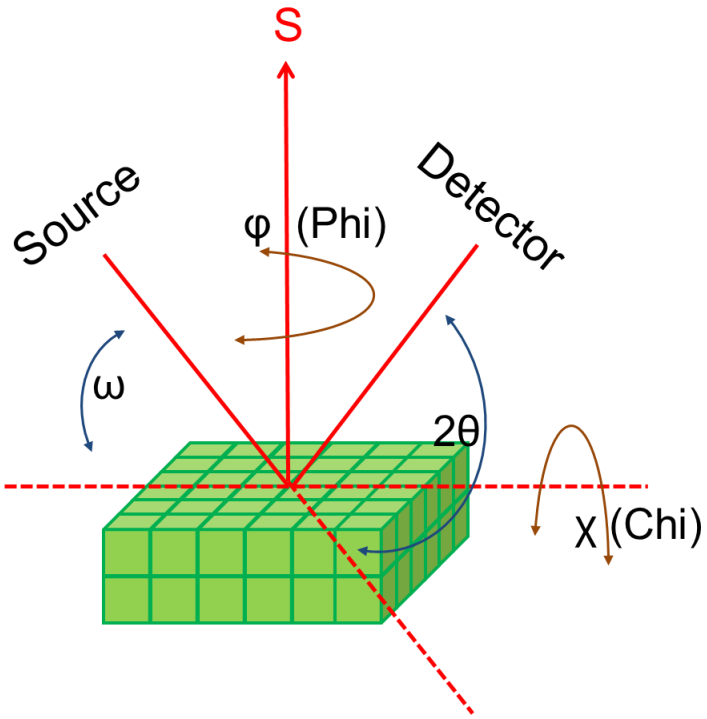

Figure 3-3. Schematic diagram of the XRD configuration with the four drives (ω, 2θ, χ, φ). S is the wave vector which is normal to the sample plane.

The crystallographic information of the thin films can be obtained via the following 4 ways:

2θ-ω (*θ-2θ*) scan

2θ-ω scan is the most basic structural characterization method used in this work, which aims at phase identification and determination of the epitaxial relationship in the first instance. It is performed in a Bragg-Brentano geometry, where the diffraction angle *2θ* moves at twice the speed of the incident angle *ω* (as illustrated in Fig. 3-3). According to equation (3-1), diffraction peaks appear when the Bragg's Law is satisfied. Here *θ* corresponds to a certain series of lattice planes with a specific interspacing *d*. Through the *d* spacing values, the out-of-plane lattice constant of this crystal orientation can be determined. Meanwhile, the crystal phases with specific Miller indices (*h k l*) can be identified by comparing the diffraction peak position with that of the standard reference diffraction patterns. Reference patterns can be found in JCPDS (Joint Committee on Powder Diffraction Standards) card or ICDD (the International Center for Diffraction Data) database search.

Phi (φ) scan

φ scan is a useful way to determine the crystal symmetry and the in-plane matching relationship of the film with respect to the substrate. As illustrated in Fig. 3-3, it is done by measuring the diffraction intensity of a certain crystal plane when scanning the *φ* angle over 360^{o}, while all the other configurations are kept constant. For example, if one phase in the film has a 6-fold hexagonal symmetry, there will be 6 lattice planes with equal d-spacing which satisfy Bragg's Law. Therefore, when the *φ* angle is scanned over 360^{o}, 6 diffraction peaks show up at 6 different *φ* positions. Meanwhile, the crystal symmetry of the substrate generates a diffraction pattern at another set of *φ* angles. By comparing the diffraction peak position of the film with regard to the substrate, one can tell the in-plane epitaxy relationship between the films and the substrate.

ω scan (rocking curve)

Rocking curve is a useful tool for evaluating the imperfection of the crystal structures. It is performed by fixing the diffraction angle to the diffraction peak position 2θ for a certain crystal phase, while the incident angle ω is scanned over a small range (usually several degrees), as shown in Fig. 3-3.

In an ideal case, a perfect crystal shows a sharp and strong rocking curve. However, in real cases, the full width at half maximum (FWHM) is broadened because of the following factors[89]: (1) instrumental broadening due to limited equipment resolution, (2) limited size of the phase (L), (3) tilt (and twist) of the unit cells (α) and (4) microstrain (ε) due to the strain gradient from different depth levels or from the periphery to the center of the phase. In reciprocal space, these broadening factors can be expressed as:

$$\Delta s_L = \frac{1}{L} \tag{3-2}$$

$$\Delta s_\alpha = \alpha s \tag{3-3}$$

$$\Delta s_\varepsilon = 2\varepsilon s \tag{3-4}$$

where s is the scattering vector and Δs is the broadening in reciprocal space and for ω scans, their relationships to the real space parameters are defined as:

$$s = \frac{1}{d} = \frac{2sin\boldsymbol{\theta}}{\lambda} \tag{3-5}$$

$$\Delta s = \beta s \tag{3-6}$$

where β is the integral breadth measured by ω, which is obtained from dividing the peak area by the peak height.

In general, the broadening can be expressed as:

$$\beta_L = \beta_{\text{sample}} + \beta_{instrument} \tag{3-7}$$

$$\beta_{\text{sample}} = \beta_{\text{size}} + \beta_{\text{misorientation}} + \beta_{\text{microstrain}} \tag{3-8}$$

when the peak shape is assumed to be Lorentzian.

$$\beta_G^2 = \beta_{sample}^2 + \beta_{instrument}^2 \quad (3\text{-}9)$$

$$\beta_{sample}^2 = \beta_{size}^2 + \beta_{misorientation}^2 + \beta_{microstrain}^2 \quad (3\text{-}10)$$

when the peak shape is assumed to be Gaussian.

The broadening factors for β_{sample} are closely related to the existence of dislocations, misorientations or mosaic spread, which may cause disruptions of the lattice planes. For symmetric ω scans, there is no contribution from the microstrain and twist to the peak broadening[83]. Besides, the instrumental resolution for ω scan is 0.006^{o}, which is much smaller than the measured peak width. Therefore, for symmetric ω scans, equations (3-7) to (3-10) can be simplified to:

$$\beta \frac{2sin\theta}{\lambda} = \alpha \frac{2sin\theta}{\lambda} + \frac{1}{L} \quad \text{(Lorentzian peak shape)} \quad (3\text{-}11)$$

$$\beta^2 \frac{4\sin^2\theta}{\lambda^2} = \alpha^2 \frac{4\sin^2\theta}{\lambda^2} + \frac{1}{L^2} \quad \text{(Gaussian peak shape)} \quad (3\text{-}12)$$

The contribution from the size (L) and tilt (α) can be deconvoluted using equations (3-11) and (3-12). Detailed structural analysis of imperfections, size and tilt using ω rocking curves will be presented in Chapter 4 and 5 using equations.

Reciprocal Space Map (RSM)

Compared to the 2θ-ω scan, asymmetric RSM is more powerful in detecting the in-plane lattice parameters, which can be used to analyze the information regarding strain and relaxation. It is done via a 2-axis scan: by performing a series of 2θ-ω scans at a series of fixed ω positions, a contour map in the 2θ-ω space is obtained. RSM uses ω and 2θ as the scan axes, which can be converted to the lattice constants in the reciprocal space (Q_x and Q_z) using the following equations:

$$Q_x = \frac{cos\,\omega - \cos\,(2\theta - \omega)}{\lambda} \quad (3\text{-}13)$$

$$Q_z = \frac{\sin\,\omega + \sin\,(2\theta - \omega)}{\lambda} \quad (3\text{-}14)$$

and by using the following relationship between the lattice constants in the real and reciprocal space:

$$Q_x^2 = \frac{h^2}{a^2} + \frac{k^2}{b^2} \tag{3-15}$$

$$Q_z^2 = \frac{l^2}{c^2} \tag{3-16}$$

the in-plane (a and b, where a=b in cubic or tetragonal phases) and out-of-plane (c) lattice constants of the real space can be obtained. The information enables us to:

1. Analyze the strain state of the film phase with respect to the substrate. By comparing the in-plane lattice constants and the diffraction peak positions, one can tell whether the film phase is fully strained ($a_{\text{film}} = a_{\text{substrate}}$) or relaxed ($a_{\text{film}} \neq a_{\text{substrate}}$).

2. Determine the crystal symmetry of the film phase. Different crystal phases have different symmetries which can be reflected through certain features in the asymmetric RSMs. For example, the unit cells of a certain class of perovskite films show periodic twinning to orthorhombic or rhombohedral bulk structures as a way of strain relaxation, which can be reflected as paired twinning peaks in RSM. Details on twinning will be discussed in Chapter 5.3.

3. Evaluate the crystal quality of the phase: a sharp and intense peak indicates a high crystallinity while a broad and weak peak is usually caused by a low crystal quality, relaxation, or large variations in the lattice parameters.

The collected XRD data was processed using professional software. X'pert HighScore Plus® was used for profile fitting of the diffraction peak parameters, such as the peak position, FWHM, intensity, background, etc. Epitaxy® was used to calculate the film thickness (via laue interference fringes), and to extract RSM peak positions for the calculation of the in-plane and out-of-plane lattice constants.

3.2.2 Scanning Probe Microscopy (SPM)

Scanning probe microscopy (SPM) encompasses a family of techniques that probe the surface topography and other physical properties on the atomic scale. The first developed SPM technique was Scanning Tunneling Microscopy (STM), which was restricted by the requirement for a conductive sample surface. This brought about the development of Atomic Force Microscopy (AFM), which relies on the detection of atomic forces instead of a tunneling electrical current used in STM. AFM is mainly divided into three parts: the cantilever, detector, and controller. The cantilever is equipped with a sharp tip that is sensitive to the atomic forces and can be vibrated by piezoelectric actuators. When the tip scans over the sample surface, the change of the tip-sample force alters the cantilever deflection (in contact mode) or oscillating frequency (in tapping mode). This tiny change can be detected and sent to the feedback system, which maintains the vibration frequency or deflection at a constant value (setpoint). The difference between the detected signal and the setpoint will be recorded as a reflection of the surface topography or other physical properties.

AFM has 3 working modes: contact mode, tapping mode, and non-contact mode. The non-contact mode has the slowest scan speed, while the contact mode has a high possibility to damage the sample surface, therefore the tapping mode is the most widely used for probing the topography information, where the oscillation frequency of the cantilever is the setpoint. During one scan, not only the surface topography, but also lots of other information can be detected. For example, mechanical properties are detected through the phase image, and accurate surface roughness information can be probed using the amplitude or amplitude error image. By choosing different kinds of cantilevers and setups, the detection signal can be switched from topography (normal AFM) to conductivity (Conductive AFM, C-AFM), local electrical polarization (piezoelectric force microscopy, PFM) or magnetic domain (magnetic force microscopy, MFM).

In this work, an AFM (Multimode 8 SPM with Nanoscope V controller) in tapping

mode was used to collect surface morphology images of the VAN films. The lateral resolution was 512x512 pixels and the scanning area could be changed from 500 nm to 10 μm. The AFM tips used for normal topography were Al-coated Si tips with a resonant frequency of 300 kHz and a constant force of 40 N/m. For the detection of current maps or local conductivities, C-AFM was performed on an Agilent 5500 scanning probe microscope with commercial Pt/Ir-coated Si tips. All the collected images were processed and analyzed using the WSxM (version 5.0) software.

3.2.3 Transmission Electron Microscopy (TEM)

TEM is a precise tool that provides detailed structural and compositional information with the highest resolution among all the microscopic techniques. It uses a heated cathode to generate a high-energy electron beam, which is focused by electromagnetic lenses and then transmit through a sample with a low thickness (~30 μm). The electron-sample interactions reflect the sample information in great detail.

TEM is powerful in structural/compositional detection with versatile setup parameters. The magnification (the degree of enlargement of the object in the image with respect to the original object) can be changed by adjusting the individual magnifying powers of all the lenses. TEM works in diffraction mode or imaging mode, which can be switched by changing the focal length of the intermediate lenses. Bright-field or Dark-field images can be obtained by selectively choosing the transmitted or diffracted electrons to pass through the sample for imaging. Scanning TEM (STEM) is a working mode of TEM in which the electron beam is focused on the sample in a tiny spot, and then rastered over the sample. By using a STEM with a high-angle detector, it is possible to reflect real atomic arrangements with Z-contrast (where the contrast is directly related to the atomic number). This is superior to the conventional high-resolution TEM (HR-TEM) which uses phase contrast to produce results that need further interpretation.

Cross-sectional HR-TEM and STEM, and plain view STEM images of the film

were obtained by a FEI TALOS F200X operated at 200 kV equipped with ultrahigh resolution high angle annular dark field detectors and Supper-X^{TM} electron-dispersive x-ray spectroscopy. The selected area electron diffraction (SAED) and EDS element mapping were also collected. The specimen for TEM analysis were obtained through mechanical grinding, dimpling, and a final ion milling step. TEM works in this thesis were conducted by Xing Sun, Dr. Jie Jian, Dr. Sichuang Xue in Prof. Haiyan Wang group at Purdue University (USA), Dr. Ping Lu in Sandia National Laboratory (USA), and Dr. Quanxi Jia in Los Alamos National Laboratory (USA).

3.2.4 Scanning Electron Microscopy (SEM)

SEM is another surface-probing tool to reveal the morphology of a nanostructure with a wide scanned area and magnification range. It also uses a high-energy electron beam to interact with the sample as in other electron microscopic techniques. Unlike TEM, a collimated electron beam scans over the sample surface and produces various by-products including secondary electrons, back-scattered electrons, and x-rays which contain useful information regarding the topography and composition of the sample surface. The secondary electrons are the most commonly-used signal in SEM.

In this work, SEM images of the VAN films were acquired using a Hitachi S-5200 SEM operated at 15 kV. The sample surfaces were coated with Ag prior to the detection in order to minimize the charging effects caused by insulating samples.

3.3 Magnetic measurements using the Superconducting Quantum Interference Device (SQUID)

SQUID is one of the most powerful tools for magnetic measurements over a wide temperature range. The principle is based on the Josephson effect[90,91], and the basic working unit contains superconducting loops consisting of two superconductors separated by thin insulating layers which form two parallel Josephson junctions, as shown in Fig. 3-4. The change in the magnetic signals induces a change in the

magnetic flux which results in a voltage change in the junctions. SQUID is operated with a constant bias current, allowing the measured voltage to oscillate with the phase changes of the current between the two junctions, which depends on the change in the magnetic flux. The changes in magnetic flux are quantized in units: $\varphi_0 = 2.07 \times 10^{-15}$ $T.m^2$. This one flux quantum is the smallest magnetic flux that can be detected, which enables the SQUID to detect low magnetic signals with great sensitivity. In spite of its high measurement capability, background noise is a big issue which sometimes distracts the data interpretation, since SQUID collects all the magnetic signals in the measurement chamber. The background signal can be reduced by careful sample cleaning or using sample probes with lower diamagnetic/paramagnetic signals (such as quartz, or a plastic straw).

Before the measurement, the sample with a proper probe was loaded into a vacuum chamber and the low-temperature measurements were performed in a vacuum atmosphere. A sample centering operation was conducted by calibrating the "center" position to where the magnetic signal of the sample showed a maximum when moving the sample position over a range (4–6 cm) in which four magnet coils are placed (2 coils in the center and 2 others on both sides with opposite current flow). This can be done with or without a magnetic field applied (by measuring the residual signals). The centering scan ensures that the sample is placed in the right initial position, i.e. at the center of the two Josephson junctions.

In this work, a Quantum Design cryogen-free Magnetic Property Measurement System (MPMS) was used. The magnetic moment sensitivity is 10^{-8} emu, and the operational temperature range was between 1.8 and 400 K. To obtain a magnetic hysteresis loop, the magnetization (M) was recorded with changing the magnetic field (H) at a certain temperature. For temperature-dependent measurement, the magnetization (M) was recorded by varying the temperature (T) either with or without a magnetic field applied.

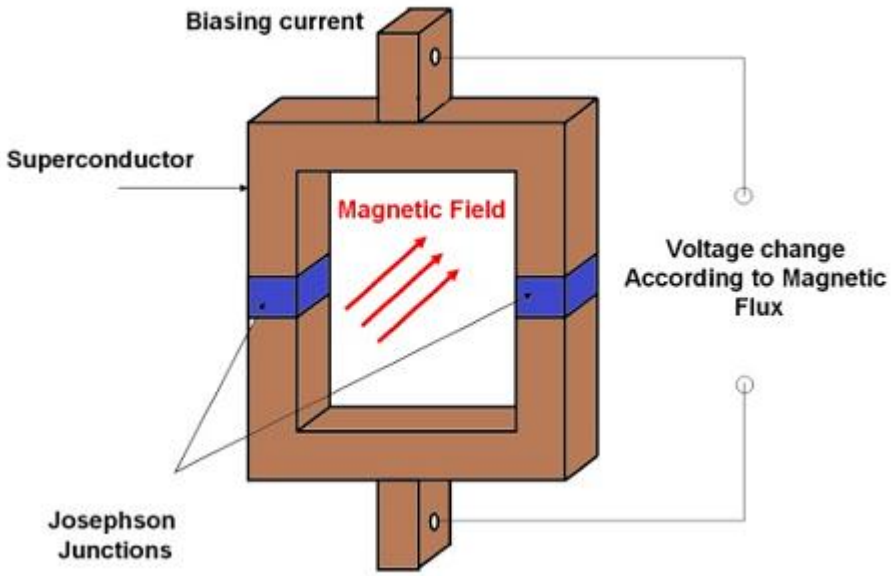

Figure 3-4. The basic unit of a SQUID magnetometer consisting of two parallel Josephson junctions (Figure taken from[92])

3.4 Electrical measurements

3.4.1 Measurement of resistive switching

The resistive switching was measured in a two-probe configuration. The device with electrode dots was placed on a flat insulating plate and a probe station (Signatone S-725PLM micropositioner) equipped with two tungsten tips is used for electrical circuit connection. A 3-dimensional adjustment of the position of the tips was achieved via spiral micro drivers. The probes were connected with Keithley source meters (2400 series) driven by Labview programs using GPIB commands. Detailed measurement parameters will be discussed in Chapter 4.

3.4.2 Measurement of electrical transport using the Physical Properties Measurement System (PPMS)

PPMS is a versatile tool for the measurement of all kinds of physical properties

including resistance, magnetization, heat capacity, etc. For the resistance measurement, the samples were mounted with an in-line 4-terminal configuration as shown in Fig. 3-5:

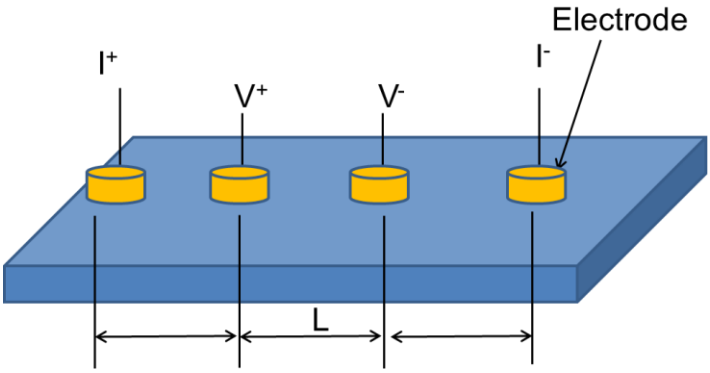

Figure 3-5. Measurement configuration for the resistance using PPMS

A DC source current (1 μA) was applied and the voltage was collected which was converted to the resistance. The resistivity (ρ) and resistance (R) have the following relationship:

$$R = \rho \frac{l}{A} \tag{3-17}$$

where l is the distance between the two electrodes to which the voltage was measured, A is the cross-sectional area of the current flow and R is the measured resistance. The resistance can be converted to resistivity. For samples with different shapes, different models are used[93,94]:

◆ **Resistivity of bulk samples**

For bulk samples, four electrodes with equal space were made on the sample surface using silver paint and the electrodes were then connected to sample puck (holder) using Au wires. When the probe spacing << the sample dimension, the "three-dimensional infinite model" is satisfied. Using equation (3-17) and by integration of differential resistance between two inner probes, the resistivity is calculated as:

$$\rho = 2\pi L\left(\frac{V}{I}\right) = 2\pi LR \tag{3-18}$$

where L is the probe spacing and R is the measured resistance.

◆ **Resistivity of thin films**

The surface of the thin film sample was deposited with Pt electrode dots (300 μm), and the electrodes were contacted to the sample puck using Al wires (25 μm in diameter) by an ultrasonic wedge wire bonder.

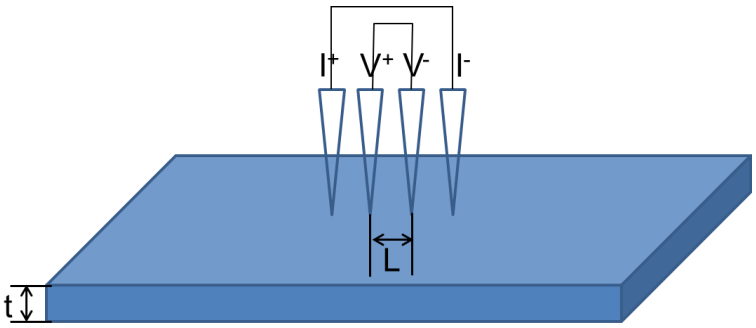

Figure 3-6. Standard in-line four-probe measurement configuration for the resistance

In a standard four-probe configuration (Fig. 3-6), the "two-dimensional infinite model" is satisfied and using equation (3-17), the resistivity is calculated as:

$$\rho = \frac{\pi t}{ln2}\left(\frac{V}{I}\right) = 4.53*k*tR \tag{3-19}$$

where k is a correction factor correlated to the dimension of the probe size, probe spacing and sample size.

In a simplified model considering our configuration, the current flow is assumed to be located just under the electrode area (as shown in Fig. 3-7). Equation (3-17) becomes

$$\rho = \frac{D}{L}tR = 0.6*tR \tag{3-20}$$

However, this model assumes that the current only goes through the area under the electrodes and therefore the area for the current flow is likely to be underestimated, so the calculated ρ can be smaller than the real ρ.

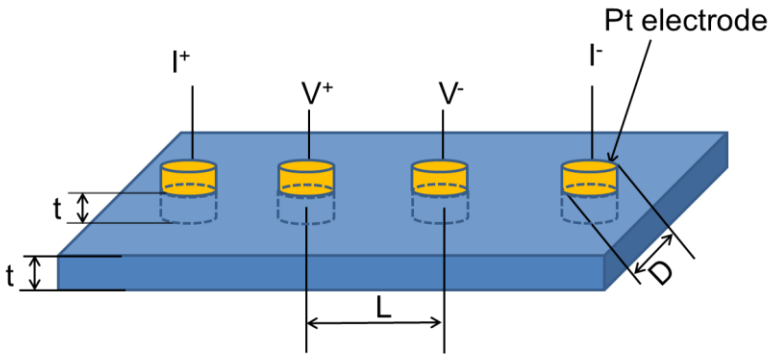

Figure 3-7. A simplified model for calculation of the resistivity of thin films using our measurement configuration.

It can be seen from above that the accurate determination of resistivity is influenced by many factors, including size, shape and even the difference in current flow path. On the other hand, film resistance is influenced by thickness ($\rho \propto t*R$) when resistivity is the same. Despite these factors, the transport behavior (such as phase change) is not influenced whether a *R-T* or ρ-*T* curve is used.

In this work, a Quantum Design PPMS DynaCool with a 14 Tesla Magnet was used for the measurement of electrical transport properties, e.g. the temperature dependence of resistance (*R-T* curve). For the magnetoresistance measurement, the *R-T* curve was recorded with a constant magnetic field applied, or the resistance value was recorded by sweeping the magnetic field at a constant temperature.

3.4.3 Measurement of ionic conductivity

The DC electrical measurement can only reflect the electrical conductivity of a material. To obtain the ionic conductivity, the AC impedance spectra are needed. The AC impedance is expressed as:

$$Z = Z' + jZ'' \tag{3-21}$$

where *Z'* and *Z''* are the real and the imaginary part, respectively. By measuring the *Z'* and *Z''* over a range of frequencies, one gets the "Nyquist plot" (*Z'* as the y-axis and *Z''* as the x-axis). A pure resistor corresponds to a point in the *Z'*-axis while a pure

capacitor is equal to a straight line in the *Z''* axis. The Nyquist plot can be fitted by an equivalence circuit, from which the DC ionic conductivity (σ_{ionic}) can be obtained.

An alternative way to obtain the σ_{ionic} value is to use the AC conductivity plot. The AC conductivity can be measured as:

$$\sigma_{AC} = \frac{z'}{z'^2+z''^2}\frac{d}{A} \tag{3-22}$$

where d is the film thickness and A is the electrode area. The frequency (f) dependence of σ_{AC} shows three regions: (1) a high-f region where σ_{AC} decreases with f, (2) a low-f region and (3) an intermediate frequency-independent region where σ_{AC} is not a strong function of f and forms a "plateau". The conductivity value within this region is due to long-range ionic transport following "diffusive dynamics", reflecting DC conductivity of ions[95].

In this work, ionic transport characteristics with temperature variations were measured using an Agilent 4294A Precision Impedance Analyzer. The temperature was varied from 450 to 600 K and the frequency changed from 1 MHz to 0.1 Hz. The measurements were conducted in collaboration with Dr. Seungho Cho.

3.5 Measurement of electronic structure using the X-ray Photoemission Spectroscopy (XPS)

X-ray Photoemission Spectroscopy (XPS) is a quantitative surface-sensitive technique that measures the elemental composition, empirical formula, chemical state and electronic state of the elements in a material. In XPS, the specimen is irradiated by a beam of x-ray photons with constant energy of hv in a high vacuum environment ($<10^{-7}$ Pa). Due to the photoemission effect[96] (shown in Fig. 3-8), the core electrons with binding energy (E_B) less than the energy of the photons are ejected, and these energies are directly correlated by Einstein's law of photoemission:

$$E_B = hv-(E_k-\Phi) \tag{3-23}$$

where E_B is the binding energy needed to promote a core electron from the nucleus to the Fermi Level (E_F), hv is the energy of the x-ray photons, Φ is the work function of the material (the difference between the vacuum energy level and E_F) and E_k refers to the kinetic energy of the photo-emitted electron.

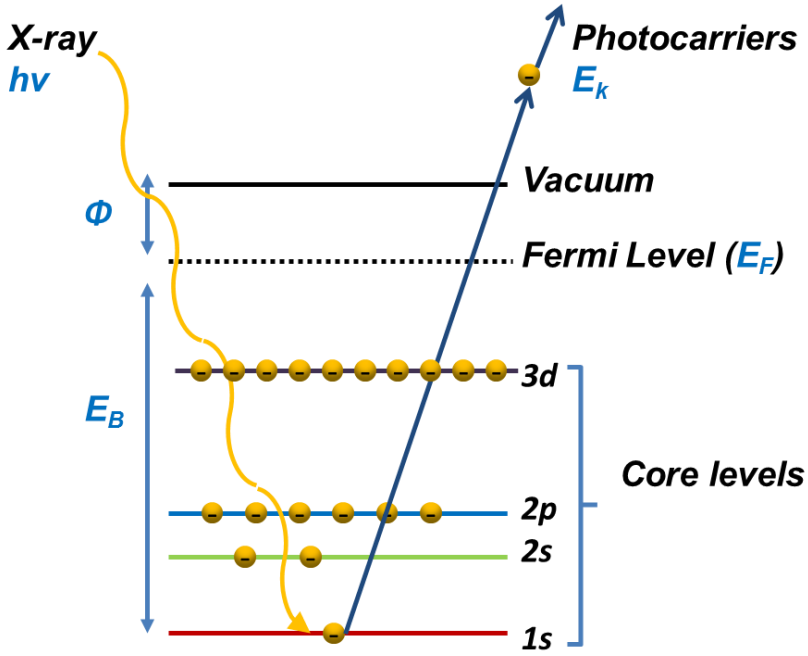

Figure 3-8. Schematic diagram of the photoelectric effect.

The XPS spectra are obtained by simultaneously measuring the E_k and the number of electrons escaped from the surface (0–10 nm) of the material irradiated. According to equation (3-23), the measured energy and intensity of the photoelectron peaks in the analyzer output correspond to the E_B of the material. The value of E_B differs with the change in chemical elements, electron orbitals and chemical environment of the atoms, and thus can be used for identification or quantification of surface elements and chemical environment of the specimen.

In this work, the valence band spectra of the films were collected using a SPECS PHOIBOS 150 electron energy analyzer with a total energy resolution of 500 meV. A monochromatic Al $K\alpha$1 x-ray source (hv= 1486.6 eV) was used to irradiate the sample surface. To prevent charging effects during the measurements, the samples were grown on conductive Nb:STO (001) substrates. Data analysis was carried out using

CasaXPS 2.3.15 software. The XPS measurements in the thesis were conducted by my collaborator, Dr. Weiwei Li.

Chapter 4 Optimizing the resistive switching performance in the Sm:CeO_2–$SrTiO_3$ VAN

This chapter studies on the resistive switching (RS) properties in a novel RRAM candidate: Sm:CeO_2 – $SrTiO_3$ VAN which allows separate tailoring of the ionic and electronic channels. This chapter starts off with a literature review on the basics and technical limitations in resistive switching studies and proposes the structural advantage of VAN for RRAM devices, based on which the materials systems is selected as the Sm:CeO_2–$SrTiO_3$ VAN. Then part two shows the growth and characterization of the high-quality VAN. In part three, electroforming-free RS with an enhanced ON/OFF ratio is realized through delicate optimization via changing the VAN growth rate and thickness. Then in part four, the conduction mechanism is studied using the optimized sample. Based on this, in part five, a separate ionic/electronic channel model is proposed as the mechanism for the RS effect. Additional proofs are then provided to support the model and explain the optimization factors.

The main part of this work was done in collaboration with Dr. Seungho Cho and we contributed equally to this work. The films were grown and characterized by Dr. Seungho Cho and previous colleague Dr. Shinbuhm Lee. TEM works were done by collaborators in Prof. Haiyan Wang's lab at Purdue University and Dr. Ping Lu in Sandia National Laboratory in USA. I mainly focused on designing and conducting the measurements, optimization of RS performances, fitting of conduction mechanisms, and explanation of RS mechanisms. Unless specified in figure captions, all the data were collected/processed by myself or together with Dr. Seungho Cho.

4.1 Literature review

4.1.1 Resistive random access memory (RRAM) and resistive switching (RS): history and basics

Among all the NV-RAMs, resistive random access memory (RRAM, or memristive device) is one promising candidate. First predicted by Chua in 1971[97] and then physically modeled by Strukov *et al*. in 2008[98], RRAM is one of the first recognized examples of a memristor (memory resistor), the fourth fundamental passive circuit element (apart from resistor, capacitor, and inductor). The operation of a RRAM device is based on the electric-field-driven switching of the resistance state, also known as the resistive switching or RS effect. RRAM has the potential for high-density integration, fast operation, low-power consumption, and fabrication compatibility with silicon complementary metal-oxide-semiconductor technology. In addition, by mimicking biological neurons, memristive devices have the potential to combine logic and memory operations, hence are of interest in future cognitive computing[99].

The immense advances of RRAM studies benefit from the following distinctions:

1. A simple structure. As illustrated in Fig. 4-1 (a), the RS effect is realized in a capacitor-like metal-insulator-metal (MIM) structure with insulating or semiconducting materials sandwiched between two metal electrodes. In "MIM" the "M" denotes any good electron conductor (metal or non-metal), often different on the two sides, and the "I", which can be a binary or multinary oxide, stands for an electron insulator, but usually shows ionic conductivity. When applying a voltage, devices with this structure can be switched between at least two resistance states.

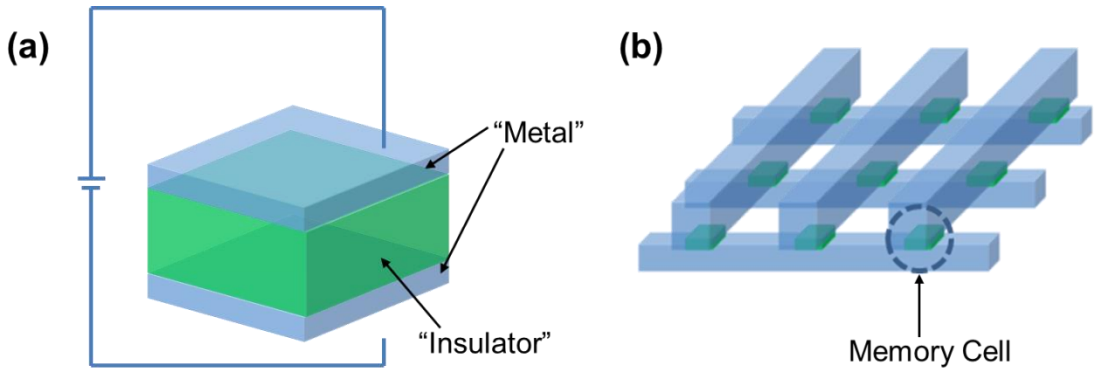

Figure 4-1. (a) Schematic diagram of a RRAM memory cell consisting of an "insulator" sandwiched between two "metals". (b) Schematic diagram of a cross-point memory structure.

2. A simple study approach. Electrical resistance is one of the simplest physical properties to measure. For RRAM the change in resistance state can easily be seen through discrete changes in direct current vs. voltage (*I-V*) curves, which only require a simple source meter and a few electrical contacts.

3. The potential for high-density memories. The simple sandwiched structure of RRAM memory cells makes it easy to fabricate highly-scalable multilevel stacking or multi-layer cross-point (as shown in Fig. 4-1(b)) memory structures[100]. The increased dimensionality of these multilayer structures allows the spatial area for the devices to be decreased and so greatly increases the total memory storage density.

In a typical RRAM device, a low resistance state (LRS, or "ON" state) can be "SET" and a high resistance state (HRS, or "OFF" state) can be "RESET" by two different voltages, and the triggered states can be maintained when the applied voltage is withdrawn. Therefore, a hysteretic *I-V* curve is an important criterion for the determination of a non-volatile RS effect.

According to the polarity of voltage which is required to trigger resistance change, RS effect is classified into unipolar and bipolar switching (as shown in Fig. 4-2). A RRAM device shows unipolar switching when the "SET" and "RESET" processes occur at voltages with the same voltage polarity. The "SET" current is usually limited by the compliance current (CC) of the control circuit, in order to protect the source

meter and the memory cell and to ensure switching occurs properly. The "RESET" into the OFF state takes place at a higher current and a lower voltage. Sometimes a unipolar RS is also nonpolar, where the "SET" and "RESET" processes can take place not only at voltages with the same polarity but also at voltages with opposite polarities[101]. Unipolar RS is usually shown in highly insulating oxides such as binary metal oxides, (e.g. NiO[102]). In comparison, in bipolar switching, the "SET" and "RESET" processes take place at voltages with opposite polarities. The current compliance may or may not be needed depending on the structure of the memory cells. In a bipolar switching device, the structure must have some asymmetry, such as different materials for two electrodes[103]. Most semiconductive oxides, including perovskite oxides, show bipolar switching[104–106], which is the main focus of this work.

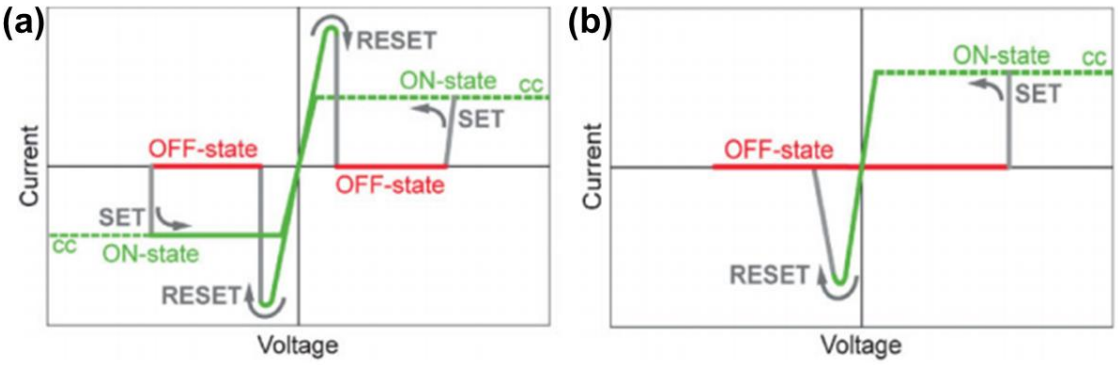

Figure 4-2. Classification of resistive switching based on the voltage polarities needed to "SET" or "RESET" the memory cells. (a) Unipolar, where "SET" and "RESET" processes are triggered by voltages of the same polarity. (b) Bipolar, where the "SET" and "RESET" require voltages of opposite polarity. "cc" and dashed lines denote the compliance current. (Figure taken from[107])

According to Waser *et al.*, to meet the circuit requirements of the next-generation NVMs, a good RRAM device should follow several criteria[107]:

1. A low "write" voltage (from a few hundred mV to a few V). The pulse length needs to be less than 100 ns in order to compete with the DRAM and even less than 10 ns to outperform SRAM.

2. A significantly lower "read" voltage than "write" voltage in order not to alter the triggered resistance states.

3. A large ON/OFF ratio. ON/OFF ratio is defined as the resistance ratio between the HRS and LRS. An ON/OFF ratio of > 10, as suggested by Waser *et al.*[107], allows for small and highly efficient sense amplifiers. A large ON/OFF ratio, together with low variance, can effectively maintain a decent separation between memory states and avoid undistinguishable memory states. Currently, most reported ON/OFF values vary from 10^2-10^5.

4. A long endurance time. Currently, endurance of over 10^3 cycles have been widely reported, which competes with Flash memory, and the ultimate goal is $>10^{12}$ cycles, as suggested by Waser *et al.*[107]. To test the endurance, a RRAM memory cell consistently undergoes alternate "write" operations into different resistance states and "read" operations immediately after each "write" operation. To avoid fatigue when being triggered back and forth, a good memory device needs a large ON/OFF ratio with stable, non-degraded readout resistances, and hence enhancing these is important for improving the endurance of a RRAM device.

5. A long data retention time, with over ten years being the ultimate goal as suggested by Waser *et al.*[107]. Currently, reported retention time in literature ranges from hours to months. Retention can be evaluated by "write" the device into the LRS or HRS and then "read" the memory cell continuously over a long period of time. Both endurance and retention are needed to fully reflect the stability and variability of the device.

4.1.2 Mechanisms of RS

Despite the seemingly simple phenomena of RS, the underlying physics is quite controversial and still not fully understood, especially in complex oxides which are electronically active. Therefore, an optimized design guide for RRAM devices has not yet been adequately produced. These are the reasons why the development of RRAM is less advanced than other non-volatile memories such as PCRAM and FeRAM[100]. From a technical point of view, the development of RRAM requires not only the improvement of device performance but also the elucidation of driving mechanisms.

The classification of RS mechanisms has different categories based on different standards. In general, the "SET" process generates a conductive path (or state), which is erased in the "RESET" process.

Sawa *et al.* classified RS simply based on whether the conductive path is filamentary or interfacial type[100]. As shown in Fig. 4-3 (a), the basis for filamentary RS is the formation/rupture of the conductive filament that spans the insulating oxide between two metals. This type of RS therefore emphasizes on a localized bridge between the anode and cathode and so is effectively quasi-one-dimensional (compared to the whole contact area). Interfacial RS (Fig. 4-3 (b)) concerns the modification of the metal/oxide interfacial Schottky barrier, and so involves the whole two-dimensional electrode/film contact area. Determination of the electrode area dependence of the cell resistance (especially for the LRS) is one effective way to elucidate whether the RS effect is filament- or interface-limited[108].

According to Waser *et al.*, RS mechanisms can be explained based on whether the driving force comes from a thermal effect, an electronic effect, or an ionic effect[103], and these effects are not mutually independent, as discussed below:

1. Joule heating is unavoidable when current flow exists under the application of an electric field. With the increase in thermal energy, a conductive filament can be formed due to the orderly migration of the electrode metals or decomposition of the insulating matrix, so causing a partial dielectric breakdown of the memory cell. The successive rupture/formation of the filament can then result in unipolar switching. This model is similar to a nano-scale fuse-antifuse, and usually shows filamentary characteristics as illustrated in Fig. 4-3 (a). Temperature-induced structural transition is another driving force for the switching of the resistance states, especially in materials systems with an intrinsic insulator-to-metal transition (e.g. Fe_3O_4[109]). However, this type of transition is usually volatile (termed as "threshold switching"[110]).

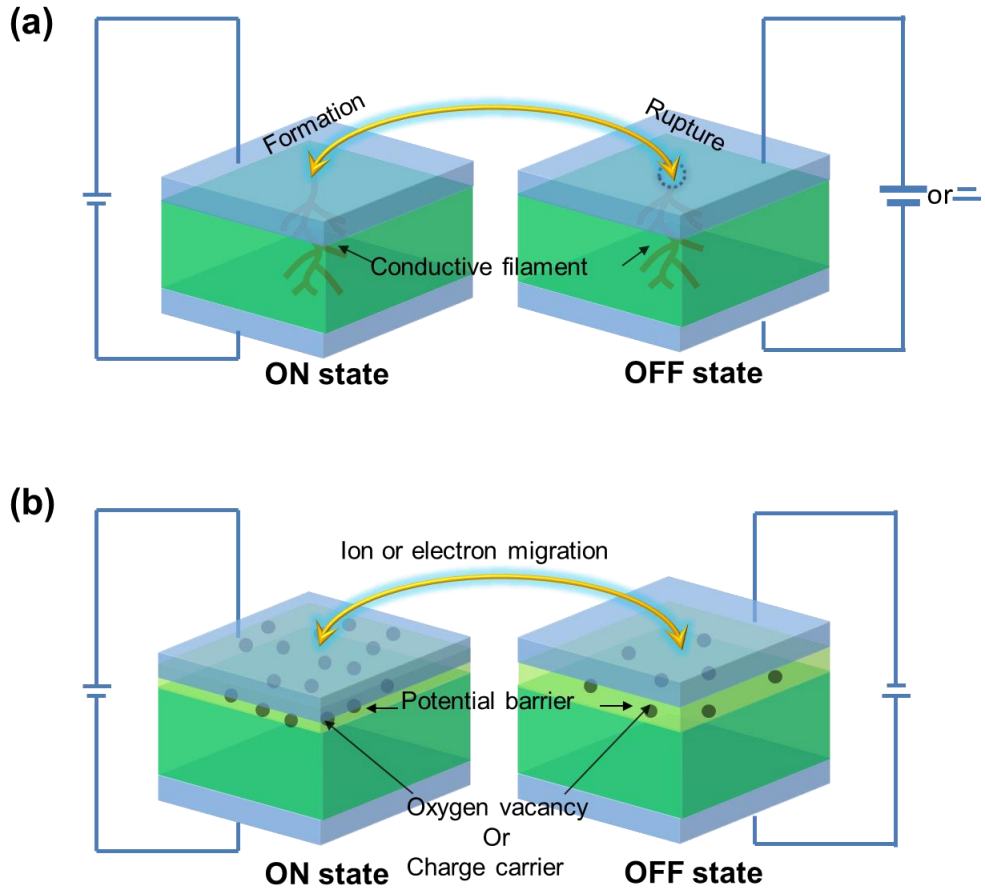

Figure 4-3. Schematic diagram of the two different types of conductive path: (a) filamentary type path and (b) interfacial type path. The direction and the size of the electrode symbol in the circuit stand for the relative direction and strength of the source voltage.

2. The metal/semiconductor oxide interface usually forms into a Schottky contact (i.e. with a potential barrier to electron transport) due to the high work function of the metal electrode (as discussed in Chapter 2.1.2 and shown in Fig. 2-2). The potential barrier can be modified under an electric field, resulting in an electronic-driving RS effect. One famous theory is the carrier trapping/detrapping model[111], which explains the RS effect in a more physical way. According to this theory defects in the interface can generate defect energy levels below the potential barrier and so create carrier trapping centers. The injection and release of charge carriers (electrons or holes) from the trapping centers under an electric field can change the effective carrier concentration and modify the barrier profile (height or width), and thus the resistance state can be altered[112]. The trap and release of carriers need to overcome obstacles,

which result in a memory effect[113].

3. Lastly, the ion migration model is based on the ionic conduction in an electronically insulating but ionically conductive matrix. In many oxides, especially in transition metal oxides (TMO), the anions and/or oxygen vacancies (V_os) are much more mobile than the cations, thus there is a strong likelihood that trapping centers and conductance channels are generated by V_os. The metal/oxide Schottky barrier can also be modified by the accumulation and depletion of V_o.

i). In insulating oxides (such as TiO_2) where ion exchange is blocked by the cathode, when an electric field is applied, an oxygen-deficient region first forms and then expands towards the anode. The electronically-active transition metal cations can accommodate the resulting charge imbalance by trapping electrons from the cathode[103]. This leads to a change in the stoichiometry or cation valence and so to the formation of a less oxidized, more conductive sub-oxide. The final result is the formation of a conductive path between the anode and cathode, which produces a similar effect to that of a metallic bridge. At the anode, an oxidation reaction of the gathered oxygen ions may result, which leads to the generation of O_2 gas[104]. This is essentially a redox-based process and produces a filamentary effect as illustrated in Fig. 4-3 (a). However, unlike the thermal-driven transition mentioned above, bipolar switching is shown due to the polarity-dependent redox nature of this process[103].

ii). In semiconductive oxides, V_o acts as an *n*-type impurity and V_o migration can modify the metal/oxide interfacial potential profile. The increase in V_o concentrations near the interface of metal/*n*-type semiconductors (such as Nb-doped $SrTiO_3$ or oxygen-deficient $SrTiO_{3-x}$) increases the majority carrier concentration in the semiconductor, inducing interface energy states and therefore results in the decrease in the width of the interfacial depletion layer (W_d)[100], as shown in Fig. 4-4. Recall Fig. 2.2 and equations (2-1) and (2-2), the decrease in W_d may alter the degree of band bending which results in the modification of the height ($e\varphi_B$, eV_B) and width (W_B) of the interface potential barriers, and in most cases, decreases them[114–116]. This decreases the contact resistance and eventually results in the LRS[100]. In *p*-type oxides

(such as perovskite manganite) the opposite effect occurs. The influence of V_o on the depletion layer width is illustrated in Fig. 4-4. In this model, an ionic effect contributes to a strong modification of the electronic structure of the Schottky barrier, and unlike the model in point **2**, the trapping/detrapping effect is much weaker. The ionic migration model is the most important basis for our later discussions on RS mechanisms (see Chapter 4.5).

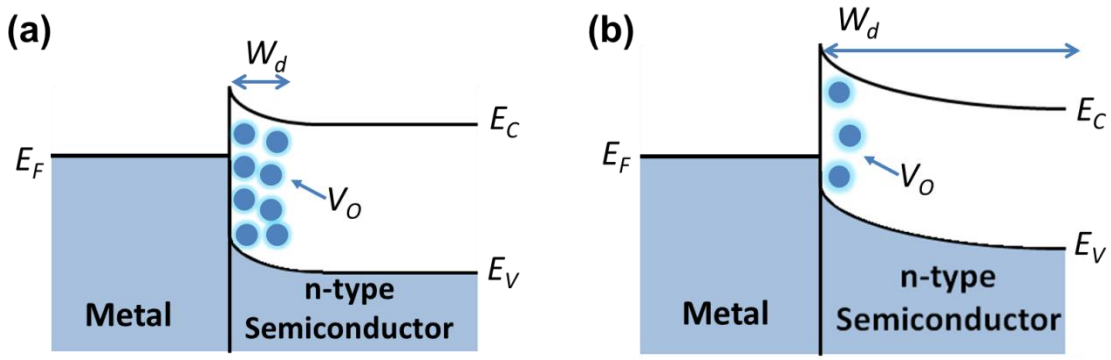

Figure 4-4. Influence of the oxygen vacancy (a) accumulation and (b) depletion on the depletion layer width (W_d) of a metal/*n*-type semiconductor interfacial Schottky barrier.

As discussed above, both electron trapping/detrapping and ionic migration can modify the metal/oxide Schottky barrier. It is therefore important to differentiate between them. As proposed by Shibuya *et al.*, these two interfacial-type mechanisms exhibit different switching polarities[117]: in *n*-type materials, the HRS is triggered to LRS by a negative voltage in the "V_o migration" model, while the switching polarity is opposite in the "trapping/detrapping" model.

Although the ionic effect is often closely related to the electronic effect, there is a key difference. In the ionic process, a large concentration of mobile ion species is a prerequisite, which can only be realized in an anion conductor. The presence of anion conductivity or high concentration of mobile V_o (which are different from the existence of immobile V_os in some defective oxides) can drastically enhance the RS effect in a different way, i.e. by directly modifying the potential profiles. In comparison, the trapping/detrapping model stresses more on the influence of the mobility of electrons by defects (e.g. by the nearly fixed V_o trapping sites), where the

V_o migration is much less stressed.

Despite the difference in appearance, the above-mentioned mechanisms are not mutually exclusive but usually inter-correlated, especially in TMOs and composite systems where electronic and ionic effects coexist. Usually, one model is more dominant than others.

4.1.3 Limitations in conventional RRAM devices

Apart from the complex driving mechanisms mentioned above, several technical limitations also slow down the development of the RRAM technique:

1. The degradation problem of dense, nano-scale structures. In conventional RRAM devices using plain oxide films, degradation is unavoidable in the fabrication process of the dense nano-scale memory cells using ion/electron beam milling steps. These processes lead to surface oxygen defects with associated uncontrollable electronic conductions, which affect the quality of the devices. Self-assembly of the nanostructured memory cells provides one possible solution for this problem.

2. Electroforming. In many single-phase oxides, especially insulating oxides, an "electroforming" process is required before the device can be irreversibly maintained at a tunable condition between two or more resistance states. "Electroforming" is somewhat like dielectric breakdown, but under the delicate control of a compliance current, this breakdown is only partially realized[118]. According to Yang *et al.*, electroforming in many oxides is driven by an electro-reduction process followed by the creation and migration of O^{2-} ions under electric fields, which can be enhanced by Joule heating[119]. Following this, a conductive bridge between the anode and cathode is formed, and the following "SET" and "RESET" processes rely on the reduction and oxidation of this conductive bridge[120].

In many cases, "electroforming" is harmful to the samples due to destructive gas eruption and bubble formation near the electrodes, which are induced during the redox process of O^{2-} [119]. It is also undesirable for computer circuit applications as a

very high voltage (5–30 V) is usually needed[119–121]. Additionally, since electroforming depends largely on the compliance current, it is uncontrollable and random, thus causing problems for the uniformity of the memory device[122]. As mentioned earlier, the compliance current works by limiting the current to protect the source meter and the memory cell. If the compliance is set too low, the conductance channels between the electrodes cannot be adequately formed and thus effective RS cannot be obtained. On the other hand, if the compliance is too high, the RS effect may disappear[123] or the resulting dielectric breakdown may totally destroy the memory cell.

Several approaches have been suggested to eliminate the "problematic" electroforming process, either by reducing the thin film thickness to highlight the "switching interface" via eliminating the "bulk" region or by artificially creating the electronically conductive channels during the device fabrication process[119]. For example, it is possible to reduce and even eliminate electroforming by simply inserting an oxygen-deficient TiO_{2-x} layer in a TiO_2-based memory cell, which can act as a vacancy reservoir[124]. Novel "electroforming-free" RRAM devices have become a heated topic in recent years[122,124,125].

3. Mixed ionic and electronic channels. In the memristor model initially proposed by Strukov *et al.*, coupled equations for the electronic and ionic motion were proposed, but scientific disputes of this model have been raised in recent years[126,127]. As discussed previously, electronic and ionic effects are usually correlated in single-phase metal oxides, as V_o can act as an electron carrier trapping center and its migration can modify the interfacial potential profile as well. This makes it difficult to decouple the ion and electron channels, which add in complexities to the study of RS mechanisms. Besides, as the optimized fabrication conditions for optimized ionic and electronic transport may be in conflict, an overall optimization may never be reached within one single-phase system. In terms of applications, the mixed channels restrict the application of RRAM devices in the neuron computing field, as bio-neurons usually have spatially separate conductance channels. Therefore, separation of the conductance channels is desirable for both research and applications.

4.1.4 The advantage of VAN for RRAM devices

Based on the limitations mentioned above, the aim of this work is to search for a nano-scale, self-assembled, electroforming-free RRAM candidate with separate ionic/electronic channels. We expect devices built with a VAN structure will provide these benefits. As schematically illustrated in Fig. 4-5, VAN consists of three active parts: the matrix, the nanocolumn and more importantly, the vertical interface between the two phases. The VAN structure is unique not only for its enhanced interface/bulk ratio but also because of the vertical interfaces, which may align from the anode all the way to the cathode. This vertical interface is usually more electronically active due to the structural disorder generated as a result of the mismatched lattices at the phase boundary[128]. This provides a potential platform for pre-aligned conductive paths in the fabrication process[122], without the need for an electrically-driven forming process. Additionally, the three structurally different components provide three different combinations (matrix/column, matrix/vertical interface or column/vertical interface) to separately undertake the role of ionic and electronic channels, which makes it easy to make delicate designs. Besides, exposed vertical interfaces provide additional convenience for microscopic studies. Moreover, as the VAN self-assembly is on the nano scale, a thin film device can have very high-density and high-quality conductance channels and memory cells.

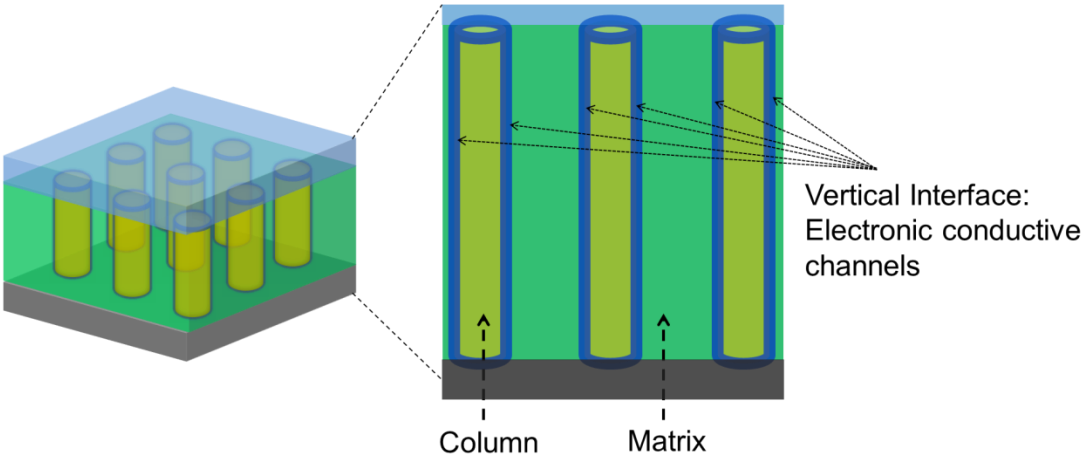

Figure 4-5. Schematic diagram of the three components of a VAN structure: matrix (green), column (orange) and electronic conductive vertical interface (blue).

These useful attributes have led to a collection of studies on the RS effects of VAN devices. For instance, as reported by Lee *et al.*, a $SrTiO_3$-Sm_2O_3 VAN memristive device exhibited high uniformity, tunability, and was electroforming-free. The simultaneous observation of oxygen deficiency and enhanced conductivity in the vertical interface confirmed the presence of localized V_o channels, which in turn eliminated the electroforming process as well as enhanced RS uniformity in this structure[122]. This study was the first report on RS properties in VAN structure. However, an ON/OFF ratio of only ~10^2 was realized, below the high-performance criteria of >10^3 mentioned in Chapter 4.1.1. Other studies, such as current mapping of the topography of a Nb_2O_5-$NaNbO_3$ VAN via scanning with Conductive-AFM, also revealed an enhanced V_o profile (which here formed these electronically conductive channels at the phase boundary)[129]. However, the highly mismatched interfaces found in this device led to a low reproducibility and uniformity between measurements. Altogether this means that VAN structures are quite promising for RRAM devices, but clear improvements in their performance and full understanding of their various mechanisms still need a tremendous amount of work. These are parts of the motivation for this work.

4.1.5 Selection of materials

In order to obtain a high-quality VAN with separate electronic/ionic channels and electroforming-free switching, materials selection should follow the guidelines mentioned in Chapter 2.3.2. Meanwhile, the ionic channel should have limited electronic conductivity and the electronic channel should have limited ionic conductivity. Based on these requirements, Sm-doped CeO_2 (SDC) and $SrTiO_3$ (STO) were selected as the ionic conductor and electronic conductor, respectively.

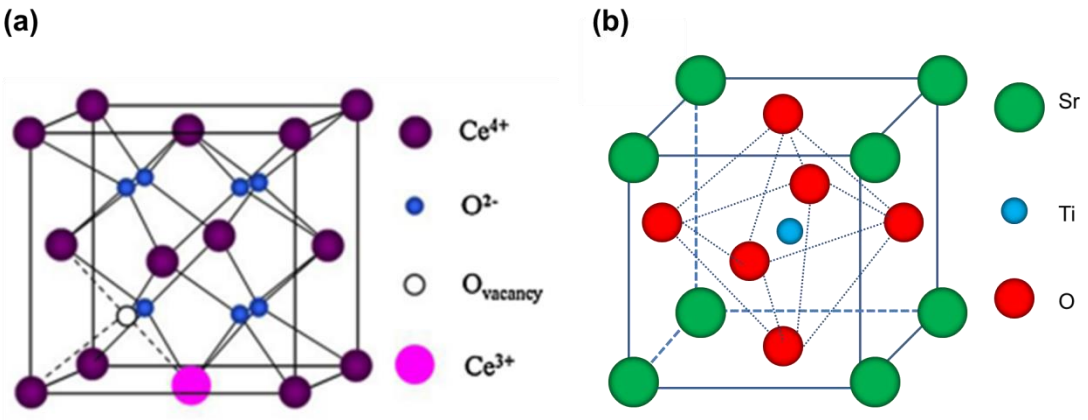

Figure 4-6. The unit cell of (a) fluorite CeO_2 (Figure taken from[130]) and (b) perovskite $SrTiO_3$.

1. Stoichiometric Cerium Oxide (CeO_2) is an electronic insulator with a calcium fluorite structure (space group $Fm\bar{3}m$) at room temperature. As shown in Fig. 4-6 (a), Ce^{4+} ions are in a face-centered cubic (FCC) close-packed arrangement, and O^{2-} ions only occupy the 8 tetrahedral sites, leaving all the 4 octahedral sites unoccupied[131]. This open structure favors interstitial occupation and ion migration. In the presence of V_os, the insulating CeO_2 becomes conductive due to V_o migration. These can be created due to oxygen deficiency or by doping CeO_2 with tri- or divalent metals, as V_os form to compensate the charge imbalance. These can then act as potential pathways for oxygen ion diffusion, and so the ionic conductivity will thus be greatly enhanced[132,133]. Among all the transition metals (including rare earth metals), Gd^{3+} and Sm^{3+} have the smallest association enthalpy (and thus lowest metal-V_o binding energy) for the V_o in the fluorite lattice, thus providing the largest enhancement of ionic conductivity[134–136]. The defect chemistry for Sm-doped CeO_2 can be expressed via Kröger–Vink notation:

$$Sm_2O_3 \xrightarrow{CeO_2} 2Sm'_{Ce} + 3O_O^x + V_O^{\bullet\bullet} \qquad (4\text{-}1)$$

The advantage of V_os formed in this way is that they do not introduce unwanted electronic conductivity associated with the reduction of CeO_2.

2. Strontium titanate (STO) has a perovskite structure (space group *Fm3m*), as shown

in Fig. 4-6 (b). The Sr^{2+} and O^{2-} form a face-centered cubic (FCC) close-packed lattice with Ti^{4+} ions occupying a quarter of the octahedral interstices, i.e. those created by the O^{2-} ions. Looking from another perspective, the perovskite structure is formed by a three-dimensional network of TiO_6 octahedra with shared corners, while the Sr^{2+} ions occupy the twelve-fold cavities in the polyhedral formed by the octahedral net[137]. STO stays stable in a cubic phase at room temperature, and transforms into a tetragonal structure below 105 K. Pure STO is a wide band-gap semiconductor, high-*k* dielectric oxide, and quantum paraelectric insulator and is widely used as a substrate for the growth of epitaxial oxide thin films due to its structural compatibility with many oxides.

Earlier researchers have reported the high-quality vertical epitaxy of a perovskite-fluorite VAN combination[67,72,74,138,139] on perovskite substrates and here we expect similar results.

4.2 Growth and characterization

Sm-doped CeO_2-$SrTiO_3$ VAN and reference plain films were grown on 0.5 wt.% Nb-doped $SrTiO_3$ (001) substrates by PLD via a one-step growth process. Polycrystalline targets containing Sm: CeO_2 (Sm^{3+} concentrations: 0, 10, 20 and 30 at.%) and $SrTiO_3$ (50:50 molar ratio) were used for making the VAN films used to study the influence of ionic conductivity on the resistive switching performance. A polycrystalline 20 at.% Sm-doped CeO_2 (SDC) target and a polycrystalline $SrTiO_3$ (STO) target were also used for growing the reference plain films (denoted as PF). The laser energy fluence was varied from 1.5 to 4.5 J/cm^2 and the repetition rate was varied from 1 to 10 Hz. During deposition, the substrate temperature was 825℃ and the O_2 partial pressure was 0.2 mbar. The samples were post-annealed at 700℃ for 1h under 900 mbar O_2. For electrical measurements, Pt electrode dots were deposited onto the films by DC-magnetron sputtering onto the film surface with shadow masks.

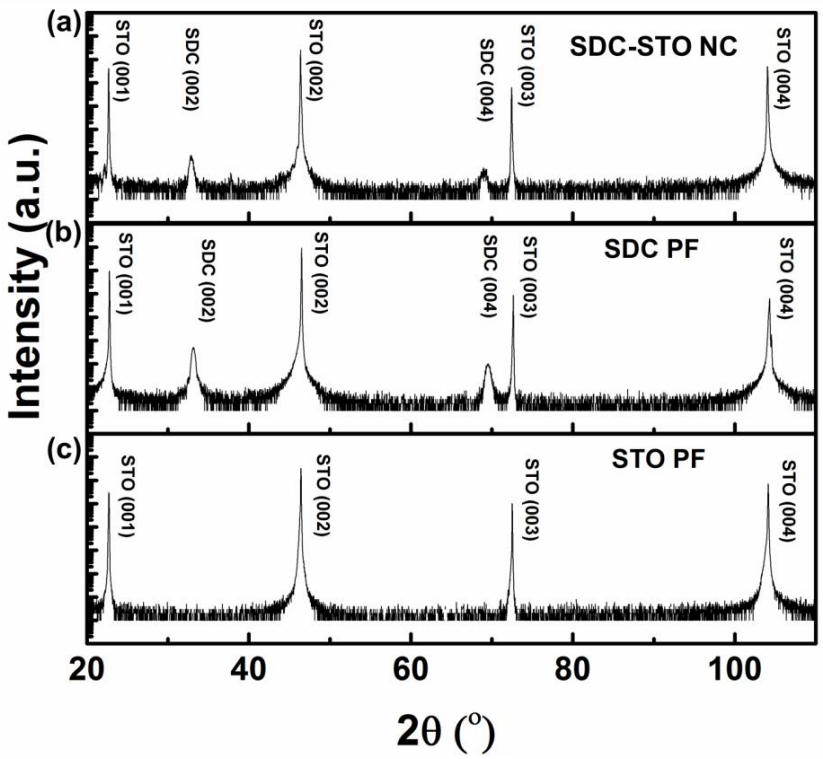

Figure 4-7. XRD *2θ-ω* scans of (a) the 20 at.% Sm-doped CeO_2 (SDC) : STO (molar ratio 1:1) VAN (NC), (b) SDC plain film (PF) and (c) STO plain film (PF) on 0.5 wt.% Nb-doped STO substrates. The three samples have the same thickness (~30 nm) and growth rate (0.033 nm/s) (Data collected by Dr. Seungho Cho).

Fig. 4-7 shows the XRD *2θ-ω* scans of a 30-nm 20 at.% SDC: STO VAN (denoted as NC hereafter) grown using a laser energy of 60 mJ and repetition rate of 1 Hz (growth rate 0.033 nm/s, which is the NC film with the optimized RS performance, as discussed later) in comparison with a SDC PF and STO PF grown under the same conditions. The diffraction peaks of only the STO and SDC (*00l*) phases are shown in the NC film (Fig. 4-7 (a)), without traces of other phases (such as Sm-related sub-oxides) or other SDC orientations, confirming their high degree of crystallographic orientation. The STO film peaks are overlapped with those of the strong STO substrate peaks. Further structural information is obtained from the reciprocal space map (RSM) shown in Fig. 4-8. With a combination of the *2θ-ω* scan and the RSM, the in-plane and out-of-plane lattice constants of the SDC phase are determined to be 5.443 Å and 5.430 Å, respectively, while those of the STO phase are taken to be equal to the STO substrate (3.905 Å).

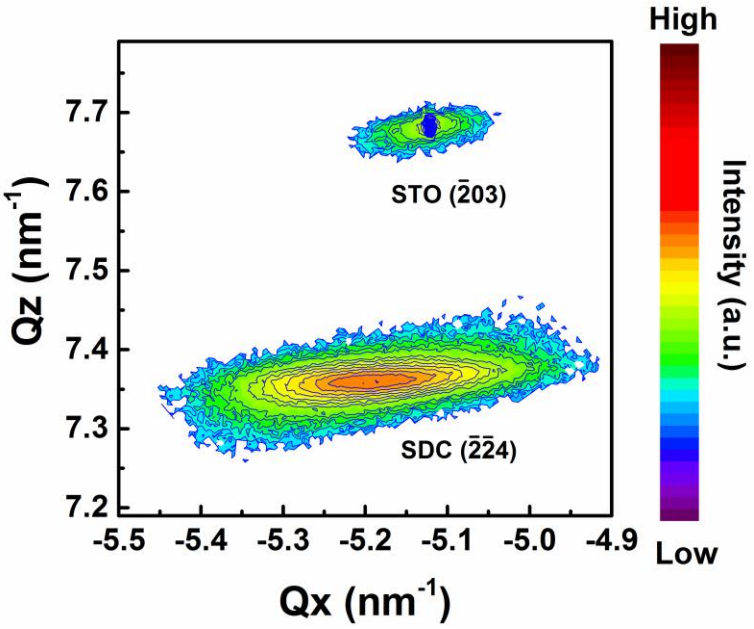

Figure 4-8. Reciprocal space map (RSM) of the 20 at.% Sm-doped CeO_2 (SDC)- STO NC around the STO (2̄03) (Data collected by Dr. Seungho Cho).

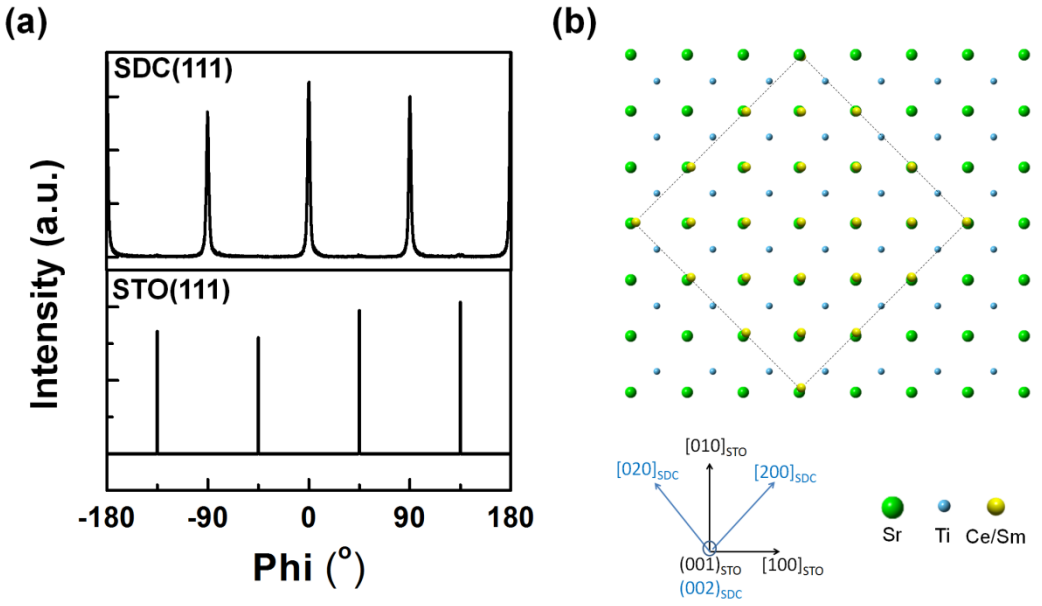

Figure 4-9. (a) 360° Phi scans of the (111) peak of STO and the (111) peak of SDC of the NC film (Data collected by Dr. Seungho Cho). (b) Schematic diagram of in-plane crystallographic matching between the SDC phase and the STO substrate.

The Phi scan in Fig. 4-9 (a) indicates that the SDC phase is grown on the Nb:STO (001) substrate with a 45° in-plane rotation, which is expected from energetic

considerations as it minimizes the large lattice mismatch between the SDC (a=5.433 Å in bulk) and STO (a=3.905 Å) phase. Therefore, the in-plane epitaxy relationship is determined to be STO_{Sub}[100]//STO_{Film}[100]//SDC[110], which is schematically illustrated in Fig. 4-9 (b).

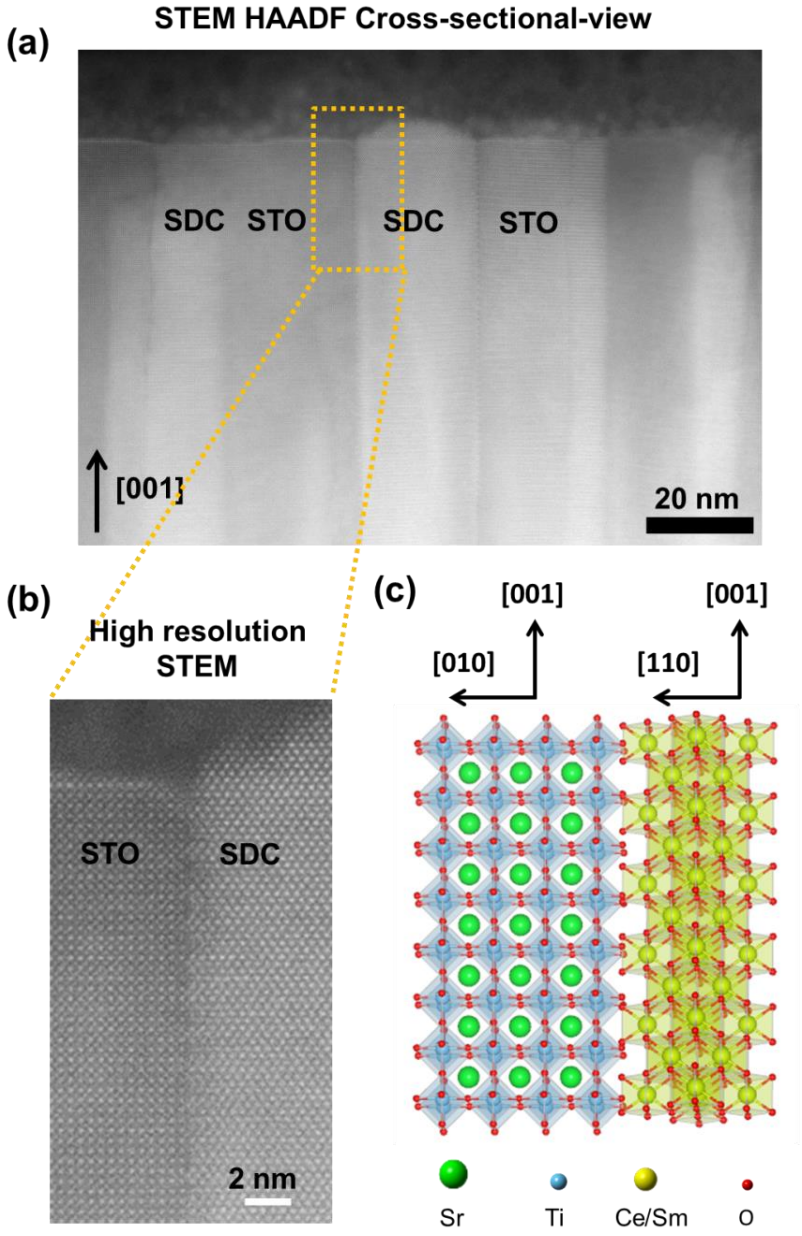

Figure 4-10. (a) Cross-sectional STEM HAADF image of the SDC-STO NC film. (b) High-resolution HAADF image revealing high-quality phase separation and vertical heteroepitaxy. (c) Schematic diagram of the out-of-plane crystallographic matching between the SDC phase and STO phase. (TEM images in (a) and (b) taken by Dr. Ping Lu from Sandia National Laboratory, USA)

The cross-section scanning transmission electron microscopy (STEM) high-angle annular dark-field (HAADF) image in Fig. 4-10 (a) additionally confirms the high-quality crystallinity and the vertically-aligned phase separation of the SDC-STO VAN. The High-resolution HAADF image in Fig. 4-10 (b) shows an atomic-scale sharp and epitaxial vertical interface. These, combined with the 2θ-ω scan shown in Fig. 4-7 (a), indicate the following out-of-plane epitaxy relationship: $STO_{Sub}(001)//STO_{Film}(001)//SDC(001)$, as schematically illustrated in Fig. 4-10 (c).

4.3 Optimization of the resistive switching performance of the 20 at.% Sm-doped CeO_2-STO VAN-based RRAM devices

As mentioned in Chapter 4.1.2, the RS effect is closely related to the behavior of the interfacial or filamentary conductive paths, and therefore structural factors of the memory cells largely influence the device performance. As discussed in Chapter 2.3.2, in VANs, growth rate is one of the most important factors in determining the growth kinetics and spatial distribution of the phases. Therefore, it should also have a big impact on the structural quality of the vertical interface which forms and on the electrode/film potential barrier which develops. The VAN thickness is also important since it can change the effective electric field that drives the resistive switching.

In this section, I optimized the RS performance of the 20 at.% Sm-doped CeO_2-STO (denoted as SDC-STO hereafter) VAN-based RRAM devices by systematically studying the role of growth rate and thickness of the films on the electroforming characteristic, the reproducibility of *I-V* curves, the ON/OFF ratio and the cycling durability in endurance measurements. A 20 at. % Sm doping ratio was used which provided the optimized RS performance when other parameters were kept the same (as discussed later). A series of SDC-STO NC films with two different thicknesses (30 nm and 150 nm) and four different growth rates (0.033, 0.083, 0.167 and 0.5 nm/s), hereby termed as rates 1 to 4, were used. The growth rates were changed by changing the laser energy (60 mJ, 120 mJ, and 180 mJ), with a

corresponding change in the laser fluence (1.5 J/cm^2, 3 J/cm^2, and 4.5 J/cm^2), and by changing the repetition rate (1 Hz, 4 Hz and 10 Hz). For the films with 150-nm thicknesses, the samples grown with rates 1 to 4 were labeled as A1 to A4, whilst the respective 30-nm samples were labeled as B1 to B4. The growth rate values were calculated via dividing the thickness by the growth time. The thicknesses were changed by changing the growth time whilst keeping the growth rate constant.

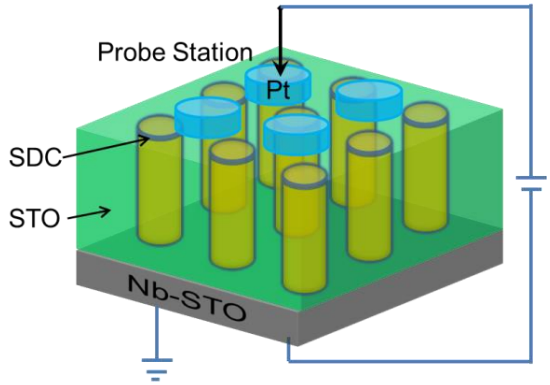

Figure 4-11. Schematic diagram of the measurement configuration of resistive switching for the Pt/SDC-STO/Nb:STO device. The SDC column size and the Pt electrode dot size are not to scale.

Fig. 4-11 shows a schematic diagram for a Pt (top)/ SDC:STO NC film (middle) /Nb:STO (001) (bottom) device. For all the electrical measurements, bipolar voltage signals were applied to a circular top Pt electrode (with a diameter of 300 μm) using a Tungsten probe station connected to a Keithley 2440 source meter, while the bottom Nb:STO electrodes were grounded. For measurement of *I-V* curves, the DC voltage was continuously varied in cycles. For endurance and retention measurements, optimized "write" and "read" voltage pulses of ±5V and 0.3 V were used (the optimization process will be shown later). The optimized *I-V* curves and endurance measurements of each sample are shown in figures below. The optimized performance for each sample was obtained after reproducing the results on many memory cells on each sample (for those forming-free samples, at least 13 memory cells were tested, and for the samples which need electroforming, at least 3 memory cells were tested).

◆ **The influence of growth rate (thick films, 150 nm)**

Starting from sample A4 with the highest growth rate (thickness: 150 nm, growth rate: 0.5 nm/s), highly resistive behavior with an asymmetric *I-V* shape is shown in the initial state (Fig. 4-12 (a)), and the intertwined *I-V* curve indicates no memory effect. An electroforming process at 17.2 V (Fig. 4-12 (b)) is needed before a weak RS effect is exhibited (Fig. 4-12 (c)). Here the electroforming voltage is defined as the voltage point where the current jump has the largest slope. The current compliance for an effective RS transition (after electroforming) is 10 mA. Despite the weak *I-V* hysteresis in Fig. 4-12 (c) after electroforming, no distinct ON or OFF states are shown in the endurance measurement (Fig. 4-12 (d)).

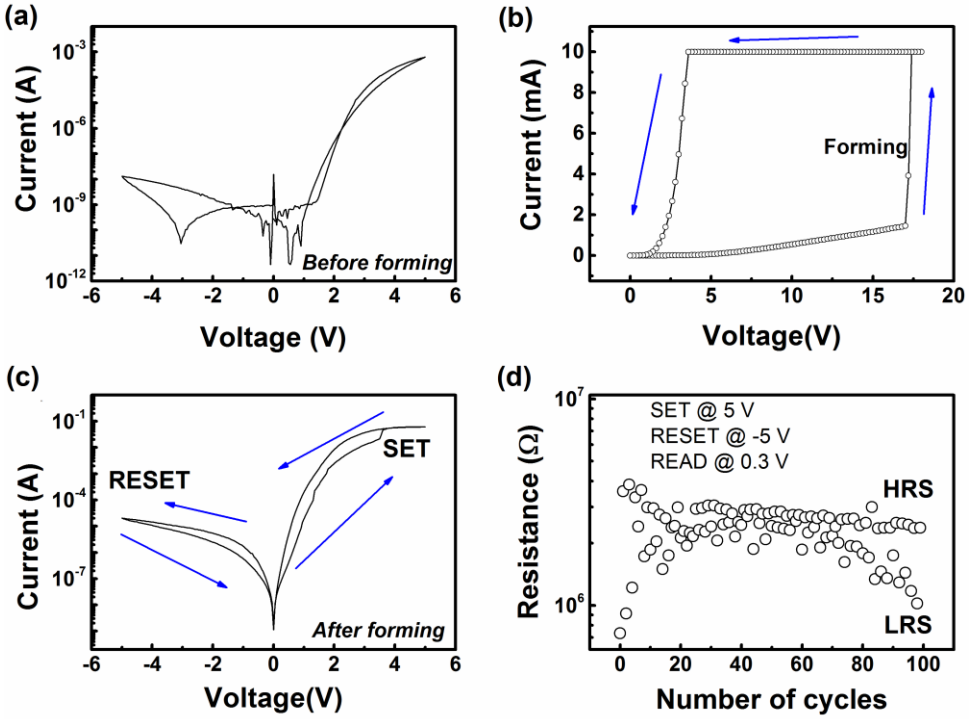

Figure 4-12. Resistive switching performance of sample A4. (thickness: 150 nm, growth rate: 0.5 nm/s): (a) *I-V* curve under a ±5 V cycle before electroforming. (b) The electroforming process, which occurs at 17.2 V. (c) *I-V* curve under a ±5 V cycle after electroforming. (d) The endurance characteristics under 100 cycles ("write" at ±5 V and "read" at 0.3 V).

When the growth rate is decreased from 0.5 to 0.167 nm/s (sample A3, Fig. 4-13), similar behavior is shown, i.e. an intertwined *I-V* curve in a ±5 V cycle before electroforming (Fig. 4-13 (a)). The electroforming occurs at 17.6 V (Fig. 4-13 (b)), after which a stable RS effect is exhibited in a ±5 V cycle (Fig. 4-13 (c)). Compared

to sample A4, the hysteresis in the *I-V* curve is more obvious in sample A3, and two discernible resistance states are observed in the endurance measurement under the same measurement condition, as shown in Fig. 4-13 (d). However, the resistance states are unstable, as the resistance values are distributed over a large range, and vary a lot with the increase in the number of measurement cycles.

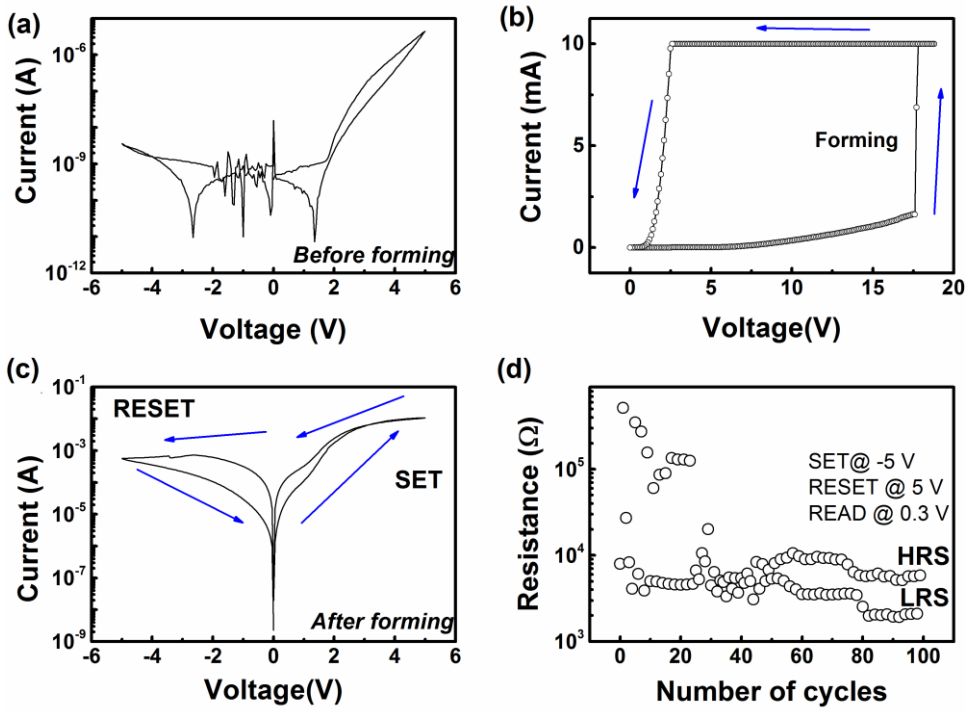

Figure 4-13. Resistive switching performance of sample A3. (thickness: 150 nm, growth rate: 0.167 nm/s). (a) *I-V* curve under a ±5 V cycle before electroforming. (b) The electroforming process, which occurs at 17.6 V. (c) *I-V* curve under a ±5 V cycle after electroforming. (d) The endurance characteristics under 100 cycles.

When decreasing the growth rate further to 0.083 nm/s (sample A2, Fig. 4-14), a discernible *I-V* hysteresis is shown in a small voltage cycle of ±1 V (Fig. 4-14 (a)) and ±3 V (Fig. 4-14 (b)), but no clear memory effect is shown, as the *I-V* curve becomes intertwined at around 0 V. When increasing the voltage cycle to ±5 V, this sample starts to show resistive switching, which, in contrast to sample A4 and A3, does not need electroforming, as shown in Fig. 4-14 (c). The memory cell is "SET" to the LRS at a negative voltage of -0.85 V, and the "RESET" process to the HRS takes place at a positive voltage of 0.85 V. The blue arrows show the flow direction of the *I-V* curve. Here the "SET" and "RESET" voltages are defined as the points where the *I-V*

curvature changes, i.e. the "SET" voltage is the negative voltage point where the current has the sharpest jump, while the "RESET" voltage is the positive voltage point where the current starts to saturate. Fig. 4-14 (d) shows the endurance property over 100 cycles. Two resistance states with an average ON/OFF ratio of ~10^2 can be maintained, but a large variation of resistance values is still observed for both resistance states.

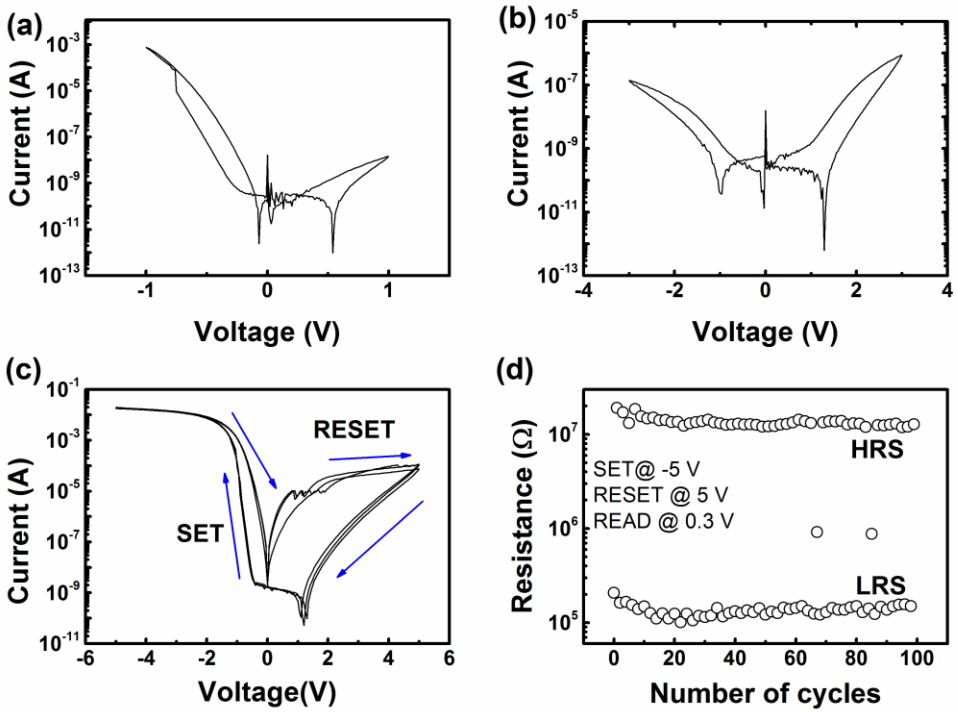

Figure 4-14. Resistive switching performance of sample A2. (Thickness: 150 nm, growth rate: 0.083 nm/s). *I-V* curve under a (a) ±1 V cycle, (b) ±3 V cycle and (c) ±5 V cycle. (d) The endurance characteristics under 100 cycles.

◆ The influence of thickness

The above comparison for thick films suggests that the growth rate plays an important role in the electroforming process and on the RS performance (both before and after electroforming), with a lower growth rate favoring electroforming-free switching and the maintenance of discernible resistance states. However, these thick samples cannot exhibit highly pronounced RS effects. In our measurements, we found that a lower thickness can effectively improve the ON/OFF ratio while other characteristics, such as electroforming, are less influenced, as discussed below:

Firstly, the growth rate is maintained on the same level as that of sample A2 (0.083 nm/s) with only the thickness being reduced from 150 nm to 30 nm (sample B2, Fig. 4-15). As shown in Fig. 4-15 (a), sample B2 acts similarly to sample A2 at a low voltage cycle (±1 V), i.e. an intertwined *I-V* curve is shown. However, a nonvolatile RS effect starts to show from a much lower voltage cycle (±2 V, compared with the ±5 V required for sample A2), as shown in Fig. 4-15 (b). When increasing the voltage further, a ±5 V cycle produces a pronounced RS effect (Fig. 4-15 (c)), but the reproducibility is poor, as indicated by the non-overlapping *I-V* curves under 3 voltage cycles and the wide distribution of the resistance (between 10^3 and 10^4 Ω) of the LRS (R_{LRS}) in the endurance measurement (Fig. 4-15 (d)). Although a larger ON/OFF ratio of 10^3~10^4 is shown compared to that of sample A2 (10^2, Fig. 4-14 (d)), the variance of resistance values is still large and the resulting distribution of ON/OFF ratios of sample B2 is undesirable for device applications. Despite the poor stability, sample B2 exhibits a much improved endurance under >3000 cycles (Fig. 4-15 (d)).

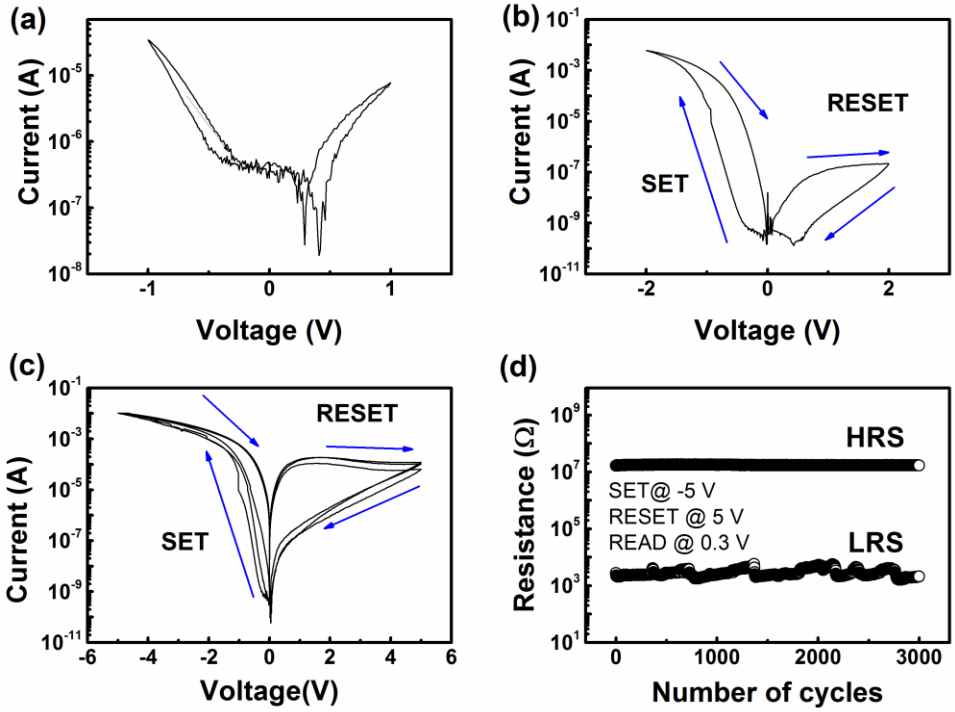

Figure 4-15. Resistive switching performance of sample B2. (thickness: 30 nm, growth rate: 0.083 nm/s). *I-V* curve under a (a) ±1 V cycle, (b) ±3 V cycle and (c) ±5 V cycle. (d) The endurance characteristics under 3000 cycles.

The comparison between samples A2 and B2 indicates that the thickness doesn't play a vital role in elimination of the electroforming process or on the reproducibility of *I-V* curves and programming tolerance or cycling durability in endurance measurements (i.e. the extent of degradation in endurance cycles), but is important for enhancing the ON/OFF ratio.

◆ **The influence of growth rate (thin films, 30 nm)**

As suggested above, when the sample is thick (150 nm), a lower growth rate favors an electroforming-free RS. To check whether this is also applicable in low thicknesses, two thin samples (30 nm) with higher growth rates (than sample B2): sample B3 (thickness: 30 nm, growth rate: 0.167 nm/s, Fig. 4-16) and sample B4 (thickness: 30 nm, growth rate: 0.5 nm/s, Fig. 4-17) were measured for comparison. As expected, both of these two samples need electroforming (Fig. 4-16 (a) and (b) and Fig. 4-17 (a) and (b)). Since the growth rates of samples B3 and B4 are equal to those of samples A3 and A4, these results therefore support a preliminary guideline mentioned above: decreasing the growth rate is a vital approach toward the direction of eliminating the electroforming process, while changing the thickness does not make much difference to electroforming. Besides, the average ON/OFF ratio of sample B3 (~28 in Fig. 4-16 (d)) and B4 (~12 in Fig. 4-17 (d)) are much lower than that of the electroforming-free sample B2 (~7700 in Fig. 4-15 (d)).

On the other hand, compared to samples A3 and A4, the *I-V* curves of samples B3 and B4 show enlarged hysteresis (Fig. 4-16 (c) *cf*. Fig. 4-13 (c), and Fig. 4-17 (c) *cf*. Fig. 4-12 (c)). Meanwhile, the ON/OFF ratios after electroforming are also higher (~28 in Fig. 4-16 (d) *cf*. ~9.5 in Fig. 4-13 (d) and ~12 in Fig. 4-17 (d) *cf*. ~1.6 in Fig. 4-12 (d)). These results again suggest that a lower thickness favors a higher ON/OFF ratio.

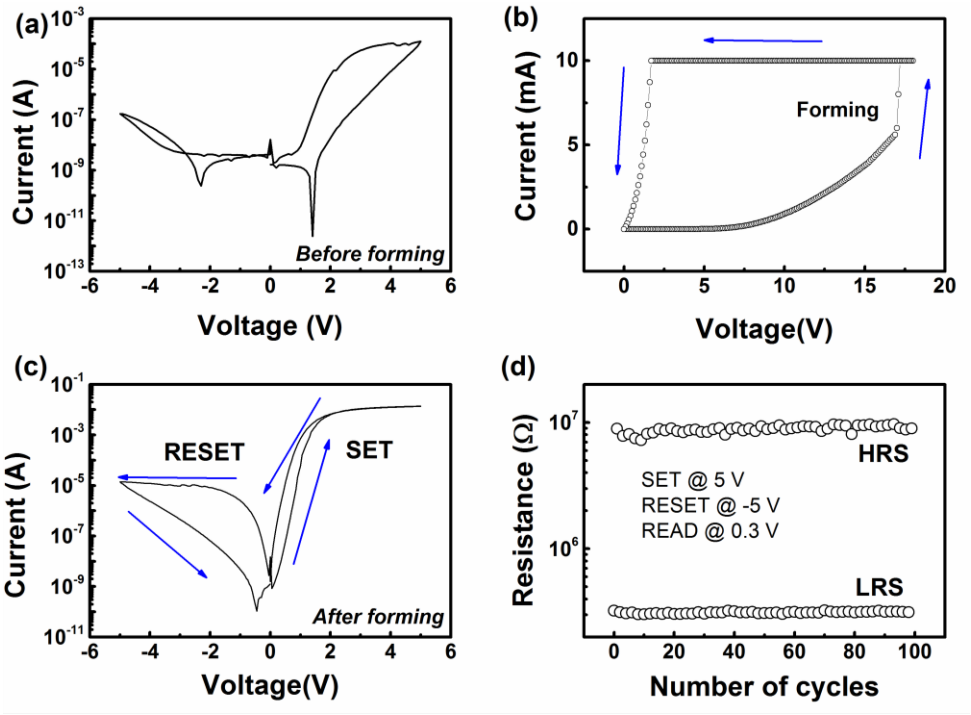

Figure 4-16. Resistive switching performance of sample B3 (thickness: 30 nm, growth rate: 0.167 nm/s). (a) *I-V* curve under a ±5 V cycle before electroforming. (b) The electroforming process. (c) *I-V* curve under a ±5 V cycle after electroforming. (d) The endurance characteristics under 3000 cycles.

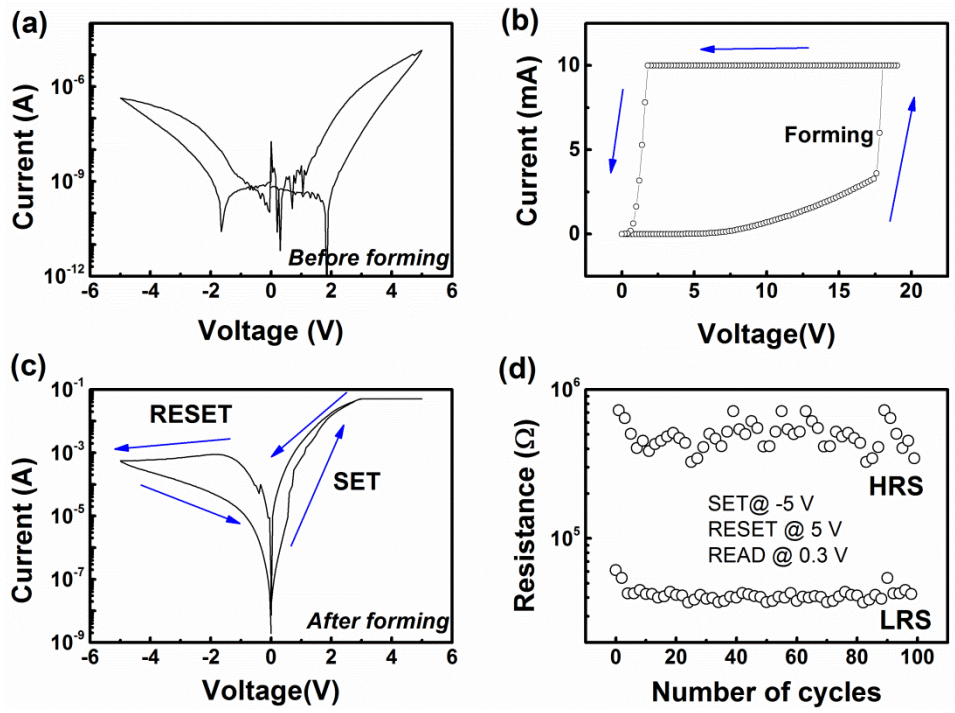

Figure 4-17. Resistive switching performance of sample B4 (thickness: 30 nm, growth rate: 0.5 nm/s). (a) *I-V* curve under a ±5 V cycle before electroforming. (b) The electroforming process. (c) *I-V* curve under a ±5 V cycle after electroforming. (d) The endurance characteristics under 3000 cycles.

◆ Optimization of the RS performance

Based on the above results, we summarize the following guideline for the improvement of RS performance of the SDC-STO VAN-based RRAM device:

(1) Overall, the electroforming-free samples tend to show better performances (higher ON/OFF ratios) and can be achieved by using slower growth rates.

(2) In order to increase the ON/OFF ratio, the sample should be thin and a slow growth rate should be used.

Based on this guideline, measurements were conducted on a 30 nm sample (sample B1) grown using a much slower growth rate (0.033 nm/s, the slowest growth rate used in this work). As shown in Fig. 4-18, sample B1 does not need electroforming, and the minimum voltage required for a nonvolatile resistive switching is decreased further to ±0.5 V (Fig. 4-18 (a)), which is much lower than the ±2 V required for sample B2 (Fig. 4-15 (b)) and the ±5 V for sample A2 (Fig. 4-14 (c)). It is clear from Fig. 4-18 (b), which shows the *I-V* curves from ±1 V voltage cycles to ±5 V voltage cycles, that the hysteresis gets larger as the voltage increases.

The resistance vs. voltage (*R-V*) curves in ±1, ±3V and ±5V voltage cycles (converted from the corresponding *I-V* curves) in Figure 4-18 (c) also show a nonvolatile behavior, and the nonvolatility (i.e. the hysteresis of the *I-V* and *R-V* curves) increases with increasing voltage. *I-V* curves under 20 consecutive cycles are shown in Fig. 4-18 (d) and the corresponding *R-V* curves are shown in Fig. 4-18 (e). Compared to sample B2 (Fig. 4-15 (c)), the *I-V* cycles of sample B1 are much more reproducible, with nearly no discrepancy between the first and last voltage cycle.

When increasing the voltage cycle from ±5 V to ±8 V, the hysteresis of *I-V* curves cannot be increased but instead be deteriorated, as shown in Fig. 4-18 (f). This indicates that ±5 V is the optimum operating voltage for these *I-V* measurements.

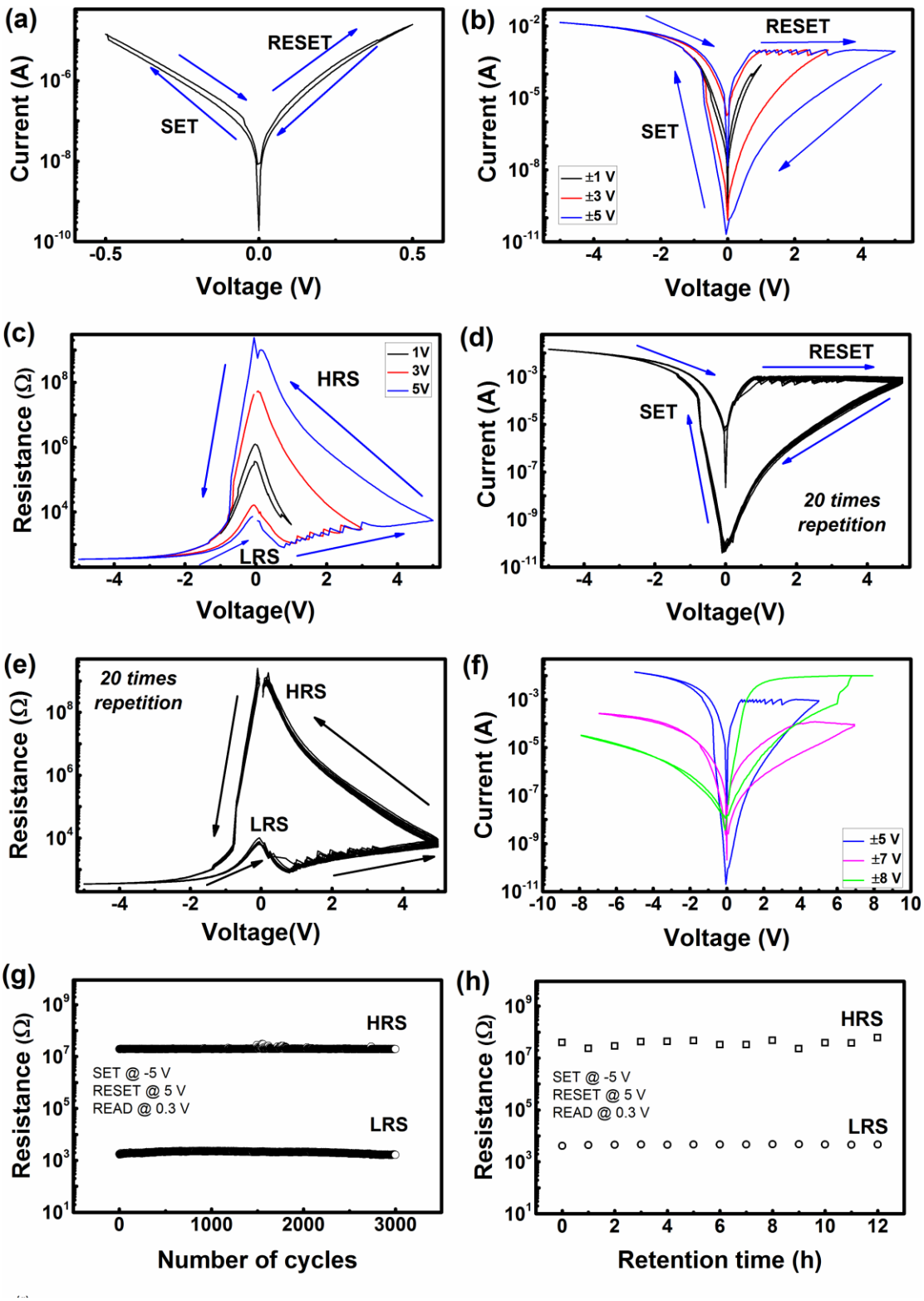

Figure 4-18. Resistive switching performance of sample B1. (thickness: 30 nm, growth rate: 0.033 nm/s). (a) *I-V* curve in a ±0.5 V cycle. Comparison of (b) *I-V* curves and (c) the corresponding *R-V* curves in ±1 V, ±3 V, and ±5 V cycles. (d) *I-V* curves and (e) the corresponding *R-V* curves in ±5 V cycle with 20 times of repetition. (f) Comparison of *I-V* curves between ±5 V, ±7 V, and ±8 V cycles. (g) The endurance characteristics under 3000 cycles and (f) retention characteristics over 12 h.

Sample B1 also exhibits uniform resistance variations for over 3000 cycles' endurance and a large ON/OFF ratio (>10^4) (Fig. 4-18 (g)). The variability, durability and ON/OFF ratio are much improved compared to the other two electroforming-free samples (Fig. 4.14 (d) and Fig. 4-15 (d)). Meanwhile, the triggered resistance states (both LRS and HRS) show stable retention without degradation (Fig. 4-18 (h)).

Therefore, optimization has been successfully realized on sample B1 using the guideline, and sample B1 shows electroforming-free switching with an enhanced ON/OFF ratio. The reproducibility in *I-V* measurements, the endurance variance and durability and the retention stability are also much improved. These are desired performances for sample B1 to act as a RRAM device.

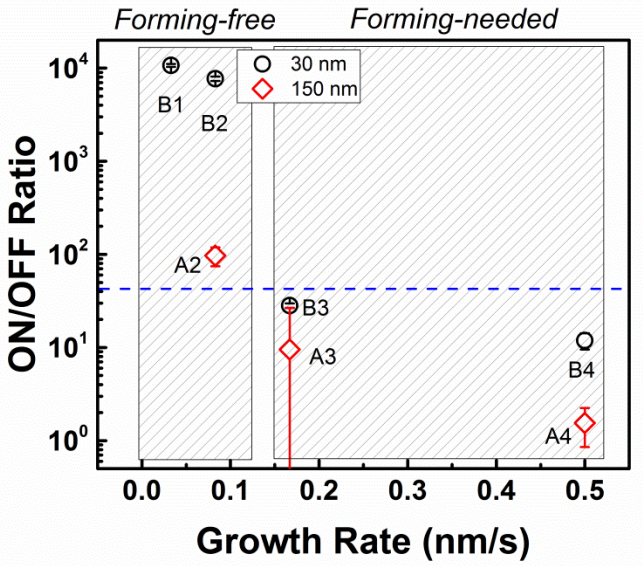

Figure 4-19. Summary of the ON/OFF ratio with the change in growth rate for the SDC-STO VAN thin films (30 nm, black dots) and thick films (150 nm, red diamonds). The ON/OFF ratio values were obtained from the average resistance values of 100 cycles of endurance measurements ("write" at ±5 V and "read" at 0.3 V). For the samples which need electroforming, the endurance measurement was conducted after forming.

In order to have a quantitative comparison on the RS performance between the samples, Fig. 4-19 shows a plot of the average ON/OFF ratios for the samples discussed above. The average value and deviation of ON/OFF ratio for each sample were obtained from the first 100 cycles of an endurance measurement which gives

reproducible result. The endurance tests were undertaken and reproduced on many memory cells on each sample (for those forming-free samples, at least 13 memory cells were reproduced, and for the samples which need electroforming, at least 3 memory cells were reproduced). As shown in Fig. 4-19, a lower thickness and lower growth rate tend to favor a larger ON/OFF ratio. The average ON/OFF ratio values of the electroforming-free samples are higher than those of the samples needing electroforming.

Table 4-1. Summary of the RS parameters for the SDC-STO VAN-based RRAM devices studied in this work

Sample No.	Growth rate (nm/s)	Thickness (nm)	Forming (Yes/No)	Forming Voltage (V)	Compliance for forming (mA)	Effective voltage for forming-free RS (V)	Average ON/OFF ratio at ±5V	Standard deviation of ON/OFF ration	Relative standard deviation of ON/OFF ratio
B1	0.033	30	No	NA	NA	0.5	10716	365	3.41%
B2	0.083	30	No	NA	NA	2	7705	421	5.46%
B3	0.167	30	Yes	17.1	10	NA	28.24	1.61	5.70%
B4	0.5	30	Yes	17.2	10	NA	11.89	2.37	19.98%
A2	0.083	150	No	NA	NA	5	96.86	22.39	23.12%
A3	0.167	150	Yes	17.2	10	NA	9.52	17.15	180.25%
A4	0.5	150	Yes	17.6	10	NA	1.55	0.70	44.95%

* *"Forming" is a shortened form of "electroforming"*
Relative standard deviation=standard deviation/the arithmetic mean

A summary of the RS parameters with the corresponding growth rates and thicknesses are listed in Table 4-1. Apart from the trend shown in Fig. 4-19, additional information can be obtained: the relative standard deviation (defined as the standard deviation/the arithmetic mean) of the ON/OFF ratio, which can be used as an evaluation of the variability or programming tolerance of the RRAM device, increases with increasing the growth rate and thickness. This is an indication that a slow growth rate and a low thickness favors a high stability and low variability of the SDC-STO VAN-based RRAM device. The reasons for the influence of the thickness and growth rate will be discussed later in Chapter 4.5.5 after probing the underlying RS mechanisms.

◆ The influence of "write" and "read" voltages on the RS performance

Having obtained a SDC-STO VAN-based RRAM device with an optimized ON/OFF ratio and good endurance/retention, we turn to discussing the optimization of the "write" and "read" voltages using the optimized sample B1. The study on "write" voltage was done by conducting 50 cycles' endurance measurements using four different levels of "write" voltages (from ±3 to ±7V) with the "read" voltage being kept at 0.3 V. As shown in Fig. 4-20 (a), a low level of "write" voltage (±3 V) cannot stabilize the resistance state, as seen from the wide distribution of resistance values for both the HRS and LRS (black dots). When the "write" voltage increases to ±4 V, the variance and the resistance distribution is reduced (red circles). This reduced variance is maintained as the voltage increases further to ±5 V (blue triangles) and ±7 V (magenta triangles). On the other hand, although the ON/OFF ratio is enhanced when increasing from ±3 V to ±5 V, a further increase to ±7 V does not further increase the ON/OFF ratio (as shown in Fig. 4-20 by the magenta triangles overlapping with the blue triangles). This is consistent with Fig. 4-18 (f), where increases of the voltage above 5 V do not bring about enlarged hysteresis in *I-V* curves. Considering the low operating voltage requirements for RRAM devices mentioned in Chapter 4.1.1, 5 V is determined to be a proper operating voltage for sample B1.

To study the "read" voltage, endurance measurements were conducted using multiple "read" voltages and with the "write" voltage being kept at ±5 V. As shown in Fig. 4-20 (b), 0.1 V is unable to maintain a stable endurance as the resistance of the HRS (R_{HRS}) has a large variation. This is perhaps because 0.1 V is too small for fast detection of the stable resistance states[107]. An increase in the "read" voltage from 0.1 to 0.3 V can not only decrease the variability but also enhance the ON/OFF ratio. However, considering that resistive switching starts to show from 0.5 V (Fig. 4-18 (a)) and in order not to alter the triggered resistance states, 0.3 V is selected as a proper "read" voltage.

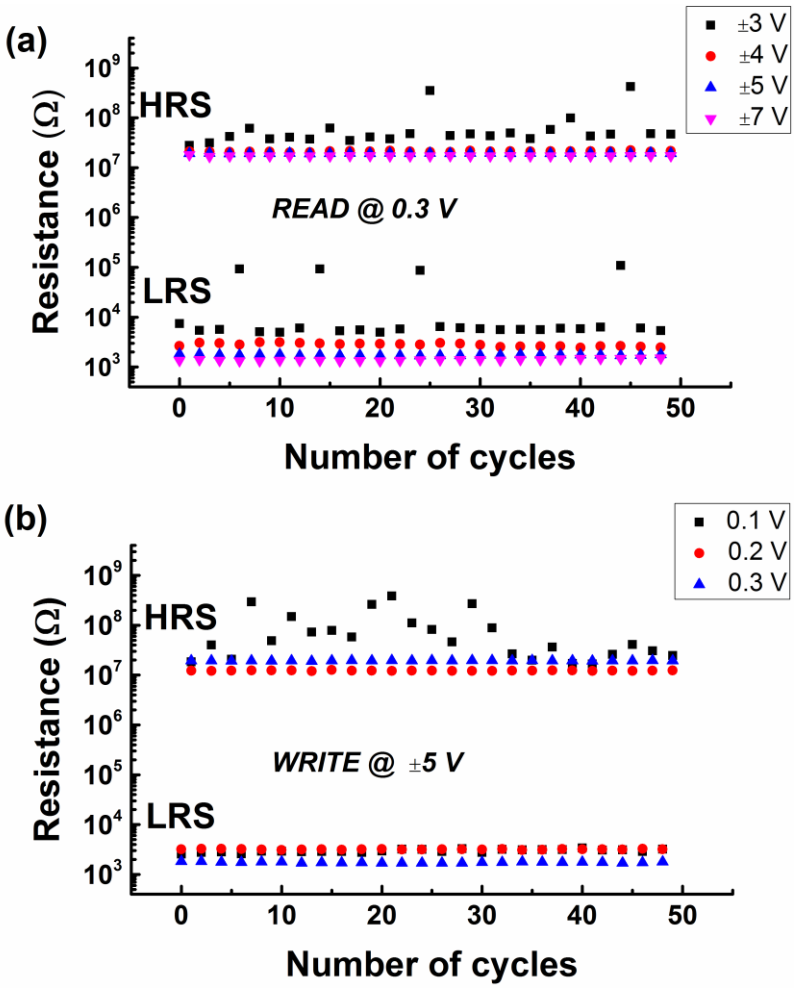

Figure 4-20. Influence of the (a) "write" and (b) "read" voltage on the ON/OFF ratio and stability of sample B1.

4.4 Study on the conduction mechanism

Having obtained the above empirical optimization guideline for device making, an in-depth study on the RS mechanism was conducted using the optimized sample B1. To probe the nature of the electroforming-free RS effect in the SDC-STO VAN-based RRAM device, it is necessary to firstly probe the nature of the conduction mechanism in this system. The following discussions will only focus on the conduction mechanisms in the electroforming-free samples.

◆ **The intrinsic conduction mechanism**

As mentioned in Chapter 4.1.2, RS mechanisms can be classified based on whether the conductive paths are filamentary (localized) or interfacial (uniformly distributed).

To gain additional insights, 100 cycles of endurance measurements were done using top electrodes with two different diameters: 100 μm and 300 μm. As shown in Fig. 4-21, the average R_{HRS} and R_{LRS} values increase simultaneously with the increase in the electrode size. This suggests that the conductive channels are uniformly distributed over the whole electrode area, and so at least form a 2-dimensional path. This behavior is quite different from that expected in a system with a 1-dimensional filament and thus indicates that the conduction mechanism is interfacial-type[108].

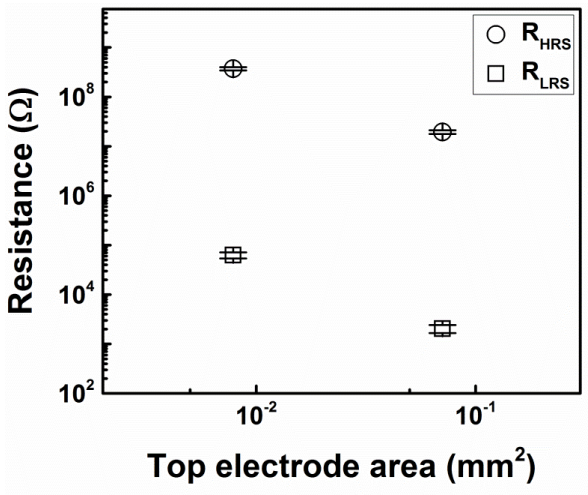

Figure 4-21. Electrode area dependence of the average R_{HRS} and R_{LRS} values of the Pt/SDC-STO/Nb:STO RRAM device. Error bars are provided as the standard deviation for the resistance values.

Applying the structural model proposed in Fig. 4-5, there are three distinct components in the SDC-STO VAN: the STO matrix, the SDC nanocolumn, and the STO-SDC vertical interface. The STO matrix is regarded as a perfect insulator when it is defect-free, while the SDC nanocolumns and STO-SDC interfaces (with lots of V_os) are regarded as *n*-type semiconductors[107,122,140]. In reality, V_os in STO are usually unavoidable, which results in it also acting like an *n*-type semiconductor[122]. Therefore, due to the high work function of Pt (5.3-5.6 eV) and relative low work functions of STO and CeO_2 (~3.5-3.9 eV), built-in potentials and Schottky barriers are expected in the Pt/STO plain film, Pt/SDC plain film and the Pt/SDC-STO VAN interfaces. On the other hand, the oxide/oxide contacts of the film/Nb:STO interfaces are regarded as Ohmic contacts[122]. These are corroborated by the asymmetric and rectifying

characteristic of the *I-V* curves shown in Fig. 4-22 (a) - (c), where rectifying behaviors are shown in all the three devices in the initial states[141]. The highly asymmetric *I-V* curve is additional evidence that these devices exhibit an interface-limited conduction mechanism.

As discussed in Chapter 2.1.2, there are four kinds of interface-limited conduction mechanisms[11,142,143]: Schottky or thermionic emission ($I \sim V^{\frac{1}{2}}$ in semi-log), direct tunneling ($I \sim \frac{1}{V}$ in semi-log), Fowler-Nordheim (F-N) tunneling ($\frac{I}{V^2} \sim \frac{1}{V}$ in semi-log), and interface-limited trap-assisted tunneling ($I \sim \frac{1}{V}$ in semi-log). The conduction mechanisms are usually different in different voltage ranges. As our main focus here is the conduction mechanism of the Pt/SDC-STO/Nb: STO device in the initial state, i.e. in the low negative voltage range before switching happens, only one mechanism should be relevant.

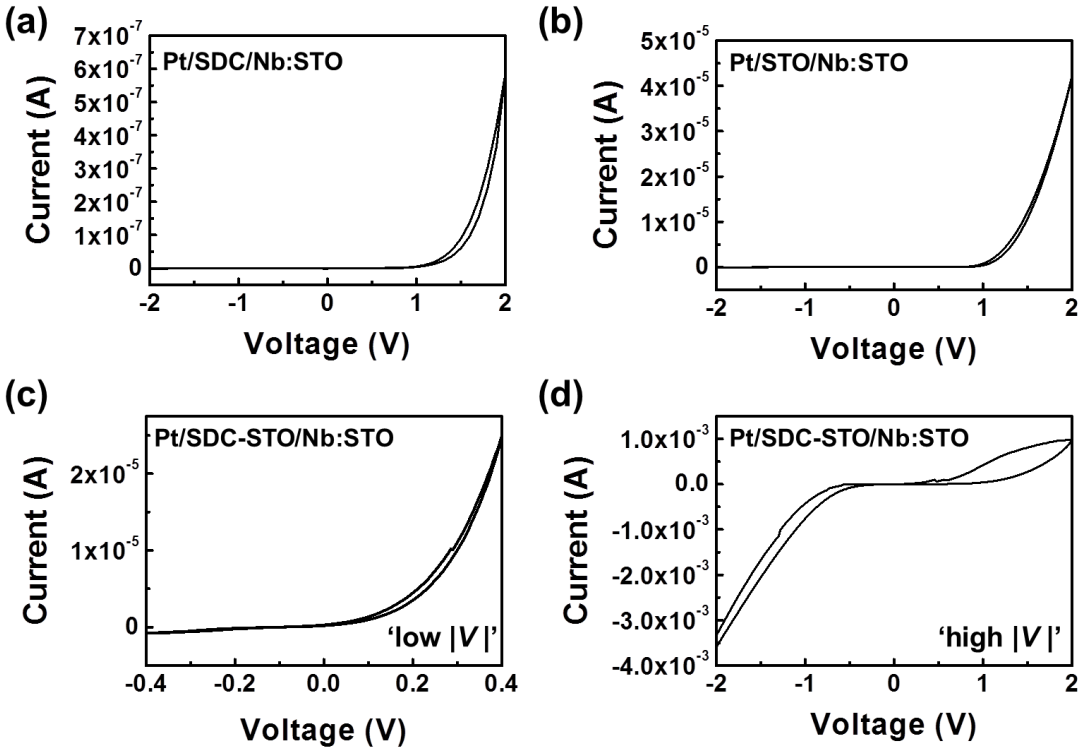

Figure 4-22. *I-V* curves in the pristine state: (a) The Pt/SDC/Nb:STO device, (b) the Pt/SDC/Nb:STO device and (c) the Pt/SDC-STO VAN/Nb:STO device in the low voltage range. (d) The Pt/SDC-STO VAN/Nb:STO device in the high voltage range.

Here, direct tunneling can be ruled out, as the SDC-STO VAN films are thick (⩾30 nm). By plotting the current (*I*) of the initial resistance state below the SET voltage in various manners as a function of the applied voltage (*V*), the nature of the intrinsic conduction mechanism is illuminated. The fitting was conducted on sample B1 based on Fig. 4-18 (d). Here the SET voltage is determined to be -0.7 V. For ease of fitting, voltages were converted to absolute values. As shown in Fig. 4-23 (b), the nonlinear relationship between log *I* and $\frac{1}{V}$ rules out trap-assisted tunneling as the conduction mechanism. Similarly, the F-N tunneling model does not work (Fig. 4-23 (c)). In contrast, the linear fit of the log *I* vs. $V^{\frac{1}{2}}$ in Fig. 4-23 (d) clearly indicates that the intrinsic conduction mechanism is the Schottky emission, where the increase in conductivity arises as a result of charges overcoming the interfacial potential barrier[144] (i.e. a Schottky barrier in the negative bias, as discussed in Chapter 2.1.2). This therefore indicates that the current conduction (including the conduction in the LRS and the transition between different resistance states) is relevant to the modulation of the Schottky barrier height/width.

Interestingly, as the absolute value of negative bias increases, the current dramatically increases, resulting in a completely different shape of the *I*–*V* curve (Fig. 4-22 (d)) to that in the low bias range (Fig. 4-22 (c)). In addition, the *I*–*V* scan with an applied bias range of ±2 V shows clear hysteresis.

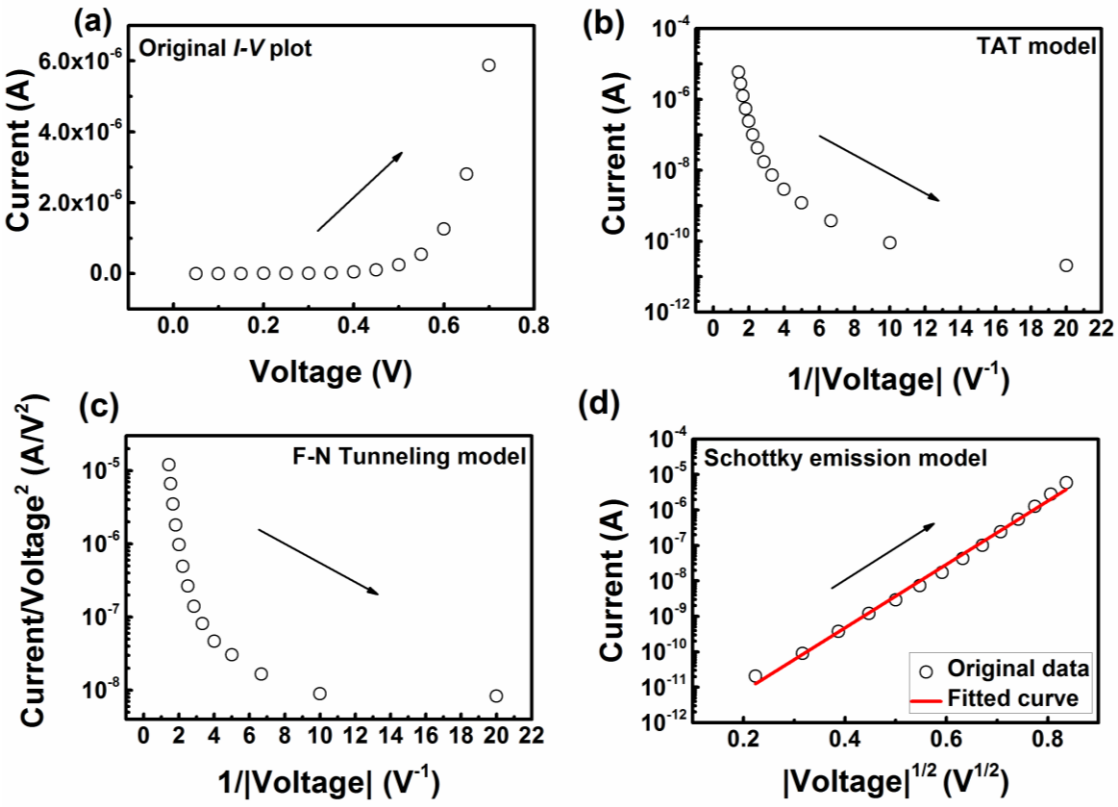

Figure 4-23. *I-V* curves of the Pt/SDC-STO/Nb:STO device (sample B1) in the initial resistance state (voltage range:0 to -0.7 V) fitted using different models. Voltages are converted to absolute values. (a) The original *I-V* plot. (b) The trap-assisted tunneling model: Semi-log $I \sim \frac{1}{V}$ plot. (c) The F-N tunneling model: Semi-log $\frac{I}{V^2} \sim \frac{1}{V}$ plot. (d) The Schottky emission model: Semi-log $I \sim V^{\frac{1}{2}}$ plot.

◆ Calculation of the Schottky barrier height

Having confirmed Schottky emission as the intrinsic conduction mechanism, we now turn to calculating the height of the Schottky barrier under zero bias. The electron affinity of STO is known to be 3.9 eV and the work function of Pt is 5.3–5.6 eV (Table 2-2). Therefore, a theoretical barrier height value of 1.4–1.7 eV is expected. On the other hand, by fitting the *I-V* curves in Fig. 4-23 (d) with the Schottky emission model using equations (2-4) and (2-5), the Schottky barrier height in a non-bias state is obtained from the intercept[11]. Assuming the Richardson constant A^* to be 120 $A/cm^2/K^2$ (as in conventional thermionic emitters where the free electron mass m_0 is used[145]) and taking the electrode diameter to be 300 μm, then the calculated Schottky

barrier height at zero bias is 1.11 eV.

The difference between the expected value and the calculated value is due to the following reasons:

1. The electron affinity of the STO phase near the vertical interface should be higher than that of the ideal defect-free phase used above[9], which means the real Schottky barrier height should be lower than 1.4-1.7 eV.

2. The effective electron mass (m^*) in the defective *n*-type STO is expected to be higher than the free electron mass (m_0),[146,147] which means that the effective Richardson constant (A^*) should be higher than 120 A/cm^2/K^2 (according to equation (2-5)). Therefore, the real Schottky barrier height should be higher than the calculated values of 1.11 eV.

After taking these two factors into account, the calculated value will be closer to the theoretical values.

◆ **Conduction mechanism in the low resistance state**

After being "SET" to the LRS, the conduction mechanism deviates from the Schottky emission and switches to bulk-limited Ohmic emission, and a linear *I*-*V* relationship (*I* ~ *V*) is exhibited in the whole LRS region, as shown in Fig. 4-24 (a) (from -1 V to -5 V) and Fig. 4-24 (b) (from -5 V to 0 V). The Ohmic conduction mechanism is expected in the LRS of most RRAM devices, as the Schottky barrier height/width are low enough to enable the movement of electrons in the conduction band and holes in the valence band[11]. This produces an effect that equals the formation of an Ohmic contact throughout the device.

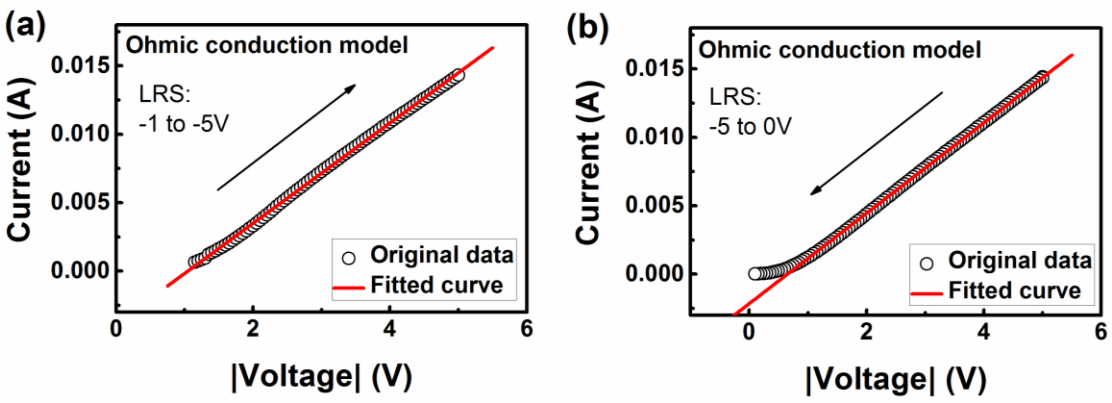

Figure 4-24. Fitting of the *I-V* curve of the Pt/SDC-STO/Nb:STO device (sample B1) in the Low Resistance State (LRS) using the Ohmic conduction model where a linear *I-V* relationship is exhibited. (a) From -1 V to -5 V. (b) From -5 V to 0 V. Voltages are converted to absolute values.

4.5 Proposal of the RS mechanism

Having confirmed the interfacial nature of the conduction mechanism, the uniform distribution of conduction paths and the essential role of the Schottky barrier, we next investigate the mechanism of the electroforming-free nonvolatile resistive switching in the SDC-STO VAN-based RRAM device. This section starts with discussing the reason for the elimination of the electroforming process. Then, by addressing the role of the vertical interface (which is electronically active) and Sm doping (which modifies the ionic conduction in the SDC phase), the mechanism for the resistive switching is explained using a proposed model, where the electronic and ionic channels are decoupled into the vertical interfacial part of STO and the SDC phase, respectively. Finally, additional proofs are presented to support the model and to gain insights into the factors which influence the optimization of the RS performances.

4.5.1 The role of the vertical interface

As discussed in Chapter 4.1.4, in VAN-based RRAM devices, the vertical interface plays a vital role to eliminate the electroforming process[122]. To confirm the unique role of the vertical interface in the SDC-STO VAN (denoted as NC), measurements were conducted on two single-phase SDC and STO plain films (denoted as PF). The

PFs were grown under the same condition as that of the NC sample B1 (thickness: 30 nm, growth rate: 0.033 nm/s). In contrast to the NC sample B1, both of the two reference PFs need electroforming (as shown in Fig. 4-25 (a) and Fig. 4-26 (a)). Additionally, the RS performances are much worse after electroforming, with nearly no hysteresis observed in the *I-V* curves, as shown in Fig. 4-25 (b) and Fig. 4-26 (b). This suggests that the coexistence and the integration of the SDC and STO phases are essential for the elimination of the electroforming process.

Besides, as shown in Fig. 4-22 (a), (b) and (d), the current of the NC sample is 2-4 orders lower than the PFs when the applied voltages are on a similar level in the initial state. This indicates that self-assembly of the SDC and STO phase results in an effective manipulation of the conductivity under the applied voltage. This manipulation of the conductivity, as discussed later, is due to the effective modification of the potential barrier in the Pt/SDC-STO interface.

Considering first the structural factors, the fact that good crystallization is shown inside the bulk part of the matrix and column phases of the NC film (Fig. 4-7 (a) and (b)) indicates no large structural difference in the SDC and STO phases between the NC and PFs. Additionally, the thin film processing is designed to fully oxidize and to (slow cooling in 900 mbar O_2 after deposition) to minimize the oxygen deficiency in the STO and SDC phases and thus the reduction of STO and SDC (which increase the conductivity) are unlikely. Therefore, the lattice-mismatched vertical interface, which is the only structurally-different area between SDC and STO phases in the NC and PF, is likely to be the origin of the enhanced electronic conductivity. This is confirmed by the Conductive-AFM (C-AFM) measurements shown in Fig. 4-27: high current areas form circular shapes indicating that the conductivity near the vertical heteroepitaxial interfaces is higher than that of the bulk part inside the matrix or the column. As mentioned in Chapter 4.1.4, this interface conduction is not new in VAN structures.

It is well-known that the electronic conductivity of STO is sensitive to doping and non-stoichiometry. The primary origin of the increased local conductivity in the SDC-STO vertical interface is likely the large lattice mismatch between the SDC

(c=5.430 Å) and STO (c=3.905 Å) phases, which either induces a non-stoichiometric region (such as one with a high concentration of V_os) or leads to electronic reconstruction (which induces polar discontinuity or additional interface states) in the STO, both of which can contribute to electron donors and increase the electronic conductivity of STO near the interfaces[122,128,148,149]. Regions in the bulk of STO matrix may also contain V_os, but the concentration is expected to be much lower than that in the disordered interfacial areas, and therefore the conductivity is much lower in the STO bulk part of the NC (Fig. 4-27 (b)) as well as in the STO PF (Fig. 4-23 (b)).

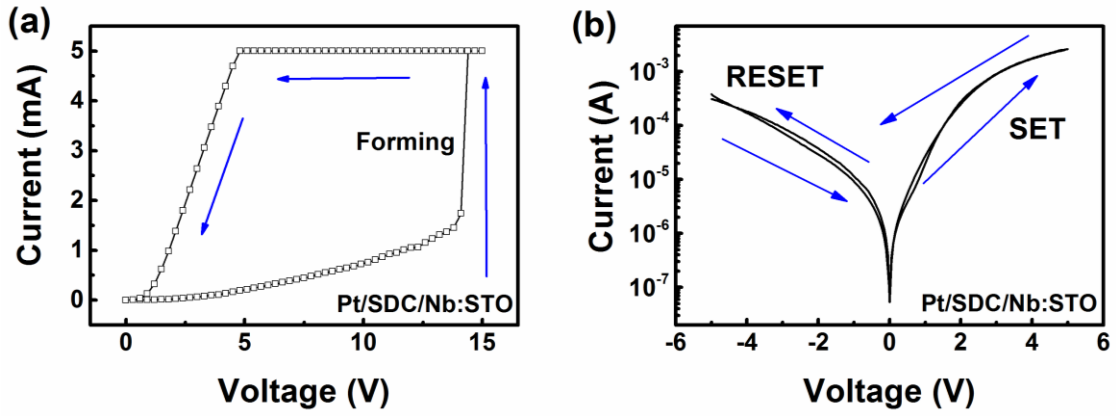

Figure 4-25. Resistive switching performance of the Pt/SDC/Nb:STO device (film thickness: 30 nm, growth rate: 0.033 nm/s): (a) The electroforming process. (b) *I-V* curve under a ±5 V cycle after electroforming.

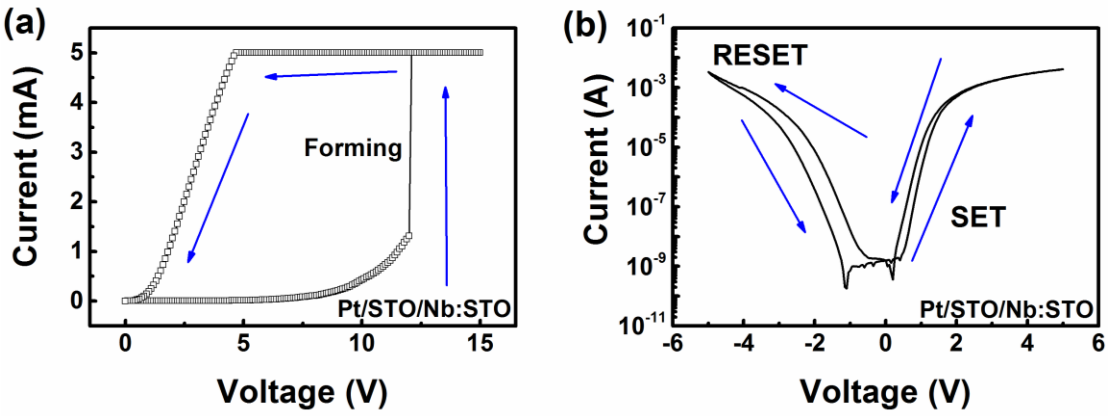

Figure 4-26. Resistive switching performance of the Pt/STO/Nb:STO device (film thickness: 30 nm, growth rate: 0.033 nm/s): (a) The electroforming process (b) *I-V* curve under a ±5 V cycle after electroforming.

The enhanced electronic conductivity in the vertical interfaces, as confirmed above, helps to explain the elimination of the electroforming process. In the VAN fabrication procedure, the self-assembly process has created an electron conduction pathway via the generation of a high concentration of defects (most likely V_os) which are localized along the vertical interfaces, and as mentioned above, they can increase the electronic conductivity without the need to be mobile. The absence of a sudden current jump in sample B1 (Fig. 4-18 (a)-(d)) indicates that the switching process is assisted by the electronic conductive pathway and occurs gradually, without the need for the formation of the electronically active channels by a high voltage.

The localized defect sites in the vertical interface also provide a medium for highly tunable carrier mobility under the application of a small electric field, making it easier to modulate the height/width of the interface potential barriers. This is consistent with the fact that the switching effect in sample B1 occurs at a very low voltage (Fig. 4-18 (a)-(b)).

In light of the above statements, the vertical interface plays two roles: it creates an electronic conductive channel, which eliminates the electroforming process, and at the same time makes it easier to modulate the interface potential barrier by increasing electron mobilities.

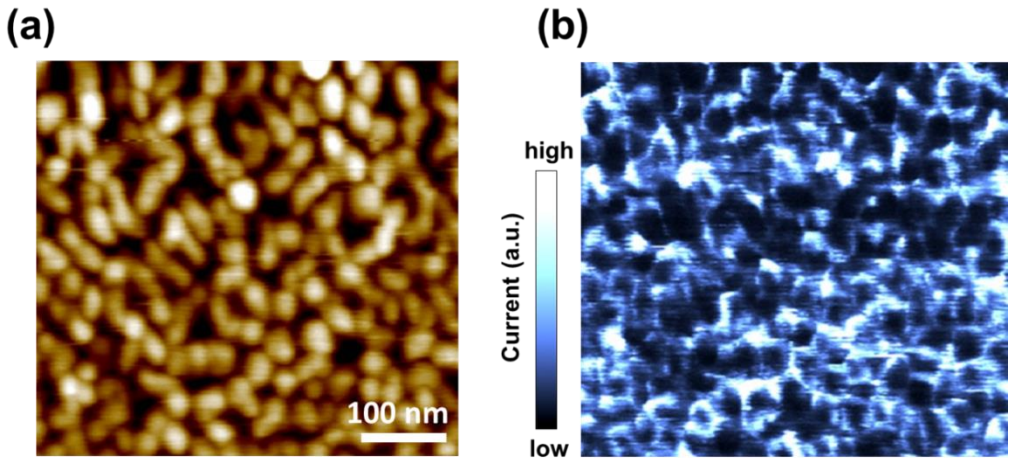

Figure 4-27. (a) Topography and (b) a corresponding current map of the SDC-STO VAN (Figure taken from[114]).

4.5.2 The role of Sm doping in the SDC phase

Apart from the electronically active vertical interfaces, the ionic conductivity in the SDC phase should also be considered as an important factor for the improvement of the RS performance. This is because the concentration of mobile V_os, which acts to modify the depletion layer width (W_d) of the Pt/film interface (as discussed in Chapter 4.1.2), can be modified by varying the ionic conductivity of the SDC phase in the presence of electric fields. The change of W_d alone (without being assisted by an electric field) is deemed to have a great influence on the interface potential barriers[114,115]. To confirm the role of the ionic conductive SDC phase in the RS performance, measurements were conducted on a reference CeO_2-STO VAN sample (without Sm doping) grown under the same condition as sample B1 (thickness: 30 nm, growth rate: 0.033 nm/s). As shown in Fig. 4-28 (a), an electroforming-free RS is observed. This is expected since the same electronically conductive vertical interface found in the SDC-STO VAN (sample B1) should form when the growth parameters are the same. However, the hysteresis in the *I-V* curve is smaller than that of sample B1, as clearly shown from the comparison of the *I-V* curves between these two samples (Fig. 4-28 (b)). Additionally, the maximum current value after the "SET" process (8 mA) is lower than that of sample B1 (14 mA in Fig. 4-18 (d)) and the ON/OFF ratio of the endurance measurement is one order of magnitude lower than sample B1 (as shown later in Fig. 4-30 (a)). This indicates that the R_{LRS} is much smaller in the sample doped with Sm, which therefore suggests that the electronically conductive channel (the vertical interface) alone cannot account for the large switching effect observed in sample B1, and doping of Sm in the CeO_2 phase is indeed another important factor. It is well-known that Sm doping increases the ionic conductivity of CeO_2 and thus the mobile V_o concentration increases massively, which is correlated to the enhanced RS performance observed here. Therefore, the existence of the ionically conductive phase (SDC), which is spatially decoupled from the electronically conductive channel (SDC-STO vertical interface), is essential to the RS effect.

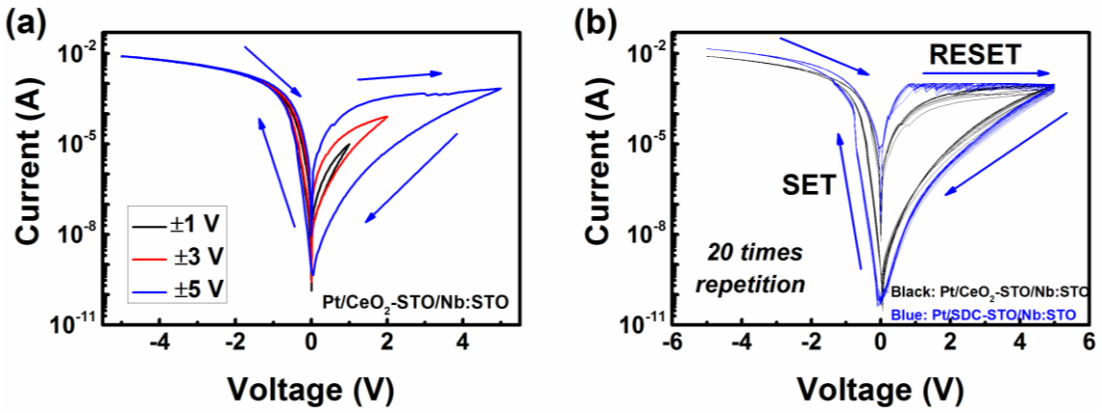

Figure 4-28. (a) *I-V* curve of the Pt/CeO_2-STO/Nb:STO device under ±1 V, ±2 V, and ±5 V cycles. (b) Comparison of the *I-V* curves under 20 repetition of ±5 V cycles between the Pt/CeO_2-STO/Nb:STO device (black) and the Pt/SDC-STO/Nb:STO device.

4.5.3 Proposal of the separate-channel model

Having confirmed the role of both the vertical interface and the SDC phase, we now turn to explaining the mechanism of resistive switching in the SDC-STO VAN-based device. We propose a simplified model based on the following experimental proofs:

1. As previously shown in Fig. 4-22, the electronic conductivity of the SDC-STO VAN (NC) film is much higher than that of the SDC PF or the STO PF in the pristine state. C-AFM (Fig. 4-27) then proves that this increased electronic conductivity comes from the SDC-STO vertical interfaces, while the bulk STO and SDC parts are more electronically insulating.

2. As proved in previous studies from our group[74], the ionic conductivities in the bulk part of the STO in the SDC-STO VAN are much lower than in the SDC columns, and the highest ionic conductivity is localized in the SDC column centers, away from the SDC-STO interfaces. Additionally, the crystallinity of the SDC phase in the VAN is enhanced compared to that of SDC single phase plain films, which enhances the ionic conductivity further.

3. Although V_os are present in both the SDC phase and the SDC-STO vertical interface, their nature is different. At the vertical interfaces, a large ionic conductivity

(a large concentration of mobile V_os) is not expected, and the presence of immobile V_os mainly enhances the electronic conductivity and electron carrier mobility. On the other hand, in the ionic channel, a large ionic conductivity is observed and thus high concentrations of mobile V_os exist.

The proposed model is illustrated in Fig. 4-29 (a): the electronic and ionic channels are decoupled into the SDC-STO vertical interface and the SDC phase, respectively. On one hand, the vertical interfaces not only eliminates the need for the "construction" of an electronic conductive channel using a high driving force but also enhances electron mobilities along this channel (Fig. 4-22, Fig. 4-25 to Fig. 4-27). On the other hand, the ionic conductivity in the SDC phase creates a high concentration of mobile V_os near the top electrode, which allows modification of the Pt/film potential barrier and is correlated to a large ON/OFF ratio (Fig. 4-18). These correlations can be explained by the mechanism discussed below.

4.5.4 Explanation of the RS mechanism

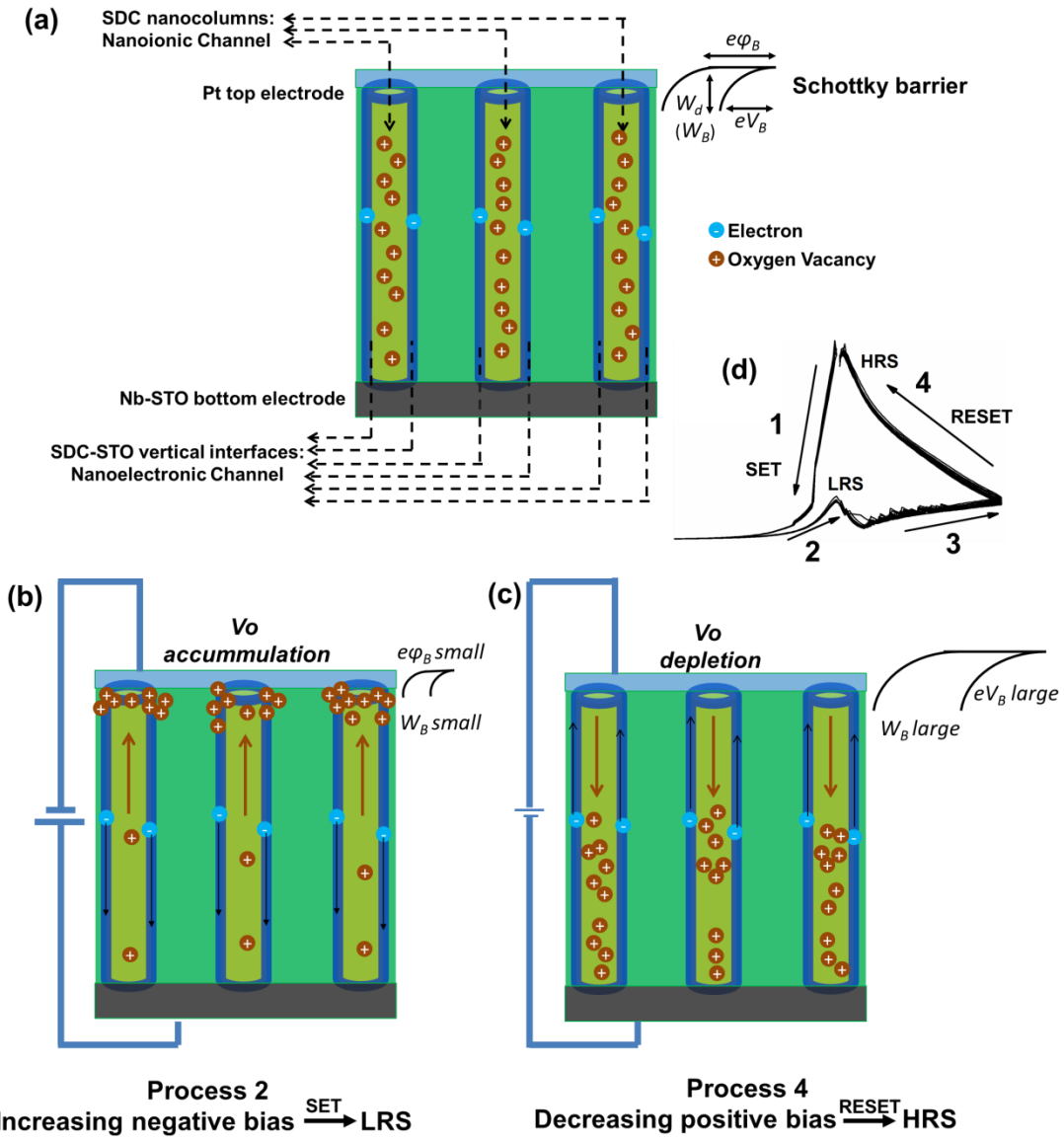

Figure 4-29. (a) Schematic diagram of the model for resistive switching of the Pt/SDC:STO/Nb:STO RRAM device with separated ionic and electronic nanochannels. (b) The increase in negative bias induces V_o accumulation near the electrode, decreasing the Schottky barrier height ($e\varphi_B$) and width (W_B), which leads to the LRS (process 1 in (d)). (c) The positive bias induces V_o depletion near the electrode, and the decrease in positive bias results in an overall increase in the Schottky barrier height (eV_B) and width (W_B), which leads to the HRS (process 4 in (d)). The black sketches beside the top electrodes illustrate the relative width and height of the Schottky barrier. The sizes of the electrode symbol in the circuit stand for the relative direction and strength of the source voltage. (d) *R-V* curve showing the resistance switching process.

In the following discussions, we assume that the two channels influence the interfacial potential barriers separately. For simplicity, we define both the metal-to-semiconductor barrier (positive bias, with a height of eV_B) and the semiconductor-to-metal barrier (negative bias, with a height of $e\varphi_B$) as Schottky barriers (illustrated in Fig. 4-29 (a)). It is known from Chapter 2.1.2 that the application of positive (negative) biases can lower eV_B and $e\varphi_B$. It is also known from Chapter 4.1.2 that the V_o accumulation near interfaces decreases the depletion layer width (W_d, equals to the barrier width W_B) and decreases the Schottky barrier heights (eV_B, $e\varphi_B$) as well. Modulation of the resistance states through modulation of the interfacial contact resistance is a result of the modulation of the Schottky barrier height and width[116].

Turning back to the separate-channel model in Fig. 4-29 (a), the existence of a well-aligned vertical interface (the electronic channel) provides enhanced electron mobility, making it easier to lower the barrier heights (eV_B, $e\varphi_B$) under biases. On the other hand, in the ionic channel, the V_o accumulation/depletion under biases adds in an additional effect to affect the barrier heights (eV_B, $e\varphi_B$) and width (W_B) through modulating the depletion layer width (W_d). The barrier height at the interface of the Pt/VAN vertical interface is considered to be lower than the Pt/SDC and Pt/STO interface, and therefore in the following discussion, we assume that switching mainly happens here. Nonvolatile resistive switching occurs when varying the voltage bias:

1. The application of a negative bias drives a large concentration of mobile V_os in the ionic channels and induces V_o accumulation near the Pt/film interface, and this decreases the W_d (and then decreases $e\varphi_B$ and W_B). Meanwhile, the negative bias alone can decrease the $e\varphi_B$, which is assisted by the electronic channels. Therefore, when increasing the negative bias (process 1 in Fig. 4-29 (d)), an overall shrinkage of the Schottky barrier results, which decreases the contact resistance, and this results in the "SET" process to the LRS, as shown in Fig. 4-29 (b). A memory effect of the LRS is maintained when the negative bias is withdrawn, as the accumulated V_o near the electrode cannot be driven back to the film without a positive bias. For simplicity, Fig.

4-29 (b) and (c) emphasis on the ionic effect.

2. When a positive bias is applied, the situation is more complex: on one hand, the V_os are depleted near the Pt/film interface, which tends to increase W_B and eV_B; on the other hand, the positive bias alone tends to decrease eV_B. Therefore, a competition between these two factors results in the maintenance of the Schottky barrier profile when the positive bias is increasing (process 3 in Fig. 4-29 (d)), and therefore the LRS is still maintained. The "RESET" process to the HRS occurs only when the V_o depletion effect surpasses the positive bias effect, i.e. when the positive bias is decreasing and both eV_B and W_B are recovered, as shown in Fig. 4-29 (c), which corresponds to process 4 in Fig. 4-29 (d)).

4.5.5 Further discussions

Having proposed the separate-channel model and explained the RS mechanism, we now turn to providing additional experimental results to prove this model and quantitatively analyze the role of the ionic and electronic channels. To do this, we study the influence of the Sm doping ratio and the film growth rate on the RS performance of the Pt/Sm:CeO_2-STO/Nb:STO devices. Using the model, the study on growth rate and the discussion on the influence of thickness also help us gain additional insights into the factors influencing the optimization of RS performances discussed in Chapter 4.3.

◆ **The influence of the Sm doping ratio**

First, the results discussed in Chapter 4.5.2 underline the importance of V_os on the RS performances (Fig. 4-28). To prove and quantify their role, the dopant (Sm^{3+}) concentrations in the SDC phase (ionic channel) of the VAN films were changed to induce different ionic conductivities (which leads to different mobile V_o concentrations here). To do this, Sm:CeO_2-STO VAN films were grown with the Sm doping ratio varied from 0 to 30 %, and endurance measurements were conducted using the same conditions as in sample B1 ("write" at ±5 V and "read" at 0.3 V). As

shown in Fig. 4-30 (a)-(d), all the reference samples exhibit electroforming-free resistive switching and the R_{HRS} values are very close (with a difference of < 15%). This is because the V_o concentration is depleted at the Pt/film interfaces by applying high positive biases across all the devices, and thus the R_{HRS} values under positive biases are similar regardless of the different intrinsic V_o concentrations in the VAN films with the different Sm^{3+} contents (as shown Fig. 4-30 (e)).

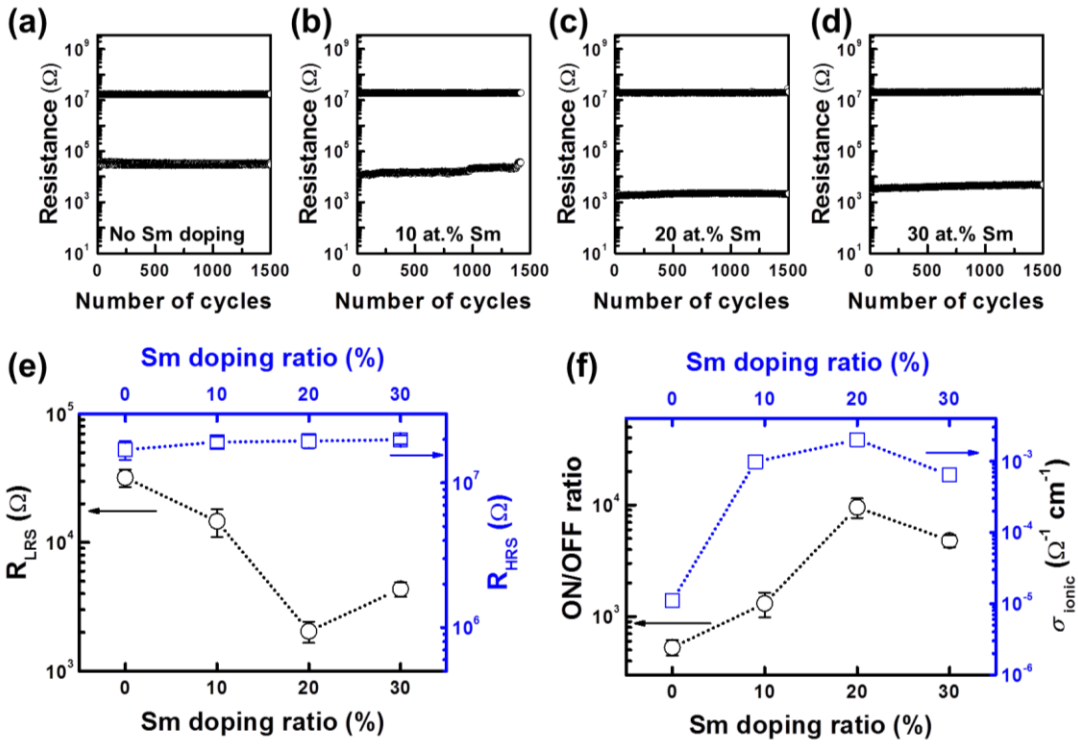

Figure 4-30. The influence of Sm doping ratio on the ionic channel. Endurance characteristics of (a) the Pt/CeO_2-STO/Nb:STO device, (b) the Pt/10 at. % Sm:CeO_2-STO/Nb:STO device, (c) the Pt/20 at. % Sm:CeO_2-STO/Nb:STO device and (d) the Pt/30 at. % Sm:CeO_2-STO/Nb:STO device. Data in (b) and (d) were collected by Dr. Seungho Cho. (e) The influence of Sm doping ratio on the average resistance values of the LRS and HRS obtained from the endurance measurements. (f) The average ON/OFF ratio and the ionic conductivity as a function of Sm doping ratio. (The ionic conductivity of Sm-doped CeO_2 bulk samples are used, cited from[133].)

In contrast to the similar R_{HRS} values, the R_{LRS} values decrease when the Sm doping ratios increase from 0 to 20% and then increase again when the doping ratio increases to 30% (Fig. 4-30 (e)). Overall, the effective tuning of the R_{LRS} whilst keeping the R_{HRS} almost constant results in precise control of the ON/OFF ratio as

shown in Fig. 4-30 (f). Comparing Fig. 4-30 (e) with (f), there is a direct inverse correlation of the R_{LRS} with the ionic conductivity, and this results in a direct correlation between the ON/OFF ratio and the ionic conductivity of the SDC phase. Here the ionic conductivities at 600℃ were quoted[133]. Though measured there at 600℃, the values below 600℃, which would be applicable for our device measurements, scale with doping concentration in the same order as that of the high-temperature data[133]. The direct inverse correlation between the ionic conductivity of the SDC and the R_{LRS} values in the SDC-STO VAN indicates that the mobile V_o concentration can be tuned by Sm doping. At 30 at.% Sm, the high concentration of defects results in defect associations that lead to a decrease in the mobile oxygen vacancy concentration[150] and hence is consistent with the rise in the R_{LRS} values measured for this highest doping level. Therefore, the role of V_o concentration on R_{LRS} is clearly proven and the increase in the ionic conductivity of SDC by Sm doping is clearly an essential factor that improves the RS performances.

◆ **The influence of the growth rate**

Having confirmed the role of Sm doping ratios on the ionic channel, we next turn to discussing the influence factor of the electronic channel. We turn back to the results discussed in Chapter 4.3, where growth rate was regarded as an important factor that greatly influences the electroforming process and gives different ON/OFF ratios and endurance variance. The separate-channel model proposed above indicates that the RS performances are correlated to the effective operation of the conduction channels. To understand the influence of the growth rate on the conductive channels, we firstly seek insights from the microstructures. Recall Chapter 2.3.2, in the nucleation-and-growth mode, the increase in the growth rate results in a smaller diffusion length of the VAN phases and therefore a smaller column size is expected. This is confirmed by the AFM topography images shown in Fig. 4-31. The decrease in the column size parallels the drop in the ON/OFF ratio (Fig. 4-19) and leads to the onset of films needing electroforming (Fig. 4-19 and Table 4-1). This, at first glance, is inconsistent with the proposed model, as more vertical interfaces (and so more

electronically conductive channels) are expected when the column sizes are smaller. Therefore, the morphology alone cannot effectively determine the device's overall properties, and more fundamental structural factors should be considered.

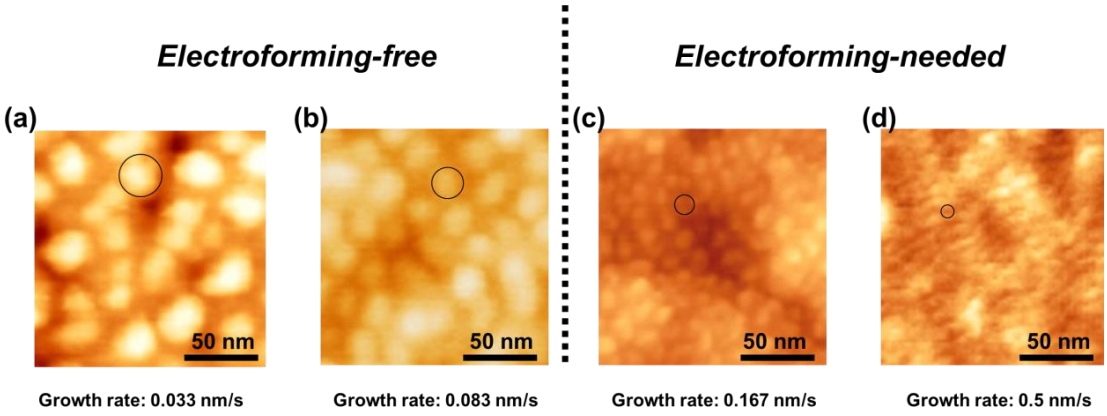

Figure 4-31. The influence of growth rate on the SDC column size in the SDC-STO VAN (Data collected by Dr. Seungho Cho).

To check the influence of growth rate on the structural quality, ω rocking curves were measured on SDC-STO VANs grown with four growth rates (from 0.033 to 0.5 nm/s). Fig. 4-32 (a) shows the full width at half maximum (FWHM) of the SDC (002) peak, which increases as the growth rate increases. As discussed in Chapter 3.2.1 (equations (3-7) to (3-12)), the peak broadening of symmetric ω scans is due to the following reasons (for more detailed analysis, also see Chapter 5.4.2)[49,50,83]:

1. The degradation of the crystallinity, arising from the increase in dislocations and misorientations, which increases the mosaic spread (or tilt). This is the primary cause for the peak broadening[50].

2. The limited lateral size (reflected as the coherent length) of the phase.

The broadening due to phases having limited size as discussed above, is due to the decrease in the column sizes measured by AFM, while broadening due to crystallinity degradation is also likely to be significant given the defects seen in the high-resolution TEM images shown in Fig. 4-32 (c) and (d): when the growth rate increases from 0.083 to 0.5 nm/s, the atomic arrangements become disordered and the phase boundaries are blurred. Therefore, the crystal structure of the SDC phase, the

STO phase and, most strikingly, the SDC-STO vertical interface, are less perfect. This means the effective pathway for both the electronic and ionic charge carriers are deteriorated due to the existence of misorientations and dislocations. As a result, as shown in Fig. 4-32 (a) and (b), the initial state resistance and the ionic conductivity both decrease with the increase in growth rates, which influence the electron carrier mobility and the mobile V_o concentrations and therefore the effective modulation of the Schottky barriers. Hence, the degraded ON/OFF ratio and the enlarged endurance variance of the SDC-STO VAN-based RRAM devices with the increase in the growth rate of the SDC-STO VAN (Fig. 4-19 and Table 4-1) are understood.

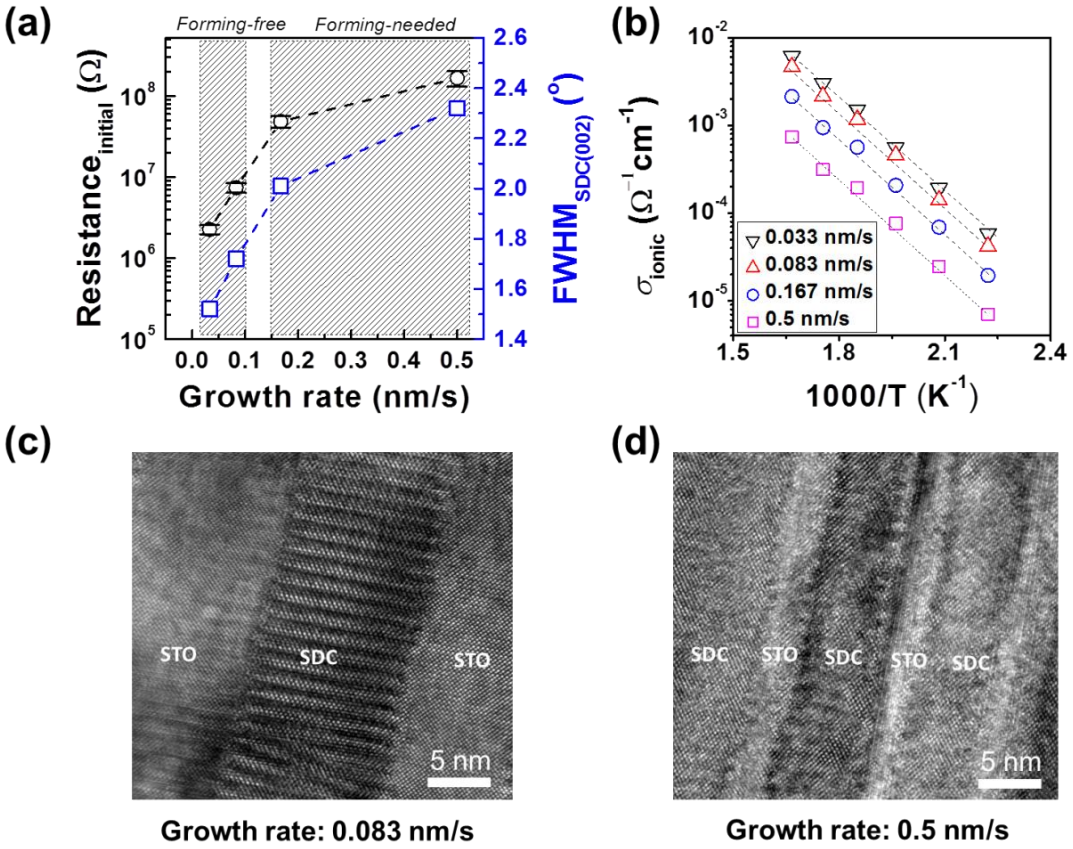

Figure 4-32. The influence of growth rate on the electronic and ionic channels. (a) The change of the resistance values of the initial state (black) and the FWHM values of SDC (002) peaks of XRD ω-rocking curves (blue) with the variation of the growth rate of the SDC-STO VANs. (b) Temperature-dependence of ionic conductivity for the SDC-STO VANs grown using different growth rates. TEM images of the SDC-STO VANs grown using two different growth rates: (c) 0.083 nm/s and (d) 0.5 nm/s. (The ω-rocking curves and the ionic conductivities were collected by Dr. Seungho Cho, and the TEM images were taken by Meng Fan and Jie Jian in Prof. Haiyan Wang's group in Purdue University, USA.)

Additionally, the formation of less-aligned electronic channels (most likely from the increased tilt) at higher growth rates (Fig. 4-32 (d)) may be the main origin for the onset of the electroforming process. This indicates that the quality of each electronic conductive channel is much more important than the quantities. In order to be electroforming-free, the electronic channels (the vertical interfaces) should be well crystallized, highly aligned and connected throughout the film thickness.

◆ The role of thickness

In the final stage, we discuss the role of thickness. As shown in Fig. 4-19 and Table 4-1, a lower thickness favors a higher ON/OFF ratio. The thickness effect is likely related to the effective electric field applied over the Schottky barrier. According to equation (2-4), the current density in the Schottky emission process is directly related to the electric field *E*. Since the SDC-STO VAN film is not a metallic conductor and the electric field is applied through the anode (Pt) and the cathode (Nb:STO), the effective electric field across the Schottky barrier is expected to be larger in a thinner film at a given voltage, especially in the LRS when the interface is more conductive. This leads to an overall decrease in the ON/OFF ratio in thicker films when other growth parameters are the same. For the electroforming-free samples, A2 and B2, it is noticeable that the average R_{HRS} values are similar (~$10^7\ \Omega$) while the average R_{LRS} of the 30 nm sample B2 (10^3-$10^4\ \Omega$ in Fig. 4-15 (d)) is over 10 times lower than that of the 150-nm sample A2 ($10^5\ \Omega$ in Fig. 4-14 (d)).

Also, the effective working voltage of sample B2 (2 V in Fig. 4-15 (b)) is much higher than that of A2 (5 V in Fig. 4-14 (c)), which is perhaps due to the longer electronic and ionic channels needing higher voltages to operate normally. Other factors, such as the change in crystal quality of the SDC ionic channels with the change in thickness, are also possible factors. More works, such as XRD and TEM, are needed for getting a quantitative analysis.

Although the thickness affects the value of the resistance, it does not change the nature of electroforming (i.e. both sample A2 and B2 are electroforming-free, while

A3, A4 and B3, B4 need electroforming), which indicates that the quality of the electronic channels, such as the tilt of the vertical interfaces suggested above, should change very little with thickness, thus the crystal quality of the electronic channel can be maintained without thickness limitation[42]. This thickness insensitivity, as described in Chapter 2.3.1, is the structural advantage of VAN.

4.6 Summary

In this work, the RS effect was systematically studied in a highly phase-separated, crystalized candidate: the SDC-STO VAN. Electroforming-free RS with an enhanced ON/OFF ratio and device durability was shown when the VAN growth rate and the thickness were low. This VAN-based RRAM device exhibited improved performance compared to plain film-based devices and other reported VAN systems.

The mechanism for the RS effect was explained using a model based on having separate ionic and electronic channels in the films. The nanoelectronic channels, which are localized at the SDC-STO vertical interfaces, are essential for the elimination of the electroforming process. They need a high crystal quality and so need to be grown using a slower growth rate. The nanoionic channels, which are localized in the ionically conductive SDC nanocolumns, provide high concentrations of mobile oxygen vacancies. The performance of the ionic channels is tunable by Sm doping due to changes in the concentration of mobile V_os. The tunable electron mobility (and ionic conductivity) in the electronic (and ionic) channel can alter the electrode/film Schottky barrier height and width, and thus the contact resistance is highly tunable by applied electric fields.

This work provides four important prospects in the RRAM field:

1. Not only has an electroforming-free device been designed, but also a practical guideline on how to eliminate electroforming is provided (by increasing the column size and crystallinity via slowing down the growth rate).

It's worth mentioning that all the reported VAN systems (Sm_2O_3-STO[122],

Nb_2O_5-$NaNbO_3$[129] and SDC-STO studied in this work[114]) show electroforming-free RS, which indicates that this is a shared characteristic in VANs. However, the comprehensive studies in this work reveal that the existence of self-assembled VAN vertical interfaces is not a sufficient condition for an electroforming-free RS. Additionally the feature size and the quality of the interfaces need to be considered.

2. A novel separate-channel model is proposed, which is promising for neuromorphics as it can emulate the spatially separated channels of bio-neurons. Such an analogy is not found in conventional memristive systems (where the ionic and electronic paths are locally indistinguishable), making the spatially separate vertical channel structure a model system for artificial cognitive systems based on solid-state ionotronics.

3. Decoupling the conductance channels makes it much easier to enhance the performance of electronic and ionic conductivity separately (in this work by decreasing the growth rate and increasing the Sm doping ratio independently). This is hard in systems with mixed channels.

4. The conduction channels in VAN-based RRAM devices are localized and self-assembled at the nano scale (~10s nm), which enables a very high storage density (10^{12} $inch^{-2}$) and avoids degradation problems in device fabrications.

Chapter 5 Tuning the physical properties of $La_{0.9}Ba_{0.1}MnO_3$ using the $La_{0.9}Ba_{0.1}MnO_3$ –CeO_2 VAN

The works in this chapter focuse on engineering the ferromagnetic insulating (FMI) and ferromagnetic metallic (FMM) properties in manganites for potential applications in MRAM, spintronic and MERAM devices. This chapter starts with a literature review on the properties, distinctions, and limitations of manganites, with stress on the lightly-doped manganite $La_{0.9}Ba_{0.1}MnO_3$ (LBMO). The advantage of tuning the manganite property using VAN is then discussed, based on which the material system is selected as the LBMO–CeO_2 VAN. In part two, the growth and characterization are presented. Part three studies on the FMI property of LBMO: via VAN strain + Ce doping in the LBMO-CeO_2 VAN, LBMO maintains the FMI property. Part four presents a new nanoengineering route to tuning the LBMO property: by tuning the lateral size of LBMO via changing the growth temperature of the LBMO: CeO_2 VAN, LBMO is tuned from a FMM to a FMI. Also, a highly tunable magnetotransport property is realized.

In this work, I made the target, grew the films, and conducted the characterization, electrical and magnetic measurements. TEM works were done by collaborators in Haiyan Wang's lab in Purdue University, USA. XPS was conducted by Dr. Weiwei Li.

5.1 Literature review

Manganites have attracted a lot of research interest due to their strong coupling between the charge, orbital, and spin degrees of freedom[151]. The interplay among ferromagnetic double-exchange (DE) interaction, super-exchange (SE) interaction, Jahn-Teller (J-T) distortion, and charge-orbital ordering (COO) interactions enable

them to exhibit ferromagnetic-paramagnetic-antiferromagnetic, charge order-disorder and metal-insulator transitions[152]. As discussed in Chapter 1 and 2, ferromagnetic insulators and ferromagnetic metals are important components in MRAM and spintronic devices and ferromagnetic insulators are important for MERAMs. Strongly correlated perovskite manganites are a fascinating family which exhibit the whole spectrum of these functionalities.

5.1.1 Manganite: structure and basic physics

◆ **Crystal structure**

The manganite family has a perovskite ABO_3–type unit cell with a generalized chemical formula of $RE_{1-x}AE_{1-x}MnO_3$, as illustrated in Fig. 5-1 (a). The A-site is occupied by the trivalent ion of rare earth (RE) metals (such as La, Pr, Nd, Sm, etc) in solid solution with divalent alkaline earth (AE) metal ions (such as Ca, Sr, Ba, etc), while the B-site is taken up by Mn ions which have smaller ionic radii than those of the A-site. The manganite crystal structure is formed by a 3-dimensional network of MnO_6 octahedra with shared O corners, as shown in Fig. 5-1 (b), and the A-site ions occupy the twelve-fold cavities in the polyhedra formed by the octahedral net.

The unique perovskite structure of manganites possesses several structural factors which closely influence the physical properties:

1. Tolerance factor: In an ideal case, the perovskite structure has a close-packed cubic unit cell. However, in real cases, it occasionally shows distortion from the cubic structure, due to the crystal field splitting of the Mn 3*d* electron orbitals, or the connective pattern of the MnO_6 octahedra[151]. The extent of lattice distortion (termed as Jahn-Teller distortion) can be evaluated by the tolerance factor defined as:

$$f = \frac{r_A + r_O}{\sqrt{2}(r_B + r_O)} \tag{5-1}$$

where r_i (i=A, B, O) represents the average ionic radius of each site. The tolerance factor is a measure of the lattice-matching between the sequential AO and BO_2 planes.

It defines the ability of the A-site cation to be accommodated into the cavities between the MnO_6 octahedra. When *f* decreases, the lattice distortion increases and the crystal structure transforms from cubic (f=1) to rhombohedral (0.96<f<1) and then to orthorhombic (f<0.96)[151]. In manganites, the tolerance factor is strongly influenced by A-site doping. Hwang *et al*. reported an empirical phase diagram in which the T_c of alkaline earth metal-doped $LaMnO_3$ increases with the increase of *f* and a peak of 370 K is reached in $La_{0.67}Sr_{0.33}MnO_3$[153].

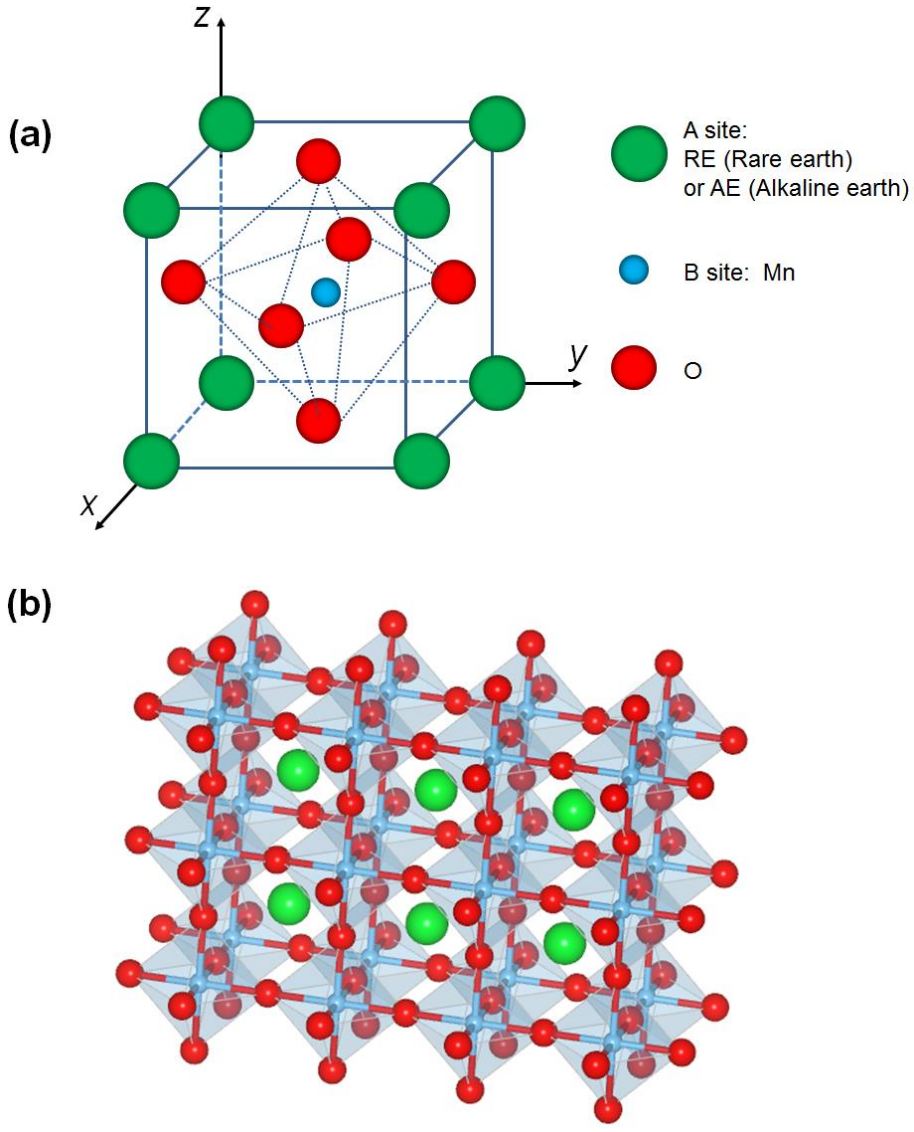

Figure 5-1. (a) The unit cell of the perovskite ABO_3 structure of manganites. (b) The 3-dimensional stacking of the MnO_6 octahedra.

2. Mn-O bond: The Mn-O ionic bond has two characteristic parameters: (1) The Mn-O-Mn bond angle θ. In a perfect cubic structure, it should be 180^o. (2) The bond length d, which is equal to $r_B + r_O$. When the manganite perovskite lattice deforms, the bond angle θ is likely to be bent and deviated from 180^o[154]. θ and d are not only influenced by A-site doping, but are also sensitive to external pressure or strains[155]. The Mn-O bond is closely related to the "one electron bandwidth" and double exchange coupling and thus the physical properties, which will be discussed later.

3. Octahedral rotation: The octahedra in manganites are connected through the shared oxygen corners, and this enables them to have freedom of connective rotation in the presence of high pressure (physical pressure) in bulk form. When grown into epitaxial thin films, the octahedra patterns are influenced by the epitaxial strain or crystal symmetry mismatch in a more complex way. Although strain has been used for interfacial engineering for a long time, its long-range nature makes it less informative at the atomic scale. This brings about more microscopic-level studies such as interfacial oxygen octahedral coupling (OOC)[156]: to ensure the corner connectivity of octahedra across the substrate/film interface, the magnitude and pattern of the substrate octahedral rotation can be transferred to the film lattice, thus influencing the crystal symmetry and physical properties of the films on a much smaller scale.

◆ **Electronic band structure and Mn 3*d* orbitals**

The structural parameters mentioned above are closely related to the manganite electronic band structure. Band structure is determined by two important parameters: one is the "one-electron bandwidth" W_a (which, differs from the band gap E_g, is another important parameter in manganites), another is the band filling (which correlates to the density of states near the Fermi Level)[151]. These parameters are determined by structural and compositional factors, which in turn strongly influence the exchange interactions and thus the physical properties.

In hole-doped manganites, the active physical properties are determined by the feature of the Mn 3*d* electron band, which is influenced by the five degenerated

orbitals. The degeneracy is a result of the strong coupling between the spin, charge and orbital degrees of freedom. The Mn ions in perovskite manganites are in octahedral coordination and due to the crystal field, the Mn 3*d* electron orbital degeneracy is partially lifted into two higher-energy e_g states and three lower-energy t_{2g} states[151]. The t_{2g} electrons are more localized and stabilized by the crystal field because of less hybridization with the O 2*p* states, whereas the e_g electrons can be itinerant when electron vacancies or holes are created (e.g. by inducing Mn^{4+} through doping), hence acting as the conduction electrons[157]. In doped manganites, Jahn-Teller distortion further lifts the e_g states into plane-type (such as x^2-y^2) and rod-type (such as $3z^2$-r^2) orbitals, and the t_{2g} states into *xy*, *yz*, *zx* orbitals[158], as shown in Fig. 5-2 (taking Mn^{3+} as an example).

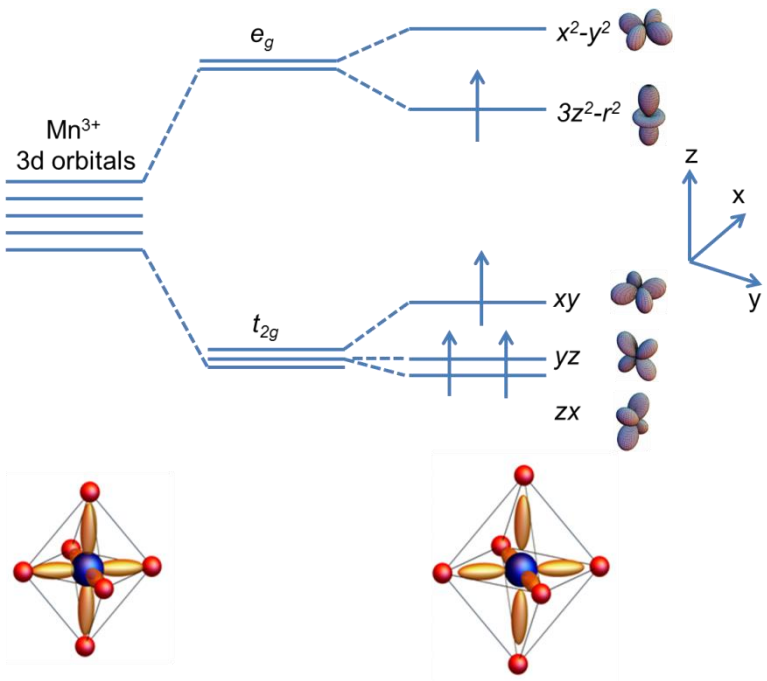

Figure 5-2. The crystal field splitting of the 3*d* e_g electron orbitals in a Mn^{3+} ion under an axial elongation of the MnO_6 octahedron.

The occupancy of 3*d* electron orbitals, which is a result of complex structural interplays, influences the physical properties. Starting from the parent phase of the Lanthanum manganites, $LaMnO_3$, the A-site is undoped and therefore the B-site Mn has a single valence of +3. The collective Jahn-Teller distortion strongly influences

the 3*d* orbital occupancy of $LaMnO_3$ and gives rise to the ordering of orbitals[159]. The orbital ordering results in anisotropic electron-transfer interaction, which favors or disfavors ferromagnetic (FM) or antiferromagnetic (AFM) interactions in an orbital direction-dependent manner[158]. In $LaMnO_3$, $3x^2$-r^2 and $3y^2$-r^2 orbitals order alternatively in the in-plane direction forming FM coupling within the plane, while AFM interactions exist between the planes. The resulting spin ordering is called an A-type AFM configuration, and therefore $LaMnO_3$ is an AFM insulator. With hole doping, the Jahn-Teller distortion is diminished, and FM interactions emerge and the orbital state tends to be disordered. The resulting orbital occupancy, either mixed-type or preferential occupancy, depends on the way of lattice deformation[158,160].

Orbital occupancy determines the overlap between Mn 3*d* and O 2*p* orbitals which influences the one electron bandwidth and transfer integral between the neighboring Mn atoms and thus the exchange interactions[158], as discussed later.

◆ **Exchange interactions**

Double exchange (DE) coupling. The coexistence of ferromagnetism and metallicity (FMM) in hole-doped manganite is interpreted by the Mn^{3+}-O-Mn^{4+} DE coupling as shown previously in Fig. 2-8 (b). The DE coupling is closely related to various kinds of structural and compositional changes of manganites:

1. Mn-O bond length/angle. The mixed valence of Mn gives rise to electrons which can hop between adjacent Mn sites (*i* and *j*) through the hybridization of Mn 3*d* and O 2*p* orbitals. The effective transfer integral t_{ij}, which is directly related to the "one electron bandwidth" W_a[151], is determined by the relative direction of the two spins (illustrated as θ_{ij} in Fig. 5-3 (a)) and the distance between two spins (illustrated as *a* in Fig. 5-3 (a)). An empirical formula of t_{ij} is expressed as[161]:

$$t_{ij} \propto W_a \propto d^{-3.5}\sin(\theta/2) \tag{5-2}$$

where *d* is the bond length ($a=2d\sin(\theta/2)$) and θ is the bond angle ($\theta=\pi-\theta_{ij}$, where θ_{ij} is the angle between the adjacent spins). It has been experimentally proven that a larger θ or a smaller *d* result in a larger W_a and t_{ij} and therefore a higher ferromagnetic

T_c[155]. θ and d are closely related to the lattice parameters.

2. 3d e_g orbital occupancy. The transfer integral in doped manganites is also determined by the overlap of the Mn 3d orbitals with the O 2p orbital, and the extent of the overlap is anisotropic[158]. For example, as illustrated in Fig. 5-3 (b), the overlap between the d_{x2-y2} and p_x (p_y) orbitals is maximized, due to the similar symmetry with respect to the holding in the xy plane, and therefore the electron hopping is favored in the xy plane, whereas the hopping of d_{3z2-r2} electrons are disfavored in the xy plane due to the lack of effective orbital overlap. Therefore, the preferential occupancy of the Mn 3d orbitals is another important factor for the modification of spin alignment and charge transport.

Strain is one effective external force to alter the orbital occupancy in manganites, thus tailoring the electronic/magnetic properties[40,160,162,163]. It has been reported that in $La_{0.7}Sr_{0.3}MnO_3$, an in-plane tension (with $c<a$) favors the occupancy of the plane-type x^2-y^2 orbital while a compressive strain (with $c>a$) favors the rod-type $3z^2$-r^2 orbital[162].

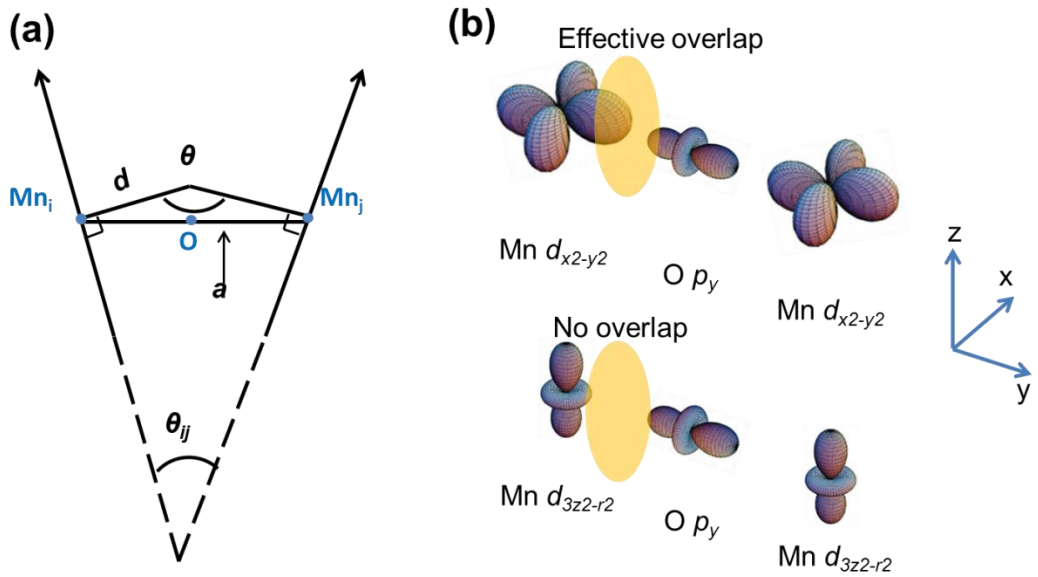

Figure 5-3. (a) Illustration of the Mn-O-Mn bond angle (θ) and length (d) in the DE coupling. (b) The overlap between the different Mn 3d orbitals and the O $2p$ orbitals.

3. Hole carrier concentration. The above two factors reflect the structural aspects and influence the bandwidth. As a compositional factor, the hole carrier concentration

(determined by the ratio of Mn^{4+}/Mn^{3+}) essentially influences the "band filling" and hence the effective strength of the DE coupling[151]. The filling of the conduction band is given as n=1-x, where x is linked to the alkaline metal doping concentration[157].

There are certainly other factors that influence the DE coupling, which are beyond the scope of this work and will not be discussed in detail.

Superexchange (SE) coupling. Unlike DE coupling, SE interaction exists between Mn ions with equal valences (as previously shown in Fig. 2-8 (a)), which can give either ferromagnetic or antiferromagnetic coupling. The corresponding SE interactions depend on the orbital configuration and follow the Goodenough–Kanamori rules[164]. The Mn^{3+}-O-Mn^{3+} coupling usually leads to an antiferromagnetic insulating state, with the undoped $LaMnO_3$ being an example.

DE alone is not sufficient to explain the rich physical properties of manganites. In higher or optimum doped $LaMnO_3$, DE coupling is more dominant. When the doping level is low, Mn^{3+} ions take a larger part of the B-site, and therefore there is a strong competition between the DE (Mn^{3+}-O-Mn^{4+}, giving rise to FMM) and SE (Mn^{3+}-O-Mn^{3+}, giving rise to FMI) couplings. The FMI property is one result of such competition[165,166]. Besides, since the perovskite manganites have strong correlation between the spin, orbital, and charge degrees of freedom, there are certainly other important factors, such as the electron-lattice interaction (with Jahn–Teller distortion being dominant), the intersite exchange interaction between the e_g orbitals (orbital ordering) and the intrasite/intersite Coulomb repulsions among the e_g electrons[151]. The overall magnetic and transport properties are a result of complex competitions between these interactions.

◆ Magnetotransport

In manganites, the magnetoresistance can be divided into intrinsic and extrinsic based on the origin. Intrinsic MR is also termed as Colossal Magnetoresistance (CMR). It is closely related to the interplay between the DE coupling and the Jahn–Teller distortion, both of which are sensitive to the application of a magnetic field. Since the

magnetic field can effectively suppress the spin fluctuations and change the paramagnetic-ferromagnetic phase separations/transitions near the T_c, the CMR usually shows a maximum around this temperature[167,168], i.e. the largest drop of resistance under a magnetic field, due to the alignment of Mn^{3+} and Mn^{4+} spins which favors electron hopping.

Some manganites are half-metals, where the conduction band for one spin orientation is partially filled while a gap exists in the density of states for the opposite spin orientation. This spin polarization enables them to behave like a conductor to electrons for one spin orientation while acting as an insulator to electrons of the opposite spin direction, which can induce extrinsic MR whose maximum does not rely on the T_c. In polycrystalline materials or composite systems, the existence of phase boundary or grain boundary acting as thin tunneling barriers assists in spin-polarized electron tunneling, which induces tunneling magnetoresistance (TMR)[168]. In some cases, grain boundaries can induce large TMR at small magnetic fields (<0.1 T), which is termed as low-field MR (LFMR)[169]. Giant magnetoresistance (GMR) is another kind of extrinsic MR existing in a ferromagnetic metal/non-magnetic metal/ferromagnetic metal configuration, and the mechanism relies on spin-dependent scattering[168]. In both TMR and GMR, the electrical resistance of the system is highly dependent on the relative spin alignment between the two adjacent ferromagnetic parts, which can be controlled by the application of a magnetic field.

5.1.2 Distinctions of lightly-doped manganites

The higher or optimum-doped manganites are well-known for their FMM property and the high T_c near or above room temperature. They are a widely-used source of spin-polarized carriers in spintronic and MRAM devices[170].

In spintronic devices, FMIs have also gained more interest. When doped with a low concentration of alkaline metal, it is known that certain classes of manganites in bulk

form show the coexistence of ferromagnetism and insulating conductivity. As discussed previously in Chapter 2.2.2, FMI is required in spin filter devices, MRAMs with reduced power consumption or MERAM devices[171,172]. Indeed, at practical operating temperatures (e.g. above 77 K of liquid N_2), the coexistence of ferromagnetism and insulating conductivity is very rare in known materials[171,173]. Examples of FMIs are $SeCuO_3$ (ferromagnetic Curie temperature, T_c ~25 K)[174], and EuO (T_c~77 K)[175], but their relatively low T_cs hinder their application. Double perovskites (such as La_2CoMnO_6, T_c~220 K), ferrites (such as $NiFe_2O_4$, T_c>300K) and garnets (such as $Bi_3Fe_5O_{12}$, T_c>300 K) have high T_cs[176–178], but their complex structures, difficult growth conditions or moderate conductivity in thin film form make them problematic. In comparison, hole-doped manganites, especially the $La_{1-x}A_xMnO_3$ (A=Ca, Sr or Ba) family, have perovskite structures which are structurally compatible with widely available perovskite substrates of $SrTiO_3$-buffered Si, and other perovskite oxides with wide-ranging functionalities for multifunctional devices[179]. Fig. 5-4 shows the phase diagrams of $La_{1-x}A_xMnO_3$ (A=Ca, Sr or Ba). Lightly doped $La_{1-x}A_xMnO_3$ (x<0.2) in bulk form has FMI properties with a T_c higher than the liquid N_2 temperature[151]. The mechanism for the coexistence of ferromagnetism and insulating conductivity in lightly doped manganites is still controversial. The competition between the DE (which gives metallicity) and SE (which gives insulating conductivity), and the ordering of charge/orbitals are considered as two main causes[152,165,180–182].

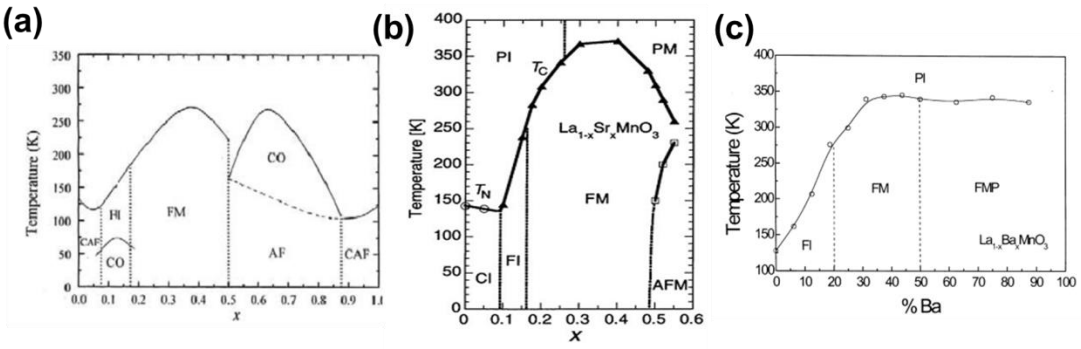

Figure 5-4. Phase diagrams of (a) $La_{1-x}Ca_xMnO_3$[183], (b) $La_{1-x}Sr_xMnO_3$[151] and (c) $La_{1-x}Ba_xMnO_3$[184] (CAF=canted antiferromagnetic, CO=charge-ordered insulating, FI=ferromagnetic insulating, FM=ferromagnetic metallic, AF or AFM=antiferromagnetic, PI=paramagnetic insulating, CI=spin-canted insulating, PM=paramagnetic metallic, FMP= ferromagnetic multiphase.)

Lightly doped $La_{1-x}A_xMnO_3$ lies in a narrow region where the physical properties are very sensitive to structural and compositional perturbations. For example, it has been reported that a 0.65% in-plane tensile strain enhances the T_c of $La_{0.9}Ba_{0.1}MnO_3$ by almost 100 K[185]. A similar case has been reported in lightly doped $La_{1-x}Sr_xMnO_3$[152]. It is also clearly shown in Fig. 5-4 that the T_c of the $La_{1-x}A_xMnO_3$ family is more sensitive to compositional change in the lightly doped region. This indicates that the physical property of lightly-doped manganites can be highly tunable under external forces, including but not limited to strains and compositional modulations. The tunability of functionality in lightly doped manganites, as indicated by the phase diagram, can range from a FMI to a FMM, which can expand their application capability in MRAM, spintronic or MERAM devices.

5.1.3 Limitations in lightly-doped manganite plain films

Currently, the application of lightly-doped manganites in thin film devices is limited, a key reason being that the desired FMI bulk properties is modified, deteriorated or even vanish when grown on $SrTiO_3$ or other substrates[163,185,186], and an anomalous metallic behavior with an insulator-to-metal (*I-M*) transition is observed over a wide range of temperatures depending on the growth and heat treatment process. This

anomaly exists even above the relaxation thickness (>100 nm). The reason for the modified properties of lightly-doped $La_{1-x}A_xMnO_3$ thin films is controversial, with epitaxial strain (modification of the Mn-O bond length/angle and orbital occupancy being part of this), electronic reconstruction, and non-stoichiometry all claimed to be possible origins[152,161,185–189]. Indeed, the lack of ability to translate bulk properties to thin films is well-known in the broad range of manganite compositions[40,152], and in many other functional perovskites (including ferroelectrics and superconductors) too[190,191], which are caused by the existence of the substrate-induced "dead layer" effect or other reasons[192–195]. Although progress has been made in reducing the so-called "dead layer" thickness and realizing bulk-like FMM properties in higher doped manganites or other perovskite oxides via delicate design[196,197], the inability to achieve insulating performance in lightly doped manganites still remains.

In manganite thin films in general, strain is controlled only by the substrate, i.e. by the in-plane (*ip*) strain from epitaxial constraints, and the out-of-plane (*op*) strain is modified as a consequence of elastic effects. The strain uniformity tends to deteriorate and it relaxes gradually in a variety of ways as the film thickens. Since the formation energy of point defects is lower than misfit dislocations, and the octahedra in perovskite oxides have high freedom of tilt/rotation, relaxation can occur by other phases forming, lattice modulation, or by cation/oxygen vacancy generation[47,198–200]. Many of these problems are uncontrollable, which add burdens to tuning the functionality of manganites when grown into plain thin films. The modified properties of thin film manganites are a serious problem in terms of their device applications.

5.1.4 The advantage of VAN for tuning the manganite property

As discussed previously in Chapter 2, VAN has provided new routes to tuning the physical properties of heteroepitaxial oxides[38,48], e.g. simultaneous tuning of both the *op* and *ip* strain states of a softer matrix phase by a stiff nanocolumn phase with a substrate to vertical strain transition above a certain thickness[40,44], and an enhanced strain homogeneity without thickness limitation[42]. Strain tunability and uniformity

provide possible solutions to the above-mentioned problems in manganite thin films, i.e. to tune the properties and restore some of the FMI bulk characteristics of lightly-doped manganites, to enhance the strain homogeneity, and to engineer the functionalities of manganites without the influence of relaxation or substrate modification.

It is known that apart from strain and compositional variation, physical properties of manganites are also sensitive to "dimension cross-over"[192–195] (i.e. a variation in the film dimension which induces a modification of physical properties such as reduction of T_c or emergence of new electronic states when it is very thin, due to orbital reconstruction/interfacial oxygen octahedral coupling, etc). The tunable growth kinetics in VANs, as mentioned in Chapter 2.3.2, make it possible to tune the dimensionality of manganites through self-assembly, rather than by the time-consuming artificial design. By controlling the self-assembly kinetics, the tuning of properties can be elaborated by will. This tuning is controllable, which is different from and superior to the uncontrollable structural modulation in plain films.

5.1.5 Selection of materials

Lightly-doped manganites are the main focus of this work, not only because of the intriguing FMI property but also for their sensitivity to external stimuli which results in highly tunable physical properties (i.e. from FMI to FMM).

Compared to $La_{1-x}Sr_xMnO_3$ and $La_{1-x}Ca_xMnO_3$, lightly doped $La_{1-x}Ba_xMnO_3$ has a higher T_c[151,163,183,184]. For example, T_c is 185 K for x = 0.1, whereas it is $\leqslant$150 K for the same x value in $La_{1-x}Sr_xMnO_3$ and $La_{1-x}Ca_xMnO_3$ (as shown in Fig. 5-4). High spin polarization has also been reported in $La_{0.9}Ba_{0.1}MnO_3$[201] which makes it a candidate material for spintronics studies. Therefore, $La_{0.9}Ba_{0.1}MnO_3$ (denoted as LBMO hereafter) was selected as the matrix phase of the VAN. $La_{0.9}Ba_{0.1}MnO_3$ has an orthorhombic structure in bulk (space group Pnma), and the reported pseudocubic lattice constants in literature are close to that of the STO substrate (~3.905 Å[185,186,202–

[205]) but varies in a range from 3.88 to 3.92 Å, due to the easy existence of non-stoichiometry.

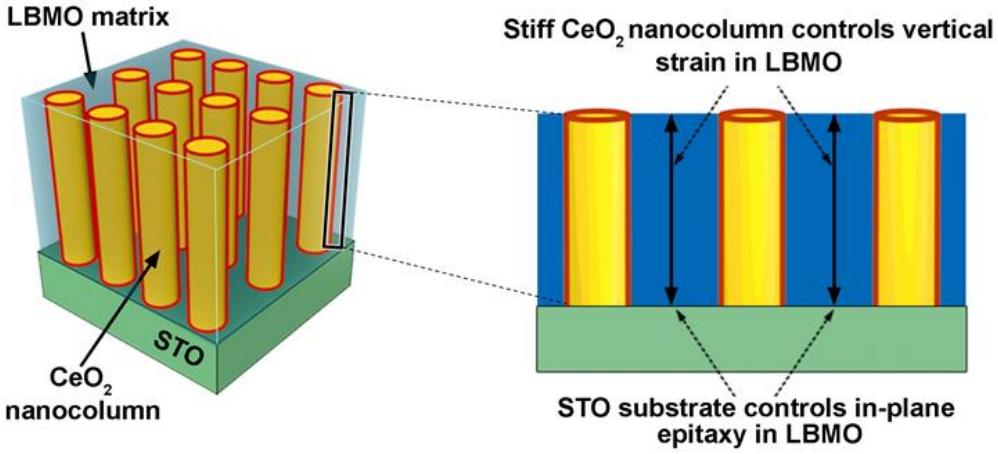

Figure 5-5. Schematic diagram for the role of strain tuning in a $La_{0.9}Ba_{0.1}MnO_3$ (LBMO)-CeO_2 VAN.

CeO_2 was selected as the strain controlling phase for LBMO, as CeO_2 is stiffer than LBMO (the Young's Modulus E_{CeO_2}=220–240 GPa[206,207], while the reported E for manganite is ~120–140 GPa[208,209,210]). Thus, in the VAN films, CeO_2 is predicted to control the strain state of LBMO (as shown in Fig. 5-5) as reported in other similar systems (e.g. perovskite manganite-CeO_2 combinations)[43]. The addition of CeO_2 is also deemed to be beneficial from a doping point of view: Ce is known to substitute on the A (La) site in La manganites[211], this being promoted by the known cation deficiency of the La site[212] (as discussed later in Chapter 5.3). For more detailed structural properties of CeO_2, see Chapter 4.1.5.

5.2 Growth and characterization

5.2.1 Making the target

The targets for the VAN and reference plain films were made using the procedure shown in Fig. 3-1. Fig. 5-6 shows the XRD 2θ-ω scans of the LBMO single phase and LBMO-CeO_2 (molar ratio 1:1) composite target. All the diffraction peaks belong to

either CeO_2 or LBMO, indicating high-quality polycrystalline phases.

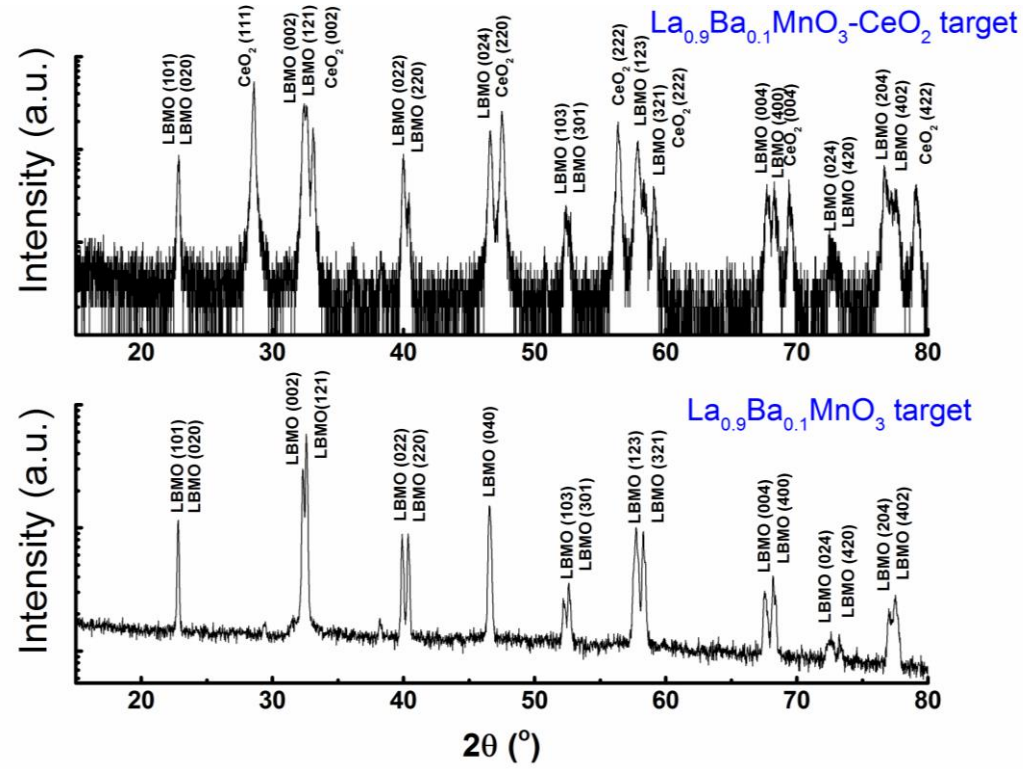

Figure 5-6. XRD 2θ-ω scans of the $La_{0.9}Ba_{0.1}MnO_3$-CeO_2 composite target and the $La_{0.9}Ba_{0.1}MnO_3$ single-phase target.

5.2.2 Growth of the $La_{0.9}Ba_{0.1}MnO_3$–CeO_2 VAN films

$La_{0.9}Ba_{0.1}MnO_3$ (LBMO)-CeO_2 (molar ratio 1:1) VAN (denoted as NC) films and reference $La_{0.9}Ba_{0.1}MnO_3$ plain films (denoted as PF) were grown on single crystalline $SrTiO_3$ (001) substrates via a one-step process by pulsed laser deposition (PLD) using the same composite target. During deposition, the oxygen partial pressure was maintained at 0.2 mbar. The repetition rate and laser fluency were 1 Hz and 1 J/cm^2, respectively. For studies of thickness influence in Chapter 5.3, the growth temperature was kept at 720℃ and the film thickness varied. For temperature-dependent studies in Chapter 5.4, the growth temperature was varied from 690℃ to 800℃ while the film thickness was kept at around 45 nm. After deposition, the samples were cooled down to room temperature under an oxygen pressure of 0.4 atm with a cooling rate of 10℃/min.

The TEM and XRD results of a 46 nm thick LBMO-CeO_2 NC film grown at 720℃ are shown in Fig. 5-7. Clear phase separation, high crystalline quality and epitaxy are observed in the TEM cross section and plan view images in Fig. 5-7 (a) and (b). The CeO_2 nanocolumns (average radius 6–8 nm) are densely distributed within a continuous LBMO matrix, and the average spacing between the CeO_2 nanocolumns is only ~3–6 nm. This structure is common when a combination of manganite-binary oxide are coherently grown on a perovskite substrate[213].

Fig. 5-7 (c) shows the XRD 2θ-ω scan of the NC film (and a 42 nm LBMO PF grown under the same conditions as a reference). The thickness fringes of both the LBMO and CeO_2 phases are shown in the NC indicative of a high-quality epitaxy and smooth surface of both phases on the STO substrate. The thickness fringe of the NC around the STO (001) peak was simulated using the converted ω-2θ scan by Lee's kinematic program[214] (as shown in Fig. 5-7 (d), for the fringe only), where an average thickness of 46 nm for the LBMO phase gives the best fit. This is in good agreement with the TEM result in Fig. 5-7 (a), indicating the single-crystalline nature of the LBMO (001) phase throughout the film thickness. Apart from the LBMO (00*l*) phase, there is also a weak peak at 39.4^o which is likely from the LBMO (111) phase[66].

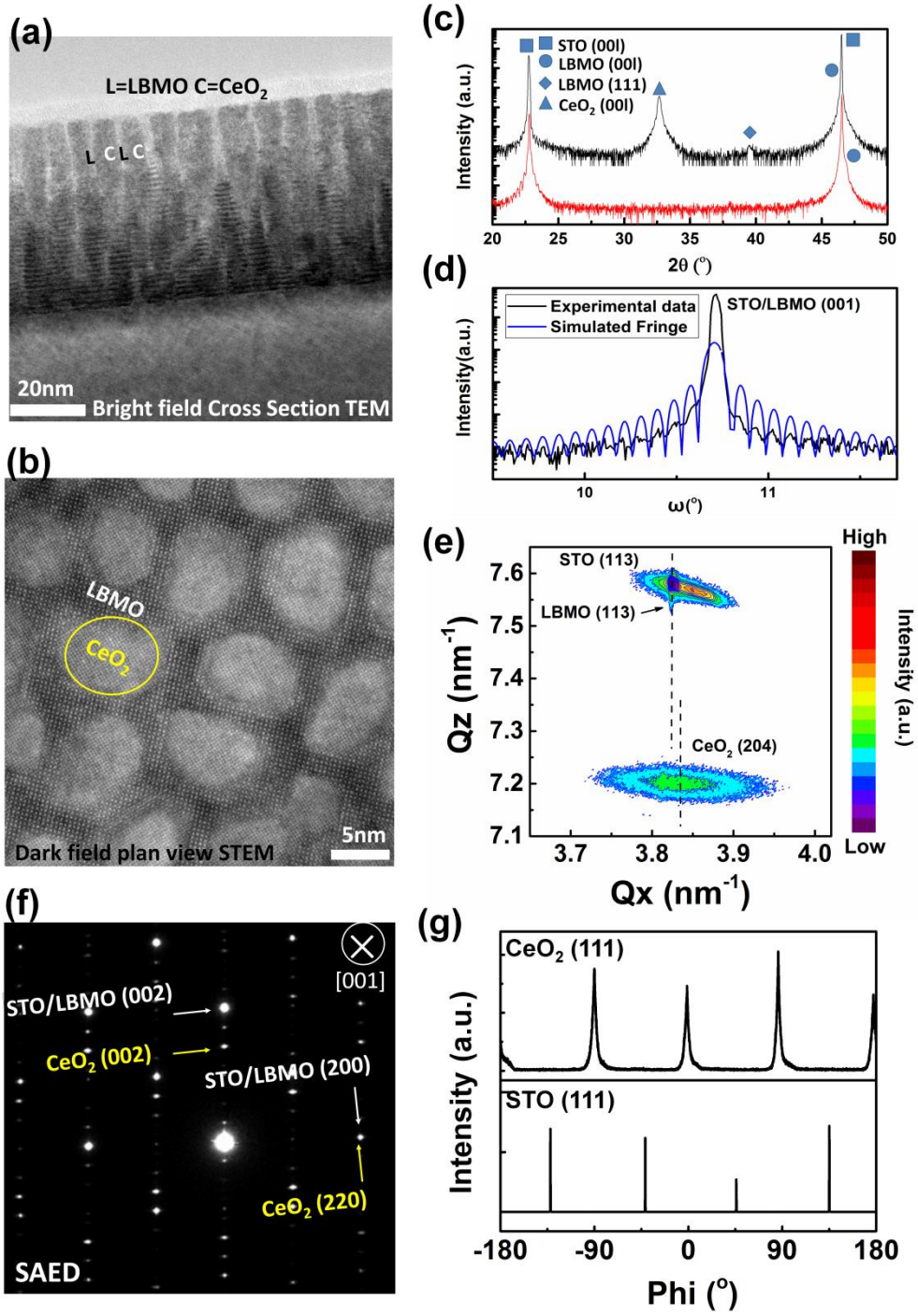

Figure 5-7. Structural characterization of a LBMO-CeO_2 VAN film grown at 720℃: (a) Bright-field TEM cross-section image. (b) High-resolution high angle annular dark-field plan view STEM image. (c) XRD 2θ-ω scan (the 2θ-ω scan of a 42-nm-thick LBMO plain film is included as a reference). (d) Thickness fringe simulation around the (001) peak (using the converted ω-2θ scan). (e) Reciprocal space map (RSM) around STO (113). (f) Selected area electron diffraction (SAED) index. (g) Phi scans of the STO (111) and the CeO_2 (111). (TEM images taken by Xing Sun and Jie Jian in Prof. Haiyan Wang's group, Purdue University, USA)

Fig. 5-7 (e) shows the reciprocal space map (RSM) (around STO (113)) of the NC film, which confirms the coexistence of the LBMO and CeO_2 phases. The high-intensity tail on the right of the STO (113) peak comes from the imperfections from the STO substrate (as the substrates from the same batch also show this peak), and the tail at the bottom of the STO (113) peaks belongs to the LBMO (113) phase (as confirmed by the 2θ-ω scans shown later in Fig. 5-15 (d)), indicating that the LBMO phase is fully strained on the STO substrate. The CeO_2 phase is relaxed, as indicated by the non-overlapping diffraction peak center of the CeO_2 (204) phase with respect to the STO (113) phase (illustrated by dashed lines).

The selected area electron diffraction (SAED) pattern is shown in Fig. 5-7 (f). It is noticeable that the diffraction spot of STO (002) is broadened compared to that of the STO single crystal, indicative of the close overlap of the LBMO and STO *op* diffraction spots because of their similar lattice constants.

The phi scans of the STO (111) and CeO_2 (111) peaks are shown in Fig. 5-7 (g), which indicate a 45^o *ip* rotation of the CeO_2 phase with respect to the STO substrate, as illustrated in Fig. 5-8 (a). As reported previously, the *ip* lattice constant of CeO_2 can be matched with STO after this 45^o rotation[72,138,139]. This crystallographic matching relationship is confirmed by the SAED pattern, and thus the *ip* epitaxy relationship is determined to be STO [100]//LBMO [100]//CeO_2 [110].

By using the SAED pattern and the XRD results, the *op* epitaxy relationship is determined to be STO (001)//LBMO (001)//SDC (001), as illustrated in Fig. 5-8 (b).

More detailed and systematic structural analysis will be presented later in Chapter 5.3 and 5.4 as a part of the discussion.

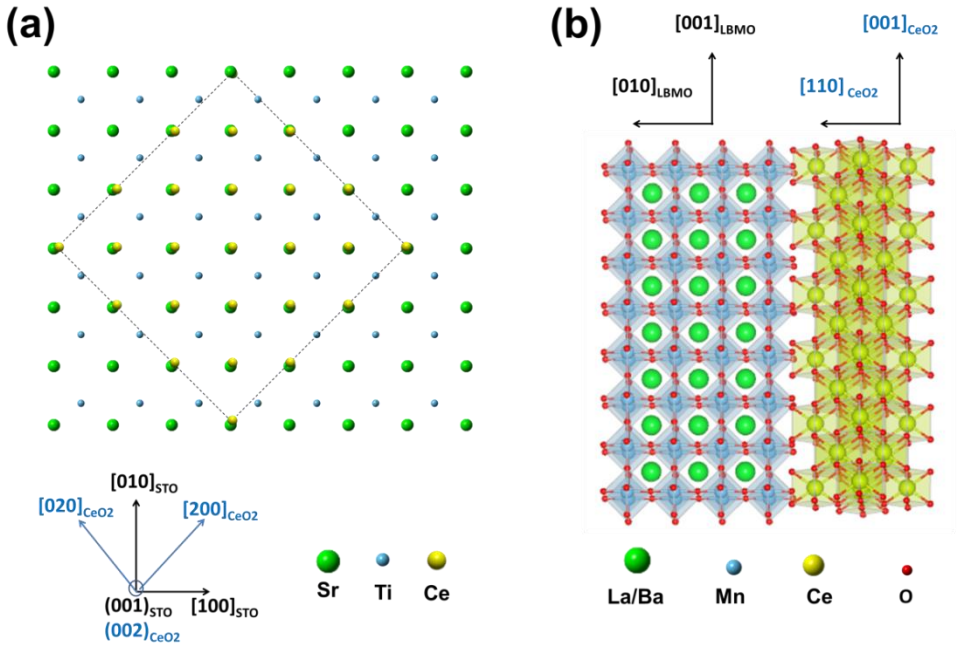

Figure 5-8. (a) In-plane crystallographic matching between the CeO_2 phase and the STO substrate. (b) Out-of-plane crystallographic matching between the LBMO and CeO_2 phase.

Having obtained the basic crystallographic information, comprehensive growth studies were followed. The influences of post-annealing, thickness, and growth temperature will be presented in the following discussions.

1. The influence of high-temperature annealing. High-temperature post-annealing was used in the growth of plain manganite thin films (mainly higher-doped ones) in many works to improve the stoichiometry and crystallization. In this work, post-annealing was conducted (900℃, 10 h) on the 46 nm LBMO-CeO_2 VAN grown at 720℃, and the plan-view TEM images before and after annealing are shown in Fig. 5-9. The morphology of the nanocolumns evolves from a round shape to a maze-like shape, and the phase boundary is blurred after annealing.

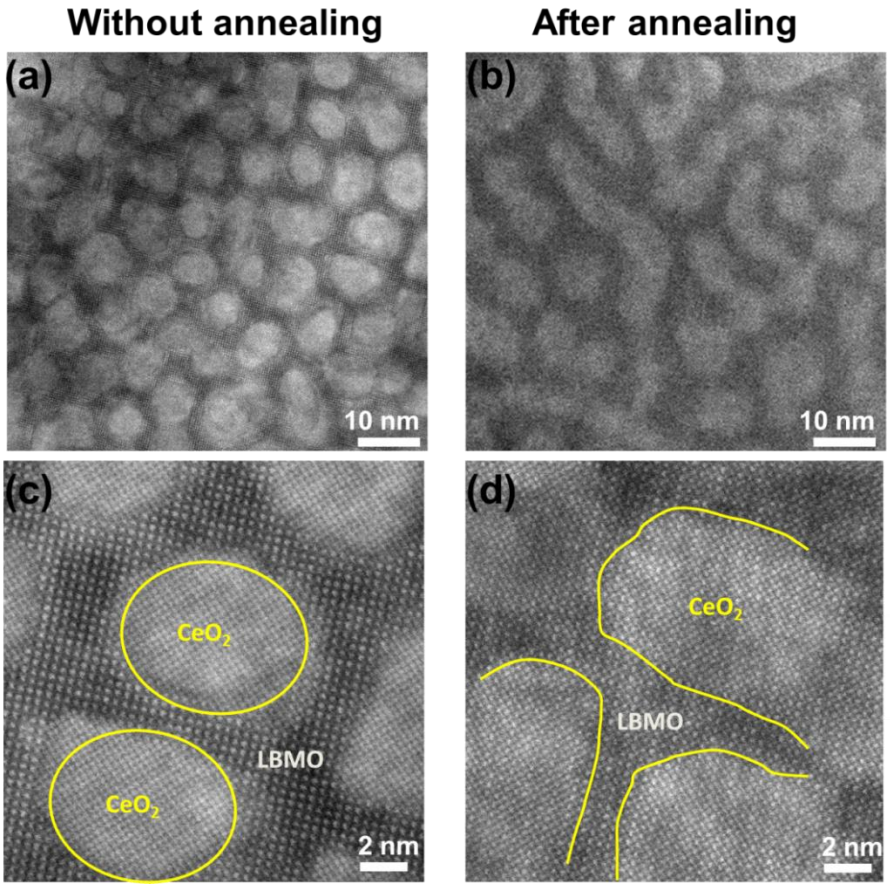

Figure 5-9. Influence of annealing on the plan-view TEM microstructure of the LBMO-CeO_2 VAN: (a) and (c) before annealing, (b) and (d) after annealing. (TEM images taken by Xing Sun and Jie Jian in Prof. Haiyan Wang's group, Purdue University, USA)

Fig. 5-10 shows a comparison of the XRD 2θ-ω scans. Although annealing can enhance the crystallinity (as the LBMO peak is sharpened after annealing), impurity phases are brought in (e.g. an unknown diffraction peak is observed at 65^o after annealing). The overall rightward shift of the diffraction peaks (as indicated by the dotted arrows) is a result of excessive oxygen coming into the LBMO and CeO_2 lattices. As discussed later, this excessive oxygen, which results in cation-deficiency, is also unwanted for the lightly doped $La_{0.9}Ba_{0.1}MnO_3$.

In short, the results above suggest that high-temperature annealing is not a proper treatment for the phase separation of the LBMO-CeO_2 VAN.

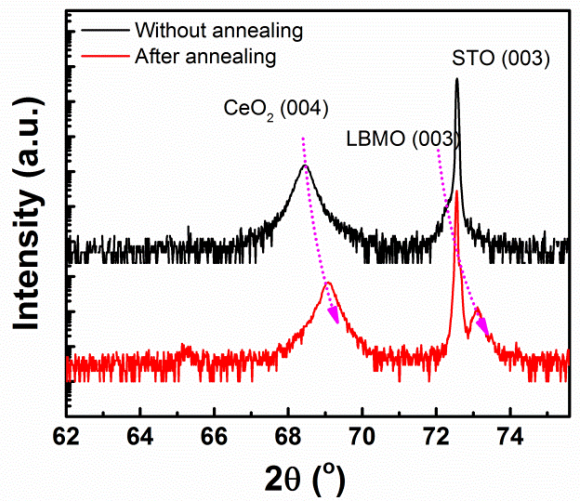

Figure 5-10. XRD *2θ-ω* scans for the LBMO-CeO_2 VAN before and after annealing.

2. The influence of thickness. With increasing thickness, substrate to vertical strain transition is observed, and the details will be described in Chapter 5.3.

3. The influence of growth temperature. With changes in the growth temperature, the CeO_2 column size is tuned, which will be discussed in Chapter 5.4.

5.3 Maintaining the ferromagnetic insulating property of LBMO in thin films through VAN doping+strain

In this section, we firstly show that the ferromagnetic insulating property of $La_{0.9}Ba_{0.1}MnO_3$ (LBMO) is achieved in the LBMO-CeO_2 VAN, and then discuss the compositional/structural origins. The films in this section were all grown at 720℃.

5.3.1 Maintaining the FMI property in the LBMO–CeO_2 VAN

A series of LBMO PF and LBMO-CeO_2 NC films were made, and the thickness varied from 12 to >100 nm. Above ~50 nm, the film properties did not show further marked changes in functional performance but instead long time deposition may cause thermal annealing or strain relaxations. Hence, we mainly focus on the change in film properties up to ~50 nm.

Fig. 5-11 (a) shows resistance vs. temperature (*R-T*) curves for two LBMO PFs. An insulator-to-metal (*I-M*) transition is present in the PF, and when the thickness is increased from 21 to 42 nm, the *I-M* transition temperature, T_M, remains almost constant at around 220-223 K (with a slight increase of 3 K), as shown by the arrow. This is consistent with the general trend in manganite thin films that relaxation occurs above a certain thickness, which leads to an almost constant T_M (T_c)[196]. The existence of metallicity in the thicker PF indicates that, apart from the strain, there is another cause of the metallicity in the PF, which is likely non-stoichiometry.

The *I-M* transition (and the corresponding paramagnetic-ferromagnetic transition discussed later) occurs as a result of the DE coupling between Mn^{3+} and Mn^{4+} mediated by O[23]. The DE coupling in doped manganites is influenced by both doping and strain[179]. Charge-orbital ordering (COO), which is characteristic of lightly doped manganites[182], occurs at a much lower temperature T_{COO}. This brings about the observed resistance upturn in the PFs in Fig. 5-11 (a). The increase in T_{COO} with the

increase in thickness: from 120 K (21 nm) to 155 K (42 nm) can be correlated to the change in the Jahn-Teller distortion caused by the change in the strain state[182].

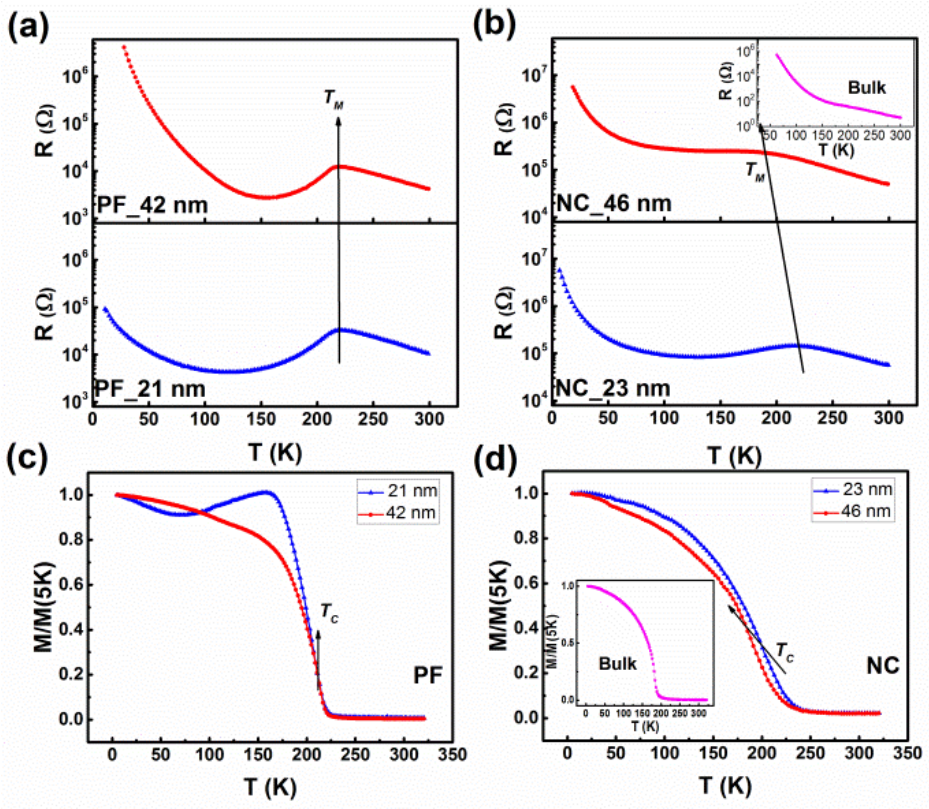

Figure 5-11. Thickness dependence of the resistance vs. temperature (*R*-*T*) curves of (a) LBMO plain films (PFs) and (b) LBMO-CeO_2 nanocomposite (NC) films. The *R*-*T* curve for the LBMO bulk is also shown as a comparison. Thickness dependence of the field cooling *M*-*T* curves of (c) the LBMO PFs and (d) the LBMO-CeO_2 NC films. *M*-*T* curve for the LBMO bulk target is also shown for comparison. The applied field was 200 Oe.

The resistance in Fig. 5-11 is not converted to resistivity using the methods discussed in Chapter 3.4.2 considering the different nature of conductive paths (and different cross section areas for current flow) between the PF and NC. The *R*-*T* plot for two NC films and the $La_{0.9}Ba_{0.1}MnO_3$ bulk target (inset) are shown in Fig. 5-11 (b). The LBMO bulk is insulating, as expected. A thickness dependence is found in the NC films: a lower thickness ($\leqslant$23 nm) favors a more metallic transport property while a larger thickness NC film ($\geqslant$46 nm) gives insulating behavior without any metallicity. The insulating and metallic behaviors are defined based on the slope of d*R*/d*T*, i.e. a negative slope indicates an insulating behavior and a positive slope a

metallic behavior. Since it is hard to determine the *I-M* transition temperature for the 46 nm NC, the T_M is estimated by extrapolating the inflection point in the *R-T* curve (the trend is shown by the arrow).

The temperature-dependent magnetization (*M-T*) data for the PF and NC are shown in Fig. 5-11 (c) and (d). The applied magnetic field was 200 Oe and it was applied parallel to the substrate plane. The T_c, determined at the temperature where the d*M*/d*T* reaches the maximum, changes in a similar way as T_M: the T_c of PF remains almost constant at around 212 K (with a slight increase of 3 K) while the T_c of NC decreases from 201 K to 188 K when the thickness increases from 23 to 46 nm. The *M-T* curve for the $La_{0.9}Ba_{0.1}MnO_3$ bulk target is also included in the inset of Fig. 5-11 (d) for comparison and a T_c of 182 K is observed, as expected for bulk of this composition[204].

The above results show that the FMI property is maintained in the thicker NC. To explain this, we focus mainly on the modification of DE coupling, whose influencing factors have been well established, while the SE interaction is regarded as a background[215]. In the following sections, we firstly probe the compositional origin and then discuss the structural modification.

5.3.2 A compositional origin: Ce doping of LBMO

Fig. 5-12 (a) shows the plan view EDS element mapping of the 46 nm NC. These results, together with the TEM images shown in Fig. 5-7, prove the clear phase separation. As shown in the local EDS spectrum in Fig. 5-12 (b) and the La/Ce EDS line profile in Fig. 5-12 (c), Ce doping of the LBMO phase is observed, and the level is estimated to be 5-10% Ce doping on the La site. Also, La doping of the CeO_2 phase occurs on an estimated level of ~10-20%.

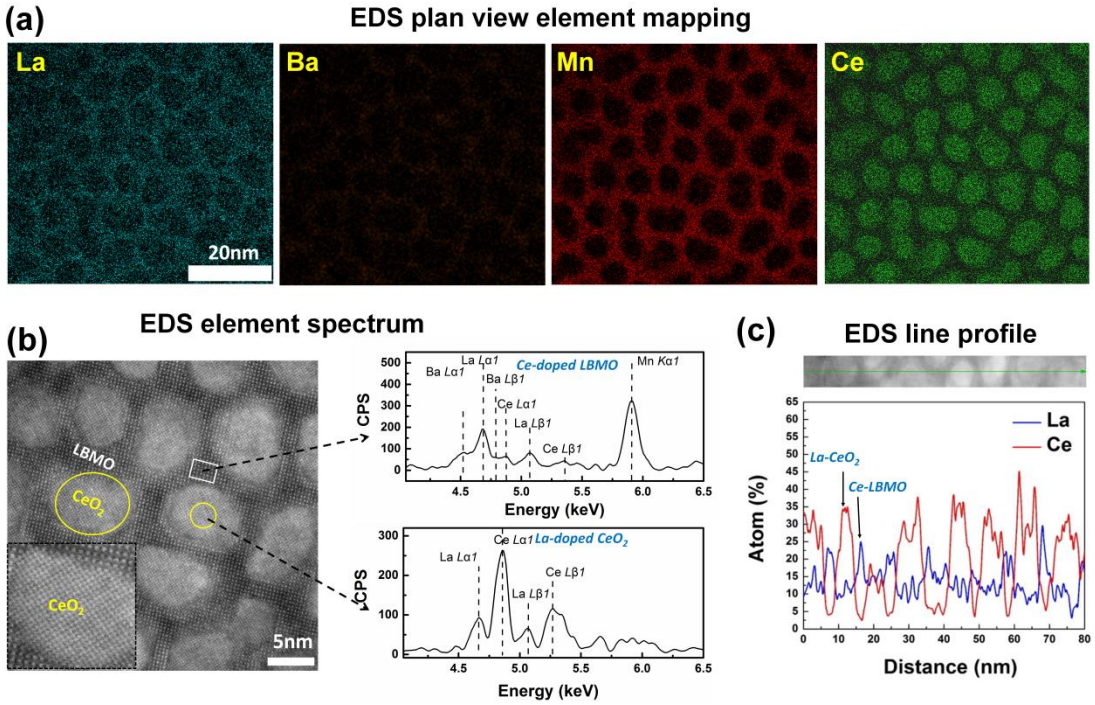

Figure 5-12. Proof of Ce doping in LBMO in the 46-nm NC. (a) Energy Dispersive X-ray Spectroscopy (EDS) plan view element mapping of the 46-nm NC film (color online). (b) EDS element spectrum showing a small amount of Ce exists in the LBMO area (top) and La exists in the CeO_2 area (bottom). (c) Plan view EDS line profile for the La and Ce elements.

It is now important to differentiate the effects of Ce doping and nanocolumn-induced strain on the electrical and magnetic properties. To learn about the Ce doping effect alone, two reference 100-nm-thick PFs were studied. The films were deposited using stoichiometric targets of $La_{0.85}Ce_{0.05}Ba_{0.1}MnO_3$ and $La_{0.8}Ce_{0.1}Ba_{0.1}MnO_3$. The growth condition was exactly the same as the nanocomposite and plain films in Fig. 5-11. A 100 nm thickness was chosen to eliminate additional epitaxial strain effects from the substrate.

As shown in Fig. 5-13 (a), CeO_2 is observed only in the XRD scan of the $La_{0.8}Ce_{0.1}Ba_{0.1}MnO_3$ film but is not present in $La_{0.85}Ce_{0.05}Ba_{0.1}MnO_3$. Hence, this indicates that the effective Ce doping level in our VAN films is between 5 and 10%. This is in agreement with the estimated Ce doping level from the EDS data, which is consistent with the limited solubility of Ce into the parent $LaMnO_3$ phase[216,217]. On the other hand, the reported solubility of La in CeO_2 is very high[218]. This explains our

observed Ce doping level in LBMO being lower than the level of La in CeO_2.

The *R-T* curves of the 100 nm PFs (with Ce doping ratio varying from 0 to 5% and 10%) are shown in Fig. 5-13 (c), and a 110 nm NC is shown in Fig. 5-13 (d). The ~100 nm films show similar *R-T* behavior as the ~46 nm films: the metallicity and T_M (~224 K) is maintained in the PF while the NC remains insulating.

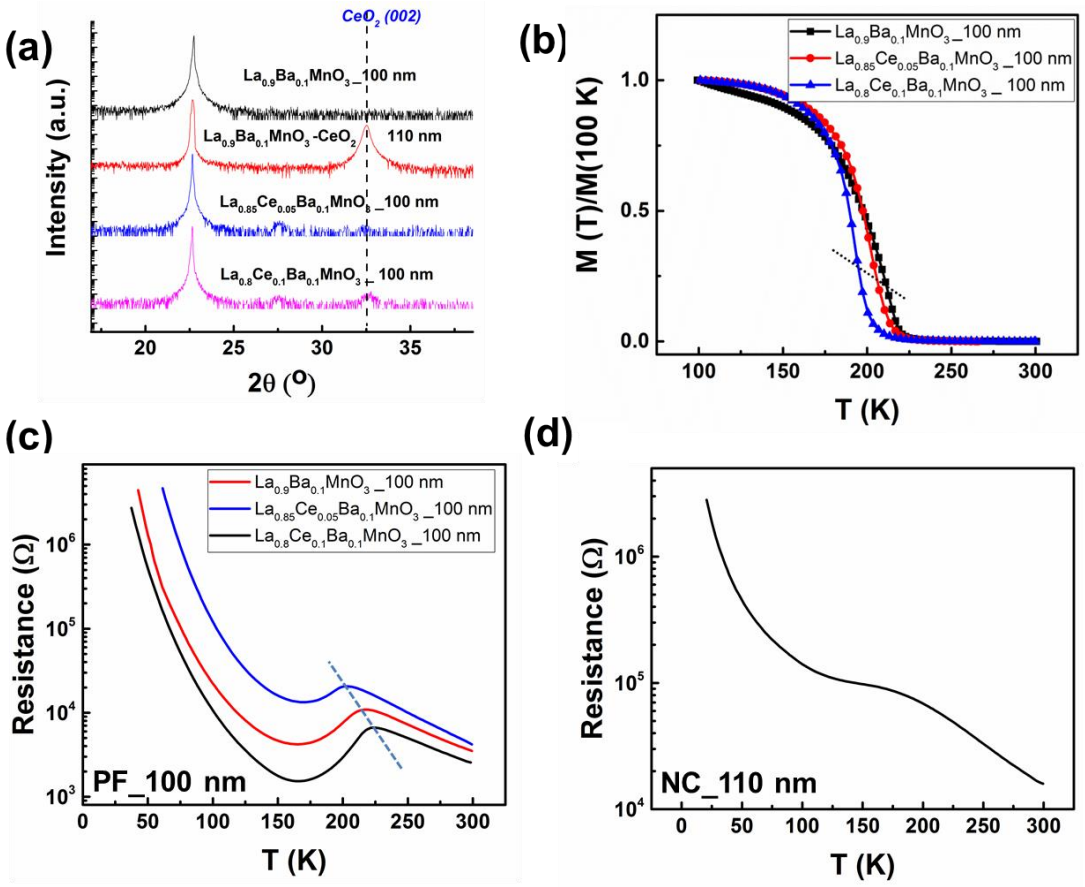

Figure 5-13. (a) Comparison of the XRD 2θ-ω scans for the $La_{0.9}Ba_{0.1}MnO_3$ PF, $La_{0.9}Ba_{0.1}MnO_3$-CeO_2 NC, $La_{0.85}Ce_{0.05}Ba_{0.1}MnO_3$ PF and $La_{0.85}Ce_{0.05}Ba_{0.1}MnO_3$ PF. (b) Magnetic transition of the $La_{0.9-x}Ce_xBa_{0.1}MnO_3$ (x=0, 0.05 and 0.1) PFs with a thickness of 100 nm. (c) Influence of Ce doping on the transport property of the $La_{0.9-x}Ce_xBa_{0.1}MnO_3$ (x=0, 0.05 and 0.1) plain films (PFs) with a thickness of 100 nm. (b) *R-T* curve of a 110 nm LBMO-CeO_2 NC.

From Fig. 5-13 (c), it is observed that compared to the LBMO film with no Ce doping, for Ce doping levels of 5% and 10%, T_M is reduced by 7 K and 18 K, respectively. T_c is also reduced by a similar amount (Fig. 5-13 (b)). Also, the films become progressively more insulating with Ce doping, i.e. the resistance increases by

an order of magnitude for the 10% Ce doping *cf*. the undoped PF.

The chemical/structural disorder caused by inhomogeneous Ce doping in manganites is well-known: it increases the overall resistivity (resistance), but the disorder alone cannot well explain the decrease in T_M/T_c that we observe[219,220]. On the other hand, since Ce^{3+} or Ce^{4+} doping on the La site (or on La vacancy sites) induces a charge imbalance on the A site, the B site Mn valence changes also, i.e. the amount of Mn^{4+} decreases, which reduces the DE coupling and thus T_M/T_c, and also increases the overall resistivity (resistance). This charge compensation should be a stronger reason for the observed change in the resistive/magnetic behavior.

5.3.3 The influence of Ce doping on DE coupling: defect equations

To understand how Ce^{3+} (or Ce^{4+}) doping of LBMO reduces the DE coupling and metallicity (Fig. 5-13 (c)) in the PFs, we consider defect equations (using Kröger–Vink notation)[221]. We first consider the defect chemistry of the parent film, $La_{1-x}Ba_xMnO_3$. Ba^{2+} on the La^{3+} site donates holes which are compensated for by the generation of Mn^{4+}. As mentioned in Chapter 5.1.1, the formation of Mn^{3+}/Mn^{4+} pairs is the origin of the DE coupling, and ferromagnetism/conduction in manganites:

$$La_{La}^{x} + BaO = Ba'_{La} + h^{\bullet} + \frac{1}{2}O_2 \quad (5\text{-}3)$$

$$Mn_{Mn}^{x} + h^{\bullet} = Mn_{Mn}^{\bullet} \quad (5\text{-}4)$$

where La_{La}^{x} represents a La^{3+} ion on a La site, and Mn_{Mn}^{x} and $Mn_{Mn}^{\bullet}$ represent Mn^{3+} and Mn^{4+} on the Mn site, respectively. Hence, for every Ba ion doped on the La site in LBMO, one Mn^{4+} ion is created.

For low Ba doping levels as we have here (x=0.1), a weak level of DE interaction is induced which competes with the SE interactions, resulting in an overall FMI[215]. For manganite *films*, on the other hand, cation (both La and alkaline earth) vacancies are prevalent[212] due to the sensitivity of manganites to oxidation atmosphere. Hence, under the growth conditions, cation-deficient LBMO is more stable than the

stoichiometric LBMO. This tendency for cation vacancies is higher when the doping level is lower[186,212].

If we consider the formation of La vacancies only, holes are produced which increase the Mn^{4+}/Mn^{3+} ratio, leading to an enhanced DE coupling. Hence,

$$La_{La}^{x} + \frac{3}{2}O_2 = V_{La}''' + \frac{1}{2}La_2O_3 + 3h^{\bullet} \quad (5\text{-}5)$$

$$3Mn_{Mn}^{x} + 3h^{\bullet} = 3Mn_{Mn}^{\bullet} \quad (5\text{-}6)$$

where V_{La}''' represents a La vacancy on a La site.

In the NC films, when La vacancies pre-exist, Ce^{3+} or Ce^{4+} doping of the La vacancies occurs as a consequence of chemical equilibrium. Two possibilities exist:

(a) Ce exists as Ce^{3+}, and 3 electrons are generated by filling the La^{3+} vacancies, and these electrons are then compensated for by the reduction of the Mn^{4+} to Mn^{3+}:

$$V_{La}''' + \frac{1}{2}Ce_2O_3 = Ce_{La}^{x} + \frac{3}{2}O_2 + 3e' \quad (5\text{-}7)$$

$$3Mn_{Mn}^{\bullet} + 3e' = 3Mn_{Mn}^{x} \quad (5\text{-}8)$$

The reduction of the Mn^{4+} concentration will reduce the DE coupling.

(b) Ce exists as Ce^{4+}, and 4 electrons are generated by filling the La vacancies. Again, the electrons are compensated for by the reduction of Mn^{4+} to Mn^{3+}. Even more Mn^{4+} is reduced compared to the case of Ce^{3+}, and then the DE is further weakened.

$$V_{La}''' + CeO_2 = Ce_{La}^{\bullet} + O_2 + 4e' \quad (5\text{-}9)$$

$$4Mn_{Mn}^{\bullet} + 4e' = 4Mn_{Mn}^{x} \quad (5\text{-}10)$$

The overall result of Ce doping on the cation-deficient LBMO, as discussed above, is a decrease in both the T_c and T_M, which ultimately produces LBMO films that maintain the FMI behavior. Hence, the reason that Ce doping increases the resistivity (resistance) and decreases the T_M (T_c) of both the Ce-doped reference PFs in Fig. 5-13 and the NC films in Fig. 5-11 (b) is understood.

5.3.4 A structural origin: vertical strain

It is notable that the form of *R-T* curves of the 100 nm Ce-doped reference PFs (Fig. 5-13 (c)) are very different from the 100 nm NC film (Fig. 5-13 (d)). There is a clear *I-M* transition in the former (just as there is in other PFs) but *not* in the latter NC. We also note that T_c of the 100 nm $La_{0.8}Ce_{0.1}Ba_{0.1}MnO_3$ (10% Ce doping) reference film is 195 K, which is 13 K higher than the 110 nm NC (Fig. 5-13 (b)). These results indicate that Ce doping of the PF reduces the DE coupling, but does not eliminate it and so the FMI properties cannot be maintained by Ce-doping alone. It is clear, therefore, that while Ce-doping reduces the DE effect, strain engineering in the NC films adds a further and more significant *structural* tuning effect.

To understand the vertical strain effect on the electrical and magnetic properties of the NC films further, we study how the strain of the NC films evolve with thickness. The 3D strain states of the NC and PF were analyzed using asymmetric reciprocal space maps (RSM) around the STO (103) peaks, as well as symmetric 2θ-ω scans near the STO (003) peaks, as shown in Fig. 5-14 and Fig. 5-15. Here two thicknesses ~20 nm and ~40 nm were analyzed. The dashed lines show the trends of the lattice parameters with film thickness. The XRD data of a 100 nm PF and a 110 nm NC are also shown in Fig. 5-16 to support the analysis.

◆ **Strain state of the LBMO plain films**

It is clear from Fig. 5-14 that the PFs contain diffraction peaks from three phases: two tetragonal phases (A and A') that are both *ip* strained by the STO, as observed by the same Q_x positions in the RSMs of Fig. 5-14 (a), although some *ip* relaxation is observed in phase A' at 100 nm thickness (Fig. 5-16 (a)). The other phase is a twinning phase, labeled T. A schematic film structure showing the location of three phases in the PFs is shown in Fig. 5-17 (a). For reasons explained below, we predict that A lies at substrate surface and is fully strained by it, and A' lies above the initial A layer region, while the T phase starts to appear from a certain thickness (as discussed later).

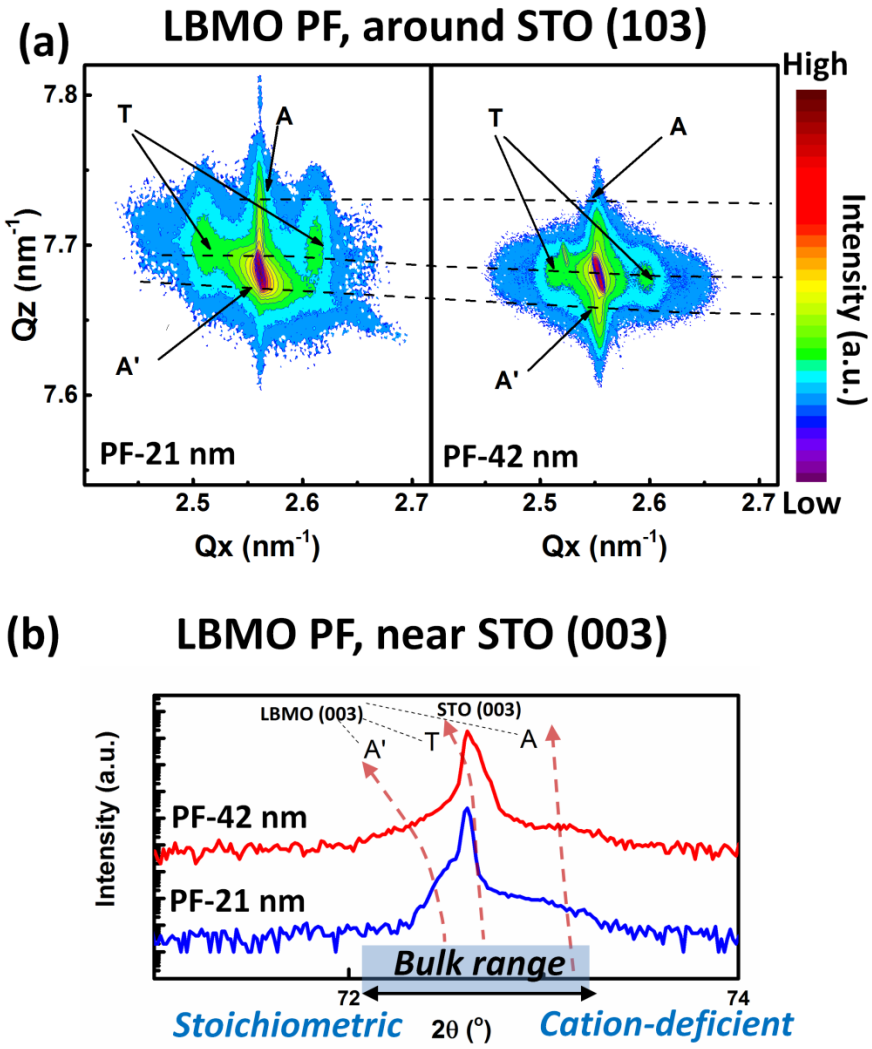

Figure 5-14. (a) Asymmetric reciprocal space maps (RSM) around the STO (103) peak for the LBMO plain films (PF) with increasing thickness. (b) Symmetric XRD 2θ-ω scans near the STO (003) peak for the LBMO PF. The blue shadowed area in (b) shows the range for the peak positions of reported bulk lattice constants of $La_{0.9}Ba_{0.1}MnO_3$. (c) Selected area electron diffraction (SAED) pattern of the 100-nm LBMO PF. The yellow arrows show the spot splitting indicating the twinning.

Phase A has *ip* tension to match the STO substrate lattice parameter (3.905 Å), with a corresponding *op* compression. Hence, the (003) peak for A is at a higher angle than STO (003) in the 2θ-ω scan. This phase is likely cation deficient since its lattice parameter should be <3.905 Å, in order to achieve *ip* tension. Non-stoichiometry in thin manganites is a well-known mechanism for strain accommodation[47]. Hence, apart from oxidation-atmosphere-induced cation vacancies as in bulk samples, strain is an additional driving force for the cation vacancy formation observed here.

For Phase A', the (003) peaks of LBMO are at a lower angle than STO (003), which would suggest *op* tension of the A' phase, at least if it were strained to the STO. This would mean it had larger lattice parameters than STO, indicating it to be more stoichiometric than A. It is likely that A' is stable towards the upper part of the film and is more stoichiometric because it doesn't need to change its stoichiometry so much to accommodate the substrate strain. The *op* lattice parameter of A' expands rapidly with thickness, and reaches 3.923 Å when the thickness of the PF reaches 100 nm (Fig. 5-16 (a)).

It is noted that a wide lattice parameter (pseudocubic) range for $La_{0.9}Ba_{0.1}MnO_3$ bulk and films has been reported in the literature, from ~3.88 - 3.92 Å[185,186,202–205], and this range is shown in Fig. 5-14 (b) and Fig. 5-16 (a). The range is consistent with variations in cation non-stoichiometry, with a smaller lattice parameter indicating a greater cation deficiency. The calculated lattice constants of the PFs range from 3.883 Å (A phase) in the 21 nm PF (Fig. 5-14) to 3.923 Å (A' phase) in the 100 nm PF (Fig. 5-16 (a)). This is consistent with the range of lattice parameters reported for bulk LBMO, confirming again the susceptibility of LBMO (whether bulk or films) to non-stoichiometry and structural modulation.

The T phase is characterized by a pair of twinning peaks (T) (Fig. 5-14 (a) and Fig. 5-16 (a)), which indicates the presence of periodically tilted unit cells. Besides, diffraction spot splitting is observed in the SAED patterns in the film part (illustrated by yellow arrows in Fig. 5-14 (c)), which additionally proves the existence of the twinning phase[222]. Periodic octahedral tilting of the MnO_6 octahedra occurs in

manganites as an energy-efficient way to accommodate lattice mismatch strain[223,224] rather than conventional tetragonal deformation or stoichiometry change. The T phase is not constrained by the STO lattice *ip*, as determined by the Q_x peaks for T being at a different position to the STO peak in the RSM of Fig. 5-14 (a). Hence, the T phase is towards the upper region of the film[225], as we predict A' to be also.

The fact that the rapidly changing lattice constant of the A' phase has little influence on the T_c indicates that the T phase has the most dominant effect on the magnetic and transport properties of the PFs. The presence of the T phase in all PF films in the upper region explains the almost constant T_M (T_c) with film thickness in the PFs (recall Fig. 5-11 (a) and (c)). Extensive studies have shown that twinning is one mechanism for partial or total relaxation to the bulk lattice structure[223] and the twinning starts to appear above a certain thickness[225]. Therefore, for the PFs studied here, for the same or very similar levels of relaxation in the T phase, no matter if it is a partial or total relaxation, the T_M (T_c) will stay almost constant.

◆ Strain state of the LBMO-CeO_2 nanocomposites

Now we turn to discussing the phases and strain states of the NC films. From the RSMs and 2θ-ω scans (Fig. 5-15), we observe only one homogeneous LBMO phase with a sharp (103) or (003) x-ray peak, which somewhat overlaps with the STO (103) or (003) peak. This contrasts to the inhomogeneous phases observed in the PF.

All the films are *ip* strained by STO as observed by the same positions of the centers of the (103) peak Q_x values in Fig. 5-15 (a). In the thin NC films (23 nm), similar to the case of phase A in the PFs, vertical *op* compression results, as observed by the shoulder peak on the right hand side of the STO (003) peak, i.e. at higher 2θ in the 23 nm NC in Fig. 5-15 (b). The *op* compression is caused by the epitaxial *ip* tension induced by the STO substrate (a= 3.905 Å) on the smaller lattice parameter of $La_{0.9-x}Ce_xBa_{0.1}MnO_3$. Even though Ce filling of La vacancies tends to enlarge the LBMO lattice (c= 3.900 Å in the 23-nm NC, as compared to 3.883 Å of the A phase in the 21 nm PF), the lattice is still smaller than the vacancy-free $La_{0.9}Ba_{0.1}MnO_3$ bulk

(*a*=3.92 Å), because the Ce^{n+} (n=3 or 4) has a smaller ionic radius than La^{3+}[226,227]. With increasing the thickness, i.e. for the 46 nm film, as observed by the shoulder peak shifting to the left hand side of the STO (003) peak in Fig. 5-15 (b), the vertical strain state in LBMO is switched from *op* compression to *op* tension. Owing to the vertical clamping of the *op* lattice parameters by the CeO_2 nanocolumns, there is no elastic compensation of strain in the *op* direction as there is in the phase A of PFs.

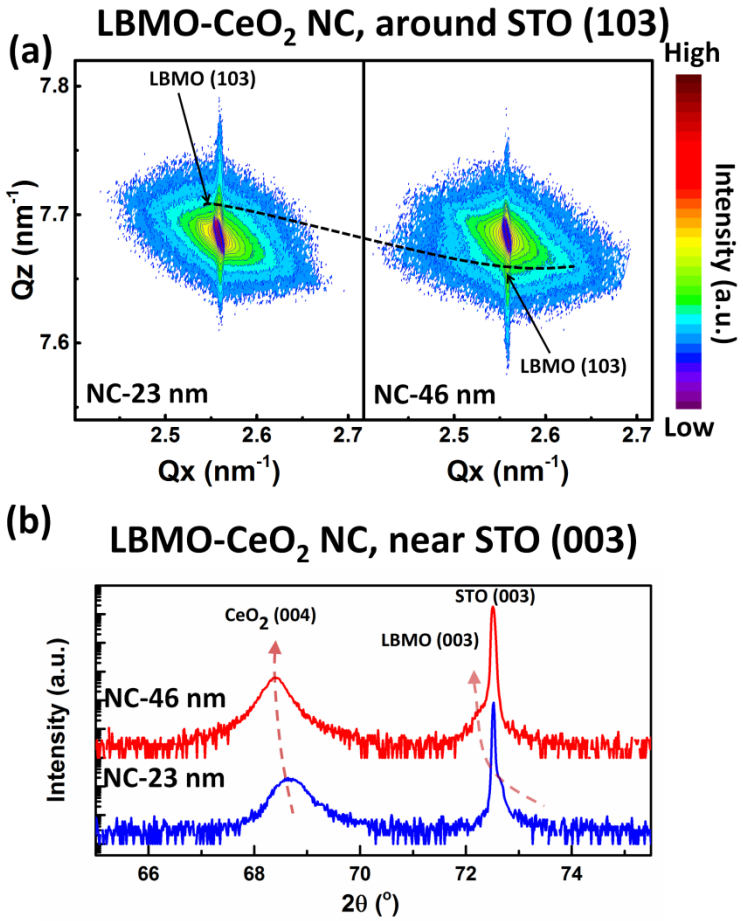

Figure 5-15. (a) Asymmetric reciprocal space maps (RSM) around the STO (103) peak for the LBMO-CeO_2 nanocomposite (NC) films with increasing thickness. (b) Symmetric XRD 2θ-ω scans near the STO (003) peak for the LBMO-CeO_2 NC films.

A schematic diagram of the NC film strain state is shown in Fig. 5-17 (b) shows the strain tuning of the NC films. We note that for a >100 nm film thickness, the vertical tension stabilizes and saturates while the *ip* strain remains the same (Fig. 5-16 (b)) since it is controlled by the substrate.

The *op* lattice parameters of the LBMO phase in the NC films are extracted by profile fitting of the 2θ-ω scans of Fig. 5-15 (b). The estimated *op* lattice parameter, *c*, changes from 3.900 Å (23 nm) to 3.910 Å (46 nm). For the 46 nm film, the *op* strain is increased by 0.25 % compared to the 23 nm film where the substrate controls the film strain state. The slight strain increase is significant for reducing the DE coupling in lightly doped LBMO, as discussed later.

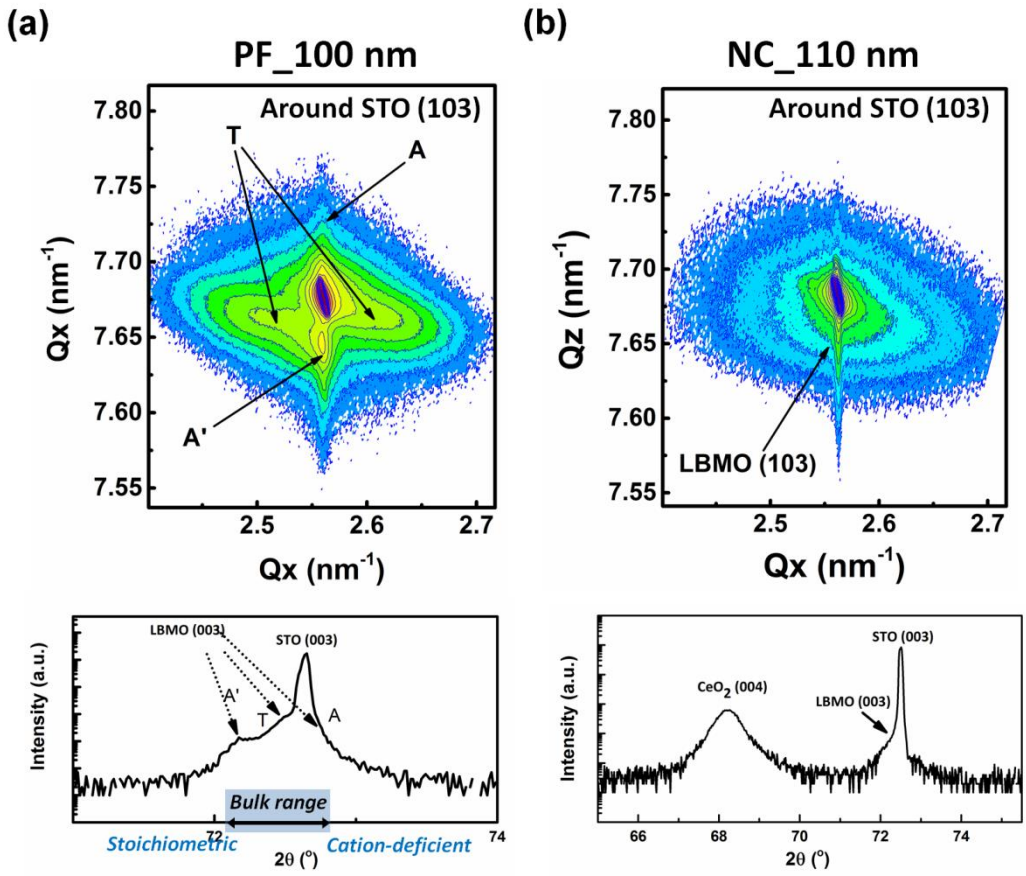

Figure 5-16. RSM around STO (103) and XRD 2θ-ω scans around STO (003) of (a) 100 nm PF and (b) 110 nm NC.

The strain state in the NC film is very different from the PF because in the PF a combination of different LBMO phases is formed for strain relaxation. In the NC film, on the other hand, vertical epitaxy between the sub-5 nm wide LBMO regions with the CeO_2 scaffold locks the strain vertically and laterally and, very importantly, makes it more uniform. We also note that the lateral width of the LBMO between the nanocolumns is below the reported minimum size (~20 u.c.) for the formation of the

twinning domains in manganites[223], and this therefore precludes their formation.

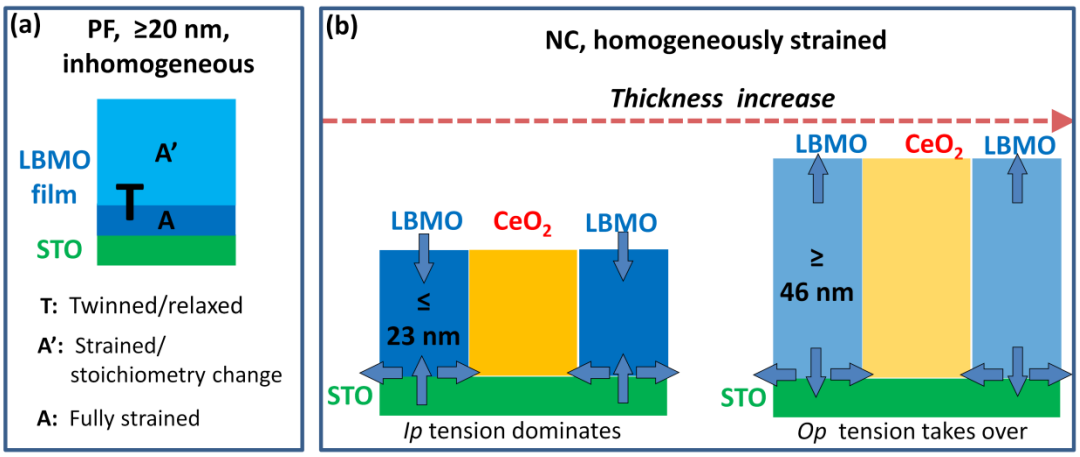

Figure 5-17. (a) Illustration of the phase coexistence in the PF. A lighter color corresponds to a larger lattice constant. The illustrated thickness regions are not to scale. (b) Illustration of strain tuning in the LBMO-CeO_2 NC films when the thickness is increasing. A lighter color corresponds to a larger lattice constant.

5.3.5 The influence of VAN vertical strain on the DE coupling

We now analyze the connection between the strain and physical properties in the NC films. As discussed above, the T_cs of the PFs stay at around 212 K, which are higher than the bulk, owing mainly to non-stoichiometry effects, and we hypothesize that the T phase lies towards the film surface and dominates the measured T_c (T_M). Here it is not possible to determine the exact *c* for the T phase from the 2θ-ω scans, because the tilting of twin domains prevents accurate measurement of *c*. For the NC films the average LBMO *op* lattice constant tends to increase with thickness. At the same time, T_c decreases from 201 to 188 K, mirroring the rise in *c*, indicating that a stretch of the LBMO lattice reduces the DE coupling. Similarly, a sharp reversible dependence of T_c on *c*-axis was shown in previous work via He ion implantation in $La_{0.7}Sr_{0.3}MnO_3$ thin films[228]. As previously discussed in Chapter 5.1.1, epitaxial strain in manganites influences the Mn 3*d* e_g electron orbital occupancy or the Mn-O bond[40,161,163,228]. It is known that T_c in hole-doped manganites is determined by DE interactions which are directly related to the transfer integral between neighboring Mn ions through the

oxygen bridge[161].

In the NC films, *c* expands with increasing thickness while *a* axis remains unchanged, leading to an increase in the *c*/*a* ratio. A low *c*/*a* ratio (<1) is reported to enhance the electron occupancy of the *ip* $d_{x^2-y^2}$ orbital, which enhances the DE coupling and induces metallicity in lightly doped LBMO[185]. A high *c*/*a* ratio, on the other hand, is more favorable to the preferential occupancy of the $d_{3z^2-r^2}$ orbitals rather than the $d_{x^2-y^2}$ orbitals, leading to a reduction of the *ip* DE hopping integral *t*[228], and to reduced DE. We recall that a 0.25% *op* strain increase was achieved in the 46 nm film compared to the 23 nm film. The corresponding *c*/*a* ratios are 0.999 and 1.001, which explains the much reduced DE coupling in the 46 nm film.

It is also worth noting that LBMO is fully *ip* strained by the STO and hence a tetragonal phase is maintained irrespective of thickness. If one assumes that the Mn-O bond angle θ of the tetragonal phase is unchanged[229], for a constant θ with thickness, the DE hopping integral, *t*, as defined by equation (5-2) will reduce with film thickness because the *op* bond length, *d*, increases. This is also consistent with the reduced DE coupling in the thicker films.

Previously, independent *c* and *a* straining has not been achieved in lightly doped lanthanum manganites. Also, uniform straining to induce a single-phase manganite has not been demonstrated. However, both these factors are critical for maintaining the FMI properties in thin films. It is clear from Fig. 5-14 that uniform straining in PFs is not possible merely via substrate strain engineering as strain relaxation and multiple phases are formed. As for bulk, mechanical and chemical pressure engineering of the structures have been undertaken but both these produce hydrostatic straining. Neither can be applied to thin films. Also, by those methods *c* and *a* cannot be independently tuned. On the other hand, the VAN method for straining enables precise tuning of the T_c of LBMO by expanding the *c* without reducing the *a*, resulting in an enhanced *c*/*a* ratio, and thus giving a novel way to carefully tune the DE coupling.

5.3.6 Conduction mechanisms and structural correlations

Having probed the compositional and structural origin for the modified DE coupling in the LBMO-CeO_2 NC films, we next turn to analyze and understand in detail the electrical properties and focus on the films with ~40 nm thickness. This analysis was be done by fitting the ρ-T curves (R is converted to ρ using equation (3-20)) to the conduction mechanisms discussed in Chapter 2.1.2. The results are shown in Fig. 5-18.

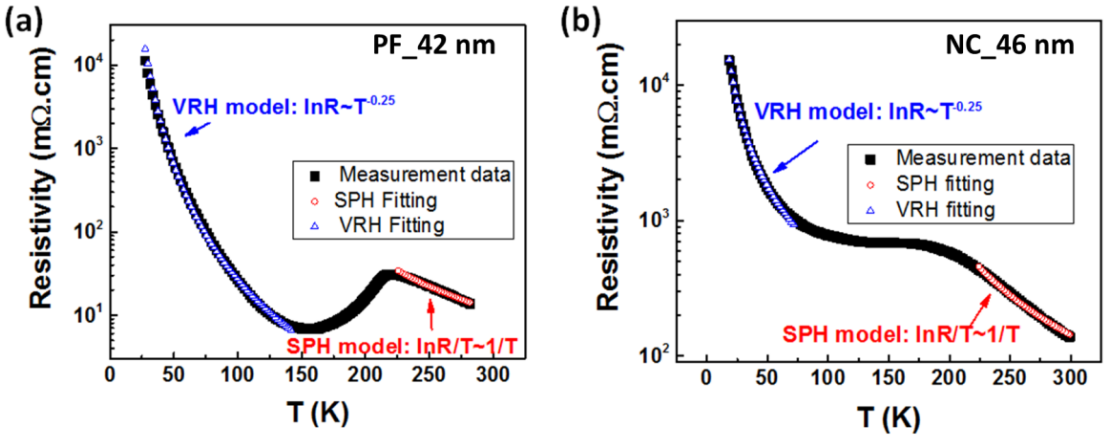

Figure 5-18. ρ-T fitting with different conduction mechanisms for (a) the 42-nm-thick LBMO PF and (b) the 46-nm-thick LBMO-CeO_2 NC.

For T>T_M (T_c), the electrical conduction can be fitted by a small polaron hopping (SPH) model[18] given by equation (2-18): $\rho(T) = ATe^{\frac{E_A}{k_BT}}$. E_A is the activation energy, which is related to the height of the potential barrier and can be used to evaluate the high temperature resistive behavior. The SPH fitting gives an E_A of 109 meV and 116 meV for the PF and NC, respectively, indicating a higher potential barrier in the NC, which is consistent with the more insulating nature of the LBMO in the NC.

Below T_M (or T_c) the variable range hopping (VRH), equation (2-17) $\rho(T) = \rho_0 e^{\left(\frac{T_0}{T}\right)^{\frac{1}{4}}}$ provides the best fit[230]. T_0 is related to the density of states at the Fermi Level $N(E_F)$ and the localization length $\xi_L = \left(\frac{21}{k_B T_0 N(E_F)}\right)^{\frac{1}{3}}$ which reflects how

disordered the structure is, k_B is the Boltzmann constant, and $N(E_F)$= 10^{21}/eV cm^3 for bulk $La_{0.9}Ba_{0.1}MnO_3$ is used[231]. The ξ_L value obtained from VRH fitting are 0.45 and 1.33 nm, respectively, indicating that the PF is more structurally disordered at low T due to the existence of inhomogeneous phases. The calculated ξ_L in the NC film is smaller than the average size of LBMO matrix (~ 3–5 nm) between the CeO_2 nanocolumns, indicative of an intra-grain conduction mechanism[73] instead of the scattering from the LBMO/CeO_2 boundaries.

5.4 Nanoengineering LBMO from a ferromagnetic insulator to a ferromagnetic metal via self-assembled modulation of the lateral size

As presented in Chapter 5.3, the FMI property of LBMO can be maintained via VAN doping and strain. In device applications, the FMM property of manganite is also desired. The VAN tuning opens up a large study area to expand the tunability of manganites (i.e. from FMI to FMM), this being promoted by the sensitive nature of $La_{0.9}Ba_{0.1}MnO_3$ to external stimuli. Thickness tuning in VAN usually has some limitations as revealed in Chapter 5.3, while other growth parameters, such as growth temperature and growth rate, may enable a larger tunability by changing the self-assembly kinetics.

In this section, the thickness of the LBMO-CeO_2 NC films is kept at the optimal thickness (~46 nm). We show that the T_c and metallicity of LBMO are tuned much more remarkably by varying the growth temperature (690℃, 720℃, 750℃ and 800℃) and then the origins are discussed. To eliminate the effect of growth temperature alone, 3 reference LBMO PFs (with the growth temperature 690℃, 720℃ and 800℃) were also prepared.

5.4.1 Tuning the physical property of LBMO via the VAN growth temperature

As shown in Fig. 5-19 (a) and (c), all the PFs show a clear *I-M* transition at around 221 K, and growth temperature alone has little influence on the T_M. Meanwhile, the T_c (defined as the temperature where d*M*/d*T* reaches the maximum) is almost constant at around 213 K. In contrast, the NC has a tendency to evolve from a ferromagnetic metal (FMM) to a ferromagnetic insulator (FMI) when the growth temperature is decreased from 800 to 690 ℃, as illustrated by the dashed arrow in Fig. 5-19 (b) and (d). The extrapolated T_c value, as shown in Fig. 5-20 (a), has a large drop (> 55 K), and changes from lower to higher than that of the PFs.

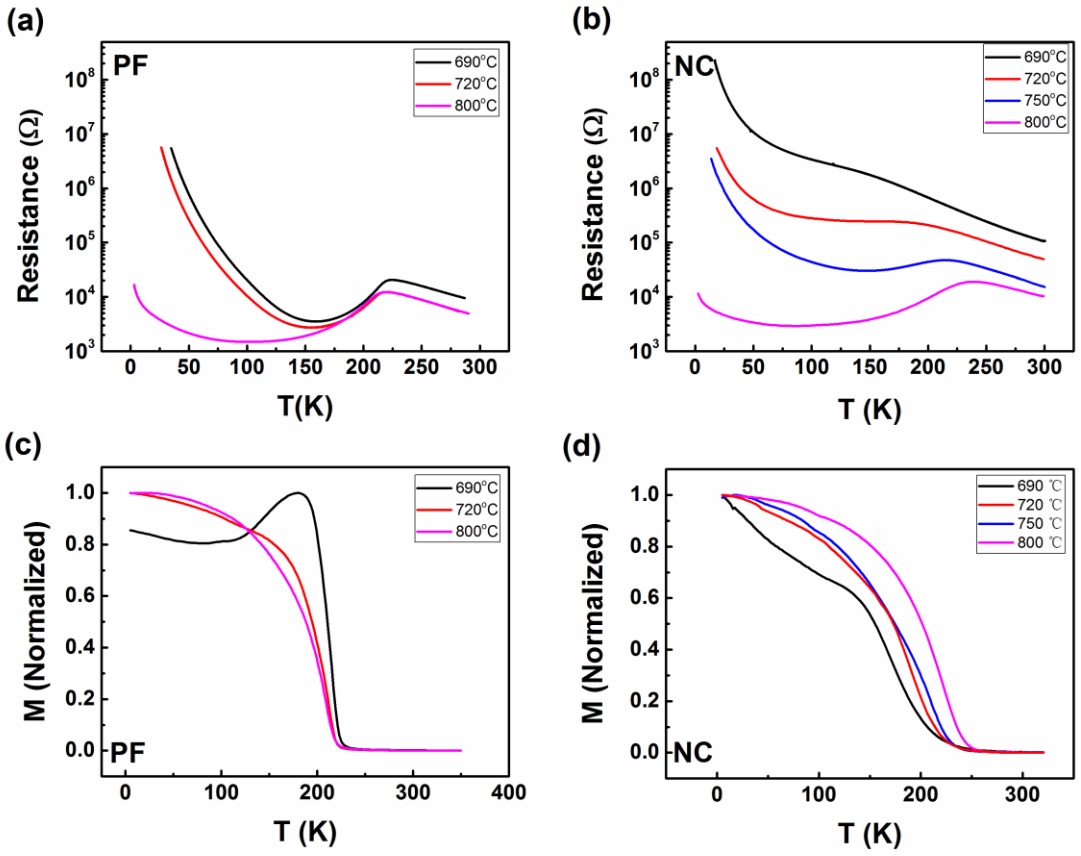

Figure 5-19. Growth temperature-dependent ρ-*T* curve for (a) the PF and (b) the NC. Growth temperature-dependent *M*-*T* curve for (c) the PF and (d) the NC. The applied magnetic field was 200 Oe.

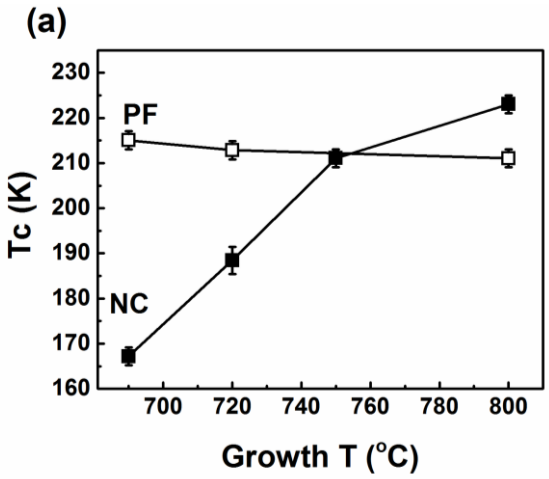

Figure 5-20. Comparison of T_c between the PF (open squares) and NC (closed squares) with changes in growth temperature.

As discussed in Chapter 3.1.2, growth temperature has a strong influence on the diffusion length of the VAN constituent phases, which results in the modification of self-assembly kinetics in composite films and this modification is absent in single-phase films. Therefore, the drastic tuning of T_c in the NCs as opposed to the stable T_c in the PFs is indicative of a strong modification of the DE coupling due to structural modification. In the following discussions, the origins will be illuminated by studying the microstructure and electronic structure.

5.4.2 Microstructure evolution with varying the VAN growth temperature: modulation of the lateral size

In VAN films, it is assumed that each nanocolumn blocked by the matrix can be regarded as an independent single crystallite (called a mosaic block) with a certain vertical/lateral length and mosaic spread, and each mosaic block coherently scatters the x-ray[232]. This applies similarly to the matrix phase which also has a limited size. As illustrated in Fig. 5-21, the coherence length L of each phase is correlated to the mean extension of the crystal lattice regions (i.e. the average geometric size of the nanocolumn or the matrix), and the mosaic spread/tilt angle α is a reflection of the misorientations of the phases perpendicular to the film surface[50]. In VANs, the

evolution in L and α are two unique parameters that depend strongly on the growth conditions[50,83]. As reported previously, a higher growth temperature is favorable for a larger lateral size[38,208], while misorientations can be reduced by choosing a proper growth temperature[233,234]. Therefore, studying these two structural parameters would be helpful for finding out the dependence of structural evolution on the growth temperature.

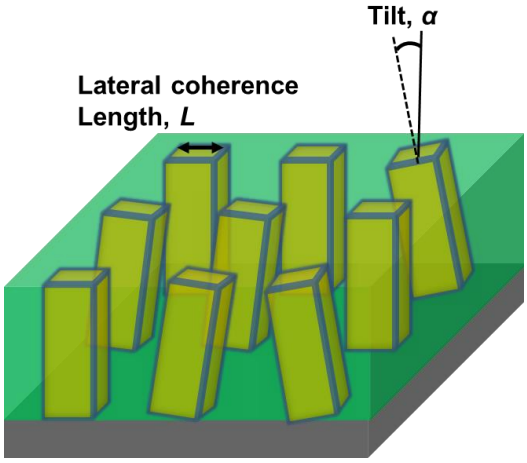

Figure 5-21. Schematic diagram showing the correlation between coherence length (L), and tilt (α).

◆ Fitting the column size and tilt using the Williamson-Hall plot

As discussed in Chapter 3.2.1, limited size (L) and misorientations (α) contribute to the broadening of the symmetric ω rocking curves. By combining equations (3-2)–(3-12), these two contributions can be defined using the Williamson-Hall (W-H) expressions[89,232,235,236]:

$$\Delta s = \alpha . s + \frac{1}{L} \quad \text{(for Lorentzian peak)} \tag{5-11}$$

$$\Delta s^2 = \alpha^2 s^2 + \frac{1}{L^2} \quad \text{(for Guassian peak)} \tag{5-12}$$

where $s=\frac{2sin\theta}{\lambda}$ is the scattering vector and $\Delta s= \beta \frac{2sin\theta}{\lambda}$ is the broadening in reciprocal space, β is the integral breadth (peak area divided by the height) of the ω rocking curve, θ is the diffraction peak position in the corresponding 2θ-ω scan, α is the tilt

angle, L is the coherence length of the phase, λ is the x-ray wavelength (λ=1.54 Å is used here).

Via linear fitting of the W-H plot (a plot of the s-Δs (or s^2-Δs^2) relationship as a function of the reflection order), the y coordinate intercept is taken to be the reciprocal of L (or L^2) while the slope is equal to α (or α^2)[89]. The influence of growth temperature on the lateral size and tilt of the CeO_2 phase was studied. ω rocking curves were conducted on all the NC samples, and the W-H fitting plots are shown in Fig. 5-22 (a) and (b). Assuming Pseudo-Voigt peak profile, the results of peak fitting for both the Lorentzian and Gaussian shapes are quoted because the shape factor (Lorentzian: Gaussiaon ratio, defined as a function of the FWHM/β ratio) for all the rocking curves vary between 0 and 1[89].

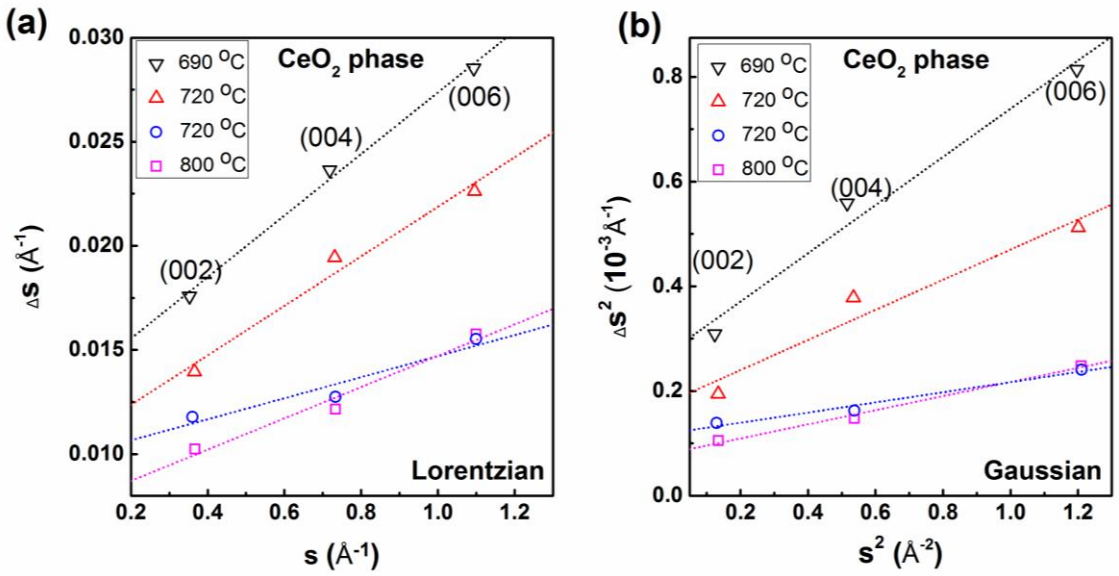

Figure 5-22. Williamson-Hall plots for the CeO_2 phase in the LBMO-CeO_2 NC films grown at different temperatures: (a) Lorentzian peak fitting and (b) Gaussian peak fitting.

The extrapolated column size d_C of the CeO_2 phase, as shown in Fig. 5-23 (a), increases with the increase in growth temperature, indicating a nucleation-and-growth mode[38], where d_C is proportional to the diffusion length L_D given by

$$L_D \approx 2\sqrt{D\tau} \qquad (5\text{-}13)$$

Here τ is the diffusion time. D is the diffusion coefficient[38] which follows the Arrhenius equation:

$$D = D_0 * e^{-\frac{E_A}{kT}} \tag{5-14}$$

where D_0 is a pre-exponential factor, E_A is the activation energy, k is the Boltzmann constant, and T is the temperature. When the deposition time and laser repetition rate are constant, the diffusion time τ is constant, and thus the CeO_2 column size d_C changes with the growth temperature in the following relationship: $\ln d_C^2 \propto \frac{1}{T}$. As plotted in Fig. 5-23 (b), a linear relationship is exhibited between $\ln d_C^2$ and $\frac{1}{T}$, which is consistent with the nucleation-and-growth mode.

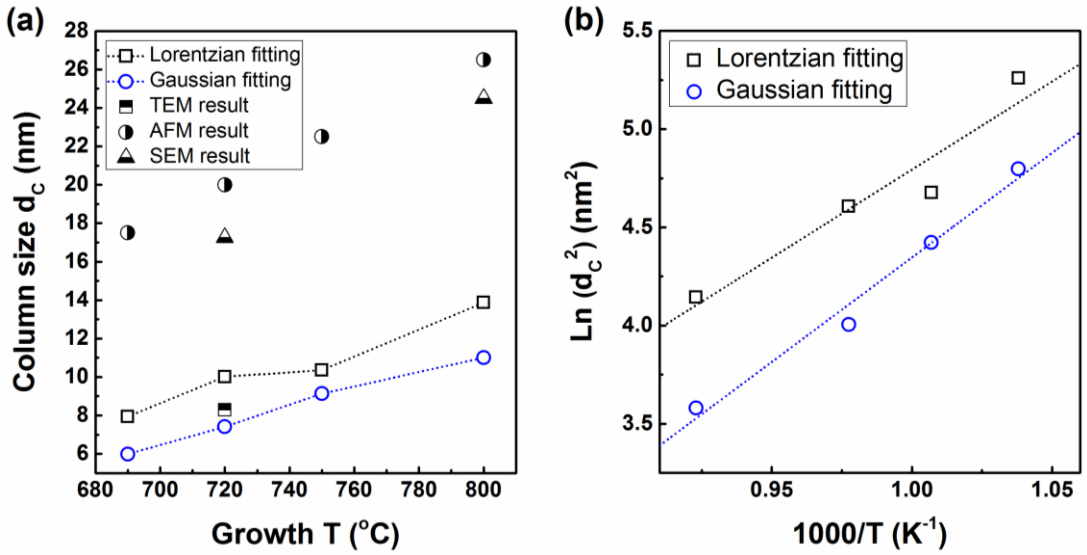

Figure 5-23. The plot of (a) the CeO_2 coherence length (column size d_C) with increasing the growth temperature. The average column sizes measured by TEM, AFM and SEM are included. (b) Temperature-dependent fitting of the calculated CeO_2 column size based on the nucleation and growth mode.

The fitted tilt angle, as shown in Fig. 5-24, decreases first and then remains almost constant with increasing the growth temperature, which indicates that a higher growth temperature tends to generate a better crystal quality and less misorientation.

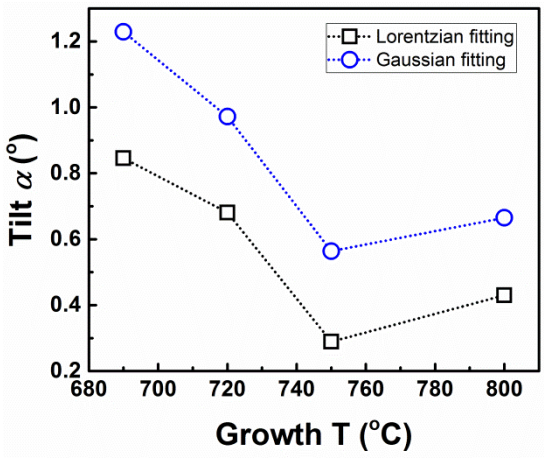

Figure 5-24. The plot of mosaic spread (tilt angle) of the CeO_2 phase with the change in growth temperature.

◆ **Confirming the column size evolution using SEM and AFM**

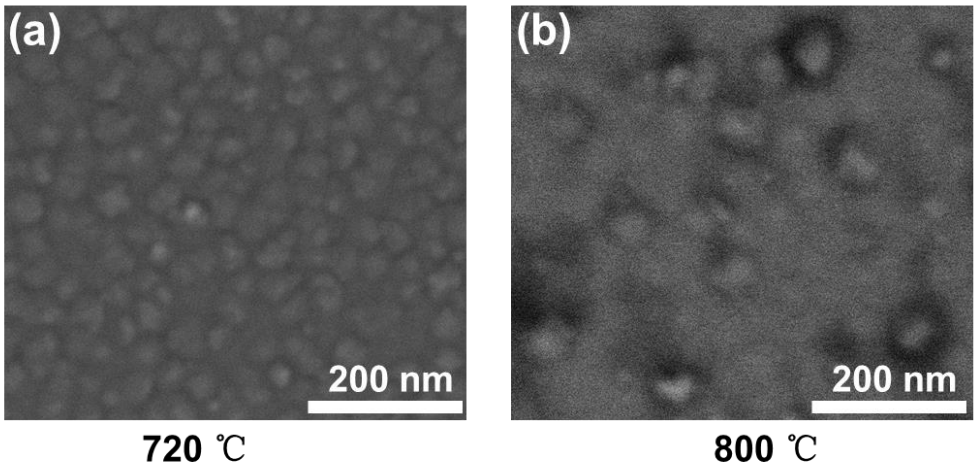

Figure 5-25. Scanning Electron Microscope (SEM) image of the LBMO-CeO_2 NC grown at (a) 720℃ and (b) 800℃.

The extrapolated column size of the NC sample grown at 720℃ (7.5 nm for Gaussian fitting and 10.6 nm for Lorentzian fitting) is in agreement with the average size obtained from TEM (6~10 nm, Fig. 5-7). This consistency is further confirmed by comparison with the experimental results obtained from Scanning Electron Microscopy (SEM) and Atomic Force Microscopy (AFM). As shown in Fig. 5-25 (a), the CeO_2 columns of the sample grown at 720℃ have a round shape and are densely distributed inside the continuous LBMO matrix network, and the columns have a very

uniform size. This structure layout is consistent with the plan-view STEM shown in Fig. 5-7 (b). In comparison, the columns of the sample grown at 800 ℃ (Fig. 5-25 (b)) tend to become more square-shaped, with the in-plane 45^o rotation and orthogonal alignments being more clearly seen. The columns have a larger average size and the distribution is more sparse, leaving larger spaces for the LBMO matrix.

Fig. 5-26 shows the AFM surface topography of the four NC samples, where a simultaneous increase in the column (illustrated by the white circles) and matrix size is observed with the increase in the growth temperature.

The average column sizes obtained from AFM, SEM, and TEM are included in Fig. 5-23 (a) to compare with the fitting results. The experimental and fitting results are consistent in trend, although the absolute values obtained from the AFM and SEM are larger than the TEM and fitting result. The overestimation of lateral size in AFM is well-known as “tip convolution”, which occurs when the feature size is comparable to or smaller than the AFM tip[237]. For SEM, “tip convolution” is also expected when the feature size is similar to the electron wavelength. The convolution and the nature of its 2-dimensional surface projection cannot reflect the real 3D size which may lead to overestimation of the lateral sizes of particles with blurred edges[238]. Despite the difference in absolute values, the fitting result of the CeO_2 lateral coherence length shows a good agreement with the experimental CeO_2 column size in trend (an increase in size with increasing growth temperature), which together verify the role of growth temperature on tuning the CeO_2 lateral size.

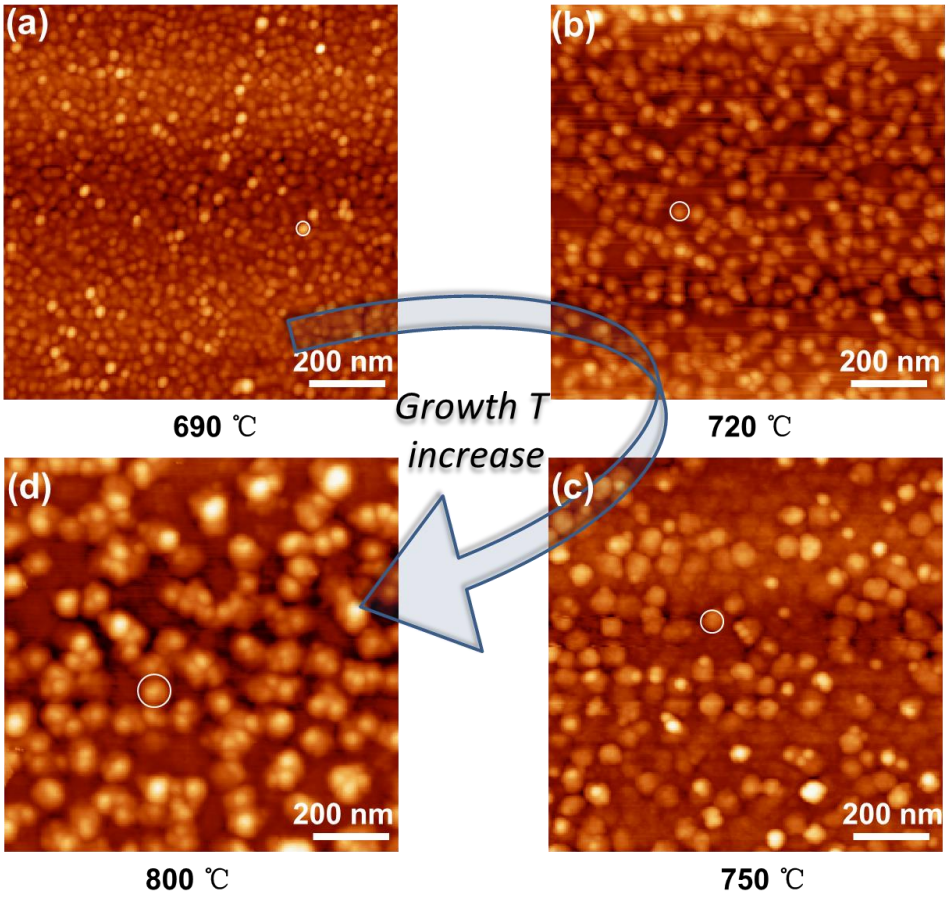

Figure 5-26. Atomic Force Microscopy (AFM) topography image of the LBMO-CeO_2 NC films grown at (a) 690 ℃ (b) 720 ℃ (c) 750 ℃ and (d) 800 ℃.

Based on the above results, W-H plots exhibit several advantages compared to microscopy techniques for obtaining the column size:

1. They are convenient and non-destructive. TEM is known to be the most accurate method for obtaining the size of each phase in a VAN. However, it is destructive to the sample and requires complex processes. In comparison, XRD is a more user-friendly and sample-friendly way to obtain structural information.

2. They are accurate. The consistency between the fitting and TEM result in Fig. 5-23 (a) confirms the accuracy of the W-H plots. Although the alternative non-destructive AFM and SEM can be used to replace TEM, the information obtained is less accurate. The W-H plots exhibit more accuracy, especially when the feature size is comparable or smaller (less than 10 nm) than the lateral resolution limitation of AFM and SEM.

◆ **Schematic model of the simultaneous size evolution**

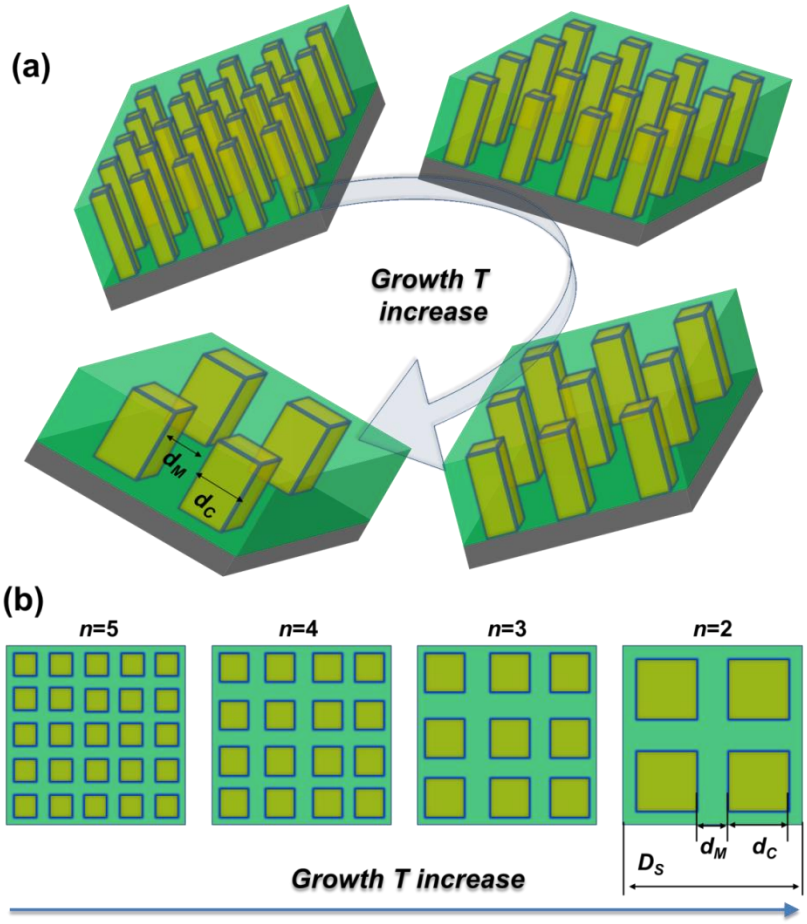

Figure 5-27. (a) 3D schematic illustration for the simultaneous change of column size (d_C) and matrix size (d_M) with increasing growth temperature and (b) the corresponding plan view.

In the nucleation-and-growth mode, the change in the size of the nanocolumns is closely related to that of the matrix networks anchored among them. Since the matrix: column phase ratio is fixed, the only way to respond to a larger diffusion length is by simultaneously expanding the size of both phases. This is consistent with the trend shown in Fig. 5-25 and 5-26: when the column size is larger, the distribution is more sparse, which leaves more space for the matrix in between.

In order to obtain a semi-quantitative relationship between the matrix size (d_M) and column size (d_C), we propose a simplified model of the simultaneous growth of matrix/column, which is illustrated in Fig. 5-27 (a) and stands for VAN structures in

general. For ease of calculation, we assume the columns have a square shape and the whole sample is also square. In the case where the columns are evenly distributed, the relationship between d_M and d_C is obtained using the corresponding plan view diagram in Fig. 5-27 (b), and can be expressed as:

$$n*(d_M + d_C) = D_S \tag{5-15}$$

$$(n*d_C)^2 = \frac{x}{D_S^2} \tag{5-16}$$

where x is the volume ratio of the column phase, n is the number of nanocolumns per row along the side of the whole sample, and D_S stands for the lateral size of the whole sample. For simplicity, the structures with four integer numbers of n (5 to 2) are shown in the structural evolution process. Using equation (5-15) and (5-16), d_C and d_M are determined as below:

$$d_C = \sqrt{x} * \frac{D_S}{n} \tag{5-17}$$

$$d_M = (1 - \sqrt{x}) * \frac{D_S}{n} \tag{5-18}$$

When the volume ratio x is fixed, the two sizes change simultaneously in the following relationship:

$$\frac{d_C}{d_M} = \frac{\sqrt{x}}{1-\sqrt{x}} \tag{5-19}$$

In our NC films, the calculated CeO_2 volume ratio (based on a LBMO:CeO_2 molar ratio of 1:1) is 0.4, and therefore $\frac{d_C}{d_M}$=1.72. This relationship is consistent with the STEM image in Fig. 5-7 (b), where the average LBMO matrix size is 3-6 nm and the CeO_2 column size is 6-10 nm. Using equation (5-19), a linear relationship between the d_C and d_M is obtained, and the simultaneous increase in the column/matrix feature sizes with increasing the growth temperature (Fig. 5-25 and Fig. 5-26) is understood.

5.4.3 Correlation of the physical properties with the microstructure: modulation of the electronic band structure

Having confirmed the direct correlation between the physical properties (taken the T_c as an example) and the lateral size of the CeO_2 phase (more importantly, the LBMO phase), we turn to exploring the origin of this correlation. Recall Chapter 5.1.1, the tuning of T_c and metallicity are closely related to the tuning of the DE coupling which can be ascribed to either a compositional origin (change in band filling) or a structural origin (change in bandwidth). A possible compositional origin is a progressive change in the Mn^{4+}/Mn^{3+} ratio caused by a progressive change in the Ce doping ratio in the LBMO phase. This origin can be directly eliminated, since the T_c evolution of the NCs crosses over that of the PFs, and the NCs grown above 750℃ have higher T_cs than those of the reference PFs (Fig. 5-19 and 20), which cannot be explained by Ce doping. Besides, due to the limited solubility of Ce in the $LaMnO_3$ parent phase[216,217], a saturation in Ce doping amount is expected (as discussed in Chapter 5.3) and thus a progressive change in the Ce doping in LBMO is unreasonable. Also, intermixing in VAN is always favored by a higher growth temperature[38], based on which the postulated result is opposite to the result observed here. Therefore, even though Ce doping is deemed to exist in the NC films, it fails to explain the progressive tuning of the T_c and metallicity with the change in growth temperature. Instead, a structural origin should be a more dominant cause, i.e. a change in the bandwidth irrelevant to chemical substitution. The change in bandwidth can be studied by global structural characterizations (i.e. the change in Mn-O bond angle/length or orbital occupancy reflected by lattice parameters as discussed in Chapter 5.3) or direct, in-depth probe of the band structures. In this part of work, while precise determination of the lattice constant is difficult due to the close overlap of the XRD peaks between the film and substrate, a clear change in the electronic band structure is observed by using X-ray Photoemission Spectroscopy (XPS), as discussed below.

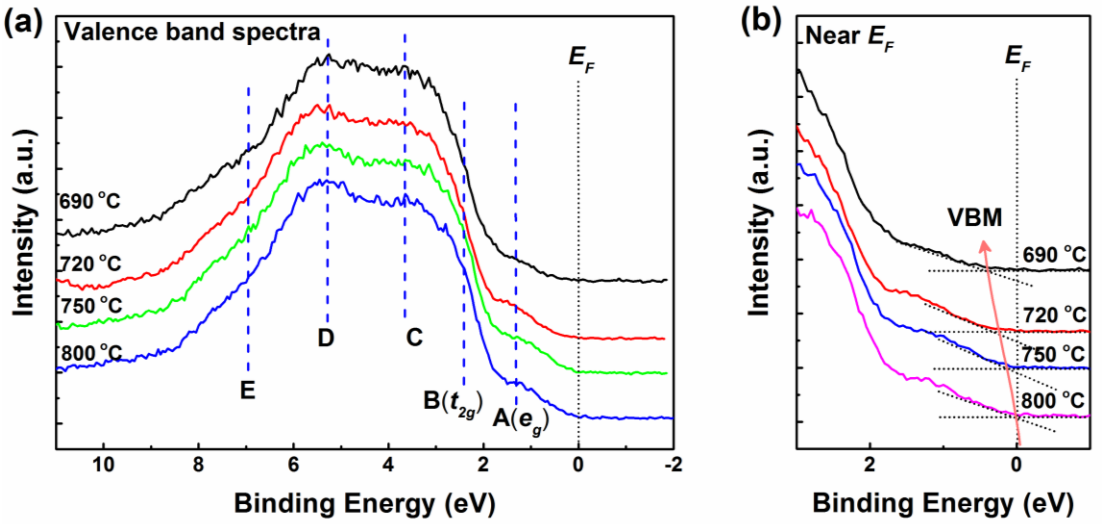

Figure 5-28. (a) X-ray Photoemission Spectroscopy (XPS) valence-band spectra of the LBMO-CeO_2 NC films grown at different temperatures (on Nb:STO (001) substrates). (b) Near-Fermi Level (E_F) spectra of panel (a). The red line shows the trend of the movement of the valence band maximum (VBM).

Fig. 5-28 (a) shows the complete XPS valence band spectra of the NC films. The samples grown on Nb:STO (001) were used to minimize charge effects. As illustrated by the blue dashed lines, five structures can be identified and assigned to[239,240]: A: ~1.32 eV: Mn 3*d* e_g band, B:~2.40 eV: Mn 3*d* t_{2g} band, C: ~3.66 eV: O 2*p* nonbonding band, D: ~5.29 eV: 3*d* t_{2g}-O 2*p* bonding band, E: ~6.96 eV: 3*d* e_g-O 2*p* bonding band. The Fermi level is illustrated by the black dotted lines.

The valence band maximum (VBM) positions were determined by linear extrapolation of the leading edge of the valence band region to the extended baseline of the spectra[188], as shown in the near-E_F spectra (Fig. 5-28 (b)). When the growth temperature is lower, the VBM shifts towards higher binding energies and the density of states near E_F is lower, indicating that the films are more insulating[188], and this is consistent with the change in magnetic and transport properties (Fig. 5-19).

The extrapolated VBM values are plotted in Fig. 5-29, which show an inverse correlation to the trend of the T_c values, the metallicity (the darkness of the shadow) and the CeO_2 column size (obtained by Gaussian fitting). This indicates that the tuning of physical properties (i.e. the decrease in T_c and metallicity with decreasing

growth temperature) with the microstructure evolution (i.e. the decrease in the matrix/column size with decreasing the growth temperature) is correlated to a modulation of the Mn 3*d* electronic band structure (a higher shift of the VBM).

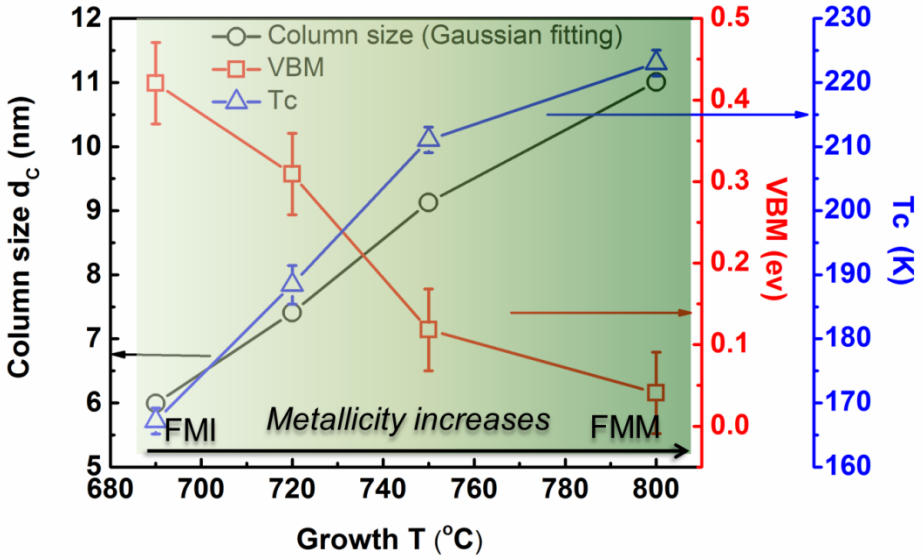

Figure 5-29. Influence of the growth temperature on the valence band maximum (VBM) as a correlation to the change in CeO_2 column size (d_C), T_c and metallicity. The depth of shading represents the extent of the metallicity. XPS instrumental errors are shown as error bars on the VBM values.

This modulation of physical properties with decreasing thin film dimension has been reported in plain manganite films or other perovskites and the origin is controversial, with nonstoichiometry, phase separation, octahedral deformation, modification of Mn-O bond and orbital occupancy being part of this[192–195]. In this work, the XPS results and its correlation to the physical properties are similar to the trend reported in $SrVO_3$[241] films, where a metal-insulator (*M-I*) transition was found with decreasing the thin film thickness, which was correlated to a higher shift of the V 3*d* states located at E_F (reflected as a higher shift of VBM). This dimension-crossover-driven *M-I* transition in perovskite oxides was ascribed to the reduction of the bandwidth and the emergence of a "pseudo" bandgap at E_F due to the absence of density of states[241], i.e. when the bandwidth equals to 0, a band gap forms. Therefore, we conclude here that the structural modulation of the physical properties in LBMO is correlated to the change of the Mn 3*d* e_g electron bandwidth (rather than

band filling): with the decrease in growth temperature, the matrix/column size is decreased, which leads to a decrease in the effective coordination number of Mn and a "pseudo" bandgap and reduction in the bandwidth results[241]. Since the doping effect is excluded here, the only possible origin for the reduction in the bandwidth could be a modification of the Mn-O bond or orbital occupancy as discussed in Chapter 5.1.1. The reduction in the bandwidth essentially reduces the DE coupling, which explains the decrease in T_c and the transition from a FMM to a FMI observed in the LBMO-CeO_2 VAN. For more detailed information on bandwidth, other supporting proofs are needed, such as the O K-edge X-ray Absorption Spectroscopy (XAS) which helps to get a more comprehensive picture of the valence band spectra, and DFT calculation which helps to get theoretical proofs.

This is the first time that a "dimension cross-over" effect in a lightly-doped manganite is realized by modulating the self-assembled kinetics of VAN through growth temperature (instead of by varying the phase ratio reported previously[72]). This dimension modulation enables highly tunable physical properties, and more importantly, the mechanism is probed on a fundamental level, i.e. the tuning of the electronic band structure.

As mentioned in Chapter 2.2.2, FMM and FMI are both important components in MRAM and spintronic devices. In a spin filter device, a FMI acts as the spin filtering layer while a FMM serves as the detection layer for the filtered spin. Integration of FMM and FMI within one device using the same material and composition is intriguing, as this can ease the fabrication process and improve the structural compatibility between device components. This work initiates a direction which leaves more space to study. One effort needed is to reduce the thickness of the FMI component required for spin filter devices.

5.4.4 Influence of the microstructure evolution on the magnetotransport property

The self-assembled VAN structure is an intriguing medium for studying the magnetotransport property due to the existence of the second phase and phase boundaries. It has been reported that a change in the column/matrix phase ratio in VANs leads to a change in the low field magnetoresistance (LFMR) due to the modulation of grain boundary tunneling[63,242]. A general trend is an increase in the LFMR with an increase in the phase ratio of the insulating column, which favors electron tunneling under magnetic fields. As an alternative way, when the column phase ratio is fixed, a simultaneous change in the column/matrix size should also produce similar effects on the magnetotransport. In this section, a switching of the dominant MR mechanism is found with changing the nanocolumn/matrix size.

To study the MR effect of the four NC films, *R*–*T* curves were measured with (9 T) and without (0 T) a magnetic field, as shown in Fig. 5-30. The data of two reference PFs (grown at 720℃ and 800℃) are shown in Fig. 5-31. In both the PFs and NCs, the magnetic field brings about a negative MR ($\frac{R_{9T}-R_{0T}}{R_{0T}}$<0) as well as an increase in the T_M. In the CMR mechanism, this is because the application of a magnetic field favors the alignment of spins and DE electron hopping, which is more sensitive near the phase transition temperature (T_c)[168]. The extrapolated MR values at different temperatures are summarized in Fig. 5-32. Here the MR is defined as $\frac{R_{0T}}{R_{9T}}$. The MR maximum (as marked by the arrows) of the NC films grown at 720℃, 750℃ and 800℃ appear at 175 K, 200 K and 225 K, respectively, which are close to the corresponding T_cs, and the maximum MR values of these three VANs are on a similar level (between 5 and 6). Therefore, the magnetotransport of these films are dominated by the intrinsic CMR effects. A slight upturn of the MR value is observed below 75 K in the VAN grown at 720℃, and thus upturn is absent in the other two VANs. Interestingly, the MR of the VAN grown at 690℃ monotonously increases with the decrease in

temperature and is >40 below 25 K. Under such a high magnetic field (9 T), an intrinsic MR is expected. However, unlike the other three NC films, no MR maximum is observed in this film around the T_c (~170 K), although an inflection point is shown at around 125 K (marked by the black arrow in Fig. 5-32). This inflection is likely from the contribution of the intrinsic CMR effect, which is, however, largely surpassed by another larger MR effect with the decrease in temperature.

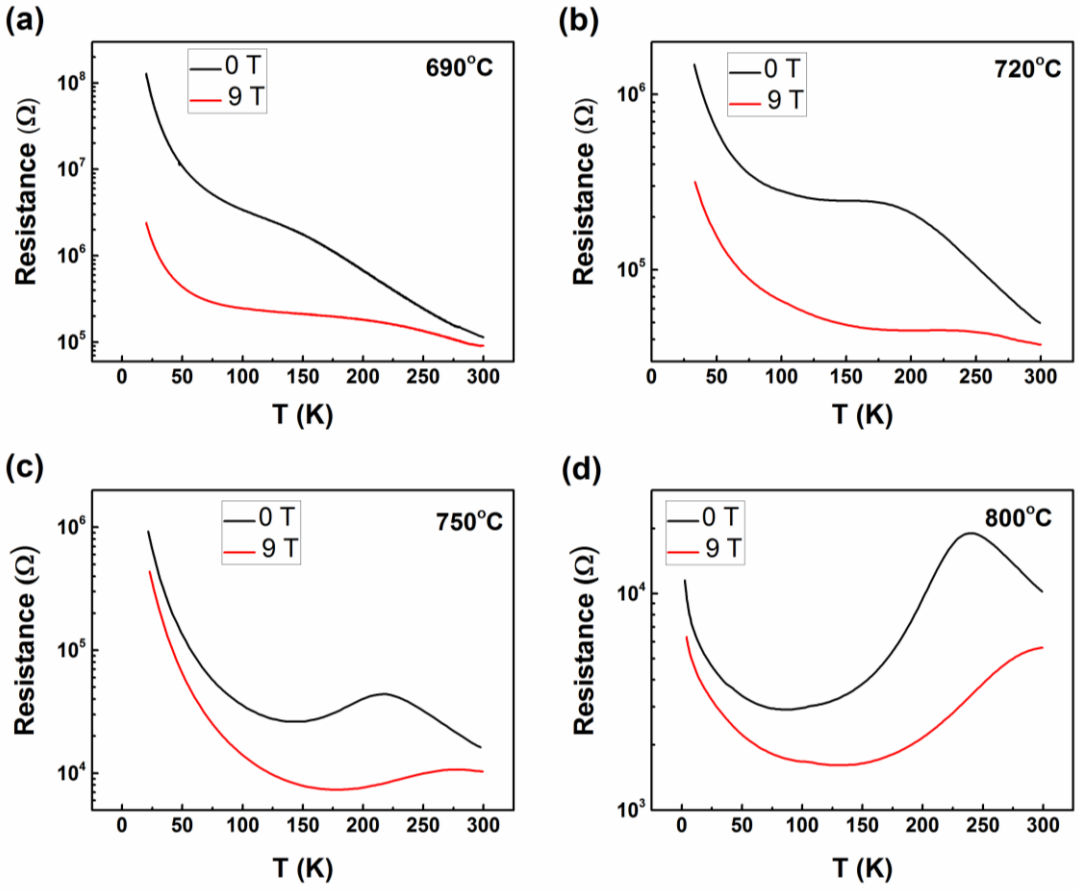

Figure 5-30. Magnetoresistance of the LBMO-CeO_2 NC films grown at different temperatures. (a) 690℃, (b) 720℃, (c) 750℃ and (d) 800℃. The applied magnetic field was 9 T and parallel to the surface of the films.

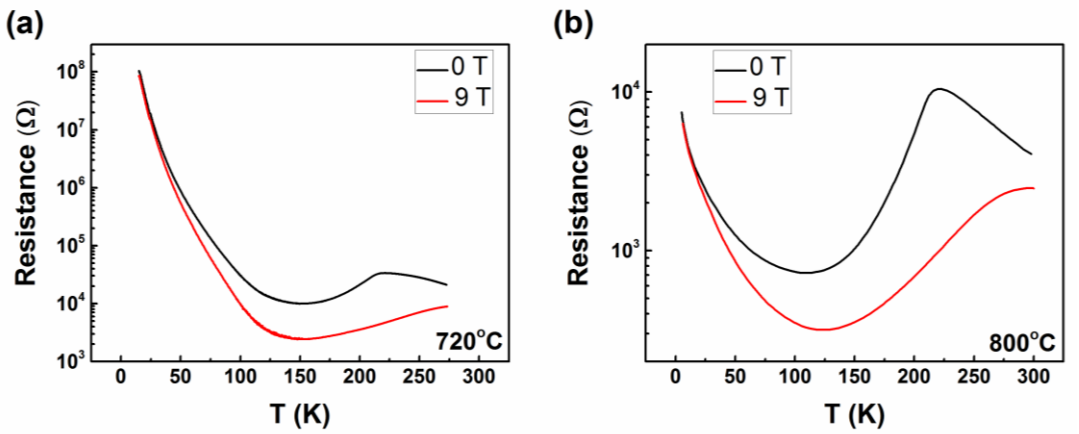

Figure 5-31. Magnetoresistance of the LBMO PFs grown at (a) 720 ℃ and (b) 800 ℃. The applied magnetic field was 9 T and parallel to the surface of the films.

In comparison to the NCs, all the LBMO PFs show a typical CMR (as plotted in Fig. 5-32 (b)), with the maximum MR shown at a constant temperature (around 225 K) irrespective of the growth temperature, and the MR values being much smaller at other temperatures, especially at low temperatures. This precludes any contribution from the growth temperature alone on the observed huge change in the magnetotransport properties of the NCs discussed above.

In the light of the above results, when the growth temperature is decreased, the dominant magnetotransport mechanism (which gives the MR maximum) in the NC films is the result of competition between different mechanisms and has a tendency to switch from intrinsic CMR to extrinsic effects. This unique effect in the NC is closely correlated to the decrease in the lateral size of the two phases, as similar results have been reported in polycrystalline $La_{0.67}Ca_{0.33}MnO_3$ (LCMO) bulk samples: when the grain size is reduced, the intra-grain CMR is replaced by inter-grain MR whose maximum is unrelated to T_c[167]. The phase boundary in the LBMO-CeO_2 VAN is similar to the grain boundary in polycrystalline LCMO. As discussed in Chapter 5.3, the intrinsic conduction mechanism of the LBMO phase at low temperature follows the VRH model, where the localization length ξ of the LBMO phase reflects the conduction length scale at low T. When the average LBMO matrix size d_M is comparable to the localization length ξ, while the phase boundary and the insulating

CeO_2 phase may have no contribution to intrinsic conduction in the absence of a magnetic field, they should act as effective tunneling barriers when a magnetic field is applied, and the spin-dependent tunneling has a high tendency to occur with the assistance of the magnetic field. This is similar to the TMR effect in granular systems or ferromagnetic tunneling junctions[72,168]: with a magnetic field applied, the alignment of the spins in the adjacent LBMO domains favors electron tunneling through the insulating CeO_2 barrier, which provides another route for current conduction.

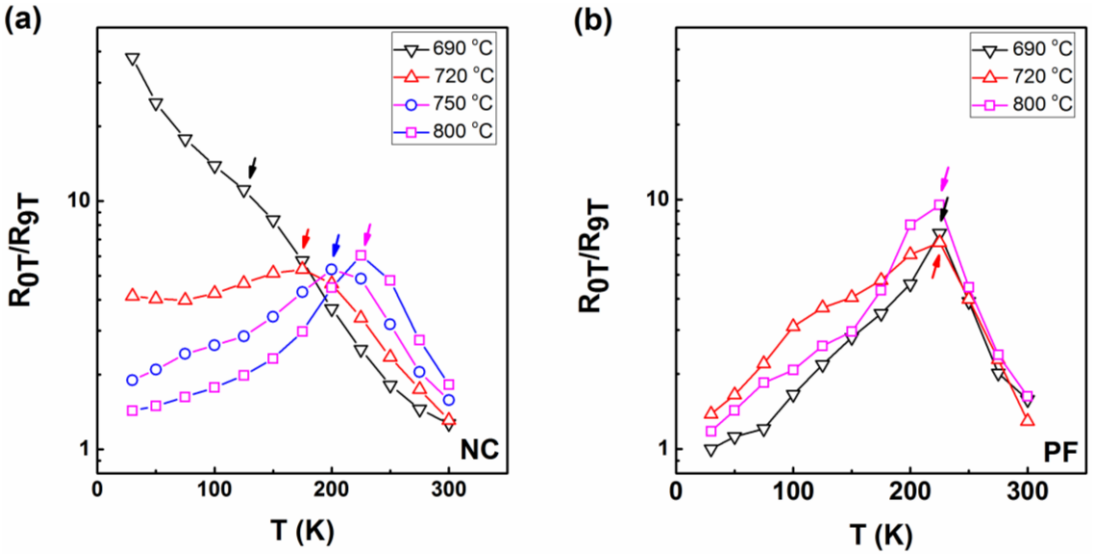

Figure 5-32. Summary of the magnetoresistance ($\frac{R_{0T}}{R_{9T}}$) values with varying the growth temperature: (a) the LBMO-CeO_2 NCs and (b) the LBMO PFs.

When the CeO_2 insulating barriers are thinner and more densely embedded in the LBMO matrix (corresponding to the cases where the LBMO and CeO_2 phases have smaller lateral sizes), the electron tunneling barrier height is reduced and the resulting tunneling probability is higher, as tunneling under a magnetic field can result in a much smaller conduction electron path[63,72,138,242]. At temperatures well below T_c, the CMR effect is weak and the electron conduction is controlled by VRH hopping. At the same time, spin alignment is more favorable under the application of a magnetic field. Thus the TMR effect in the vertical LBMO/CeO_2/LBMO junctions can contribute more strongly to the magnetoresistance[72] which results in a monotonous increase of

the MR with decreasing the temperature. This is the case for the NC film grown at 690℃. On the other hand, when d_M is much larger than ξ, the existence of the phase boundary and second phase has little contribution to the tunneling effect at low T as the tunneling barrier is high, and intragrain conduction is more favorable, therefore only an intrinsic CMR effect is exhibited. This is the case for the NC films grown at ⩾ 720℃.

The above results indicate that tuning of lateral feature size is a new and more convenient way of tuning the physical properties of VANs and for the design of memory devices using different MR mechanisms simply through self-assembled dimension control.

5.5 Summary

In this chapter, we have made use of the sensitive nature of lightly-doped manganite to external stimuli to nanoengineer the functionality of LBMO using VAN approaches by controlling the composition, strain, dimensionality and self-assembly dynamics, which are otherwise hard to achieve in single-phase plain films.

First, a long-standing problem that the FMI properties in the bulk of lightly-doped manganites are difficult to be maintained in thin films has been addressed, and we suggest one way to overcome this problem: via VAN doping and strain. The films are engineered to reduce the unwanted DE coupling shown in plain LBMO films and maintain the FMI property by embedding CeO_2 nanocolumns which provide homogeneous vertical strain and light Ce doping to fill in cation vacancies. These provide new routes to tuning high-performance spintronic and multiferroic devices.

Then, by changing the growth temperature of the LBMO-CeO_2 VAN films, the LBMO phase can be tuned from a FMI to a FMM, which is related to the simultaneous tuning of the lateral size of the CeO_2 and LBMO phases, and this dimensional change is mediated by the growth kinetics of the self-assembly process. The structural tuning of physical properties is correlated to a shift of the valence band

maximum detected by XPS, and modulation of the Mn 3*d* e_g bandwidth is suggested as the origin. This versatile tuning approach provides a new route to creating a broad spectrum of applications for manganite thin films, ranging from spin filtering to spin detection layers in MRAM and spintronic devices. Besides, a study on the magnetotransport reveals a transition from intrinsic CMR to extrinsic TMR effect with a decrease in the column (and matrix) size, which provides a new way to design memory devices using different MR mechanisms.

Compared to PFs, multilayers, or superlattices which need artificial design, the VAN structure shows a much improved capability to tune physical properties because of its unique structural configuration and the highly tunable self-assembly kinetics. The tuning of column size also exhibits superior capability than changing the phase ratio, as only one target is needed for the whole work whilst generating a similar effect.

Chapter 6 Growth of the $La_{0.9}Ba_{0.1}MnO_3$–ZnO VAN and study on the electric field tuning of magnetic properties

In this chapter, a new magnetoelectric candidate system, the manganite-ZnO VAN, is studied. This chapter begins with an introduction on magnetoelectric effects, the limitation in conventional planar structures and the advantage for the VAN structure to realize magnetoelectric effects, based on which the materials system is selected as the $La_{0.9}Ba_{0.1}MnO_3$-ZnO VAN. Part two discusses the growth of LBMO-ZnO VAN on different Nb:STO substrates and it is found that when grown on Nb:STO (111), an enhanced resistive switching effect is shown and the leakage current can be controlled. Then part three presents results on *in-situ* electric field tuning of magnetic properties of this sample. The *M-H* curves and the remanence are tuned by applying electric fields at a low temperature (10 K). The possible origins for the magnetic modification are discussed rationally, which include Joule heating, piezoelectric strain, current-induced induction field and charge trapping/detrapping effects related to the resistive switching effect (which is found to be the most likely mechanism for a hysteretic tuning of the remanence). All of these effects are correlated to the existence of the ZnO phase. In this work, I made the films and collected all the data.

6.1 Literature review

It has long been believed that alteration of the properties of magnetic materials is difficult once they have been produced. However, in strongly correlated systems, lattice-spin-orbital-charge coupling makes this possible[243]. As discussed in Chapter 2.2.2, magnetoelectric (ME) coupling provides a low power consumption route for the data to be written in magnetic storage devices[36] and is also useful in devices where multiple spin and charge signals are used to carry information[244]. To date,

single-phase ME candidates, such as Cr_2O_3, $EuTiO_3$ are fascinating, but most of them are limited by their low Curie Temperature or weak coupling effects, which hinders their implementation in practical applications[244,245]. The search for single-phase multiferroic materials is also constrained by the mutually exclusive nature of ferromagnetism (FM, requiring unpaired electrons coming from partially filled *d* orbitals) and ferroelectricity (FE, requiring off-center distortion, which is reduced by *d* electrons)[76,246]. In composites, these constraints are much lifted, as the ME coupling arises from interfacial coupling between the constituent phases[245]. This provides a platform for engineering and designing of optimal properties by varying composite combinations and configurations.

6.1.1 Magnetoelectric (ME) coupling mechanisms in composites

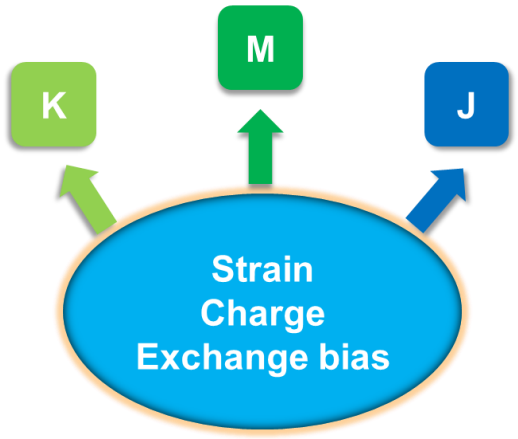

Figure 6-1. Schematic diagram showing the magnetic parameters that are amenable to modulation as a consequence of strain, charge modulation and/or exchange bias. (*K*, *M*, and *J* stand for the magnetic anisotropy constant, the saturation magnetization and the exchange constant respectively.)

This chapter studies on the tuning of magnetic properties via electric fields, often defined as the converse ME effect. According to Vaz *et al.*[244], in composite structures (nanostructured composites or thin film heterostructures), ME coupling can be realized through the modulation of the magnetic anisotropy constant *K*, the saturation magnetization *M* and the exchange constant *J* via strain coupling, charge doping and/or exchange bias, as illustrated in Fig. 6-1.

1. Strain. Strain coupling is an indirect way to achieve ME effects, where the converse piezoelectric (or electrostrictive) effect of a piezoelectric (or electrostrictive) phase (usually a FE material) generates crystal deformation under the electric field, and the magnetostrictive (or piezomagnetic) FM (or FIM) phase responds to the deformation by changing its magnetic properties, e.g. the magnetoelastic anisotropy energy is modified due to the change in the magnetic interaction arising from the change in the atomic distances and exchange interactions[247]. Here "piezo-" is exclusively defined as a linear response of electrical/magnetic polarization to stress and "converse piezo-" is defined as the linear response of deformation to electric/magnetic fields, while "-strictive" applies to systems which follow a quadratic relationship[36]. Such a coupling is the product of two distinct interactions and thus an intimate contact and effective elastic coupling between the two phases are important. Besides, a sizable ME coupling requires a large piezoelectric coefficient and a large magnetostriction effect in the constituent phases. There are several widely-studied candidates for strain-mediated ME coupling in the perovskite–spinel composites, such as $BiTiO_3$-$CoFe_2O_4$[245], $BiFeO_3$-$CoFe_2O_4$[248] and $Pb[Zr_xTi_{1-x}]O_3$-$CoFe_2O_4$[249], where the strong magnetic anisotropy of $CoFe_2O_4$ yields a strong converse magnetostrictive response to the strong converse piezoelectric effect from the FE component.

2. Charge. Charge-mediated ME coupling is a purely electronic effect. In materials where the magnetic properties are closely linked to charge carrier density (with hole-doped manganites being an example), a modulation in carrier doping level results in a change of the magnetic properties (e.g. the magnetization or magnetic moments). Charge effect usually occurs in a FE/FM interface and the mechanism is similar to the gating effect in a field effect transistor[244]: The FE oxide acts as a gate dielectric, and polarization is induced when applying an electric field. The polarized charges are then screened by the charge carriers in the FM channel layer, where a charge accumulation or depletion is induced depending on the polarization direction. This results in large changes of the magnetic moment of the FM layer in different polarization states of the FE layer[245]. For example, in the

$La_{1-x}Sr_xMnO_3$(LSMO)/$Pb[Zr_xTi_{1-x}]O_3$(PZT) heterostructure, the magnetization in LSMO is sensitive to the polarization state of PZT under the electric field, which induces depletion/accumulation of hole carriers in LSMO. The resulting modulation in the Mn^{3+}/Mn^{4+} ratio has a big influence on the DE coupling[247,250].

2. Exchange bias. Exchange bias (EB) effect exists in FM/antiferromagnetic (AFM) interfaces: upon cooling the system below the Neel temperature (T_N) of the AFM layer while keeping the FM layer in the saturated state ($T_c<T_N$), the interfacial exchange coupling gives rise to a directional biasing where the magnetic hysteresis loop has a shift along the magnetic field axis[251]. EB-mediated ME coupling links the charge polarization with the spin configuration in a FE AFM layer (such as $BiFeO_3$), and through the EB effect between the AFM layer and an adjacent FM layer, the magnetic spins of the FM layer can thus be manipulated through direct exchange coupling[245].

6.1.2 Constraints of conventional ME coupling systems

To date, most works on strain and charge-mediated ME coupling are studied in planar composites with coexisting FM and FE phases, which limits the performance of the materials system due to several constraints:

1. For strain-coupling systems, the most common configuration is a FM layer grown on a FE substrate or a FM/FE bilayer structure grown on a non-FE substrate, as shown in Fig. 6-2 (a) and (b). For single-layer films, the selectivity of a proper FE substrate is limited to several phases such as $BaTiO_3$ or the toxic PZT. For bilayer films, the effective in-plane strain that couples the FM and FE layer is parallel to the substrate, which is largely clamped by the stiff, large volume, underlying substrate[76].

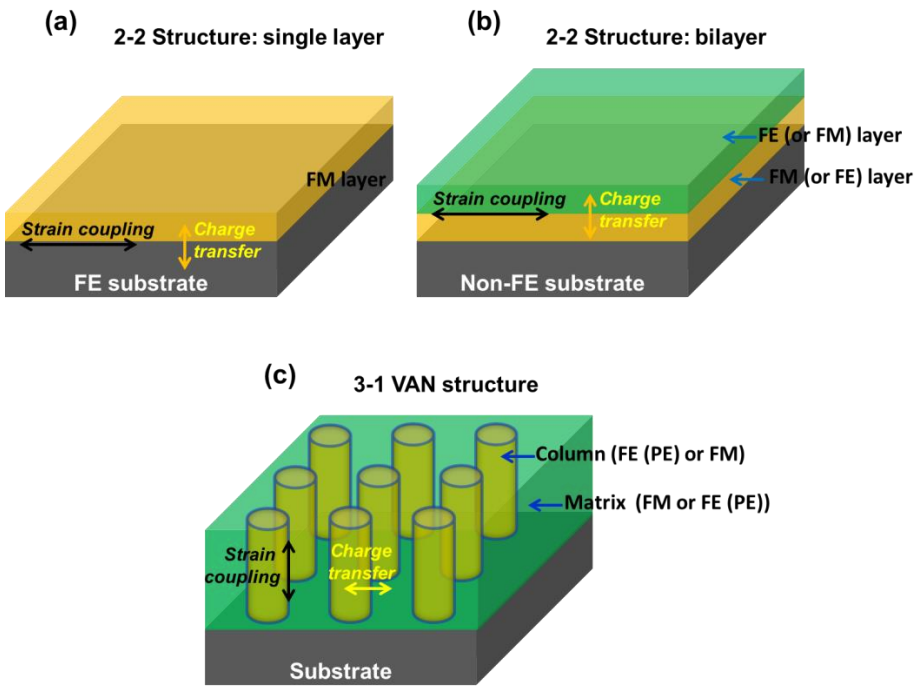

Figure 6-2. Schematic diagram of the ME coupling in different composite configurations: (a) single-layer 2-2 structure (b) bilayer 2-2 structure and (c) self-assembled VAN 3-1 structure. The black and yellow arrows illustrate the direction of strain coupling or charge transfer, respectively.

2. For charge-doping systems based on the gating effect, the charge accumulation/depletion depth is confined by the screening length of the FM material, which is determined by the charge carrier density of the material. In hole-doped manganites, the carrier density is on the order of 10^{21} cm^{-3}, and the corresponding screening length is only a few unit cells[252]. Therefore, charge-mediated ME coupling in FE/FM heterostructures is detectable only when the FM layers are ultrathin.

3. In both cases, the search for an optimized FE/FM combination with optimized structural compatibility is challenging, since there are only limited choices for candidate FE phases which have good compatibility with the FM phase.

These three constraints can be reduced in the following ways: (1) reducing the substrate clamping through the design of structures other than 2-2 planar layouts (e.g. nanostructured composites)[76], (2) increasing the scale of charge doping by introducing more interfaces and using other routes to tune the carrier concentration (using resistive switching effect is one alternative), and (3) expanding the selectivity by

reducing the constraints for the constituent phases (e.g. replacing the FE phase with non-FE piezoelectric phases[77,253], or replacing the FM phase with AFM phases). In this work, we aim to address these problems. In the following discussions, we will discuss firstly on the structure design and then on the materials selection.

6.1.3 VAN: A candidate platform for ME coupling

Compared to 2-2 planar films, the VAN structure (a 1-3 configuration, as shown in Fig. 6-2 (c)) has an enormous number of nanocolumns vertically embedded in a matrix, providing a huge amount of nano-scale coupling in the vertical direction. Since the effective strain coupling is perpendicular to the substrate plane, the substrate clamping effect is minimized. Thus, in theory, a large strain coupling is expected in the VAN structure. This has been realized in one of my collaboration works[76].

As for the charge doping mechanism, it is not easy to mimic the field gating effect using the charge screening approach in VAN structures, as the direction of the applied electric field in a two-probe configuration is parallel to the vertical interfaces, while the charge screening should occur perpendicular to this direction (shown in Fig. 6-2 (c)). Therefore, an alternative charge-doping approach needs to be considered. One solution is to use an interdigitated electrode to generate an in-plane electric field. However, this is limited by the penetration depth of the electric field[254]. Alternatively, one can make use of the unique VAN structure and focus on modulation of the carrier concentration of the FM phase near the electronically active vertical interfaces, where the carrier mobility is highly tunable under an electric field (Recall Chapter 4 and other resistive switching works in VANs[122,129]).

In contrast to the 2-2 structures, the VAN structure suffers from a shortage arising from the unburied vertical interfaces without any current blockage, which, in addition to the matrix and column phases, may generate an extra leakage source when applying an electric field[76]. As discussed in Chapter 4, one reason for the leakage from the vertical interface is the defects or the structural mismatch between the two

phases[128,149]. Since this vertical interface conduction is closely related to the crystallographic matching[128], the leakage can be controlled by delicate selection of phase combinations or control of crystallographic orientations. Besides, leakage from the matrix/column phases can also be reduced with careful structural design[76]. In this work, this problem is addressed by growing VAN films on different substrates, as discussed later.

6.1.4 Selection of materials

◆ **$La_{0.9}Ba_{0.1}MnO_3$: a ferromagnetic insulator sensitive to external forces**

As discussed above, the FM phase in a ME VAN needs to have minimized leakage, and therefore, the lightly-doped $La_{0.9}Ba_{0.1}MnO_3$ (denoted as LBMO hereafter, which is ferromagnetic insulating in bulk or VANs) is a proper candidate. The comprehensive study in Chapter 5 revealed the sensitive nature of LBMO to structural and compositional perturbations in VANs via growth control. Here, using the ME coupling between another phase through an electric field is an alternative route to tuning the magnetic properties in manganites. On one hand, volume magnetostriction ($\sim 10^{-4}$ at 8.2 kOe) has been reported in $La_{1-x}Ba_xMnO_3$ in bulk[255]. When a tiny level of structural perturbation exists, $La_{1-x}Ba_xMnO_3$ can likely respond with a change in magnetoelastic anisotropy or Jahn-Teller distortion, inducing a change in magnetic exchange interactions or anisotropy[256]. The structural perturbation under an electric field can be generated by coupling with another phase possessing piezoelectricity (or electrostriction). On the other hand, chemical doping of manganites can be induced by charge doping near the vertical interface in a VAN. As the LAMO (A=Ca, Sr, Ba) family is more sensitive to carrier concentrations[257] in the lightly doped regions (recall the phase diagram in Fig. 5-4), chemical doping can generate a similar effect as shifting of the phase diagram[258] along the doping level axis.

◆ **ZnO: a candidate second phase**

ZnO has a wurtzite phase under ambient conditions, with a hexagonal closed-packed

(*hcp*) unit cell of 6-fold symmetry. The unit cell of ZnO is shown in Fig. 6-3 (a): Zn atoms form *hcp* arrays and O atoms occupy half of the tetrahedrally co-ordinated sites. Such an atomic arrangement results in a noncentrosymmetric ZnO crystal comprising alternating Zn and O layers stacking along the *c* axis[259]. Two lattice parameters are used to describe the unit cell of ZnO: *a* (3.25 Å, which is the edge length of the hexagon basal plane) and *c* (5.21 Å, which equals to the height of the unit cell), as shown in Fig. 6-3 (b).

Due to the unique crystal structure stacking, two distinct properties are shown in ZnO, which are part of the reasons for selecting ZnO as the second phase of the VAN in this work:

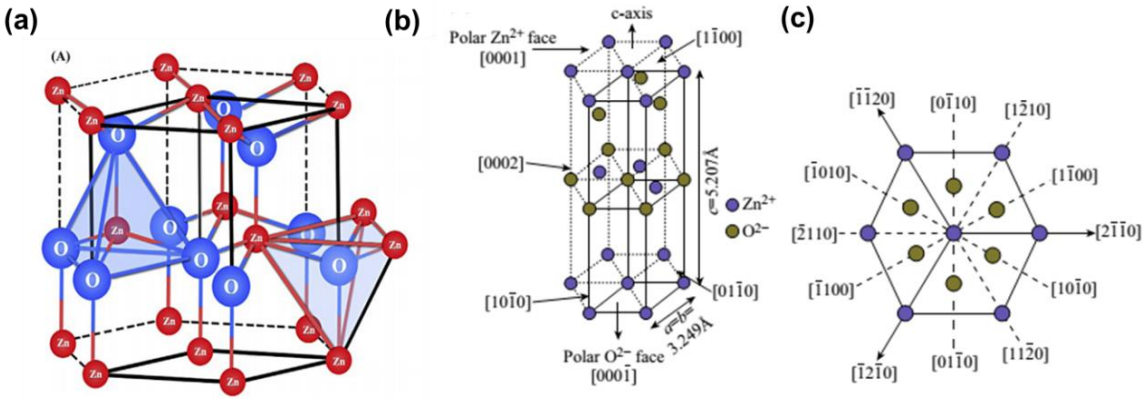

Figure 6-3. (a) The hexagonal wurtzite crystal structure of ZnO (Figure taken from[259]). (b) and (c) illustrations on various crystal orientations and planes of the ZnO crystal (Figure taken from[260]).

1. *Piezoelectricity*: The ZnO unit cell possesses a lack of center symmetry, which is a basic requirement for the existence of piezoelectricity. The piezoelectric coefficient is the ratio of the induced strain *vs*. the applied electric field or the ratio of the polarization *vs*. the external stress[261]. The highest reported piezoelectric coefficient of ZnO at room temperature is d_{33}=12.84 pC/N[262,263]. Here, d_{33} stands for the piezoelectric coefficient corresponding to the piezoelectric response along the *c*-axis (i.e. strain in the *c*-axis, ε_3) with respect to the external forces in the *c* axis (i.e. electric field applied along the *c*-axis, E_3). This means that ZnO with *c*-axis growth mode can show the maximum converse piezoelectric effect (and thus the maximum induced

strain) when an electric field is applied along the *c*-axis. In the case of a linear piezoelectric effect, $\varepsilon_3=d_{33}E_3$.

2. *Polar surfaces*[259,264]: In single-crystal ionic materials with a lack of centrosymmetry, there are certain crystal planes where the projection of the dipole moment is not zero with respect to the bulk unit cell on the surface normal, and these planes are called "polar surfaces".

The dipole moment of the ZnO bulk unit cell is directed along the [0001] orientation. As shown in Fig. 6-3 (b) and (c) and Fig. 6-5 (b), there are mainly two kinds of crystal planes in the ZnO crystal, each having different charge polarities due to different atomic arrangements:

a. The low-index planes such as $(10\bar{1}0)$ and $(11\bar{2}0)$ have stoichiometrically exposed and mixed-terminated Zn and O atomic arrangements and therefore they show no charge polarity or electrostatic instability.

b. The basal planes such as Zn-terminated (0001) and O-terminated $(000\bar{1})$ planes are both polar due to the unequal stacking of Zn and O atoms, which implies that a permanent dipole moment exists along the *c*-axis.

For polar surfaces, a finite dipole moment is generated per surface unit cell, which gives rise to an electrostatic field scaling with thickness, and this makes the surface electronically unstable. This instability can be removed through charge transfer with other surfaces, surface reconstruction, or absorption of other polar particles. This indicates that: (1) surface charge may exist in some planes of ZnO which induces a certain level of carrier mobility and (2) when *n*-type ZnO is vertically aligned with *p*-type manganites, charge transfer can likely happen in the vertical *p*-*n* junction, and the carrier mobility along this interface is likely to be different after different ways of vertical matching.

Manganite-ZnO VAN is a candidate FM-nonFE combination as proposed in Chapter 6.1.2. The growth of manganite-ZnO VAN systems has been well-studied[43,63,73,213,242], but ME works were seldom reported. Giant electric field

tuning of ferromagnetism was previously realized in a double-perovskite manganite ferromagnetic insulator La_2CoMnO_6 (LcMO) via the ZnO phase, where a giant electric field modulation of the magnetic moments and *M-H* curves were reported. The effect was ascribed to a modulation of the charge carrier concentration in the LcMO phase via the carrier trapping/detrapping effect near the LcMO-ZnO vertical interface and it generated an effect equal to a temperature increase of 70 K[77]. However, the origin was not adequately explained and the detailed role of the carrier trapping/detrapping was not well studied. Besides, the current leakage and its related heating effect was not quantitatively analyzed.

Triggered by the requirement for reducing the leakage and studying the underlying mechanism more adequately, we worked on another manganite-ZnO VAN system: LBMO-ZnO, and proposed two ways to realize ME coupling:

1. Strain tuning of the LBMO phase using the piezoelectricity in the ZnO phase. The tuning can occur as a change in the magnetic anisotropy or magnetic interactions. Since the piezoelectric coefficient of ZnO (12.84 pC/N) is small compared to that of PZT or BTO (>100 pC/N), theoretically the strain effect generated by ZnO should be weak. As mentioned above, in order to enhance the strain coupling, ZnO should have a (0001) preferred growth orientation.

2. Charge doping of the LBMO phase through ZnO. This may happen in a more complex way. The vertical epitaxy between ZnO and LBMO can provide vertical interfaces with active charge carriers, and the carrier mobility can be tuned via charge trapping/detrapping by an electric field. This can tune the carrier concentration of the LBMO phase near the interfaces, and due to the existence of enormous vertical interfaces where trap sites exist, this tuning can in theory be observable. However, the enhanced carrier mobility may also induce current leakage, and we aim to control this leakage by controlling the crystallographic matching.

6.2 Growth and characterization of the $La_{0.9}Ba_{0.1}MnO_3$–ZnO VAN on Nb:STO substrates

$La_{0.9}Ba_{0.1}MnO_3$(LBMO)-ZnO (molar ratio 1:1) nanocomposites (NC) and reference $La_{0.9}Ba_{0.1}MnO_3$ (LBMO) plain films (PF) were grown on 0.5 wt.% Nb-$SrTiO_3$ substrates via a one-step process using pulsed laser deposition (PLD) with one composite target. During deposition, the oxygen partial pressure and the growth temperature were maintained at 0.2 mbar and 770℃, respectively. The laser repetition rate and fluence were 2 Hz and 1 J/cm^2, respectively, and the thickness of the films was around 100 nm. After deposition, the films were cooled down to room temperature under an oxygen pressure of 0.4 atm at a cooling rate of 10 ℃/min.

◆ **Epitaxial relationships of the LBMO–ZnO VAN with the Nb:STO substrates**

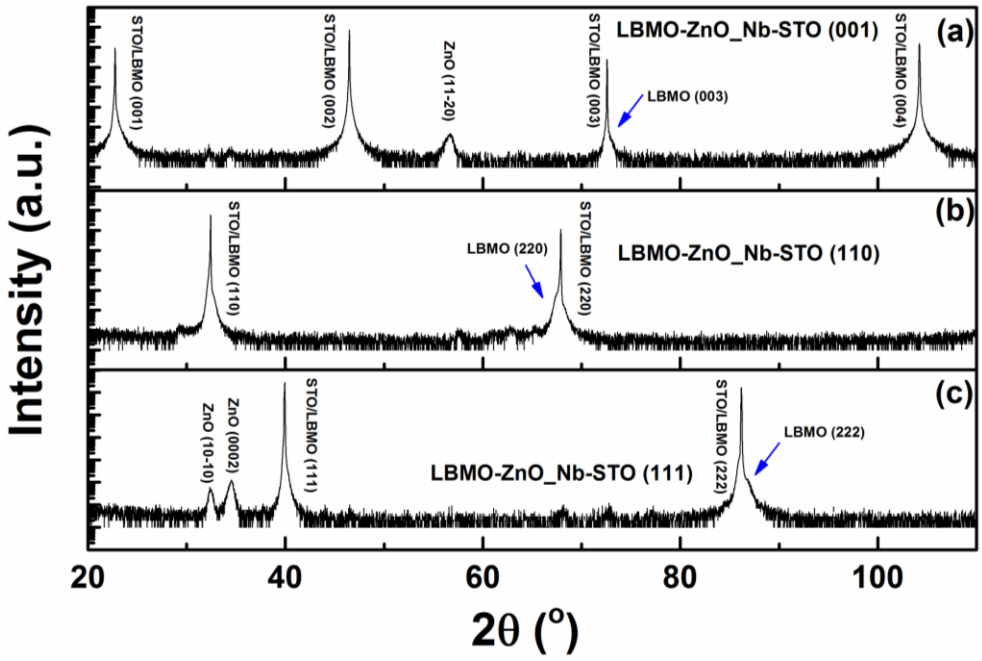

Figure 6-4. XRD *2θ-ω* scans of the LBMO-ZnO VAN grown on the (a) Nb:STO (001), (b) Nb:STO (110) and (c) Nb:STO (111) substrates.

As discussed above, ZnO shows different piezoelectric responses and charge polarities in different crystallographic orientations, and it is known that the growth orientation of ZnO can be adjusted by changing the STO substrate orientations[265].

Therefore, we started by growing LBMO-ZnO VANs on Nb:STO substrates with three different orientations: (001), (110) and (111).

Fig. 6-4 shows the XRD 2θ-ω scans of the three films, and the corresponding epitaxy relationships between ZnO and STO are illustrated in Fig. 6-5. The ZnO $(11\bar{2}0)$ peak is observed (Fig. 6-4 (a)) when grown on the Nb:STO (001) substrate, which indicates that the ZnO hexagonal unit cell lies parallel to the STO (001) plane, showing an in-plane (*ip*) growth mode, with ZnO $(11\bar{2}0)$//STO (001) in the out-of-plane (*op*) direction. As reported in the LSMO-ZnO VANs, the ZnO $(11\bar{2}0)$ unit cell matches well with the STO (001) unit cell after a 45° *ip* rotation[43,63,242], and therefore there is a ~45° angle between the ZnO [0001] orientation and the STO [100] orientation in the *ip* direction, as illustrated in Fig. 6-5 (c).

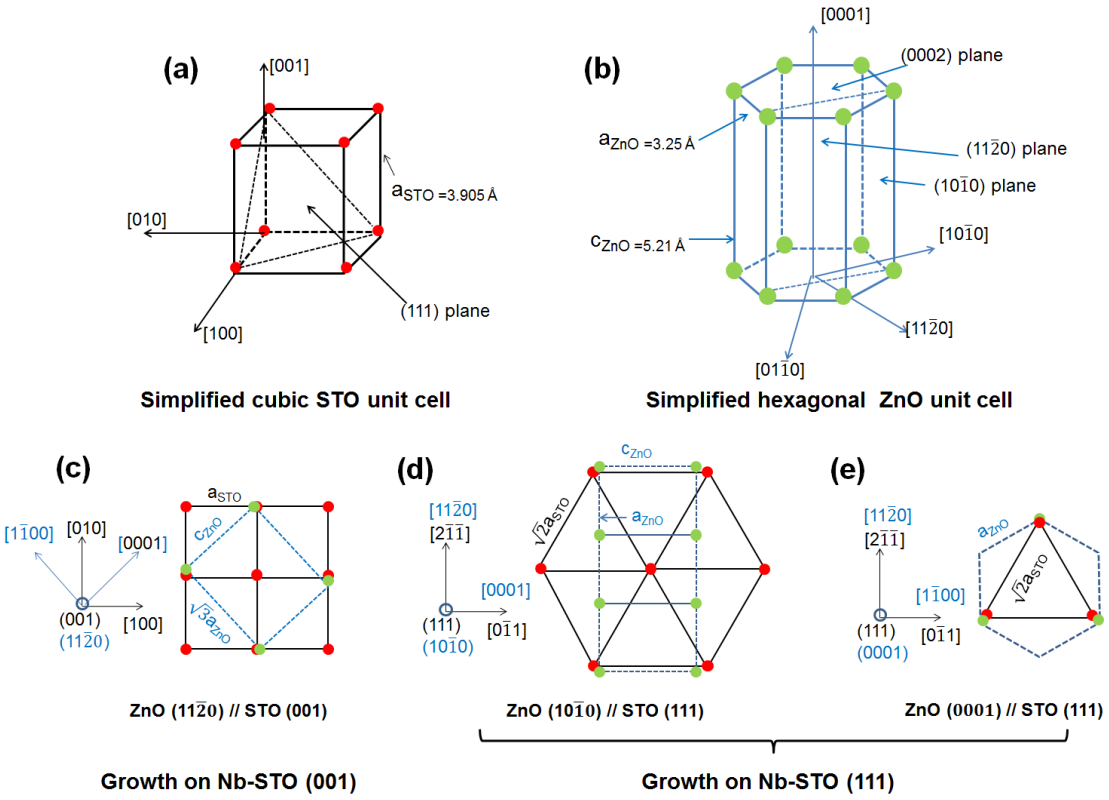

Figure 6-5. (a) The cubic unit cell of STO and (b) the hexagonal unit cell of ZnO. For simplicity, only the atoms on the corners of the unit cell are shown. The epitaxy relationship between the ZnO phase and the Nb:STO substrate: (c) when grown on Nb:STO (001), ZnO $(11\bar{2}0)$ // STO (001). (d) and (e) when grown on Nb:STO (111), ZnO $(10\bar{1}0)$ or (0002) // STO (111). The blue dashed lines and arrows represent the ZnO phase and the black represent STO.

The ZnO ($10\bar{1}0$) and (0002) peaks are observed in the film grown on Nb:STO (111) (Fig. 6-4 (c)). The ZnO ($10\bar{1}0$) peak corresponds to an *ip* growth mode, with ZnO($10\bar{1}0$)//STO(111) and ZnO [0001]//STO[$0\bar{1}1$], while the ZnO (0002) peak corresponds to an *op* growth mode, with ZnO(0001)//STO(111) and ZnO [$1\bar{1}00$]//STO[$0\bar{1}1$]. These epitaxy relationships are shown in Fig. 6-5 (d) and (e), respectively. It is worth noting that the *ip* growth mode in Fig. 6-5 (d) has no 45^o *ip* rotation, which is unlike the film grown on Nb:STO (001) (Fig. 6-5 (c)).

It is noticeable that no discernible ZnO peak is observed when the film is grown on Nb:STO (110) (Fig. 6-4 (b)), even though *c*-axis growth is expected[77]. This is perhaps because the complexity of the *ip* matching between ZnO/STO and *op* matching between ZnO/LBMO makes it difficult for the ZnO phase to show a good crystallinity. In the following discussions, the film grown on Nb:STO (110) will not be discussed.

As for the LBMO phase, when grown on Nb:STO (001), the LBMO (*00l*) peaks nearly overlap with, but are slight to the right of the STO (00*l*) peaks (Fig. 6-4 (a)). When grown on Nb:STO (111), the LBMO (*lll*) peaks are also on the right of the STO (*lll*) peaks (Fig. 6-4 (c)) and the peak intensities are higher. The results indicate that the *op* lattice constant of the LBMO phase is slightly smaller than that of STO (3.905 Å) in both of the two films.

◆ **Comparison of the surface morphologies**

The surface topography and phase images obtained by AFM provide additional proofs to the crystallographic information in Fig. 6-5. As shown in Fig. 6-6 (a) and (b), square-shaped features are observed (marked by dashed blocks) in the film grown on Nb:STO (001), which tend to have a 45^o *ip* rotation with respect to the STO [100] direction. As discussed above, these features are likely from the ZnO ($11\bar{2}0$) grains.

As shown in Fig. 6-6 (c) and (d), two types of features are observed in the film grown on Nb:STO (111), with either a rectangular or a triangular shape (marked by the dashed blocks). The rectangular features are likely from the ZnO ($10\bar{1}0$) grains which match with the STO (111) plane without *ip* rotation, and the triangular ones are

likely from the ZnO (0002) grains. The triangular shape reflects the close-packed nature of this orientation.

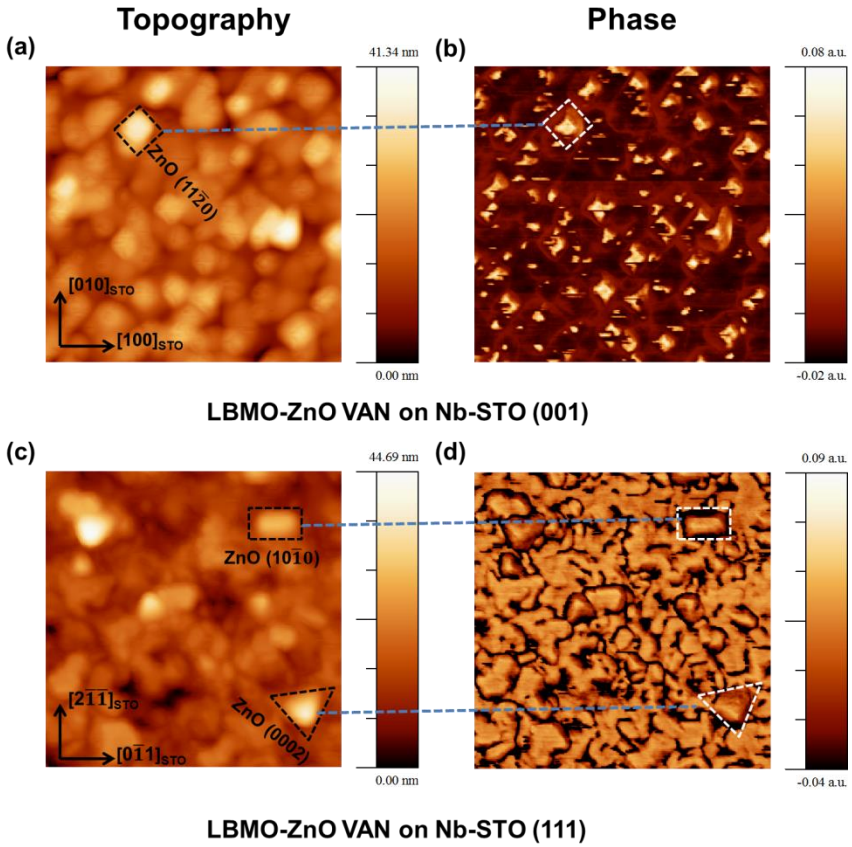

Figure 6-6. AFM (a) topography and (b) phase images of the LBMO-ZnO VAN grown on the Nb:STO (001) substrate. AFM (c) topography (d) and (d) phase images of the LBMO-ZnO VAN grown on the Nb:STO (111) substrate.

The features observed in the AFM are consistent with the schematic diagrams shown in Fig. 6-5 (c)–(e), where the possible shapes and layouts of the ZnO grains are illustrated by the blue dashed lines. The triangular (instead of a hexagonal) shape of the grains observed in Fig. 6-5 (c) and (d) is perhaps due to the difference in surface energies of crystals which determine the termination of the corresponding vertical grain surfaces and grain shapes[54] (as previously discussed in Chapter 2.3.2).

Having confirmed the growth mode and epitaxy relationships of the films grown on Nb:STO (001) and (111), we turn to comparing the magnetic and current leakage properties between the two films, based on which the candidate film for *in-situ* electric field tuning of magnetic properties is selected.

◆ Comparison of the magnetic transition and electrical transport

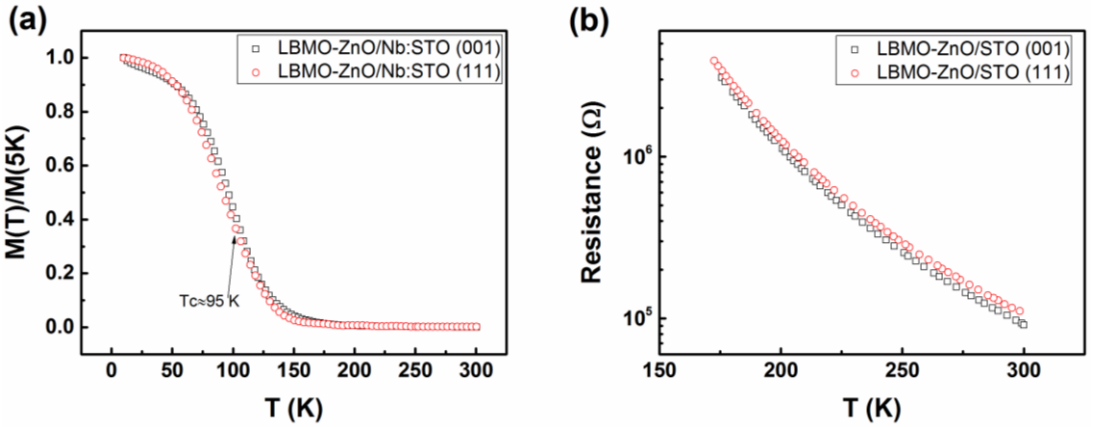

Figure 6-7. (a) Comparison of the magnetization vs. temperature (*M-T*) curves of the LBMO-ZnO VAN films grown on the Nb:STO (001) and (111) substrates. The applied magnetic field for the *M-T* curves was 200 Oe parallel to the film plane. (b) The corresponding resistance vs. temperature (*R-T*) curves of the LBMO-ZnO VAN films grown on the STO (001) and (111) substrates.

Fig. 6-7 (a) shows the Field Cooled (FC) magnetization vs. temperature (*M-T*) curve for the two films. The T_c is kept at around 95 K irrespective of the crystal orientation. The large drop in the T_c, as compared to the LBMO PF and LBMO-CeO_2 VAN in Chapter 4, is perhaps due to the Zn-Mn cross-substitution[266,267] or charge transfer between the *p*-type LBMO and *n*-type ZnO which changes the carrier concentration of LBMO. Fig. 6-7 (b) shows the resistance *vs*. temperature (*R-T*) curves obtained for two samples grown on the corresponding insulating STO (001) and (111) substrates measured using a four-point configuration, which both exhibit insulating transport properties. The resistance values below 170 K are all out of the PPMS measurement range. These results indicate that the intrinsic magnetic and transport property of the LBMO phase is ferromagnetic insulating.

In order to reduce the influence of temperature increase on the change of magnetic properties, the measurement temperature of the *in-situ* electric field tuning of magnetic properties was selected within a temperature region where the magnetization stays relatively flat in the *M-T* curve, which is below 50 K (Fig. 6-7 (a)). Besides, a higher resistance of the film is needed to allow application of high electric fields, and

this requires measurement in lower temperature regions (Fig. 6-7 (b)) as well. Therefore, the electric field tuning measurements were conducted at 10 K.

◆ Comparison of the current leakage in the Pt/LBMO–ZnO/Nb:STO device

We now turn to comparing the current leakage between the two samples. The *I-V* measurements were conducted at 10 K using PPMS with the samples mounted in a 2-probe configuration as illustrated in Fig. 6-8 (a). A 5 mA compliance current was used.

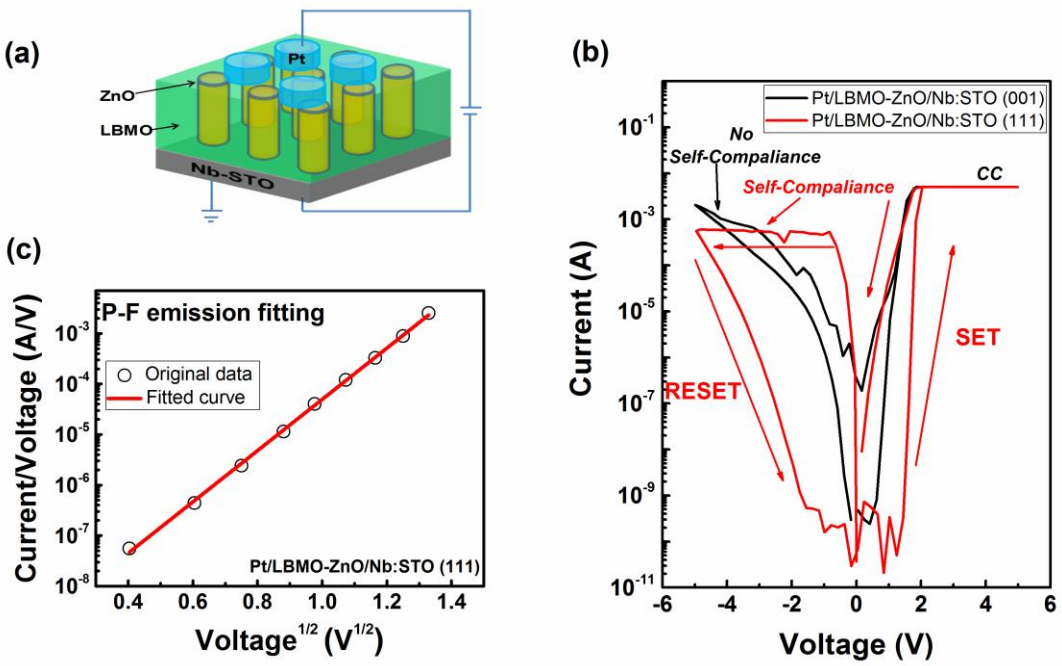

Figure 6-8. (a) Measurement configuration of the *I-V* curves. (b) *I-V* curves at 10 K. Black: the Pt/LBMO-ZnO/Nb:STO (001) device, red: the Pt/LBMO-ZnO/Nb:STO (111) device. (c) The Poole-Frenkel (P-F) emission fitting of the conduction mechanism in the Pt/LBMO-ZnO/Nb:STO (111) device at the initial resistance state.

As shown in Fig. 6-8 (b), the Pt/LBMO-ZnO/Nb:STO (111) device (denoted as $Device_{111}$) exhibits a large resistive switching (RS) effect: the memory cell is "SET" to the low resistance state at a positive voltage of 1.8 V without electroforming. A clear current self-compliance is observed when the memory cell is "RESET" to the high resistance state: when the voltage is over -0.8 V, the current is saturated at ~500 μA without any further increase even when the voltage increases to -5 V

(corresponding to an electric field of 500 kV/cm). This "self-compliance" of the current acts as a protection for the memory cell: when the negative electric field is higher, electric breakdown can be avoided. After the "RESET" process, the current value at the same negative voltage is reduced drastically (over several orders of magnitude) when the voltage is swept from -5 V back to 0, resulting in a large hysteresis in the *I-V* curve (as well as a high ON/OFF ratio).

The Pt/LBMO-ZnO/Nb:STO (001) device (denoted as $Device_{001}$) shows a similar but much reduced RS effect. The "SET" process is similar, occurring at 1.7 V, but the current flow before and during the "SET" process is much higher than that of $Device_{111}$. The "RESET" process is totally different: the current gradually increases in the low negative bias region, with no self-compliance exhibited. When the applied voltage is over -4 V, the current is >1 mA. Moreover, the current remains at high values when the voltage is swept back, without a clear "RESET" process, and therefore the hysteresis of the *I-V* curve is much smaller than the $Device_{111}$.

We note here that the switching polarity of the Pt/LBMO-ZnO/Nb:STO device ("SET" at a positive bias and a clockwise *I-V* characteristic) is opposite to that of the Pt/SDC-STO/Nb:STO device shown in Chapter 4 (the counter-clockwise *I-V* in Fig. 4-18), indicative of a different switching mechanism. Recall Chapter 4.1.1, the RS switching polarity is determined either by ionic migration (counter-clockwise *I-V*) or electron trapping/detrapping (clockwise *I-V*). Since there is no ionic conductor in the LBMO-ZnO VAN, a large concentration of mobile V_os can be neglected, and therefore the electron charge trapping/detrapping mechanism is expected to be more dominant[117]. To study the intrinsic conduction mechanism, the *I-V* curves were fitted in different manners. Fig. 6-8 (c) shows the semi-log plot of $\frac{I}{V} \sim V^{\frac{1}{2}}$ in the initial state (the low positive voltage range before "SET": from 0 to 1.8 V) of $Device_{111}$, where a linear relationship is exhibited. A similar relationship is exhibited in the $Device_{001}$ (not shown here). Recall equation (2-8), this indicates that Poole-Frenkel (P-F) emission controls the intrinsic conduction in the Pt/LBMO-ZnO/Nb:STO devices.

In the P-F emission process, the conduction current originates from electrons emitted to the conduction band of the film from the trap sites. In LBMO-ZnO VAN films, trap sites most likely arise from the defects (such as oxygen vacancies) along the vertical interfaces. The electric field increases the probability of the trapping/detrapping of electrons and modifies the electrode/film potential barrier height[11], which induces the RS effects in both of the two films.

The reason for the much larger RS effect in the $Device_{111}$ as compared to the $Device_{001}$, although not yet fully understood, is suggested as below. The LBMO-ZnO VAN films grown on the Nb: STO (001) and (111) substrates are denoted as $Film_{001}$ and $Film_{111}$, respectively, and the corresponding devices with electrode contacts are denoted as $Device_{001}$ and $Device_{111}$.

The strength of the RS effect (the hysteresis in the *I-V* curve) is assumed to be determined by the level of carrier trapping/detrapping, which depends not only on the intrinsic carrier mobilities (which determines how many carriers can be modulated) but also on the concentration of the trap sites (which determines how many trap sites exist to modulate the carrier mobilities).

On one hand, it is known that the ZnO {0001} polar surfaces alone can act as electrically conductive channels[268], and thus different layouts of the polar planes can result in different carrier mobilities along the vertical interfaces. As shown in Fig. 6-5 (c)-(e), the ZnO {0001} polar planes all lie parallel to the LBMO {110} planes along the *op* direction in the $Film_{001}$. Therefore, all the polar planes of ZnO donate to the vertical interfaces. Whereas in $Film_{111}$, the polar {0001} surfaces of the ZnO $(10\bar{1}0)$ crystals donate to the polar vertical interfaces, while those of the ZnO (0002) crystals are perpendicular to the vertical interfaces. All these factors result in different intrinsic carrier mobilities between the two films.

On the other hand, in the *op* direction, the ZnO and LBMO planes match in different epitaxy relationships and thus the resulting mismatch may result in different defect levels and thus different concentrations of trap sites.

As a final result, although the charge carriers of both films are tunable, the tunability (determined by the intrinsic carrier mobilities and the trap site concentrations) are different, which results in different RS properties.

Fig. 6-8 (b) shows that the overall leakage current of $Device_{111}$ (red curve) is less than that of $Device_{001}$ (black curve), especially in the initial state before "SET". One possible reason is the reduced number of the polar vertical interfaces in $Film_{111}$. As the polar planes of the ZnO (0002) crystals in the $Film_{111}$ are perpendicular to the vertical interfaces, the donation of these crystals to the vertical interface conduction should be minimized, which can probably reduce the overall leakage of $Film_{111}$. Moreover, it is believed that the matching of close-packed orientations is energetically more favorable, and thus the close-packed hexagonal orientation of ZnO (0002) is expected to have a high-quality epitaxy with the close-packed cubic orientation of STO (111)[269]. Therefore, the defect level in the ZnO (0002) phase is expected to be reduced, which can also reduce the overall leakage of $Film_{111}$[270].

6.3 Electric field tuning of magnetic properties in the $La_{0.9}Ba_{0.1}MnO_3$–ZnO/Nb:STO (111) sample

Based on the above results, *in-situ* electric tuning of magnetic properties was mainly performed on the LBMO-ZnO/Nb:STO (111) sample ($Film_{111}$), due to the following reasons:

1. The large RS effect and reduced leakage in $Film_{111}$ make it easier to apply a high electric field without the risk of a high current flow through the film. After the "RESET" process, the leakage current can be reduced by several orders of magnitude when the applied voltage is the same.

In the SQUID measurement, the current flow through the $Film_{001}$ increased continuously with the increase in voltage. When the voltage was higher than -3 V (electric field > 300 kV/cm), the current was above 4 mA. This made it difficult to stabilize the temperature of the SQUID chamber. Also, when such a high current

flows through the film, Joule heating may contribute to the change in the magnetic properties, making it hard to deconvolute from the real ME effect. In contrast, by careful control of $Film_{111}$, the current flow could be reduced to below 10 μA (at -3 V). It is worth mentioning that the exact current value through the sample under SQUID measurement differs from the current values shown in Fig. 6-8 (b), due to the difference in electrode sizes and measurement configuration.

2. The existence of the ZnO (0002) crystals makes it easier to study the strain coupling, since the piezoelectric response of ZnO is strongest along this direction when electric field is applied along this direction.

3. The large RS effect discussed above provides a platform to study the charge doping effect of the LBMO phase.

Fig. 6-9 (a) illustrates the measurement configuration: nearly 80% of the surface area of the film was covered by Pt (~100 nm thick) which acted as the top electrode (TE), while the edge of the Nb:STO substrate was exposed without any film deposited, serving as the bottom electrode (BE). The TE and BE were connected with cables on the SQUID probe using silver paint, and the cables were connected to a Keithley 2440 source meter where the BE was grounded. In this work, two kinds of measurement were conducted, one was to measure the *M-H* curves with different electric fields applied, and another was to tune the remanence (*Mr*) by sweeping electric field cycles.

6.3.1 Electric field tuning of the *M-H* curves

◆ The role of the ZnO phase

Magnetization vs. field (*M-H*) curves were recorded consecutively on a Pt/LBMO-ZnO/Nb:STO (111) device (denoted as NC hereafter) with varying the electric field. For comparison, the same measurements were done on a reference LBMO plain film-based device (denoted as PF hereafter). The results are shown in Fig. 6-9 (b) and (c). Negative biases were applied to the samples (changing from -500

to 0 kV/cm)) to ensure reduced current flow. The electric field values are the absolute values converted from the negative biases (based on a 100 nm film thickness).

As shown in Fig. 6-9 (b), the coercive field (*Hc*) and remanence (*Mr*) of the NC decrease substantially under the applied electric field, while the saturation magnetization (*Ms*) remains almost constant. In contrast, in the PF, there is almost no change in the *M-H* curve shape when a similar electric field is applied, and the change in *Hc* and *Mr* can be neglected, as shown in Fig. 6-9 (c).

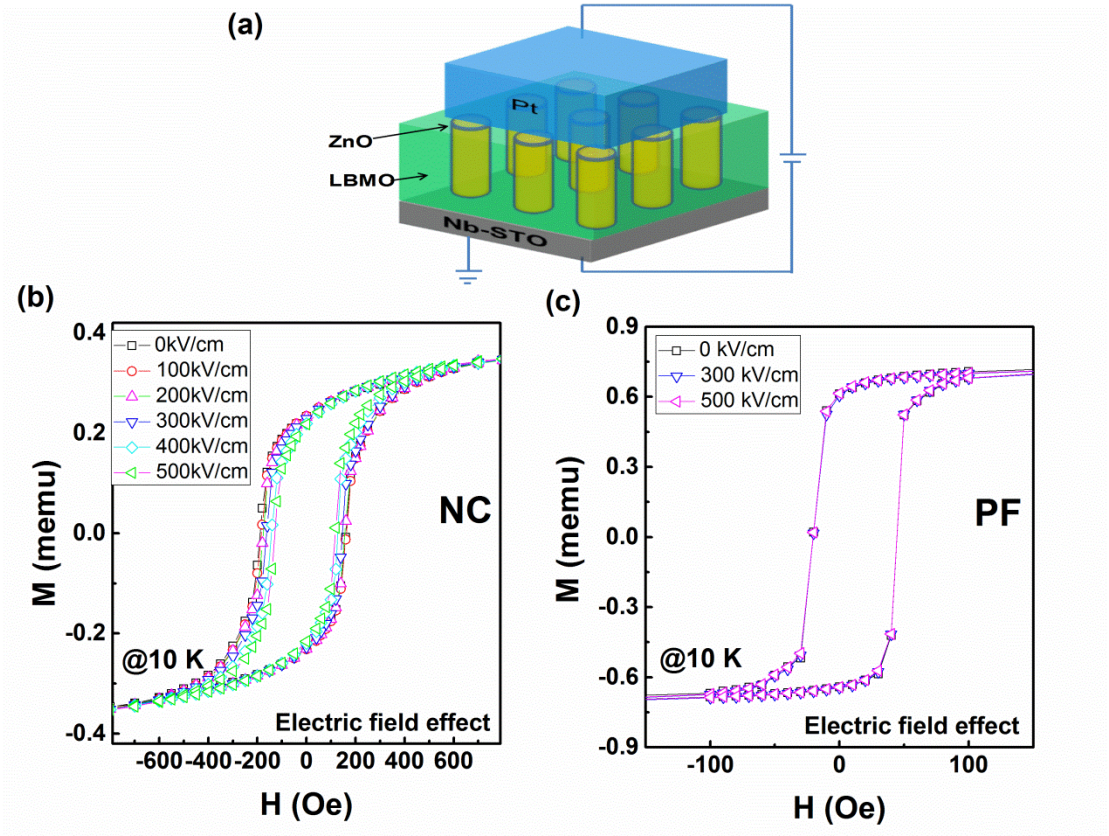

Figure 6-9. (a) Schematic diagram of the sample configuration for the *in-situ* electric field tuning of magnetic properties. Influence of the electric field on the *M-H* loops of the (b) LBMO-ZnO NC and (c) LBMO PF grown on the Nb:STO (111) substrate. The magnetic field was applied along the in-plane orientation and the measurements were conducted at 10 K.

◆ Comparison with the heating effect

It is worth mentioning that the current flow through the sample was not neglectable. In the SQUID measurements, when the electric field *E*=500 kV/cm, the average current flow in the NC and PF were around 720 μA and 900 μA, respectively.

Since the current flow is not small, it is necessary to consider the Joule heating effect before moving on to the discussion of mechanisms. To study the influence of the heating effect on the magnetic properties, *M-H* curves of the same samples were measured by varying the measurement temperature from 10 K to 20 K, with no electric field applied. The results of the NC and PF are compared, as shown in Fig. 6-10. Unlike the electric field effect in Fig. 6-9, when the films are heated up (from 10 K to 20 K), the *Hc* and *Mr* of both the NC and the PF decrease progressively. For example, the *Hc* drops from 178 to 120 Oe (by 32%) in the NC, and from 35 to 30.4 Oe (by 13 %) in the PF.

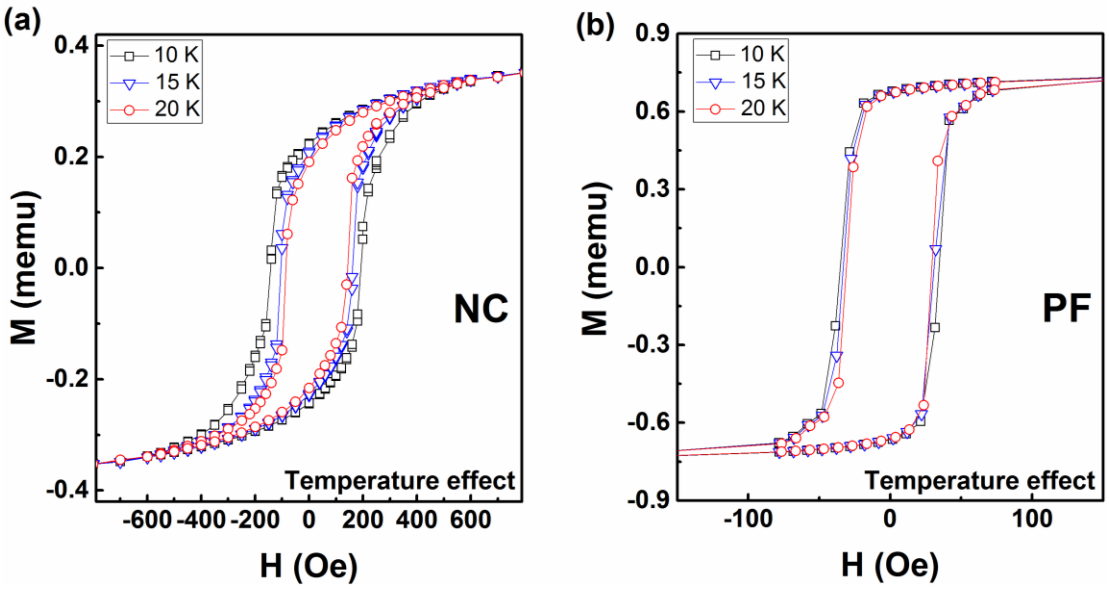

Figure 6-10. Influence of the temperature increase on the *M-H* loops of the (a) LBMO-ZnO NC and (b) LBMO PF grown on the Nb:STO (111) substrate.

To obtain a quantitative comparison of the change in magnetic properties caused by temperature rise and electric field, the *Hc* and *Mr* values are extrapolated from the *M-H* curves and plotted in Fig. 6-11. At first glance, the electric field applied to the

NC generates a similar effect as that caused by temperature rise. Comparing the black curves between Fig. 6-11 (a) and (b) (or Fig. 6-11 (c) and (d)), a 500 kV/cm electric field produces a similar effect as a temperature increase of 10 K (or 5 K), when *Hc* (or *Mr*) are independently considered, respectively. In contrast, for the PF, comparing the blue curves in Fig. 6-11, the *Hc* (*Mr*) stays almost unchanged with a similar electric field applied, while the change caused by temperature rise is quite clear.

Here we assume the effect of temperature rise caused by the amount of Joule heating is proportional to the power generated by the voltage and current ($P= I^2R$ or $I*V$). As mentioned above, when the applied electric fields are similar in the PF and NC (E=500 kV/cm), the level of Joule heating effect caused by the leakage current in the PF ($I \approx$900 μA) is expected to similar as that generated in the NC ($I \approx$720 μA). This large leakage, however, cannot cause any change in the *M-H* curves of the PF.

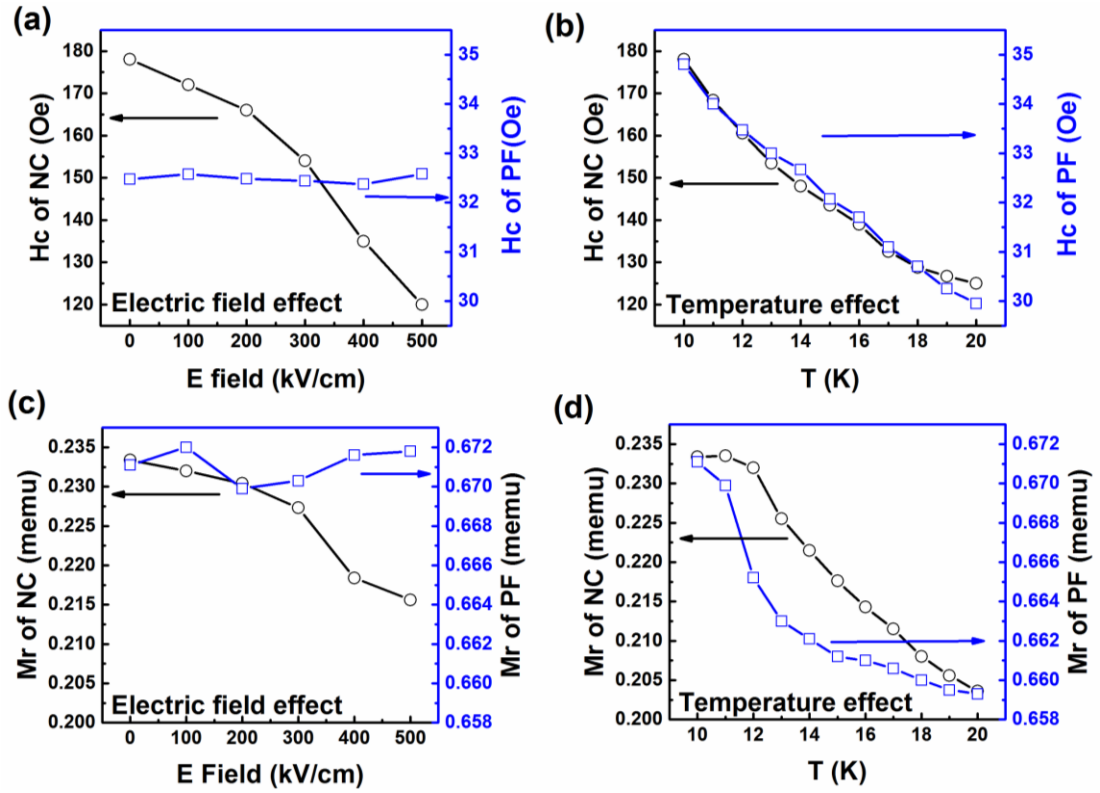

Figure 6-11. The change in the extrapolated coercive field (*Hc*) caused by the change in (a) the electric field and (b) the temperature. The change in the extrapolated remanence (*Mr*) caused by the change in (c) the electric field and (d) the temperature. The black curves stand for the NC and the blue stand for the PF.

Based on the above results, it is reasonable to conclude that although a high electric power can be generated by the leakage current in both the PF and NC, this power alone cannot produce a pure heating effect that decreases the *Hc* and *Mr* of the LBMO single-phase plain films. The modulation of the magnetic properties by the electric field (or current) is unique to the LBMO-ZnO VAN.

◆ **Investigating the strain effect**

Having discussed on the heating effect, we turn to gain an insight into other origins of the change in *M-H* curves in the NC film.

The existence of the ZnO (0002) crystals (Fig. 6-4 (c)) in this sample indicates the possibility of a piezoelectric effect. Recall Fig. 6-9 (b), the *Hc* and *Mr* of the NC film decrease substantially with the electric field applied, while the *Ms* remains almost constant. If this change were caused by a strain-mediated change of magnetoelastic anisotropy, an increase in the *Hc* and *Mr* would be expected when the magnetic field is applied in other directions[76]. Fig. 6-12 (b) shows the *in-situ* electric field tuning measurement results with the magnetic field applied perpendicular to the film plane (the *op* direction), compared to the result in the *ip* direction (Fig. 6-12 (a)). The *op* *M-H* curves are enlarged to be comparable with the *ip* curves and to show the details near the *Hc*. The *Hc* and *Mr* in the *op* measurement are getting smaller when a 500 kV/cm electric field is applied, which is similar to the *ip* measurement result. This result is, however, contradictory to the result expected from a strain-mediated change in the magnetoelastic anisotropy.

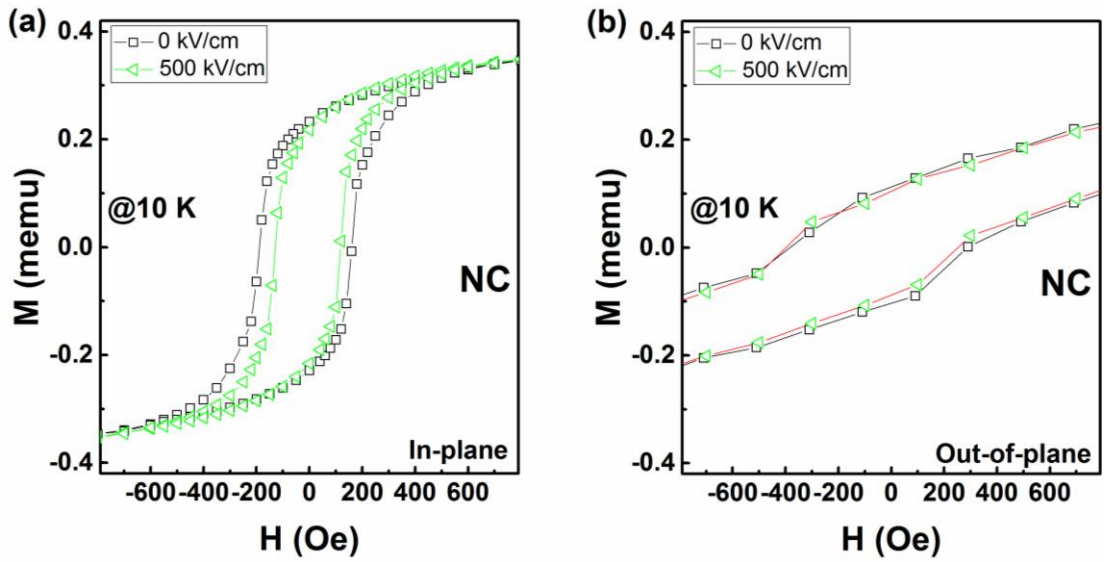

Figure 6-12. Comparison of the *in-situ* electric field tuning of the *M-H* curves of the NC film with the magnetic field applied in the (a) in-plane direction and the (b) out-of-plane direction. The out-of-plane curve is enlarged to show the details near the coercive field (*Hc*).

Up till now, we haven't found clear experimental proof of strain-mediated change in magnetic anisotropy. Considering the relatively small piezoelectric coefficient of ZnO (12.84 pC/N) as compared to BTO (>100 pC/N), it is reasonable to postulate that strain-mediated change of the magnetic anisotropy in the LBMO-ZnO VAN is expected to be much weaker, and this makes ME effect easily be overshadowed by other effects such as heating effect at such a low measurement temperature (10 K). Also, strain coupling, if it exists, may influence the magnetic properties in other ways, such as the tuning of T_c. The reason for the electric field tuning of the *M-H* curves in Fig. 6-9 (b) is not yet fully understood. It is likely, however, that the heating effect may have a contribution. Since the LBMO phase in the LBMO-ZnO VAN is expected to be in a different strain state, and its magnetic properties may become more vulnerable to leakage currents. To probe the ultimate origin, future work is needed.

6.3.2 Electric field tuning of the remanence and the correlation to the resistive switching effect

Since we haven't got a clear, independent experimental evidence of the strain-mediated change in magnetic anisotropy in the NC film, we turn to studying the charge doping effect proposed in Chapter 6.1.4.

As discussed in Chapter 6.2, the Pt/LBMO-ZnO/Nb-STO (111) device exhibits a nonvolatile tuning of the current when sweeping the electric field in cycles, which is correlated to the charge carrier modulation (charge doping). The change in the carrier concentration in the LBMO phase may be reflected as a change in the magnetic moments. In order to study the influence of charge doping effect on the magnetic moments, the remanence (*Mr*) was measured with the sample being under electric field cycles. A large in-plane magnetic field of 1 T was applied to ensure that the magnetic moments in the film were saturated, after which the magnetic field was switched off and the sample was left in the remanent state. The *Mr* value was then recorded by applying consecutive voltage cycles (from 0 → 2.2 V→ -4.5 V→ 0). This voltage cycle ensures that the current remains as low as possible (below 1 mA) throughout the measurement, in order to reduce the heating effect. The voltage values are converted to the corresponding electric field values based on a film thickness of 100 nm. The measurements were conducted on both the NC and the PF films.

As shown in Fig. 6-13 (a), overall, the *Mr* of the NC has a tendency to drop drastically with the application of electric fields. The arrows in Fig. 6-13 show the direction of the measurement history. The irreversible drop of *Mr* in the NC is perhaps due to a "thermal fatigue" effect which originates from the flow of the electric current through the films and this effect is also discernible in the PF (from arrow 1 to 2 in Fig. 6-13 (b)).

It is also noticeable from Fig. 6-13 (a) that in the 1st voltage cycle of the NC film, the *Mr* value has a tendency to increase back to the original value when the applied

voltage (electric field) decreases to zero (from arrow 3 to 4), while this tendency is not observed in the PF film (Fig. 6-13 (b)). This is indicative of a weak tuning effect of the *Mr* by the electric field. However, the tuning effect cannot be reproducible due to the "fatigue effect" mentioned above.

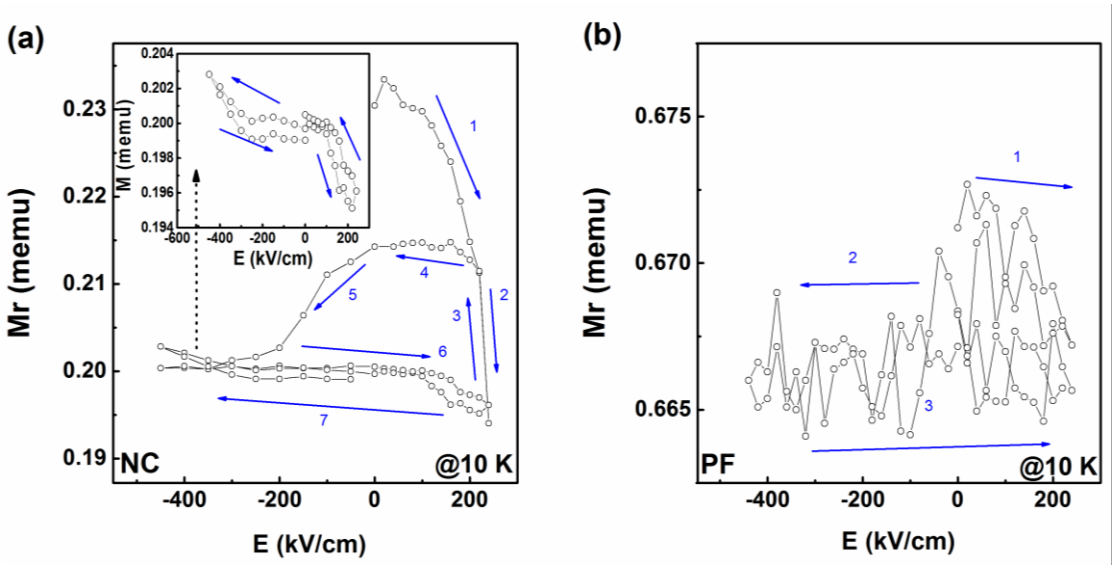

Figure 6-13. The influence of consecutive voltage cycles on the remanence (*Mr*) value of (a) the NC and (b) the PF at 10 K. The voltage values are converted to the corresponding electric field values in the figure legends.

In the NC, after the first voltage cycle (after arrow 5 in Fig. 6-13 (a)), the *Mr* value stays within a relatively stable range, indicating that the "fatigue effect" is saturated. In the following consecutive voltage cycles, two features are observed in the *Mr-E* curve, as shown in the inset of Fig. 6-13 (a) and the enlarged curve in Fig. 6-14 (a):

(1) The moment tends to drop under a positive electric field and increase under a negative electric field. One possible contribution for the drop (increase) of the moment value under a positive (negative) electric field is the magnetic induction field (B_i) caused by the leakage current[76] passing through the cables in the measurement circuit, which depends on the polarity of the current. This is absent in the PF, probably due to a different vulnerability to the induction field.

(2) A hysteresis is shown. This hysteresis is reminiscent of the RS effect observed in the same sample (Fig. 6-8 (b)). An *I-E* curve was also *in-situ* collected inside the

SQUID chamber after collecting the *Mr-E* curves and a similar RS behavior was shown (inset of Fig. 6-14 (a)). Fig. 6-14 shows a comparison of the *Mr-E* curve and the *I-E* curve of the NC film (measured by PPMS). The electric field values are converted from the applied voltage values. The current-induced magnetic induction mentioned above cannot explain the hysteresis behavior observed in Fig. 6-14 (a), as a higher current value is observed in process arrow 2 in Fig. 6-14 (b) where a larger drop of the moment should be expected, but an opposite effect is observed in process arrow 2 in Fig. 6-14 (a). Instead, the relative moment value is correlated to the relative resistance (and conductivity) value shown in the *I-E* curves: the low resistance state (arrow 2 and 3 in Fig. 6-14 (b)) corresponds to a larger moment value (arrows 2 and 3 in Fig. 6-14 (a)) and vice versa.

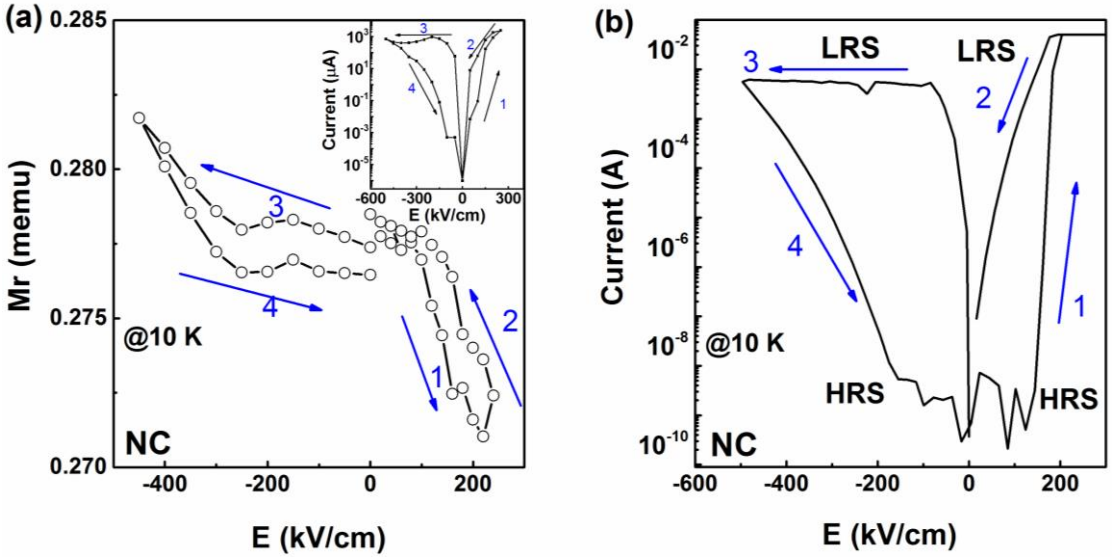

Figure 6-14. Correlation of (a) the remanence *vs.* electric field *(Mr-E)* curve and (b) the current *vs.* electric field (*I-E*) curve of the NC film at 10 K measured by PPMS. Inset of (a) is the *in-situ I-E* curve recorded inside the SQUID chamber.

The correlation between the *Mr-E* curve and the *I-E* curve is indicative of the role of charge trapping/detrapping on the modulation of the *Mr*, through which the resistance states of the sample can be correlated to the magnetization. The charge carrier trapping/detrapping from the defect sites under the electric field is considered as the origin of the change in conductivity[100] state. When the conductivity state is changed, the charge carrier concentration in the LBMO phase is modulated, and the

magnetic moments in the LBMO phase are likely to be modified[247,250]. The consistent trend that a relatively higher magnetic moment (arrow 2 and 3 in Fig. 6-14 (a)) is observed in a relatively low resistance state (arrow 2 and 3 in Fig. 6-14 (b)) is indicative of the modulation of DE coupling in hole-doped manganites, where the Mn^{4+}/Mn^{3+} ratio changes the strength of the DE coupling and the net spins, which results in a simultaneous change in the conductivity and magnetic moments. In different doping regions, the increase in Mn^{4+}/Mn^{3+} ratio can either increase or decrease the net moment values[271], while the result observed here suggests the former case. It is worth noting that the magnetic moment of the PF only has a one-off "thermal fatigue" effect under cyclings of electric field, as shown in Fig. 6-13 (b), which precludes the existence of the above-mentioned carrier-mediated magnetic moment that exists in the NC.

Based on the above results, we conclude that in the NC, the magnetic induction (B_i) causes an overall change in the moment (a drop (increase) under positive (negative) bias), which acts as a background. Another effect caused by the charge trapping/detrapping adds on this background and together they result in the eventual tuning of the *Mr* observed in Fig. 6-14 (a). It is interesting that both of the two effects were absent in the PF (Fig. 6-13 (b)) where a similar amount of leakage current was produced, and this indicates that these effects are caused due to the existence of the ZnO phase.

6.4 Summary

In summary, when the LBMO-ZnO VAN is grown on the Nb:STO (111) substrate, a large resistive switching is shown and the overall leakage is controlled and reduced (compared to the VAN grown on Nb:STO (001)). The *Mr* of this film is hysteretically tuned by the electric field and the tuning is correlated to the resistive switching caused by charge trapping/detrapping. Besides, the *M-H* curves are tuned and a decrease in *Hc* and *Mr* values are observed at 10 K under the application of electric fields. All these effects are correlated to the existence of the ZnO phase.

The hysteretic tuning of *Mr* by resistive switching is consistent with our previous work in the La_2CoMnO_6(LcMO)-ZnO VAN[77], where the charge trapping/detrapping was proposed but not fully investigated. This more detailed work helps to understand the mechanisms of electric field tuning of magnetic properties in manganite-ZnO VAN systems.

It is interesting to study the magnetoelectric effect in a ZnO-based VAN, as ZnO provides the possibility for both piezoelectric strain coupling and charge doping. Although the strain effect hasn't been proven here, charge doping is studied in detail. The results found up till now enable us to propose new ways to realize magnetoelectric effect through charge doping, i.e. in manganite-ZnO VAN systems, by modulating the charge carrier mobility through VAN vertical interfaces.

Compared to the LcMO-ZnO VAN, the leakage of the LBMO-ZnO VAN is reduced when grown on Nb: STO (111). For example, when $|V|$=1 V, the former has a current flow of 0.35 mA while the leakage of the latter is less than 1 μA.

However, a large current flow (>500 μA) is still observed when the applied electric is high, which results in a "fatigue" effect and deteriorates the nonvolatility of the LBMO-ZnO VAN when being used as a MERAM device. The current induces a magnetic induction which distracts the interpretation and deconvolution of the real ME effect. Also, the T_c of the LBMO-ZnO VAN is low (~95 K) as compared to the LcMO-ZnO VAN (220 K). Given the interesting results and the proposed charge doping approach discussed here, more engineering works can be done to carefully delicate high-T_c, less-leaky MERAM candidates.

Chapter 7 Conclusion and future works

The summary for each work, as provided in the last part of each result chapter, have outlined the bullet points. In this chapter, I conclude the thesis by summarizing the key findings, drawbacks and proposing future work plans.

The key findings, as discussed in Chapters 4 to 6, are as follows:

1. In Sm: CeO_2-$SrTiO_3$ (SDC-STO) VAN-based RRAM devices, a guideline is provided for elimination of the electroforming process (i.e. by slowing down the growth rate). Besides, the unique structure offers an ideal platform to separately explore ionic and electronic mechanisms, based on which a potential impact is expected on other nascent technologies, ranging from ionic gating to micro-solid oxide fuel cells and neuromorphics.

2. In $La_{0.9}Ba_{0.1}MnO_3$ (LBMO)-CeO_2 VAN films, not only structural modulation (vertical strain), but also compositional modification (Ce doping) are used to maintain the ferromagnetic insulating (FMI) properties of LBMO. The VAN doping is less used but unexpectedly beneficial. Meanwhile, the dimension-cross-over, which is correlated to the tuning of LBMO from a FMI to ferromagnetic metal (FMM), is realized through bottom-up control of the self-assembly kinetics, which is a more convenient alternative to top-down artificial design.

3. In the LBMO-ZnO VAN, the tuning of remanent magnetization is correlated to the resistive switching effect, which provides a wide study space to use new ways to realize charge-mediated magnetoelectric coupling, i.e. through charge trapping/detrapping.

However, in these VAN systems, some of the physical phenomena are not fully understood and problems of device performances still exist. Triggered by the need to probe the underlying nature and enhance the device performances, more works are

needed to reach the ultimate goal to bring these systems into real applications:

1. Sm:CeO_2-$SrTiO_3$ VAN-based RRAM devices:

Improving device endurance. The endurance we achieved is around 10^3-10^4 cycles (Fig. 4-18 (g)), which is below the ultimate goal of > 10^{12} cycles required in the RRAM field. Also, the 12 h retention time (Fig. 4-18 (h)) is below the >10-year goal. As proposed in Chapter 4, the RS performance can be realized by separately optimizing the electronic and ionic channels. By decreasing the growth rate (e.g. using an off-axis PLD growth mode), the structural quality of the electronic channel can be improved further. By replacing the doping element (for example, from Sm to Gd), the ionic conductivity of the CeO_2 phase can be much enhanced. By separately optimizing the two conductance channels, we aim to get an improved RS endurance and retention in the VAN-based RRAM device.

Quantitative structural analysis for the origin of the electroforming process. While an empirical guideline is proposed for eliminating the electroforming process (i.e. by decreasing the growth rate), a quantitative structural analysis is a more fundamental approach to theoretically directing the device design. A direct study of the relationship between tilt (misorientations of the nanocolumns) and the electroforming process, as mentioned in Chapter 4.5.5, is highly needed. This can be done quantitatively through William Hall plots presented in the LBMO-CeO_2 VAN (Chapter 5.4.2).

2. $La_{0.9}Ba_{0.1}MnO_3$: CeO_2 VAN-based FMI and FMM candidates

In-depth study of the electronic band structures. In Chapter 5.4, we found that the tuning of physical properties in LBMO by dimension control is correlated to the modulation of band structures. It is known that the DE coupling transfer integral *t* is closely related to the electron bandwidth of the material. At this stage, XPS results in Fig. 5-29 suggest that the bandwidth is modulated with changes in the lateral dimension of the LBMO phase. To be more convincing, information about DE coupling and bandwidth needs further XPS works and other measurements. In this work, soft x-ray ($h\nu$=1486.6 eV) was used, which has limited detection depth and

resolution. In comparison, hard X-Ray ($h\nu$=5.95 keV) Photoemission can effectively detect the well-screened Mn 2*p* Core-Level, which is directly correlated to the strength of the DE coupling[272–274]. Additionally, the whole picture of bandwidth can be further obtained from the pre-edge shift of the O K-edge X-ray Absorption Spectroscopy (XAS)[275], which can be an additional supporting proof.

3. $La_{0.9}Ba_{0.1}MnO_3$: ZnO VAN

Chapter 6 presented preliminary results for the *in-situ* electric field tuning of the *M-H* curves and the mechanism for the strain coupling is not proved though it is proposed. Besides, the system has a low T_c, which hinders its application. Therefore, several additional works are worth further study:

1. ***More studies on the strain effect.*** Since the out-of-plane measurement didn't give proof (Fig. 6-12) to explain the observed effects using strain-mediated change in magnetic anisotropy, the strain coupling, if existing in the system, may cause other effects such as changes in magnetic interactions (e.g. T_c), which can be investigated by other direct/indirect measurements. Measuring the piezoelectric response using Piezo Force Microscopy (PFM) would offer insight on whether strain effects exist. The tuning of T_c could be studied by measuring *M-T* curves under electric fields. In both cases, minimized leakage is important.

2. ***Use of other ways to tune the magnetic properties through charge doping*****.** The leakage of the LBMO-ZnO VAN, although reduced when grown on Nb:STO (111), can still cause artifacts through the thermal fatigue and magnetic induction, which may overshadow the real magnetoelectric effect. Instead of using an electric field, other indirect ways can be used to tune the magnetic properties through charge doping in ZnO-manganite VAN systems. For example, since ZnO is a wide band gap (3.37 eV) semiconductor with a large exciton binding energy, photocarrier generation can be obtained under light illumination. Therefore, an ultraviolet (UV) light could effectively tune the carrier density of the *n*-type ZnO phase, which can, in turn, affect the carrier density of the *p*-type manganite phase[276]. This doesn't require a

ferromagnetic insulating manganite, and therefore a manganite with a higher doping ratio and higher T_c can be used (e.g. $La_{0.67}Sr_{0.33}MnO_3$). Engineering magnetic properties of manganites through carrier modulation in VAN using non-magnetoelectric approaches is intriguing, which can help to indirectly understand the mechanism of charge carrier-mediated ME coupling in manganite-ZnO VAN systems.

References

(1) Rao, C. N. R.; Raveau, B. *Transition Metal Oxides: Structure, Properties and Synthesis of Ceramic Oxides*, 2nd ed.; Wiley-VCH: New York, 1998.

(2) Kittel, C. *Introduction to Solid State Physics*, 8th ed.; John Wiley & Sons, Inc: Hoboken, New Jersey, 2005.

(3) Thuselt, F. *Physik Der Halbleiterbauelemente*, 3rd ed.; Springer Spektrum: New York, 2018.

(4) E.H.Rhoderick. Metal-Semiconductor Contacts. *IEE Rev.* **1982**, *129* (1), 1–14.

(5) https://nptel.ac.in/courses/113106062/Lec9.pdf.

(6) Ameiryan Mojarad, S. Leakage Current and Resistive Switching Mechanisms in $SrTiO_3$, PhD Thesis, Newcastle University, 2013.

(7) https://public.wsu.edu/~pchemlab/documents/Work-functionvalues.pdf.

(8) Robertson, J.; Chen, C. W. Schottky Barrier Heights of Tantalum Oxide, Barium Strontium Titanate, Lead Titanate, and Strontium Bismuth Tantalate. *Appl. Phys. Lett.* **1999**, *74* (8), 1168–1170.

(9) Yang, H.; Luo, H. M.; Wang, H.; Usov, I. O.; Suvorova, N. A.; Jain, M.; Feldmann, D. M.; Dowden, P. C.; DePaula, R. F.; Jia, Q. X. Rectifying Current-Voltage Characteristics of $BiFeO_3$/Nb-Doped $SrTiO_3$ Heterojunction. *Appl. Phys. Lett.* **2008**, *92* (10), 102113.

(10) Rana, A. M.; Akbar, T.; Ismail, M.; Ahmad, E.; Hussain, F.; Talib, I.; Imran, M.; Mehmood, K.; Iqbal, K.; Nadeem, M. Y. Endurance and Cycle-to-Cycle Uniformity Improvement in Tri-Layered CeO_2/Ti/CeO_2 Resistive Switching Devices by Changing Top Electrode Material. *Sci. Rep.* **2017**, *7* (1), 39539.

(11) Chiu, F.-C. A Review on Conduction Mechanisms in Dielectric Films. *Adv. Mater. Sci. Eng.* **2014**, *2014*, 1–18.

(12) Chiu, F. C.; Mondal, S.; Pan, T. M. *High-k Gate Dielectrics for CMOS Technology*, 1st ed.; He, G., Sun, Z., Eds.; John Wiley & Sons, Inc: Hoboken, New Jersey, 2012.

(13) Lim, E.; Ismail, R. Conduction Mechanism of Valence Change Resistive Switching Memory: A Survey. *Electronics* **2015**, *4* (3), 586–613.

(14) Gantmakher, V. F. *Electrons and Disorder in Solids*, 1st ed.; Oxford University Press Inc.: New York, 2005.

(15) Mott, N. F.; Davis, E. A. *Electronic Processes in Non‐Crystalline Materials*, 2rd ed.; Mott, N. F., Davis, E. A., Eds.; Oxford University Press Inc.: New York, 1979.

(16) Emin, D.; Holstein, T. Studies of Small-Polaron Motion IV. Adiabatic Theory of the Hall Effect. *Ann. Phys. (N. Y).* **1969**, *53* (3), 439–520.

(17) Ziese, M.; Srinitiwarawong, C. Polaronic Effects on the Resistivity of Manganite Thin Films. *Phys. Rev. B* **1998**, *58* (17), 11519–11525.

(18) Prasad, R.; Singh, H. K.; Singh, M. P.; Prellier, W.; Siwach, P. K.; Kaur, A. Thickness Dependent Transport Properties of Compressively Strained $La_{0.88}Sr_{0.12}MnO_3$ Ultrathin Films. *J. Appl. Phys.* **2008**, *103* (8), 083906.

(19) Kumar, P. P.; Yashonath, S. Ionic Conduction in the Solid State. *J. Chem. Sci.* **2006**, *118* (1), 135–154.

(20) Martin, L. W.; Chu, Y.-H.; Ramesh, R. Advances in the Growth and Characterization of Magnetic, Ferroelectric, and Multiferroic Oxide Thin Films. *Mater. Sci. Eng. R Reports* **2010**,

68 (4–6), 89–133.

(21) Singh, R. Unexpected Magnetism in Nanomaterials. *J. Magn. Magn. Mater.* **2013**, *346*, 58–73.

(22) Anderson, P. W. Antiferromagnetism. Theory of Superexchange Interaction. *Phys. Rev.* **1950**, *79* (2), 350–356.

(23) Zener, C. Interaction between the D-Shells in the Transition Metals. II. Ferromagnetic Compounds of Manganese with Perovskite Structure. *Phys. Rev.* **1951**, *82* (3), 403–405.

(24) Chen, A. A Review of Emerging Non-Volatile Memory (NVM) Technologies and Applications. *Solid. State. Electron.* **2016**, *125*, 25–38.

(25) Sun, G.; Zhao, J.; Poremba, M.; Xu, C.; Xie, Y. Memory That Never Forgets: Emerging Nonvolatile Memory and the Implication for Architecture Design. *Natl. Sci. Rev.* **2018**, *5* (4), 577–592.

(26) Meijer, G. I. Who Wins the Nonvolatile Memory Race? *Science.* **2008**, *319* (5870), 1625–1626.

(27) Hai Li; Yiran Chen. An Overview of Non-Volatile Memory Technology and the Implication for Tools and Architectures. In *2009 Design, Automation & Test in Europe Conference & Exhibition*; IEEE, 2009; pp 731–736.

(28) Meena, J.; Sze, S.; Chand, U.; Tseng, T.-Y. Overview of Emerging Nonvolatile Memory Technologies. *Nanoscale Res. Lett.* **2014**, *9* (1), 526.

(29) Bowen, M.; Bibes, M.; Barthélémy, A.; Contour, J.-P.; Anane, A.; Lemaître, Y.; Fert, A. Nearly Total Spin Polarization in $La_{2/3}Sr_{1/3}MnO_3$ from Tunneling Experiments. *Appl. Phys. Lett.* **2003**, *82* (2), 233–235.

(30) Shao, Q.; Tang, C.; Yu, G.; Navabi, A.; Wu, H.; He, C.; Li, J.; Upadhyaya, P.; Zhang, P.; Razavi, S. A.; et al. Role of Dimensional Crossover on Spin-Orbit Torque Efficiency in Magnetic Insulator Thin Films. *Nat. Commun.* **2018**, *9* (1), 3612.

(31) Komori, S.; Di Bernardo, A.; Buzdin, A. I.; Blamire, M. G.; Robinson, J. W. A. Magnetic Exchange Fields and Domain Wall Superconductivity at an All-Oxide Superconductor-Ferromagnet Insulator Interface. *Phys. Rev. Lett.* **2018**, *121* (7), 077003.

(32) Gajek, M.; Bibes, M.; Barthélémy, A.; Bouzehouane, K.; Fusil, S.; Varela, M.; Fontcuberta, J.; Fert, A. Spin Filtering through Ferromagnetic $BiMnO_3$ Tunnel Barriers. *Phys. Rev. B* **2005**, *72* (2), 020406.

(33) Mesoraca, S. Growth of Spinel Oxide Thin Films for High Efficiency Room Temperature Spin Filtering, PhD Thesis, University of Cambridge, 2017.

(34) https://oxitronics.wordpress.com/research/nanoferronics/.

(35) Bibes, M.; Barthélémy, A. Towards a Magnetoelectric Memory. *Nat. Mater.* **2008**, *7* (6), 425–426.

(36) Eerenstein, W.; Mathur, N. D.; Scott, J. F. Multiferroic and Magnetoelectric Materials. *Nature* **2006**, *442* (7104), 759–765.

(37) Camargo, P. H. C.; Satyanarayana, K. G.; Wypych, F. Nanocomposites: Synthesis, Structure, Properties and New Application Opportunities. *Mater. Res.* **2009**, *12* (1), 1–39.

(38) Chen, A.; Bi, Z.; Jia, Q.; MacManus-Driscoll, J. L.; Wang, H. Microstructure, Vertical Strain Control and Tunable Functionalities in Self-Assembled, Vertically Aligned Nanocomposite Thin Films. *Acta Mater.* **2013**, *61* (8), 2783–2792.

(39) *Introduction to Nanoscale Science and Technology*; Ventra, M. Di, Evoy, S., Jr., J. R. H., Eds.; Springer: Boston, 2004.

(40) Suwardi, A.; Prasad, B.; Lee, S.; Choi, E.; Lu, P.; Zhang, W.; Li, L.; Blamire, M.; Jia, Q.;

Wang, H.; et al. Turning Antiferromagnetic $Sm_{0.34}Sr_{0.66}MnO_3$ into a 140 K Ferromagnet Using a Nanocomposite Strain Tuning Approach. *Nanoscale* **2016**, *8* (15), 8083–8090.

(41) Moshnyaga, V.; Damaschke, B.; Shapoval, O.; Belenchuk, A.; Faupel, J.; Lebedev, O. I.; Verbeeck, J.; van Tendeloo, G.; Mücksch, M.; Tsurkan, V.; et al. Structural Phase Transition at the Percolation Threshold in Epitaxial $(La_{0.7}Ca_{0.3}MnO_3)_{1-x}$:$(MgO)_x$ Nanocomposite Films. *Nat. Mater.* **2003**, *2* (4), 247–252.

(42) Harrington, S. A.; Zhai, J.; Denev, S.; Gopalan, V.; Wang, H.; Bi, Z.; Redfern, S. A. T.; Baek, S. H.; Bark, C. W.; Eom, C. B.; et al. Thick Lead-Free Ferroelectric Films with High Curie Temperatures through Nanocomposite-Induced Strain. *Nat. Nanotechnol.* **2011**, *6* (8), 491–495.

(43) MacManus-Driscoll, J. L.; Zerrer, P.; Wang, H.; Yang, H.; Yoon, J.; Fouchet, A.; Yu, R.; Blamire, M. G.; Jia, Q. Strain Control and Spontaneous Phase Ordering in Vertical Nanocomposite Heteroepitaxial Thin Films. *Nat. Mater.* **2008**, *7* (4), 314–320.

(44) MacManus-Driscoll, J. L.; Suwardi, A.; Kursumovic, A.; Bi, Z.; Tsai, C. F.; Wang, H.; Jia, Q.; Lee, O. J. New Strain States and Radical Property Tuning of Metal Oxides Using a Nanocomposite Thin Film Approach. *APL Mater.* **2015**, *3* (6), 062507.

(45) Sandiumenge, F.; Santiso, J.; Balcells, L.; Konstantinovic, Z.; Roqueta, J.; Pomar, A.; Espinós, J. P.; Martínez, B. Competing Misfit Relaxation Mechanisms in Epitaxial Correlated Oxides. *Phys. Rev. Lett.* **2013**, *110* (10), 107206.

(46) MacManus-Driscoll, J. L.; Suwardi, A.; Wang, H. Composite Epitaxial Thin Films: A New Platform for Tuning, Probing, and Exploiting Mesoscale Oxides. *MRS Bull.* **2015**, *40* (11), 933–942.

(47) Maurice, J.-L.; Pailloux, F.; Barthélémy, A.; Durand, O.; Imhoff, D.; Lyonnet, R.; Rocher, A.; Contour, J.-P. Strain Relaxation in the Epitaxy of $La_{2/3}Sr_{1/3}MnO_3$ Grown by Pulsed-Laser Deposition on $SrTiO_3$ (001). *Philos. Mag.* **2003**, *83* (28), 3201–3224.

(48) Macmanus-Driscoll, J. L. Self-Assembled Heteroepitaxial Oxide Nanocomposite Thin Film Structures: Designing Interface-Induced Functionality in Electronic Materials. *Adv. Funct. Mater.* **2010**, *20* (13), 2035–2045.

(49) Suwardi, A. Vertically Aligned Nanocomposite (VAN) Oxide Films for Improved Ferroelectrics and Ferromagnetics, PhD Thesis, University of Cambridge, 2017.

(50) Lee, O. J. Nanocomposites of $Ba_{0.6}Sr_{0.4}TiO_3$-Sm_2O_3 for Enhanced Tunability and Reduced Dielectric Loss, PhD Thesis, University of Cambridge, 2013.

(51) Zheng, H.; Zhan, Q.; Zavaliche, F.; Sherburne, M.; Straub, F.; Cruz, M. P.; Chen, L.-Q.; Dahmen, U.; Ramesh, R. Controlling Self-Assembled Perovskite−Spinel Nanostructures. *Nano Lett.* **2006**, *6* (7), 1401–1407.

(52) Wu, R.; Yun, C.; Wang, X.; Lu, P.; Li, W.; Lin, Y.; Choi, E.-M.; Wang, H.; MacManus-Driscoll, J. L. All-Oxide Nanocomposites to Yield Large, Tunable Perpendicular Exchange Bias above Room Temperature. *ACS Appl. Mater. Interfaces* **2018**, *10* (49), 42593–42602.

(53) Park, C.; Wu, R.; Lu, P.; Zhao, H.; Yang, J.; Zhang, B.; Li, W.; Yun, C.; Wang, H.; MacManus-Driscoll, J. L.; et al. Use of Mesoscopic Host Matrix to Induce Ferrimagnetism in Antiferromagnetic Spinel Oxide. *Adv. Funct. Mater.* **2018**, *28* (11), 1706220.

(54) Zheng, H.; Straub, F.; Zhan, Q.; Yang, P.-L.; Hsieh, W.-K.; Zavaliche, F.; Chu, Y.-H.; Dahmen, U.; Ramesh, R. Self-Assembled Growth of $BiFeO_3$–$CoFe_2O_4$ Nanostructures. *Adv. Mater.* **2006**, *18* (20), 2747–2752.

(55) Chen, A.; Bi, Z.; Jia, Q.; Macmanus-Driscoll, J. L.; Wang, H. Microstructure, Vertical Strain Control and Tunable Functionalities in Self-Assembled, Vertically Aligned Nanocomposite Thin Films. *Acta Mater.* **2013**, *61* (8), 2783–2792.

(56) Lebedev, O. I.; Verbeeck, J.; Van Tendeloo, G.; Shapoval, O.; Belenchuk, A.; Moshnyaga, V.; Damashcke, B.; Samwer, K. Structural Phase Transitions and Stress Accommodation in $(La_{0.67}Ca_{0.33}MnO_3)_{1-x}$:$(MgO)_x$. *Phys. Rev. B* **2002**, *66* (10), 104421.

(57) Zheng, H.; Wang, J.; Mohaddes-Ardabili, L.; Wuttig, M.; Salamanca-Riba, L.; Schlom, D. G.; Ramesh, R. Three-Dimensional Heteroepitaxy in Self-Assembled $BaTiO_3$–$CoFe_2O_4$ Nanostructures. *Appl. Phys. Lett.* **2004**, *85* (11), 2035–2037.

(58) Zavaliche, F.; Zheng, H.; Mohaddes-Ardabili, L.; Yang, S. Y.; Zhan, Q.; Shafer, P.; Reilly, E.; Chopdekar, R.; Jia, Y.; Wright, P.; et al. Electric Field-Induced Magnetization Switching in Epitaxial Columnar Nanostructures. *Nano Lett.* **2005**, *5* (9), 1793–1796.

(59) Crane, S. P.; Bihler, C.; Brandt, M. S.; Goennenwein, S. T. B.; Gajek, M.; Ramesh, R. Tuning Magnetic Properties of Magnetoelectric $BiFeO_3$–$NiFe_2O_4$ Nanostructures. *J. Magn. Magn. Mater.* **2009**, *321* (4), L5–L9.

(60) Levin, I.; Li, J.; Slutsker, J.; Roytburd, A. L. Design of Self-Assembled Multiferroic Nanostructures in Epitaxial Films. *Adv. Mater.* **2006**, *18* (15), 2044–2047.

(61) Zhang, W.; Chen, A.; Jian, J.; Zhu, Y.; Chen, L.; Lu, P.; Jia, Q.; MacManus-Driscoll, J. L.; Zhang, X.; Wang, H. Strong Perpendicular Exchange Bias in Epitaxial $La_{0.7}Sr_{0.3}MnO_3$:$BiFeO_3$ Nanocomposite Films through Vertical Interfacial Coupling. *Nanoscale* **2015**, *7* (33), 13808–13815.

(62) Wu, H.; Chai, G.; Xu, B.; Li, J.; Zhang, Z. Effect of Out-of-Plane Misfit Strain on Phase Diagrams and Ferroelectric Properties of Ferroelectric Films in Vertical Nanocomposite Structures. *Appl. Phys. A* **2013**, *113* (1), 155–160.

(63) Chen, A.; Bi, Z.; Tsai, C. F.; Lee, J.; Su, Q.; Zhang, X.; Jia, Q.; MacManus-Driscoll, J. L.; Wang, H. Tunable Low-Field Magnetoresistance in $(La_{0.7}Sr_{0.3}MnO_3)_{0.5}$:$(ZnO)_{0.5}$ Self-Assembled Vertically Aligned Nanocomposite Thin Films. *Adv. Funct. Mater.* **2011**, *21* (13), 2423–2429.

(64) Lee, S.; Zhang, W.; Khatkhatay, F.; Wang, H.; Jia, Q.; MacManus-Driscoll, J. L. Ionic Conductivity Increased by Two Orders of Magnitude in Micrometer-Thick Vertical Yttria-Stabilized ZrO_2 Nanocomposite Films. *Nano Lett.* **2015**, *15* (11), 7362–7369.

(65) Choi, H. K.; Aimon, N. M.; Kim, D. H.; Sun, X. Y.; Gwyther, J.; Manners, I.; Ross, C. A. Hierarchical Templating of a $BiFeO_3$–$CoFe_2O_4$ Multiferroic Nanocomposite by a Triblock Terpolymer Film. *ACS Nano* **2014**, *8* (9), 9248–9254.

(66) Sun, X.; Huang, J.; Jian, J.; Fan, M.; Wang, H.; Li, Q.; Mac Manus-Driscoll, J. L.; Lu, P.; Zhang, X.; Wang, H. Three-Dimensional Strain Engineering in Epitaxial Vertically Aligned Nanocomposite Thin Films with Tunable Magnetotransport Properties. *Mater. Horizons* **2018**, *5* (3), 536–544.

(67) Khatkhatay, F.; Chen, A.; Lee, J. H.; Zhang, W.; Abdel-Raziq, H.; Wang, H. Ferroelectric Properties of Vertically Aligned Nanostructured $BaTiO_3$–CeO_2 Thin Films and Their Integration on Silicon. *ACS Appl. Mater. Interfaces* **2013**, *5* (23), 12541–12547.

(68) Lee, O.; Kursumovic, A.; Bi, Z.; Tsai, C.-F.; Wang, H.; MacManus-Driscoll, J. L. Giant Enhancement of Polarization and Strong Improvement of Retention in Epitaxial $Ba_{0.6}Sr_{0.4}TiO_3$-Based Nanocomposites. *Adv. Mater. Interfaces* **2017**, *4* (15), 1700336.

(69) Sangle, A. L.; Lee, O. J.; Kursumovic, A.; Zhang, W.; Chen, A.; Wang, H.; MacManus-Driscoll, J. L. Very High Commutation Quality Factor and Dielectric Tunability in Nanocomposite $SrTiO_3$ Thin Films with T_c Enhanced to >300℃. *Nanoscale* **2018**, *10* (7), 3460–3468.

(70) Liu, H.-J.; Tra, V.-T.; Chen, Y.-J.; Huang, R.; Duan, C.-G.; Hsieh, Y.-H.; Lin, H.-J.; Lin, J.-Y.; Chen, C.-T.; Ikuhara, Y.; et al. Large Magnetoresistance in Magnetically Coupled $SrRuO_3$-$CoFe_2O_4$ Self-Assembled Nanostructures. *Adv. Mater.* **2013**, *25* (34), 4753–4759.

(71) Zhou, M.; Li, Y.; Jeon, I.; Yi, Q.; Zhu, X.; Tang, X.; Wang, H.; Fei, L.; Sun, Y.; Deng, S.; et al. Enhancement of Low-Field Magnetoresistance in Self-Assembled Epitaxial $La_{0.67}Ca_{0.33}MnO_3$:NiO and $La_{0.67}Ca_{0.33}MnO_3$:Co_3O_4 Composite Films via Polymer-Assisted Deposition. *Sci. Rep.* **2016**, *6* (1), 26390.

(72) Fan, M.; Zhang, W.; Khatkhatay, F.; Li, L.; Wang, H. Enhanced Tunable Magnetoresistance Properties over a Wide Temperature Range in Epitaxial $(La_{0.7}Sr_{0.3}MnO_3)_{1-x}$:$(CeO_2)_x$ Nanocomposites. *J. Appl. Phys.* **2015**, *118* (6), 065302.

(73) Lloyd-Hughes, J.; Mosley, C. D. W.; Jones, S. P. P.; Lees, M. R.; Chen, A.; Jia, Q. X.; Choi, E. M.; MacManus-Driscoll, J. L. Colossal Terahertz Magnetoresistance at Room Temperature in Epitaxial $La_{0.7}Sr_{0.3}MnO_3$ Nanocomposites and Single-Phase Thin Films. *Nano Lett.* **2017**, *17* (4), 2506–2511.

(74) Yang, S. M.; Lee, S.; Jian, J.; Zhang, W.; Lu, P.; Jia, Q.; Wang, H.; Won Noh, T.; Kalinin, S. V.; MacManus-Driscoll, J. L. Strongly Enhanced Oxygen Ion Transport through Samarium-Doped CeO2 Nanopillars in Nanocomposite Films. *Nat. Commun.* **2015**, *6* (1), 8588.

(75) Zhang, J. X.; Dai, J. Y.; Lu, W.; Chan, H. L. W.; Wu, B.; Li, D. X. A Novel Nanostructure and Multiferroic Properties in $Pb(Zr_{0.52}Ti_{0.48})O_3$/$CoFe_2O_4$ Nanocomposite Films Grown by Pulsed-Laser Deposition. *J. Phys. D. Appl. Phys.* **2008**, *41* (23), 235405.

(76) Wu, R.; Kursumovic, A.; Gao, X.; Yun, C.; Vickers, M. E.; Wang, H.; Cho, S.; MacManus-Driscoll, J. L. Design of a Vertical Composite Thin Film System with Ultralow Leakage To Yield Large Converse Magnetoelectric Effect. *ACS Appl. Mater. Interfaces* **2018**, *10* (21), 18237–18245.

(77) Fix, T.; Choi, E.-M.; Robinson, J. W. A.; Lee, S. B.; Chen, A.; Prasad, B.; Wang, H.; Blamire, M. G.; MacManus-Driscoll, J. L. Electric-Field Control of Ferromagnetism in a Nanocomposite via a ZnO Phase. *Nano Lett.* **2013**, *13* (12), 5886–5890.

(78) Fan, M.; Zhang, W.; Jian, J.; Huang, J.; Wang, H. Strong Perpendicular Exchange Bias in Epitaxial $La_{0.7}Sr_{0.3}MnO_3$:$LaFeO_3$ Nanocomposite Thin Films. *APL Mater.* **2016**, *4* (7), 076105.

(79) Zhang, W.; Chen, A.; Khatkhatay, F.; Tsai, C.; Su, Q.; Jiao, L.; Zhang, X.; Wang, H. Integration of Self-Assembled Vertically Aligned Nanocomposite $(La_{0.7}Sr_{0.3}MnO_3)_{1-x}$:$(ZnO)_x$ Thin Films on Silicon Substrates. *ACS Appl. Mater. Interfaces* **2013**, *5* (10), 3995–3999.

(80) Li, L.; Sun, L.; Gomez-Diaz, J. S.; Hogan, N. L.; Lu, P.; Khatkhatay, F.; Zhang, W.; Jian, J.; Huang, J.; Su, Q.; et al. Self-Assembled Epitaxial Au–Oxide Vertically Aligned Nanocomposites for Nanoscale Metamaterials. *Nano Lett.* **2016**, *16* (6), 3936–3943.

(81) Rahaman, M. N. *Ceramic Processing and Sintering*, 2nd ed.; Marcel Derker, Inc.: New York, 2003.

(82) Norton, D. P. Synthesis and Properties of Epitaxial Electronic Oxide Thin-Film Materials. *Mater. Sci. Eng. R Reports* **2004**, *43* (5–6), 139–247.

(83) Sangle, A. L. Nanostructured $SrTiO_3$ for Strongly Enhanced Tunable Microwave and Photocatalytic Performance, PhD Thesis, University of Cambridge, 2016.

(84) Singh, R. K.; Kumar, D. Pulsed Laser Deposition and Characterization of High-T_c $YBa_2Cu_3O_{7-x}$ Superconducting Thin Films. *Mater. Sci. Eng. R Reports* **1998**, *22* (4), 113–185.

(85) Krebs, H.-U.; Weisheit, M.; Faupel, J.; Süske, E.; Scharf, T.; Fuhse, C.; Störmer, M.; Sturm, K.; Seibt, M.; Kijewski, H.; et al. Pulsed Laser Deposition (PLD) - A Versatile Thin Film Technique. In *Advances in Solid State Physics*; Kramer, B., Ed.; Springer-Verlag Berlin Heidelberg GmbH: Berlin, 2003; pp 505–517.

(86) Eason, R. *Pulsed Laser Deposition of Thin Films: Applications-Led Growth of Functional Materials*, 1st ed.; Eason, R., Ed.; John Wiley & Sons: Hoboken, New Jersey, 2007.

(87) Chen, A.; Hu, J.-M.; Lu, P.; Yang, T.; Zhang, W.; Li, L.; Ahmed, T.; Enriquez, E.; Weigand, M.; Su, Q.; et al. Role of Scaffold Network in Controlling Strain and Functionalities of Nanocomposite Films. *Sci. Adv.* **2016**, *2* (6), e1600245.

(88) Culllity, B. D. *Elements of X-Ray Diffraction*; Cohen, M., Ed.; Addison-Wesley Publishing Company, Inc.: Reading, Massachusetts, 1956.

(89) Moram, M. A.; Vickers, M. E. X-Ray Diffraction of III-Nitrides. *Reports Prog. Phys.* **2009**, *72* (3), 036502.

(90) B.D.Josephson. The Discovery of Tunnelling Supercurrents. *Rev. Mod. Phys.* **1974**, *46* (2), 251–254.

(91) B.D.Josephson. Possible New Effects in Superconductive Tunnelling. *Phys. Lett.* **1962**, *1* (7), 251–253.

(92) Etier, M. S. M. Preparation and Magnetoelectric Effect of Multiferroic Cobalt Ferrite-Barium Titanate Composites, PhD Thesis, University of Duisburg-Essen, 2015.

(93) http://four-point-probes.com/four-point-probe-manual/.

(94) https://www.tek.com/materials-char_apps_guide.

(95) Ahmad, M.; Rafiq, M. A.; Imran, Z.; Rasool, K.; Shahid, R. N.; Javed, Y.; Hasan, M. M. Charge Conduction and Relaxation in MoS_2 Nanoflakes Synthesized by Simple Solid State Reaction. *J. Appl. Phys.* **2013**, *114*, 043710.

(96) HÜfner, S. *Photoelectron Spectroscopy: Principles and Applications*, 3rd ed.; Springer-Verlag Berlin Heidelberg GmbH: Berlin, 2003.

(97) Chua, L. Memristor-The Missing Circuit Element. *IEEE Trans. Circuit Theory* **1971**, *18* (5), 507–519.

(98) Strukov, D. B.; Snider, G. S.; Stewart, D. R.; Williams, R. S. The Missing Memristor Found. *Nature* **2008**, *453* (7191), 80–83.

(99) Ielmini, D. Brain-Inspired Computing with Resistive Switching Memory (RRAM): Devices, Synapses and Neural Networks. *Microelectron. Eng.* **2018**, *190*, 44–53.

(100) Sawa, A. Resistive Switching in Transition Metal Oxides. *Mater. Today* **2008**, *11* (6), 28–36.

(101) Inoue, I. H.; Yasuda, S.; Akinaga, H.; Takagi, H. Nonpolar Resistance Switching of Metal/Binary-Transition-Metal Oxides/Metal Sandwiches: Homogeneous/Inhomogeneous Transition of Current Distribution. *Phys. Rev. B* **2008**, *77* (3), 035105.

(102) Baek, I. G.; Lee, M. S.; Sco, S.; Lee, M. J.; Seo, D. H.; Suh, D.-S.; Park, J. C.; Park, S. O.; Kim, H. S.; Yoo, I. K.; et al. Highly Scalable Non-Volatile Resistive Memory Using Simple Binary Oxide Driven by Asymmetric Unipolar Voltage Pulses. In *IEDM Technical Digest. IEEE International Electron Devices Meeting, 2004.*; IEEE; pp 587–590.

(103) Waser, R.; Aono, M. Nanoionics-Based Resistive Switching Memories. *Nat. Mater.* **2007**, *6* (11), 833–840.

(104) Szot, K.; Speier, W.; Bihlmayer, G.; Waser, R. Switching the Electrical Resistance of Individual Dislocations in Single-Crystalline $SrTiO_3$. *Nat. Mater.* **2006**, *5* (4), 312–320.

(105) Beck, A.; Bednorz, J. G.; Gerber, C.; Rossel, C.; Widmer, D. Reproducible Switching Effect in Thin Oxide Films for Memory Applications. *Appl. Phys. Lett.* **2000**, *77* (1), 139–141.

(106) Sawa, A.; Fujii, T.; Kawasaki, M.; Tokura, Y. Hysteretic Current–voltage Characteristics and Resistance Switching at a Rectifying Ti/$Pr_{0.7}Ca_{0.3}MnO_3$ Interface. *Appl. Phys. Lett.* **2004**, *85* (18), 4073–4075.

(107) Waser, R.; Dittmann, R.; Staikov, G.; Szot, K. Redox-Based Resistive Switching Memories - Nanoionic Mechanisms, Prospects, and Challenges. *Adv. Mater.* **2009**, *21* (25–26), 2632–2663.

(108) Hyunjun Sim; Hyejung Choi; Dongsoo Lee; Man Chang; Dooho Choi; Yunik Son; Eun-Hong Lee; Wonjoo Kim; Yoondong Park; In-Kyeong Yoo; et al. Excellent Resistance Switching Characteristics of Pt/$SrTiO_3$ Schottky Junction for Multi-Bit Nonvolatile Memory Application. In *IEEE InternationalElectron Devices Meeting, 2005. IEDM Technical Digest.*; IEEE, 2005; Vol. 00, pp 758–761.

(109) Fursina, A. A.; Sofin, R. G. S.; Shvets, I. V.; Natelson, D. Origin of Hysteresis in Resistive Switching in Magnetite Is Joule Heating. *Phys. Rev. B* **2009**, *79* (24), 245131.

(110) Yun, C.; Chen, X. G.; Fu, J. B.; Wang, C. S.; Du, H. L.; Xiong, G. C.; Lian, G. J.; Yang, Y. C.; Yang, J. B. Fabrication of Ferrimagnetic FeOx Thin Film and the Resistance Switching of Au/FeO_x /Pt Heterostructure. *J. Appl. Phys.* **2013**, *113* (17), 17C303.

(111) Simmons, J. G.; Verderber, R. R. New Conduction and Reversible Memory Phenomena in Thin Insulating Films. *Proc. R. Soc. A Math. Phys. Eng. Sci.* **1967**, *301* (1464), 77–102.

(112) Chen, Y.; Chen, L.; Lian, G.; Xiong, G. Resistance and Superconductivity Switching Caused by Carrier Injection: Evidences of Self-Trapping Carriers in Oxide Electronics. *J. Appl. Phys.* **2009**, *106* (2), 023708.

(113) Chen, X. G.; Fu, J. B.; Liu, S. Q.; Yang, Y. B.; Wang, C. S.; Du, H. L.; Xiong, G. C.; Lian, G. J.; Yang, J. B. Trap-Assisted Tunneling Resistance Switching Effect in $CeO_2/La_{0.7}(Sr_{0.1}Ca_{0.9})_{0.3}MnO_3$ Heterostructure. *Appl. Phys. Lett.* **2012**, *101* (15), 153509.

(114) Cho, S.; Yun, C.; Tappertzhofen, S.; Kursumovic, A.; Lee, S.; Lu, P.; Jia, Q.; Fan, M.; Jian, J.; Wang, H.; et al. Self-Assembled Oxide Films with Tailored Nanoscale Ionic and Electronic Channels for Controlled Resistive Switching. *Nat. Commun.* **2016**, *7*, 12373.

(115) Waser, R. *Nanoelectronics and Information Technology-Advanced Electronic Materials and Novel Devices*, 1st ed.; Waser, R., Ed.; Wiley-VCH: New York, 2003.

(116) Sawa, A.; Fujii, T.; Kawasaki, M.; Tokura, Y. Interface Transport Properties and Resistance Switching in Perovskite-Oxide Heterojunctions. In *Proceedings of SPIE 5932, Strongly Correlated Electron Materials: Physics and Nanoengineering*; 2005; p 59322C.

(117) Shibuya, K.; Dittmann, R.; Mi, S.; Waser, R. Impact of Defect Distribution on Resistive Switching Characteristics of Sr_2TiO_4 Thin Films. *Adv. Mater.* **2010**, *22* (3), 411–414.

(118) Sun, P.; Li, L.; Lu, N.; Lv, H.; Liu, M.; Liu, S. Physical Model for Electroforming Process in Valence Change Resistive Random Access Memory. *J. Comput. Electron.* **2015**, *14* (1), 146–150.

(119) Joshua Yang, J.; Miao, F.; Pickett, M. D.; Ohlberg, D. A. A.; Stewart, D. R.; Lau, C. N.; Williams, R. S. The Mechanism of Electroforming of Metal Oxide Memristive Switches.

Nanotechnology **2009**, *20* (21), 215201.

(120) Fujiwara, K.; Nemoto, T.; Rozenberg, M. J.; Nakamura, Y.; Takagi, H. Resistance Switching and Formation of a Conductive Bridge in Metal/Binary Oxide/Metal Structure for Memory Devices. *Jpn. J. Appl. Phys.* **2008**, *47* (8), 6266–6271.

(121) Jeong, D. S.; Schroeder, H.; Waser, R. Coexistence of Bipolar and Unipolar Resistive Switching Behaviors in a Pt/TiO_2/Pt Stack. *Electrochem. Solid-State Lett.* **2007**, *10* (8), G51–G53.

(122) Lee, S.; Sangle, A.; Lu, P.; Chen, A.; Zhang, W.; Lee, J. S.; Wang, H.; Jia, Q.; MacManus-Driscoll, J. L. Novel Electroforming-Free Nanoscaffold Memristor with Very High Uniformity, Tunability, and Density. *Adv. Mater.* **2014**, *26* (36), 6284–6289.

(123) Cao, X.; Li, X. M.; Gao, X. D.; Zhang, Y. W.; Liu, X. J.; Wang, Q.; Chen, L. D. Effects of the Compliance Current on the Resistive Switching Behavior of TiO_2 Thin Films. *Appl. Phys. A* **2009**, *97* (4), 883–887.

(124) Strachan, J. P.; Yang, J. J.; Montoro, L. A.; Ospina, C. A.; Ramirez, A. J.; Kilcoyne, A. L. D.; Medeiros-Ribeiro, G.; Williams, R. S. Characterization of Electroforming-Free Titanium Dioxide Memristors. *Beilstein J. Nanotechnol.* **2013**, *4* (1), 467–473.

(125) Yoon, J. H.; Song, S. J.; Yoo, I.-H.; Seok, J. Y.; Yoon, K. J.; Kwon, D. E.; Park, T. H.; Hwang, C. S. Highly Uniform, Electroforming-Free, and Self-Rectifying Resistive Memory in the Pt/Ta_2O_5/HfO_{2-x}/TiN Structure. *Adv. Funct. Mater.* **2014**, *24* (32), 5086–5095.

(126) Linn, E.; Siemon, A.; Waser, R.; Menzel, S. Applicability of Well-Established Memristive Models for Simulations of Resistive Switching Devices. *IEEE Trans. Circuits Syst. I Regul. Pap.* **2014**, *61* (8), 2402–2410.

(127) Di Ventra, M.; Pershin, Y. V. On the Physical Properties of Memristive, Memcapacitive and Meminductive Systems. *Nanotechnology* **2013**, *24* (25), 255201.

(128) Hsieh, Y.-H.; Liou, J.-M.; Huang, B.-C.; Liang, C.-W.; He, Q.; Zhan, Q.; Chiu, Y.-P.; Chen, Y.-C.; Chu, Y.-H. Local Conduction at the $BiFeO_3$-$CoFe_2O_4$ Tubular Oxide Interface. *Adv. Mater.* **2012**, *24* (33), 4564–4568.

(129) Li, L.; Lu, L.; Wang, Z.; Li, Y.; Yao, Y.; Zhang, D.; Yang, G.; Yao, J.; Viehland, D.; Yang, Y. Anatomy of Vertical Heteroepitaxial Interfaces Reveals the Memristive Mechanism in Nb_2O_5-$NaNbO_3$ Thin Films. *Sci. Rep.* **2015**, *5* (1), 9229.

(130) Wang, L.; Meng, F.; Li, K.; Lu, F. Characterization and Optical Properties of Pole-like Nano-CeO_2 Synthesized by a Facile Hydrothermal Method. *Appl. Surf. Sci.* **2013**, *286*, 269–274.

(131) Moon, H. J. *Development of Thin Film Inorganic Membranes for Oxygen Separation*, 1st ed.; Forschungszentrum Jülich GmbH: Jülich, 2012.

(132) Mori, T. Oxide Ionic Conductivity and Microstructures of Sm- or La-Doped CeO_2-Based Systems. *Solid State Ionics* **2002**, *154–155*, 461–466.

(133) Yahiro, H.; Eguchi, Y.; Eguchi, K.; Arai, H. Oxygen Ion Conductivity of the Ceria-Samarium Oxide System with Fluorite Structure. *J. Appl. Electrochem.* **1988**, *18* (4), 527–531.

(134) Artini, C.; Pani, M.; Carnasciali, M. M.; Plaisier, J. R.; Costa, G. A. Lu-, Sm-, and Gd-Doped Ceria: A Comparative Approach to Their Structural Properties. *Inorg. Chem.* **2016**, *55* (20), 10567–10579.

(135) Dong, Y.; Li, D.; Feng, X.; Dong, X.; Hampshire, S. A High-Strength Sm-Doped CeO_2 Oxide-Ion Conducting Electrolyte Membrane for Solid Oxide Fuel Cell Application. *RSC Adv.*

2013, *3* (38), 17395.

(136) Gerhardt-Anderson, R.; Nowick, A. S. Ionic Conductivity of CeO_2 with Trivalent Dopants of Different Ionic Radii. *Solid State Ionics* **1981**, *5*, 547–550.

(137) Johnsson, M.; Lemmens, P. Perovskites and Thin Films—Crystallography and Chemistry. *J. Phys. Condens. Matter* **2008**, *20* (26), 264001.

(138) Chen, A.; Bi, Z.; Hazariwala, H.; Zhang, X.; Su, Q.; Chen, L.; Jia, Q.; MacManus-Driscoll, J. L.; Wang, H. Microstructure, Magnetic, and Low-Field Magnetotransport Properties of Self-Assembled $(La_{0.7}Sr_{0.3}MnO_3)_{0.5}$:$(CeO_2)_{0.5}$ Vertically Aligned Nanocomposite Thin Films. *Nanotechnology* **2011**, *22* (31), 315712.

(139) Shen, L.; Ma, C.; Cheng, S.; Ren, S.; Cheng, S.; Mi, S.; Liu, M. Enhanced Magnetic Properties in Epitaxial Self-Assembled Vertically Aligned Nanocomposite $(Pr_{0.5}Ba_{0.5}MnO_3)_{0.5}$:$(CeO_2)_{0.5}$ Thin Films. *J. Mater. Chem. C* **2016**, *4* (46), 10955–10961.

(140) Ding, Y.; Chen, Y.; Pradel, K. C.; Liu, M.; Lin Wang, Z. In-Situ Transmission Electron Microscopy Study of Oxygen Vacancy Ordering and Dislocation Annihilation in Undoped and Sm-Doped CeO_2 Ceramics during Redox Processes. *J. Appl. Phys.* **2016**, *120* (21), 214302.

(141) Park, J.; Biju, K. P.; Jung, S.; Lee, W.; Lee, J.; Kim, S.; Park, S.; Shin, J.; Hwang, H. Multibit Operation of TiO_2 -Based ReRAM by Schottky Barrier Height Engineering. *IEEE Electron Device Lett.* **2011**, *32* (4), 476–478.

(142) Yu, S.; Guan, X.; Wong, H.-S. P. Conduction Mechanism of TiN/HfO_x/Pt Resistive Switching Memory: A Trap-Assisted-Tunneling Model. *Appl. Phys. Lett.* **2011**, *99* (6), 063507.

(143) Houng, M. P.; Wang, Y. H.; Chang, W. J. Current Transport Mechanism in Trapped Oxides: A Generalized Trap-Assisted Tunneling Model. *J. Appl. Phys.* **1999**, *86* (3), 1488–1491.

(144) Pabst, G. W.; Martin, L. W.; Chu, Y.-H.; Ramesh, R. Leakage Mechanisms in $BiFeO_3$ Thin Films. *Appl. Phys. Lett.* **2007**, *90* (7), 072902.

(145) Crowell, C. R. Richardson Constant and Tunneling Effective Mass for Thermionic and Thermionic-Field Emission in Schottky Barrier Diodes. *Solid. State. Electron.* **1969**, *12* (1), 55–59.

(146) Ahrens, M.; Merkle, R.; Rahmati, B.; Maier, J. Effective Masses of Electrons in n-Type $SrTiO_3$ Determined from Low-Temperature Specific Heat Capacities. *Phys. B Condens. Matter* **2007**, *393* (1–2), 239–248.

(147) Frederikse, H. P. .; Thurber, W. R.; Hosler, W. R. Electronic Transport in Strontium Titanate. *Phys. Rev.* **1964**, *134* (2A), A442–A445.

(148) Mele, P.; Endo, T.; Arisawa, S.; Li, C.; Tsuchiya, T. *Oxide Thin Films, Multilayers, and Nanocomposites*; Mele, P., Endo, T., Arisawa, S., Li, C., Tsuchiya, T., Eds.; Springer International Publishing: Cham, 2015.

(149) Seidel, J.; Maksymovych, P.; Batra, Y.; Katan, A.; Yang, S.-Y.; He, Q.; Baddorf, A. P.; Kalinin, S. V.; Yang, C.-H.; Yang, J.-C.; et al. Domain Wall Conductivity in La-Doped $BiFeO_3$. *Phys. Rev. Lett.* **2010**, *105* (19), 197603.

(150) Eyring, L. Structure, Defects, and Nonstoichiometry in Oxides: An Electron Microscopic View. In *Nonstoichiometric Oxides*; Sørensen, O. T., Ed.; Academic Press, Inc.(London) Ltd.: London, 1981; pp 337–398.

(151) Tokura, Y.; Tomioka, Y. Colossal Magnetoresistive Manganites. *J. Magn. Magn. Mater.* **1999**, *200* (1–3), 1–23.

(152) Yin, L.; Wang, C.; Shen, Q.; Zhang, L. Strain-Induced Curie Temperature Variation in

$La_{0.9}Sr_{0.1}MnO_3$ Thin Films. *RSC Adv.* **2016**, *6* (98), 96093–96102.

(153) Hwang, H. Y.; Cheong, S.-W.; Radaelli, P. G.; Marezio, M.; Batlogg, B. Lattice Effects on the Magnetoresistance in Doped $LaMnO_3$. *Phys. Rev. Lett.* **1995**, *75* (5), 914–917.

(154) Dabrowski, B.; Kolesnik, S.; Baszczuk, A.; Chmaissem, O.; Maxwell, T.; Mais, J. Structural, Transport, and Magnetic Properties of $RMnO_3$ Perovskites (R=La, Pr, Nd, Sm, ^{153}Eu, Dy). *J. Solid State Chem.* **2005**, *178* (3), 629–637.

(155) Xie, C. K.; Budnick, J. I.; Hines, W. A.; Wells, B. O.; Woicik, J. C. Strain-Induced Change in Local Structure and Its Effect on the Ferromagnetic Properties of $La_{0.5}Sr_{0.5}CoO_3$ Thin Films. *Appl. Phys. Lett.* **2008**, *93* (18), 182507.

(156) Liao, Z.; Huijben, M.; Zhong, Z.; Gauquelin, N.; Macke, S.; Green, R. J.; Van Aert, S.; Verbeeck, J.; Van Tendeloo, G.; Held, K.; et al. Controlled Lateral Anisotropy in Correlated Manganite Heterostructures by Interface-Engineered Oxygen Octahedral Coupling. *Nat. Mater.* **2016**, *15* (4), 425–431.

(157) Tokura, Y. Critical Features of Colossal Magnetoresistive Manganites. *Reports Prog. Phys.* **2006**, *69* (3), 797–851.

(158) Tokura, Y. Orbital Physics in Transition-Metal Oxides. *Science.* **2000**, *288* (5465), 462–468.

(159) Mizokawa, T.; Khomskii, D. I.; Sawatzky, G. A. Interplay between Orbital Ordering and Lattice Distortions in $LaMnO_3$,YVO_3 and $YTiO_3$. *Phys. Rev. B* **1999**, *60* (10), 7309–7313.

(160) Abad, L.; Laukhin, V.; Valencia, S.; Gaup, A.; Gudat, W.; Balcells, L.; Martínez, B. Interfacial Strain: The Driving Force for Selective Orbital Occupancy in Manganite Thin Films. *Adv. Funct. Mater.* **2007**, *17* (18), 3918–3925.

(161) Yuan, Q. Comment on "Strain Effect and the Phase Diagram of $La_{1-x}Ba_xMnO_3$ Thin Films." *Phys. Rev. B* **2004**, *70* (6), 066401.

(162) Pesquera, D.; Herranz, G.; Barla, A.; Pellegrin, E.; Bondino, F.; Magnano, E.; Sánchez, F.; Fontcuberta, J. Surface Symmetry-Breaking and Strain Effects on Orbital Occupancy in Transition Metal Perovskite Epitaxial Films. *Nat. Commun.* **2012**, *3* (1), 1189.

(163) Kanki, T.; Tanaka, H.; Kawai, T. Anomalous Strain Effect in $La_{0.8}Ba_{0.2}MnO_3$ Epitaxial Thin Film: Role of the Orbital Degree of Freedom in Stabilizing Ferromagnetism. *Phys. Rev. B* **2001**, *64* (22), 224418.

(164) Goodenough, J. B. Theory of the Role of Covalence in the Perovskite-Type Manganites [La,Mn (II)MnO_3]. *Phys. Rev.* **1955**, *100* (2), 564–573.

(165) Endoh, Y.; Hirota, K.; Ishihara, S.; Okamoto, S.; Murakami, Y.; Nishizawa, A.; Fukuda, T.; Kimura, H.; Nojiri, H.; Kaneko, K.; et al. Transition between Two Ferromagnetic States Driven by Orbital Ordering in $La_{0.88}Sr_{0.12}MnO_3$. *Phys. Rev. Lett.* **1999**, *82* (21), 4328–4331.

(166) Geck, J.; Wochner, P.; Kiele, S.; Klingeler, R.; Reutler, P.; Revcolevschi, A.; Büchner, B. Orbital Polaron Lattice Formation in Lightly Doped $La_{1-x}Sr_xMnO_3$. *Phys. Rev. Lett.* **2005**, *95* (23), 236401.

(167) Hueso, L. E.; Rivas, J.; Rivadulla, F.; López-Quintela, M. A. Tuning of Colossal Magnetoresistance via Grain Size Change in $La_{0.67}Ca_{0.33}MnO_3$. *J. Appl. Phys.* **1999**, *86* (7), 3881–3884.

(168) Gu, H.; Zhang, X.; Wei, H.; Huang, Y.; Wei, S.; Guo, Z. An Overview of the Magnetoresistance Phenomenon in Molecular Systems. *Chem. Soc. Rev.* **2013**, *42* (13), 5907.

(169) Wang, X. L.; Dou, S. X.; Liu, H. K.; Ionescu, M.; Zeimetz, B. Large Low-Field Magnetoresistance over a Wide Temperature Range Induced by Weak-Link Grain Boundaries

in $La_{0.7}Ca_{0.3}MnO_3$. *Appl. Phys. Lett.* **1998**, *73* (3), 396–398.

(170) Cesaria, M.; Caricato, A. P.; Maruccio, G.; Martino, M. LSMO – Growing Opportunities by PLD and Applications in Spintronics. *J. Phys. Conf. Ser.* **2011**, *292* (1), 012003.

(171) Choi, W. S.; Kang, K. T.; Jeen, H.; Gai, Z.; Lee, H. N. Highly Insulating Ferromagnetic Cobaltite Heterostructures. *Curr. Appl. Phys.* **2017**, *17* (5), 722–726.

(172) Ramesh, R.; Spaldin, N. A. Multiferroics: Progress and Prospects in Thin Films. *Nat. Mater.* **2007**, *6* (1), 21–29.

(173) Baidya, S.; Saha-Dasgupta, T. Electronic Structure and Phonons in La_2CoMnO_6: A Ferromagnetic Insulator Driven by Coulomb-Assisted Spin-Orbit Coupling. *Phys. Rev. B* **2011**, *84* (3), 035131.

(174) Subramanian, M. A.; Ramirez, A. P.; Marshall, W. J. Structural Tuning of Ferromagnetism in a 3D Cuprate Perovskite. *Phys. Rev. Lett.* **1999**, *82* (7), 1558–1561.

(175) Matthias, B. T.; Bozorth, R. M.; Van Vleck, J. H. Ferromagnetic Interaction in EuO. *Phys. Rev. Lett.* **1961**, *7* (5), 160–161.

(176) Kleibeuker, J. E.; Choi, E.-M.; Jones, E. D.; Yu, T.-M.; Sala, B.; MacLaren, B. A.; Kepaptsoglou, D.; Hernandez-Maldonado, D.; Ramasse, Q. M.; Jones, L.; et al. Route to Achieving Perfect B-Site Ordering in Double Perovskite Thin Films. *NPG Asia Mater.* **2017**, *9* (7), e406.

(177) Vertruyen, B.; Cloots, R.; Abell, J. S.; Jackson, T. J.; da Silva, R. C.; Popova, E.; Keller, N. Curie Temperature, Exchange Integrals, and Magneto-Optical Properties in off-Stoichiometric Bismuth Iron Garnet Epitaxial Films. *Phys. Rev. B* **2008**, *78* (9), 094429.

(178) Lüders, U.; Bibes, M.; Bouzehouane, K.; Jacquet, E.; Contour, J.-P.; Fusil, S.; Bobo, J.-F.; Fontcuberta, J.; Barthélémy, A.; Fert, A. Spin Filtering through Ferrimagnetic $NiFe_2O_4$ Tunnel Barriers. *Appl. Phys. Lett.* **2006**, *88* (8), 082505.

(179) Haghiri-Gosnet, A.-M.; Renard, J.-P. CMR Manganites: Physics, Thin Films and Devices. *J. Phys. D. Appl. Phys.* **2003**, *36* (8), R127–R150.

(180) Brink, J. van den; Khaliullin, G.; Khomskii, D. Orbital Effects in Manganites. In *Colossal Magnetoresistive Manganites*; Springer Netherlands: Dordrecht, 2004; pp 263–301.

(181) Algarabel, P. A.; De Teresa, J. M.; Blasco, J.; Ibarra, M. R.; Kapusta, C.; Sikora, M.; Zajac, D.; Riedi, P. C.; Ritter, C. Peculiar Ferromagnetic Insulator State in the Low-Hole-Doped Manganites. *Phys. Rev. B* **2003**, *67* (13), 134402.

(182) Hu, L.; Sheng, Z.; Hu, X.; Zhang, R.; Wang, B.; Song, W.; Sun, Y. Control of the Charge/Orbital Ordering Transition in Epitaxial $La_{7/8}Sr_{1/8}MnO_3$ Thin Films through Compressive Strain. *J. Phys. D. Appl. Phys.* **2012**, *45* (17), 175002–175006.

(183) Moshnyaga, V. Metal-Insulator Transition and Magnetoresistance in Manganite Thin Films: Lattice Strain and Disorder Effects. In *Frontiers in Magnetic Materials*; Springer-Verlag Berlin Heidelberg GmbH: Berlin, 2005; pp 415–458.

(184) Ju, H. L.; Nam, Y. S.; Lee, J. E.; Shin, H. S. Anomalous Magnetic Properties and Magnetic Phase Diagram of $La_{1-x}Ba_xMnO_3$. *J. Magn. Magn. Mater.* **2000**, *219* (1), 1–8.

(185) Zhang, J.; Tanaka, H.; Kanki, T.; Choi, J.-H.; Kawai, T. Strain Effect and the Phase Diagram of $La_{1-x}Ba_xMnO_3$ Thin Films. *Phys. Rev. B* **2001**, *64* (18), 184404.

(186) Murugavel, P.; Lee, J. H.; Yoon, J. G.; Noh, T. W.; Chung, J. S.; Heu, M.; Yoon, S. Origin of Metal-Insulator Transition Temperature Enhancement in Underdoped Lanthanum Manganite Films. *Appl. Phys. Lett.* **2003**, *82* (12), 1908–1910.

(187) Mbatang, R.; Xue, D.; Enriquez, E.; Yuan, R.; Han, H.; Dowden, P.; Wang, Q.; Fohtung, E.; Xue, D.; Lookman, T.; et al. Enhanced Magnetism in Lightly Doped Manganite Heterostructures: Strain or Stoichiometry? *Nanoscale* **2019**, *11* (15), 7364–7370.

(188) Li, W.; Kleibeuker, J. E.; Wu, R.; Zhang, K. H. L.; Yun, C.; MacManus-Driscoll, J. L. Insulating-to-Conducting Behavior and Band Profile across the $La_{0.9}Ba_{0.1}MnO_3$/Nb:$SrTiO_3$ Epitaxial Interface. *Phys. Rev. B* **2017**, *96* (16), 165103.

(189) Murugavel, P.; Lee, J. H.; Lee, K.-B.; Park, J. H.; Chung, J.-S.; Yoon, J.-G.; Noh, T. W. Effects of Oxygen Annealing on the Physical Properties and Surface Microstructures of $La_{0.8}Ba_{0.2}MnO_3$ Films. *J. Phys. D. Appl. Phys.* **2002**, *35* (24), 3166–3170.

(190) Zhou, C.; Newns, D. M. Intrinsic Dead Layer Effect and the Performance of Ferroelectric Thin Film Capacitors. *J. Eng. Appl. Sci.* **1997**, *82* (6), 3081–3088.

(191) Meyer, T. L.; Jiang, L.; Park, S.; Egami, T.; Lee, H. N. Strain-Relaxation and Critical Thickness of Epitaxial $La_{1.85}Sr_{0.15}CuO_4$ Films. *APL Mater.* **2015**, *3* (12), 126102.

(192) Xie, Q. Y.; Wu, X. S.; Li, J.; Lv, B.; Gao, J. Probing the Dead Layer Thickness and Its Effect on the Structure and Magnetic Properties in $La_{2/3}Ca_{1/3}MnO_3$ Thin Films. *Thin Solid Films* **2013**, *545*, 89–93.

(193) Kourkoutis, L. F.; Song, J. H.; Hwang, H. Y.; Muller, D. A. Microscopic Origins for Stabilizing Room-Temperature Ferromagnetism in Ultrathin Manganite Layers. *Proc. Natl. Acad. Sci.* **2010**, *107* (26), 11682–11685.

(194) Vailionis, A.; Boschker, H.; Liao, Z.; Smit, J. R. A.; Rijnders, G.; Huijben, M.; Koster, G. Symmetry and Lattice Mismatch Induced Strain Accommodation near and Away from Correlated Perovskite Interfaces. *Appl. Phys. Lett.* **2014**, *105* (13), 131906.

(195) Koçak, A. B.; Varignon, J.; Lemal, S.; Ghosez, P.; Lepetit, M.-B. Control of the Orbital Ordering in Manganite Superlattices and Impact on Properties. *Phys. Rev. B* **2017**, *96* (12), 125155.

(196) Huijben, M.; Martin, L. W.; Chu, Y.-H.; Holcomb, M. B.; Yu, P.; Rijnders, G.; Blank, D. H. A.; Ramesh, R. Critical Thickness and Orbital Ordering in Ultrathin $La_{0.7}Sr_{0.3}MnO_3$ Films. *Phys. Rev. B* **2008**, *78* (9), 094413.

(197) King, P. D. C.; Wei, H. I.; Nie, Y. F.; Uchida, M.; Adamo, C.; Zhu, S.; He, X.; Božović, I.; Schlom, D. G.; Shen, K. M. Atomic-Scale Control of Competing Electronic Phases in Ultrathin $LaNiO_3$. *Nat. Nanotechnol.* **2014**, *9* (6), 443–447.

(198) Lee, H.-S.; Mizoguchi, T.; Yamamoto, T.; Kang, S.-J. L.; Ikuhara, Y. First-Principles Calculation of Defect Energetics in Cubic-$BaTiO_3$ and a Comparison with $SrTiO_3$. *Acta Mater.* **2007**, *55* (19), 6535–6540.

(199) Vailionis, A.; Boschker, H.; Siemons, W.; Houwman, E. P.; Blank, D. H. A.; Rijnders, G.; Koster, G. Misfit Strain Accommodation in Epitaxial ABO_3 Perovskites: Lattice Rotations and Lattice Modulations. *Phys. Rev. B* **2011**, *83* (6), 064101.

(200) Wimbush, S. C.; Li, M.; Vickers, M. E.; Maiorov, B.; Feldmann, D. M.; Jia, Q.; MacManus-Driscoll, J. L. Interfacial Strain-Indyced Oxygen Disorder as the Cause of Enhanced Critical Current Density in Superconducting Thin Films. *Adv. Funct. Mater.* **2009**, *19* (6), 835–841.

(201) Yuan, G.; Liu, J.-M.; Baba-Kishi, K.; Chan, H. L.; Choy, C.; Liu, Z. Possible Mechanism for Tunneling Magnetoresistance in $La_{0.9}Ba_{0.1}MnO_3$/Nb-Doped $SrTiO_3$ p^+–n Junctions. *Solid State Commun.* **2004**, *131* (6), 383–387.

(202) Cherepanov, V. A.; Filonova, E. A.; Voronin, V. I.; Berger, I. F. Phase Equilibria in the $LaCoO_3$–$LaMnO_3$–$BaCoO_z$–$BaMnO_3$ System. *J. Solid State Chem.* **2000**, *153* (2), 205–211.

(203) Nagabhushana, B. M.; Chandrappa, G. T.; Chakradhar, R. P. S.; Ramesh, K. P.; Shivakumara, C. Synthesis, Structural and Transport Properties of Nanocrystalline $La_{1-x}Ba_xMnO_3$ ($0.0 \leq x \leq 0.3$) Powders. *Solid State Commun.* **2005**, *136* (7), 427–432.

(204) Dabrowski, B.; Rogacki, K.; Xiong, X.; Klamut, P. W.; Dybzinski, R.; Shaffer, J. Synthesis and Properties of the Vacancy-Free $La_{1-x}Ba_xMnO_3$. *Phys. Rev. B* **1998**, *58* (5), 2716–2723.

(205) Mandal, P.; Ghosh, B. Transport, Magnetic, and Structural Properties of $La_{1-x}M_xMnO_3$ (M = Ba, Sr, Ca) for $0 \leq x \leq 0.20$. *Phys. Rev. B* **2003**, *68* (1), 014422.

(206) Gerward, L.; Staun Olsen, J.; Petit, L.; Vaitheeswaran, G.; Kanchana, V.; Svane, A. Bulk Modulus of CeO_2 and PrO_2 - An Experimental and Theoretical Study. *J. Alloys Compd.* **2005**, *400* (1–2), 56–61.

(207) Kanchana, V.; Vaitheeswaran, G.; Svane, A.; Delin, A. First-Principles Study of Elastic Properties of CeO_2, ThO_2 and PoO_2. *J. Phys. Condens. Matter* **2006**, *18* (42), 9615–9624.

(208) Chen, A.; Hu, J.-M.; Lu, P.; Yang, T.; Zhang, W.; Li, L.; Ahmed, T.; Enriquez, E.; Weigand, M.; Su, Q.; et al. Role of Scaffold Network in Controlling Strain and Functionalities of Nanocomposite Films. *Sci. Adv.* **2016**, *2* (6), e1600245.

(209) Zhu, C.; Zheng, R.; Su, J.; He, J. Ultrasonic Anomalies in $La_{0.67}Ca_{0.33}MnO_3$ near the Curie Temperature. *Appl. Phys. Lett.* **1999**, *74* (23), 3504–3506.

(210) Sankarrajan, S.; Sakthipandi, K.; Manivasakan, P.; Thyagarajan, K.; Rajendran, V. On-Line Phase Transition in $La_{1-x}Sr_xMnO_3$ ($0.28 \leq x \leq 0.36$) Perovskites through Ultrasonic Studies. *Phase Transitions* **2011**, *84* (7), 657–672.

(211) Mangalam, R. V. K.; Sundaresan, A. Structural, Magnetic and Magnetotransport Properties of $La_{0.7-x}Ce_xBa_{0.3}MnO_3$ (x=0.0-0.4). *J. Chem. Sci.* **2006**, *118* (1), 99–103.

(212) Mizusaki, J.; Mori, N.; Takai, H.; Yonemura, Y.; Minamiue, H.; Tagawa, H.; Dokiya, M.; Inaba, H.; Naraya, K.; Sasamoto, T.; et al. Oxygen Nonstoichiometry and Defect Equilibrium in the Perovskite-Type Oxides $La_{1-x}Sr_xMnO_{3+d}$. *Solid State Ionics* **2000**, *129* (1), 163–177.

(213) Pan, W.; Lu, P.; Ihlefeld, J. F.; Lee, S. R.; Choi, E. S.; Jiang, Y.; Jia, Q. X. Electrical-Current-Induced Magnetic Hysteresis in Self-Assembled Vertically Aligned $La_{2/3}Sr_{1/3}MnO_3$:ZnO Nanopillar Composites. *Phys. Rev. Mater.* **2018**, *2* (2), 021401(R).

(214) Vickers, M. E. *Advanced Handout from Graduate Lecture Course, X-Ray and Neutron Diffraction Methods.* *http://intranet.msm.cam.ac.uk/xray/camonly/Grad_Xray_Lectures_3-8_Handout_FINAL.pdf*; 2018.

(215) Yi, H.; Yu, J. Double-Exchange Model with Background Superexchange Interactions: Phase Diagrams of $La_{1-x}A_xMnO_3$ Manganites. *Phys. Rev. B* **1998**, *58* (17), 11123–11126.

(216) Chou, H.; Wu, C. B.; Hsu, S. G.; Wu, C. Y. Electron-Doped Colossal Magnetoresistance in the Sintered $La_{1-x}T_xMnO_3$. *Phys. Rev. B* **2006**, *74* (17), 174405.

(217) Loshkareva, N. N.; Mikhalev, K. N.; Fogel, I. A.; Mostovshikova, E. V. Korolev, A. V.; Solin, N. I.; Sukhorukov, Y. P.; Naumov, S. V.; Kostromitina, N. V. Balbashov, A. M.; Lukin, N. V. Effect of Cerium Doping on the Properties of $LaMnO_3$ Single Crystals. *Fiz. Met. i Met.* **2003**, *95* (2), 23–30.

(218) Morris, B. C.; Flavell, W. R.; Mackrodtb, W. C.; Morris, M. A. Lattice Parameter Changes in the Mixed-Oxide System $Ce_{1-x}La_xO_{2-x/2}$: A Combined Experimental and Theoretical Study. *J.*

Mater. Chem **1993**, *3* (10), 1007–1013.

(219) Mishra, D. K.; Sahu, D. R.; Mishra, P. K.; Singh, S. K.; Mohapatra, B. K.; Roul, B. K. Ce-Doped LCMO CMR Manganites: A Consequence of Enhanced T_c and T_{IM}. *Bull. Mater. Sci.* **2011**, *34* (7), 1501–1506.

(220) Shibata, T.; Bunker, B.; Mitchell, J. F.; Schiffer, P. Indications of Intrinsic Chemical and Structural Inhomogeneity in Lightly Doped $La_{1-x}Sr_xMnO_3$. *Phys. Rev. Lett.* **2002**, *88* (20), 207205.

(221) Kröger, F. A.; Vink, H. J. Relations between the Concentrations of Imperfections in Crystalline Solids. In *Journal of Physics and Chemistry of Solids*; 1956; Vol. 5, pp 307–435.

(222) Lebedev, O. I.; Van Tendeloo, G.; Amelinckx, S.; Razavi, F.; Habermeier, H.-U. Periodic Microtwinning as a Possible Mechanism for the Accommodation of the Epitaxial Film-Substrate Mismatch in the $La_{1-x}Sr_xMnO_3/SrTiO_3$ System. *Philos. Mag. A* **2001**, *81* (4), 797–824.

(223) Gebhardt, U.; Kasper, N. V.; Vigliante, A.; Wochner, P.; Dosch, H.; Razavi, F. S.; Habermeier, H. U. Formation and Thickness Evolution of Periodic Twin Domains in Manganite Films Grown on $SrTiO_3$ (001) Substrates. *Phys. Rev. Lett.* **2007**, *98* (9), 096101.

(224) Vigliante, A.; Gebhardt, U.; Rühm, A.; Wochner, P.; Razavi, F. S.; Habermeier, H. U. Coupling between Lattice Distortions and Magnetism in $La_{0.9}Sr_{0.1}MnO_3$ Thin Films. *Europhys. Lett.* **2001**, *54* (5), 619–625.

(225) Santiso, J.; Balcells, L.; Konstantinovic, Z.; Roqueta, J.; Ferrer, P.; Pomar, A.; Martínez, B.; Sandiumenge, F. Thickness Evolution of the Twin Structure and Shear Strain in LSMO Films. *CrystEngComm* **2013**, *15* (19), 3908.

(226) Zhu, W.; Jin, J.; Chen, X.; Li, C.; Wang, T.; Tsang, C.; Liang, C. Enhanced Activity and Stability of La-Doped CeO_2 Monolithic Catalysts for Lean-Oxygen Methane Combustion. *Environ. Sci. Pollut. Res.* **2018**, *25* (6), 5643–5654.

(227) He, C.; Ji, H.; Huang, Z.; Wang, T.; Zhang, X.; Liu, Y.; Fang, M.; Wu, X.; Zhang, J.; Min, X. Red-Shifted Emission in $Y_3MgSiAl_3O_{12}:Ce^{3+}$ Garnet Phosphor for Blue Light-Pumped White Light-Emitting Diodes. *J. Phys. Chem. C* **2018**, *122* (27), 15659–15665.

(228) Guo, H.; Dong, S.; Rack, P.; Budai, J.; Beekman, C.; Gai, Z.; Siemons, W.; Gonzalez, C.; Timilsina, R.; Wong, A. T.; et al. Strain Doping: Reversible Single-Axis Control of a Complex Oxide Lattice via Helium Implantation. *Phys. Rev. Lett.* **2015**, *114* (25), 256801.

(229) Choi, E. M.; Kursumovic, A.; Lee, O. J.; Kleibeuker, J. E.; Chen, A.; Zhang, W.; Wang, H.; Macmanus-Driscoll, J. L. Ferroelectric Sm-Doped $BiMnO_3$ Thin Films with Ferromagnetic Transition Temperature Enhanced to 140 K. *ACS Appl. Mater. Interfaces* **2014**, *6* (17), 14836–14843.

(230) Feng, Y.; Jin, K.; Gu, L.; He, X.; Ge, C.; Zhang, Q.; He, M. M.; Guo, Q.; Wan, Q.; He, M. M.; et al. Insulating Phase at Low Temperature in Ultrathin $La_{0.8}Sr_{0.2}MnO_3$ Films. *Sci. Rep.* **2016**, *6* (1), 22382.

(231) Tanaka, H.; Zhang, J.; Kawai, T. Giant Electric Field Modulation of Double Exchange Ferromagnetism at Room Temperature in the Perovskite Manganite/Titanate *p-n* Junction. *Phys. Rev. Lett.* **2001**, *88* (2), 027204.

(232) Liu, B.; Zhang, R.; Xie, Z. L.; Lu, H.; Liu, Q. J.; Zhang, Z.; Li, Y.; Xiu, X. Q.; Chen, P.; Han, P.; et al. Microstructure and Dislocation of Epitaxial InN Films Revealed by High Resolution X-Ray Diffraction. *J. Appl. Phys.* **2008**, *103* (2), 023504.

(233) Loke, W. K.; Tan, K. H.; Wicaksono, S.; Yoon, S. F.; Owen, M. H. S.; Yeo, Y.-C. Effect of Growth Temperature on the Epitaxy Strain Relaxation and the Tilt of $In_xAl_{1-x}As$ Graded Layer Grown by Solid-Source Molecular Beam Epitaxy. *J. Phys. D. Appl. Phys.* **2012**, *45* (50), 505106.

(234) Kumar, R.; Biswas, D. Tilt Investigation of In(Al,Ga)As Metamorphic Buffer Layers on GaAs (001) Substrate: A Novel Technique for Tilt Determination. *Cryst. Res. Technol.* **2016**, *51* (12), 723–729.

(235) Chierchia, R.; Böttcher, T.; Heinke, H.; Einfeldt, S.; Figge, S.; Hommel, D. Microstructure of Heteroepitaxial GaN Revealed by X-Ray Diffraction. *J. Appl. Phys.* **2003**, *93* (11), 8918–8925.

(236) Vickers, M. E.; Kappers, M. J.; Datta, R.; McAleese, C.; Smeeton, T. M.; Rayment, F. D. G.; Humphreys, C. J. In-Plane Imperfections in GaN Studied by X-Ray Diffraction. *J. Phys. D. Appl. Phys.* **2005**, *38* (10A), A99–A104.

(237) Fuentes-Perez, M. E.; Dillingham, M. S.; Moreno-Herrero, F. AFM Volumetric Methods for the Characterization of Proteins and Nucleic Acids. *Methods* **2013**, *60* (2), 113–121.

(238) Gwaze, P.; Annegarn, H. J.; Huth, J.; Helas, G. Comparison of Particle Sizes Determined with Impactor, AFM and SEM. *Atmos. Res.* **2007**, *86* (2), 93–104.

(239) Hishida, T.; Ohbayashi, K.; Kobata, M.; Ikenaga, E.; Sugiyama, T.; Kobayashi, K.; Okawa, M.; Saitoh, T. Empirical Relationship between X-Ray Photoemission Spectra and Electrical Conductivity in a Colossal Magnetoresistive Manganite $La_{1-x}Sr_xMnO_3$. *J. Appl. Phys.* **2013**, *113* (23), 233702.

(240) Hishida, T.; Ohbayashi, K.; Kobata, M.; Ikenaga, E.; Sugiyama, T.; Kobayashi, K.; Okawa, M.; Saitoh, T. Buried Well-Screened State in Photoemission Spectra of $La_{1-x}Sr_xMnO_3$. In *Proceedings of the 12th Asia Pacific Physics Conference (APPC12)*; The Physical Society of Japan, 2014; Vol. 012109, pp 1–4.

(241) Yoshimatsu, K.; Okabe, T.; Kumigashira, H.; Okamoto, S.; Aizaki, S.; Fujimori, A.; Oshima, M. Dimensional-Crossover-Driven Metal-Insulator Transition in $SrVO_3$ Ultrathin Films. *Phys. Rev. Lett.* **2010**, *104* (14), 147601.

(242) Chen, A.; Zhang, W.; Khatkhatay, F.; Su, Q.; Tsai, C.-F.; Chen, L.; Jia, Q. X.; MacManus-Driscoll, J. L.; Wang, H. Magnetotransport Properties of Quasi-One-Dimensionally Channeled Vertically Aligned Heteroepitaxial Nanomazes. *Appl. Phys. Lett.* **2013**, *102* (9), 093114.

(243) Singh, D. K.; Kamble, B.; Singh, A. Spin–charge and Spin–orbital Coupling Effects on Spin Dynamics in Ferromagnetic Manganites. *J. Phys. Condens. Matter* **2010**, *22* (39), 396001.

(244) Vaz, C. A. F. Electric Field Control of Magnetism in Multiferroic Heterostructures. *J. Phys. Condens. Matter* **2012**, *24* (33), 333201.

(245) Vaz, C. A. F.; Hoffman, J.; Ahn, C. H.; Ramesh, R. Magnetoelectric Coupling Effects in Multiferroic Complex Oxide Composite Structures. *Adv. Mater.* **2010**, *22* (26–27), 2900–2918.

(246) Hill, N. A. Why Are There so Few Magnetic Ferroelectrics? *J. Phys. Chem. B* **2000**, *104* (29), 6694–6709.

(247) Molegraaf, H. J. A.; Hoffman, J.; Vaz, C. A. F.; Gariglio, S.; van der Marel, D.; Ahn, C. H.; Triscone, J.-M. Magnetoelectric Effects in Complex Oxides with Competing Ground States. *Adv. Mater.* **2009**, *21* (34), 3470–3474.

(248) Yan, L.; Xing, Z.; Wang, Z.; Wang, T.; Lei, G.; Li, J.; Viehland, D. Direct Measurement of Magnetoelectric Exchange in Self-Assembled Epitaxial $BiFeO_3$–$CoFe_2O_4$ Nanocomposite Thin

Films. *Appl. Phys. Lett.* **2009**, *94* (19), 192902.

(249) Srinivasan, G.; Rasmussen, E. T.; Bush, A. A.; Kamentsev, K. E.; Meshcheryakov, V. F.; Fetisov, Y. K. Structural and Magnetoelectric Properties of MFe_2O_4-PZT (M = Ni,Co) and La $_x(Ca,Sr)_{1-x}MnO_3$-PZT Multilayer Composites. *Appl. Phys. A Mater. Sci. Process.* **2004**, *78* (5), 721–728.

(250) Vaz, C. A. F.; Hoffman, J.; Segal, Y.; Reiner, J. W.; Grober, R. D.; Zhang, Z.; Ahn, C. H.; Walker, F. J. Origin of the Magnetoelectric Coupling Effect in $Pb(Zr_{0.2}Ti_{0.8})O_3/La_{0.8}Sr_{0.2}MnO_3$ Multiferroic Heterostructures. *Phys. Rev. Lett.* **2010**, *104* (12), 127202.

(251) Nogués, J.; Schuller, I. K. Exchange Bias. *J. Magn. Magn. Mater.* **1999**, *192* (2), 203–232.

(252) Ahn, C. H.; Triscone, J.-M.; Mannhart, J. Electric Field Effect in Correlated Oxide Systems. *Nature* **2003**, *424* (6952), 1015–1018.

(253) Zhou, Z. Voltage Control of Magnetism, PhD Thesis, Northeastern University, 2014.

(254) Kim, C.; Li, G.; Li, J.; Jong, H.; Ro, C.; Song, Y.; Pak, G.; Im, S. Numerical Analysis on Effective Electric Field Penetration Depth for Interdigital Impedance Sensor. *J. Phys. Conf. Ser.* **2013**, *418* (1), 012020.

(255) Demin, R. V.; Koroleva, L. I.; Mukovskii, Y. M. Giant Volume Magnetostriction and Colossal Magnetoresistance at Room Temperature in $La_{0.7}Ba_{0.3}MnO_3$. *J. Phys. Condens. Matter* **2005**, *17* (1), 221–226.

(256) Ghatak, S. K.; Chaudhuri, I. A Possible Mechanism for Large Magnetostriction in Manganite System. *J. Magn. Magn. Mater.* **2003**, *261* (3), 442–448.

(257) Raveau, B.; Maignan, A.; Martin, C.; Hervieu, M. Colossal Magnetoresistance Manganite Perovskites: Relations between Crystal Chemistry and Properties. *Chem. Mater.* **1998**, *10* (10), 2641–2652.

(258) Lu, H.; George, T. A.; Wang, Y.; Ketsman, I.; Burton, J. D.; Bark, C.-W.; Ryu, S.; Kim, D. J.; Wang, J.; Binek, C.; et al. Electric Modulation of Magnetization at the $BaTiO_3/La_{0.67}Sr_{0.33}MnO_3$ Interfaces. *Appl. Phys. Lett.* **2012**, *100* (23), 232904.

(259) Kamble, A. S.; Sinha, B. B.; Chung, K.; Gil, M. G.; Burungale, V.; Park, C.-J.; Kim, J. H.; Patil, P. S. Effect of Hydroxide Anion Generating Agents on Growth and Properties of ZnO Nanorod Arrays. *Electrochim. Acta* **2014**, *149*, 386–393.

(260) Kumar, R.; Al-Dossary, O.; Kumar, G.; Umar, A. Zinc Oxide Nanostructures for NO_2 Gas–Sensor Applications: A Review. *Nano-Micro Lett.* **2015**, *7* (2), 97–120.

(261) Johnson, R. L. Characterization of Piezoelectric ZnO Thin Films and the Fabrication of Piezoelectric Micro-Cantilevers, Master Thesis, Iowa State University, 2005.

(262) Karanth, D.; Fu, H. Large Electromechanical Response in ZnO and Its Microscopic Origin. *Phys. Rev. B* **2005**, *72* (6), 064116.

(263) Gardeniers, J. G. E.; Rittersma, Z. M.; Burger, G. J. Preferred Orientation and Piezoelectricity in Sputtered ZnO Films. *J. Appl. Phys.* **1998**, *83* (12), 7844–7854.

(264) WÖll, C. The Chemistry and Physics of Zinc Oxide Surfaces. *Prog. Surf. Sci.* **2007**, *82* (2–3), 55–120.

(265) Jia, C.; Chen, Y.; Liu, X.; Yang, S.; Zhang, W.; Wang, Z. Control of Epitaxial Relationships of $ZnO/SrTiO_3$ Heterointerfaces by Etching the Substrate Surface. *Nanoscale Res. Lett.* **2013**, *8* (1), 23.

(266) Lu, P.; Romero, E.; Ihlefeld, J.; Pan, W.; Zhang, W.; Wang, H.; Jia, Q. Atomic-Scale EDS Mapping for Chemical Imaging and Quantification of Interdiffusion in Self-Assembled

Vertically Aligned Nanocomposite Thin Films. *Microsc. Microanal.* **2015**, *21* (S3), 2249–2250.

(267) Ahmed, H.; Khan, S.; Khan, W.; Nongjai, R.; Khan, I. Study of Structural, Electrical and Magnetic Properties of Zn Doped $La_{0.67}Sr_{0.33}MnO_3$. *J. Alloys Compd.* **2012**, *527*, 48–52.

(268) Schmidt, O.; Geis, A.; Kiesel, P.; Van de Walle, C. G.; Johnson, N. M.; Bakin, A.; Waag, A.; Döhler, G. H. Analysis of a Conducting Channel at the Native Zinc Oxide Surface. *Superlattices Microstruct.* **2006**, *39* (1–4), 8–16.

(269) Wei, X. H.; Li, Y. R.; Zhu, J.; Huang, W.; Zhang, Y.; Luo, W. B.; Ji, H. Epitaxial Properties of ZnO Thin Films on $SrTiO_3$ Substrates Grown by Laser Molecular Beam Epitaxy. *Appl. Phys. Lett.* **2007**, *90* (15), 151918.

(270) Cho, D.-H.; Kim, J.-H.; Moon, B.-M.; Jo, Y.-D.; Koo, S.-M. Control of a- and c-Plane Preferential Orientations of ZnO Thin Films. *Appl. Surf. Sci.* **2009**, *255* (6), 3480–3484.

(271) Trukhanov, S. V. Magnetic and Magnetotransport Properties of $La_{1-x}Ba_xMnO_{3-x/2}$ Perovskite Manganites. *J. Mater. Chem.* **2003**, *13* (2), 347–352.

(272) Ueda, S.; Tanaka, H.; Ikenaga, E.; Kim, J. J.; Ishikawa, T.; Kawai, T.; Kobayashi, K. Mn 2*p* Core-Level Spectra of $La_{1-x}Ba_xMnO_3$ Thin Films Using Hard X-Ray Photoelectron Spectroscopy: Relation between Electronic and Magnetic States. *Phys. Rev. B* **2009**, *80* (9), 092402.

(273) Ueda, S.; Takami, H.; Kanki, T.; Tanaka, H. Coherent Metallic Screening in Core-Level Photoelectron Spectra for the Strongly Correlated Oxides $La_{1-x}Ba_xMnO_3$ and $V_{1-x}W_xO_2$. *Phys. Rev. B* **2014**, *89* (3), 035141.

(274) Horiba, K.; Taguchi, M.; Chainani, A.; Takata, Y.; Ikenaga, E.; Miwa, D.; Nishino, Y.; Tamasaku, K.; Awaji, M.; Takeuchi, A.; et al. Nature of the Well Screened State in Hard X-Ray Mn 2*p* Core-Level Photoemission Measurement of $La_{1-x}Sr_xMnO_3$. *Phys. Rev. Lett.* **2004**, *93* (23), 236401.

(275) Ramos, A. Y.; Souza-Neto, N. M.; Tolentino, H. C. N.; Bunau, O.; Joly, Y.; Grenier, S.; Itié, J.-P.; Flank, A.-M.; Lagarde, P.; Caneiro, A. Bandwidth-Driven Nature of the Pressure-Induced Metal State of $LaMnO_3$. *Europhys. Lett.* **2011**, *96* (3), 36002.

(276) Endo, T.; Nonomura, S.; Yokura, M.; Nagashima, M.; Choi, W.; Reddy, S. L.; Kaneko, S.; Nishikawa, H.; Iwata, N.; Nakamura, Y. Light Switching of Resistance of LBMO/ZnO Hetero *p-n* Junction. In *2015 International Conference on Microwave and Photonics (ICMAP)*; IEEE, 2015; Vol. 111, pp 1–3.